DISSERTATION

Defence held on 04/12/2023 in Esch-sur-Alzette

to obtain the degree of

DOCTEUR DE L'UNIVERSITÉ DU LUXEMBOURG

EN PHYSIQUE

by

Alice DEBOT

Born on 29 September 1994 in Arlon (Belgium)

INKJET PRINTED BUFFER LAYERS FOR CU(IN,GA)(S,SE)₂ SOLAR CELLS

Dissertation defence committee

Prof. Dr Phillip Dale, dissertation supervisor
Professor, Université du Luxembourg

Dr Negar Naghavi
CNRS – IPVF, Palaiseau

Prof. Dr Susanne Siebentritt, Chairman
Professor, Université du Luxembourg

Dr Emmanuel Defay, Vice Chairman
Luxembourg Institute of Science and technology

Contents

Abstract

The demand for photovoltaics (PV) is increasing to meet the requirement of the Paris agreement. $Cu(In,Ga)(S,Se)_2$ (CIGSSe) technology is gaining some parts of the market which is currently dominated by silicon cells. This thesis focuses on the electron transfer layer (buffer layer) of CIGSSe technology. An increase in the demand of PV means an increase in the consumption of raw materials. The current deposition techniques of the buffer produce significant waste of materials because of their low utilization efficiency. In this thesis, inkjet printing, a high material utilization deposition technique, is proposed as an alternative for the buffer layer.

Inkjet printing requires the synthesis of an ink that is deposited on a substrate to form a continuous film with the appropriate properties to form a pn junction with CIGSSe. In this work, In_2S_3, CdS and Zn(O,S) layers are synthesized through combustion reaction. Their morphology, chemical composition, crystallinity and optical properties are investigated and their efficiency as buffer layers is tested in CIGSSe devices. In order to form a desirable film morphology, different solvent mixtures were tested and the ternary water, ethanol and propylene glycol mixture showed the highest power conversion efficiency when applied to the solar cell, which was attributed to a smoother macro-morphology.

Solution processed In_2S_3 has already been studied in the past and it was argued that a pre-synthesized S-In bond (called tristhioureaindium(III) chloride Complex) in the ink was essential for an oxygen free In_2S_3. It is shown in this work that the Complex is spontaneously created in solution and no pre-formation (powder) is required. The formation of oxide is avoided in both cases and the efficiency of completed devices was comparable to a reference with a Zn(O,S) buffer.

In this Complex, the ratio of sulfur to indium ([S]/[In]) is 3. Inks with [S]/[In] ratios of 2, 1.5 and 1 (without pre-synthesis of a complex) were studied and it was shown that a [S]/[In]=2 is optimal in terms of efficiency. The record In_2S_3 based device has an efficiency of 16.5%, which is 0.5% higher than the reference with a Zn(O,S). In terms of morphology, a high porosity was found for [S]/[In]$\geq$2, while the layers were dense for [S]/[In]$\leq$1.5. This porosity is found to be related to solid state dewetting and is influenced by the sulfur content as well as the substrate nature. The film based on [S]/[In]$\geq$2 did not show the presence of oxide, while the [S]/[In]$\leq$1.5 incorporated oxygen, proving the importance of an excess of thiourea in the ink.

An inkjet printable CdS layer was synthesized to replace the wasteful chemical bath deposition. Due to the instability of the ink containing both the cadmium and sulfur sources, two inks were printed successively. The layer ordering is important and the highest efficiency and smoothest morphology was obtained by printing the cadmium source, followed by the thiourea. The efficiency of this inkjet printed buffer in a CIGSSe device was similar to the conventional chemical bath deposited CdS reference.

$Zn(O,S)$ is a semiconductor that has attracted interest thanks to its wide band gap, increasing light absorption in the absorber layer. In this work, the band gap of In_2S_3, CdS and $Zn(O,S)$ buffer layers were found wider than their bulk counterparts. This was associated to the small crystallite size producing quantum confinement effects. The Brus equation gave a trend in the variation of the band gap with the crystallite size which can be controlled via the annealing temperature of the material.

Inkjet printing is a versatile technique that enables the near zero waste deposition of buffer layers. The efficiency of the devices with inkjet printed buffers are similar to the common deposition techniques that have been used for decades. Many more materials can be synthesized using this technique and the future development is nearly infinite.

Work done in collaboration

The measurements presented in this thesis were carried out by the author, with the following exceptions:

- The XPS measurements and analysis were done by Jérôme Guillot and Christèle Vergne from the Luxembourg Institute of Science and Technology (LIST).

- The TGA measurement was performed by Régis Vaudemont from LIST.

- The Raman measurements were carried out by Ricardo Poeira (University of Luxembourg (UniLu)) except for fig 7.7 that was done by Mael Guennou (LIST).

- Michele Melchiorre (UniLu) performed the FE SEM from fig 5.41 as well as the deposition of gold, Mo, window layers and front contacts of the cells.

- The AFM data were acquired and treated by Jonathan Rommelfangen (UniLu).

- The TEM images and SAED analysis were performed by Adrian-Marie Phillipe from LIST.

- The FIB SEM image from fig 5.6 was measured by Didier Arl from LIST. The Pt deposition was done by Brahime El Adib from LIST.

- The PL measurements and qFLs extraction were carried out by Aubin Prot (UniLu).

- The HIM-SIMS measurements were performed by Jean-Nicolas Audinot (LIST).

The absorbers used as of section 5.5 were kindly provided by Avancis.

Chapter 1

Introduction

"Humanity has opened the gates to hell", dixit Antonio Guterres (secretary general of the United Nation 2023).

From 1990 to 2017, the world electricity consumption has doubled. The sources of this electricity are essentially coal, oil, natural gas and nuclear. Since 2010, more environment friendly methods, such as hydro, wind and photovoltaics have been deployed. Nevertheless, in 2017, 38.5% of the electricity production still came from coal and only 1.7% from photovoltaics [1]. This discrepancy between clean and carbon contributing energy sources has damaging effects on the Earth's health. Indeed, the emission of greenhouse gas (GHG), such as CO_2, the deforestation for cattle production, etc lead to climate change and the destruction of ecosystems [2]. Greenhouse gas, produced in huge volume every year, are responsible for the global warming by trapping the reflected sun's radiations inside the Earth's atmosphere which leads to the increase of its total temperature.

In the period 2006-2015, the global Earth's surface temperature has increased by 0.87°C relative to the pre-industrial period (1850-1900). The estimated current rise is of 0.2°C per decade due to past and ongoing pollution [3]. The Intergovernmental Panel On Climate Change (IPCC) from the United Nations have published a report on the impacts of 1.5°C global warming above the pre-industrial level. This level is the maximum that should be reached during the 21st century to limit critical damage to the Earth.

One of the reasons to switch to renewable energies is to decrease the production of greenhouse gas. The main GHG, CO_2, which leads to global warming, comes from the burning of coal, oil and gas. An important point of the IPCC report is the urge to arrive to a **net zero** CO_2 emission. Depending on the date of this achievement, the **cumulative** CO_2 emissions, which is directly related to the global warming, can be decreased. Thus, the faster the net zero CO_2 emission is achieved, the lower the final temperature on Earth. Four different scenarios have been imagined to decrease the global net CO_2 emissions. One of them involves the switch to clean energy production and to a lesser extent the reduction in energy demand [4]. In this scenario, by 2030, primary energy from coal should decrease

by 75% compared to the current production and renewable energies should increase by 48% [3].

One form of renewable energy technology with few emissions is PV. A lot of research has already been conducted in this field. Different materials and techniques have been used, each of them having advantages and disadvantages depending on the final application of the PV devices. Since a long time ago, photovoltaics has proven its efficiency outside the laboratory to the point that it is now common to see building applied photovoltaics in cities: a well known example of it is panels installed on the roof of houses.

The demand in private solar panels is increasing fast which induces a bigger demand in raw materials. However, the Earth has limited resources and these should be used with parsimony. Silicon solar cells are the most well known material used in photovoltaics for general public and this material is not only used in photovoltaics but also in most electronic devices. Alternative materials are already of interest in PV, such as $Cu(In,Ga)(S,Se)_2$ (CIGSSe) since it requires less energy to make per watt peak compared to silicon. This technology is exploited in this thesis. Usually, the materials used in CIGSSe cells are deposited with techniques creating considerable waste. To circumvent this issue, inkjet printing, which is nearly waste-free, is used to investigate a new deposition and annealing methodology to create layers (called buffers) present in the CIGSSe devices. A focus is given to indium sulfide and cadmium sulfide synthesized through combustion reaction and $Zn(O,S)$ will be briefly discussed. CdS has been used for decades in CIGSSe but is often deposited through chemical bath which is wasteful. This disadvantage can be circumvented by using inkjet printing. In_2S_3 is a buffer that has often been used to replace CdS, thanks to its low toxicity. $Zn(O,S)$ has also attracted interest for its low toxicity but mainly because of its wide band gap. More details can be found in chapter 2.

The research of this thesis is structured as follow. First, the basics of semiconductors and CIGSSe technology are discussed (chapter 2). Then, the measurement techniques (chapter 3) enabling the characterization of the inks (used for the inkjet printing process), the synthesized films (morphology, crystallinity, chemical composition, optics) and finally the performance of the solar cells. In chapter 4, the basics of inkjet printing and the requirements on the ink properties (viscosity and surface tension) are explained. The wetting of the inks on different substrates is assessed. It is also shown that controlling the wetting is essential to ensure a satisfying morphology of the layer. In chapter 5, an inkjet printable In_2S_3 is presented. The effect of many parameters on the cells performance is studied. To do so, the solvents mixture, salts complex pre-formation, sulfur content and annealing temperature are varied. Different characterization techniques are used to determine the influence of these parameters on the morphology, crystallinity, chemical composition and optical properties of the layer. This study leads to a record In_2S_3 based device with an efficiency of 16.5%, which is 0.5% higher than the reference with a $Zn(O,S)$

buffer. In chapter 6, a buffer layer made of CdS is developed. CdS is the material that was commonly used in the past as a buffer layer. In the meantime, scientists have tried to remove it from their devices because of its toxicity. An inkjet printable CdS is proposed to enable its use with near zero waste. Finally, a quantum approach for these layers is proposed in chapter 7 to explain some of the observed optical/electronic properties of the films. Indeed, the buffer forms a pn junction with the CIGSSe absorber. However, the light absorbed in the buffer is nearly completely lost. A wide band gap is thus required. The band gap of the buffer layers synthesized in this work is discussed as a function of the crystallite size in the material based on the Brus model describing quantum confinement effects. It is then followed by a conclusion and outlook of this work.

Chapter 2

Background

This chapter introduces the essential knowledge to understand the results shown in this work. An introduction of semiconductor physics is first presented, followed by the description of the CIGSSe technology and a buffer layer review (which is the core of this work).

2.1 Physics of semiconductors

In this section, the basic principles of semiconductors will be exposed. The type of the semiconductor is introduced as well as the pn junction formation and working principle. Then, the generation of the electron-hole pair is discussed as well as the possible recombination paths. All these principles can be found with more details in the following textbooks [5], [6], [7] [8],[9].

2.1.1 Doping of semiconductors

Semiconductors are characterized by a forbidden region between the valence and the conduction band: no electron is allowed in this region. The width of the forbidden region is defined as the band gap which corresponds to the energy difference between the maximum of the valence band and the minimum of the conduction band.

The Fermi level represents the occupation of the valence and the conduction bands. At 0K in an intrinsic semiconductor, the Fermi level is near the valence band because all electrons have the minimum energy and are in the valence band. When the temperature is near room temperature, the Fermi level is somewhere in the middle between the valence and the conduction bands (fig 2.1). Indeed, when temperature increases, electrons gain enough energy to occupy higher energy levels which shifts the Fermi level up. The electrons that jump from the valence to the conduction bands leave "the counter particles" called holes. For intrinsic semiconductors, the concentration of electrons (n_0) and holes (p_0) are identical.

$$n_0 = N_C \ exp\left(-\frac{E_c - E_F}{k_B T}\right) \quad (2.1)$$

$$p_0 = N_V \ exp\left(-\frac{E_F - E_V}{k_B T}\right) \quad (2.2)$$

with N_C and N_V the effective density of states of the conduction and valence band respectively, E_F is the Fermi level energy, E_C and E_V are the conduction band minimum and valence band maximum energies, k_B is the Boltzmann constant and T is the temperature.
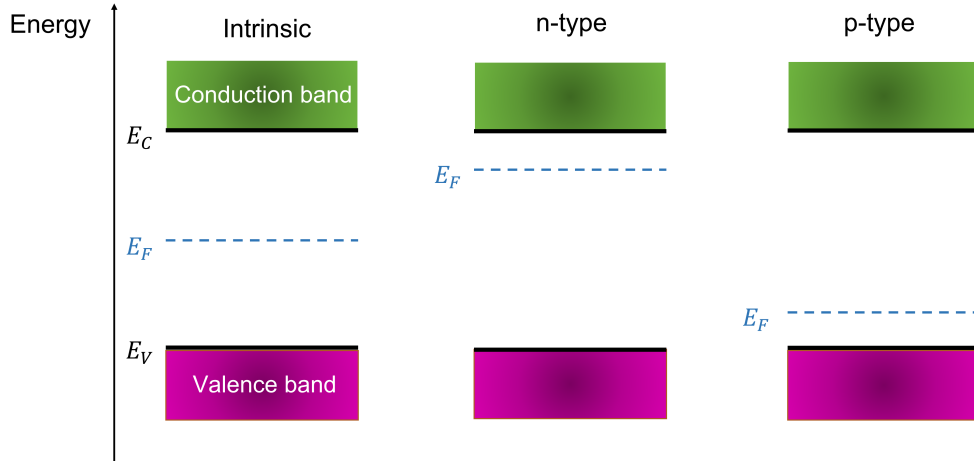
Figure 2.1: Band diagrams of an intrinsic, an n-doped and a p-doped semiconductors.

Semiconductors can have different doping that moves the Fermi level up or down. The doping consists on adding foreign atoms to the host materials to change the total amount of electrons. As already discussed, in an intrinsic semiconductor, the Fermi level lies around midgap. When a semiconductor is doped with electron rich atoms (meaning that the foreign atom has more electrons than the hosting atoms), it is called n-type. The foreign atoms, called donors, provide electrons that fill the higher energy levels, shifting the Fermi level up (fig 2.1). For p-type semiconductors, the foreign atoms, called acceptors, have less electrons than the host atoms, which can also be interpreted as atoms rich in holes, which shifts the Fermi level down (fig 2.1).

When a semiconductor is illuminated, more electrons jump to the conduction band and holes are created. This illumination acts as a perturbation, that if not too big, enables the formation of a quasi thermal equilibrium, i.e. a state in which the charge carriers are in equilibrium after relaxation. In other words, the electrons distribute themselves in the conduction band as if they are at equilibrium and they have their own Fermi level. The same description is true for the holes in the valence band. These apparent Fermi levels are called quasi Fermi levels (fig 2.2). This representation is possible because the relaxation of the electrons and holes (also called thermalization) within the bands is faster than the relaxation between the band (i.e recombination). Indeed, the former happens by

scattering from the lattice while the latter occurs through the interaction with another carrier. The time scale associated to each process is on the order of $10^{-15} - 10^{-12}$ s and $10^{-9} - 10^{-6}$ s respectively. The electron (hole) quasi Fermi level E_{FC} (E_{FV}) represents
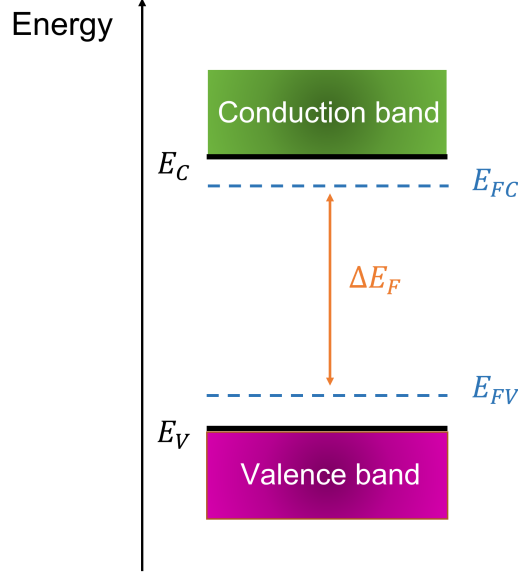
Figure 2.2: Quasi Fermi level splitting of semiconductor under illumination.

the electrons (holes) concentration. Their density is thus changed compared to the eq 2.1 and 2.2 and are given by

$$n = N_C \ exp \left(-\frac{E_C - E_{FC}}{k_B T} \right) \tag{2.3}$$

$$p = N_V \ exp \left(-\frac{E_{FV} - E_V}{k_B T} \right) \tag{2.4}$$

The product of the charge carriers densities gives

$$np = N_C \ N_V \ exp \left(\frac{\Delta E_F - E_g}{k_B T} \right) \tag{2.5}$$

where ΔE_F is the quasi Fermi level splitting (qFLs) which represents the maximum voltage possible for the solar cell. This will be further discussed in section 3.6.2.

2.1.2   pn junction

When a p-type and a n-type semiconductors are put in contact, a pn junction is formed. The electrons from the n-type material diffuse to the p-type material, while the holes diffuse from the p to n type semiconductor (fig 2.3a). The p-type (n-type) material is rich in negative (positive) charges at the junction. This charge separation creates an electric field that drives the movement of the charges in the opposite direction, which ultimately leads to an equilibrium state for the distribution of positive and negative

charges. The width of this region, called depletion region, depends on the doping of each semiconductor. Figure 2.3b shows the distribution of the charges as a function of the depletion charge. The product of the width of the region and the depletion charge of the first semiconductor should be equal to the same product for the second semiconductor, i.e. the area of the rectangles should be equal. As a result, if the first semiconductor is highly doped compared to the second, the width of the depletion region in the second semiconductor is big. The size of the depletion region is given by the sum of the widths in both semiconductors $W = W_{D,p} + W_{D,n}$, with $W_{D,p}$ ($W_{D,n}$) the space charge region in the p-type (n-type) semiconductor.
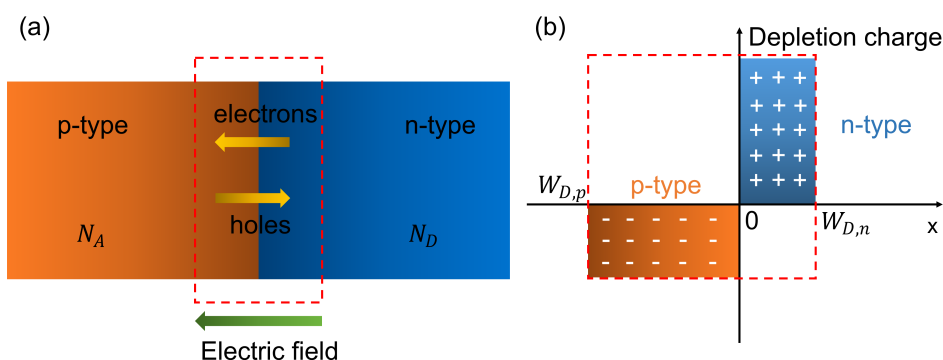
Figure 2.3: Sketch of (a) a pn junction and (b) the spatial distribution of charges in the depletion region. The dashed red region represents the depletion region.

In terms of energy, the n and p types semiconductors have different Fermi levels: the n type is rich in negative charges and the Fermi level is near the conduction band, and the p type is poor in negative charges which gives a Fermi level near the valence band (fig 2.4a). When put in contact, the Fermi levels of the n and p type semiconductors align and the valence and conduction bands bend (fig 2.4b). This bending occurs in the depletion region, also called space charge region (SCR). Outside this region, the n and p type semiconductor are called quasi neutral regions (QNR). The diagram shown here is a simplified version. Indeed, the band gap of both the n and p type semiconductors is identical, which is in our case not true. This will be discussed further when the CIGSSe solar cell structure is introduced (section 2.2.1).

2.1.3 Generation of electron-hole pairs

The working principle of a solar cell is based on the generation of the electron-hole pair through the absorption of a photon. Once the couple is generated, the electric field at the pn junction separate them: the electrons are sent to the n-type semiconductor, while the holes are kept in the p-type semiconductor. In order to extract the electrons

Figure 2.4: Band diagram of (a) p and n semiconductors and (b) a pn heterojunction.

from the device and produce a current, the semiconductors have to be connected to an external circuit.

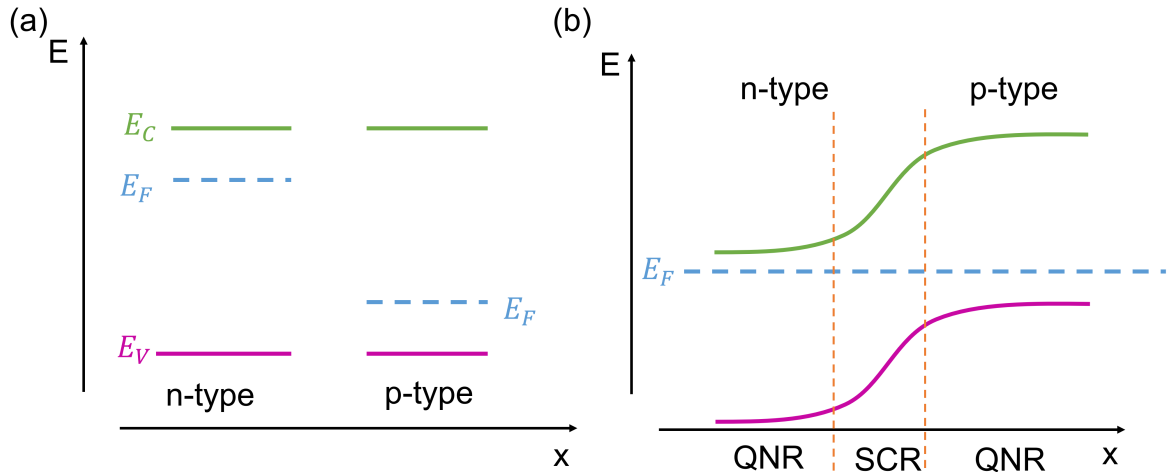The energy required to create a pair depends on the band gap of the absorber. The excitation of an electron can occur only if the energy of the incoming photon is higher than the band gap. It is thus possible to choose which part of the solar spectrum is absorbed. Indeed, the energy of a photon depends on its wavelength via the relation

$$E = hf = h\frac{c}{\lambda} \tag{2.6}$$

with f, h, c and λ the frequency of the photon, Planck's constant, light velocity and wavelength of the photon. A semiconductor with a narrow band gap can absorb a significant part of the solar spectrum (fig 2.5a), however photons with an energy much higher than the band gap generates electron in the conduction band (CB) with an energy much higher than the CB minimum (CBM). These electrons decrease their energy by thermalization to reach the CBM and this energy is lost. A semiconductor with a wider band gap (fig 2.5b) absorbs a shorter range of the solar spectrum but less energy is lost in thermalization. The Shockley-Queisser limit, which is a model in which the solar cell efficiency limit is calculated by taking into account all the losses inside and outside the cell, showed that the band gap giving the highest efficiency is 1.1 eV under one Sun illumination.

Once the electron-hole pair is generated, the electric field separate them and a current flows through the circuit connected to the solar cell. However, several losses can occur through recombinations that will be described in the next section.
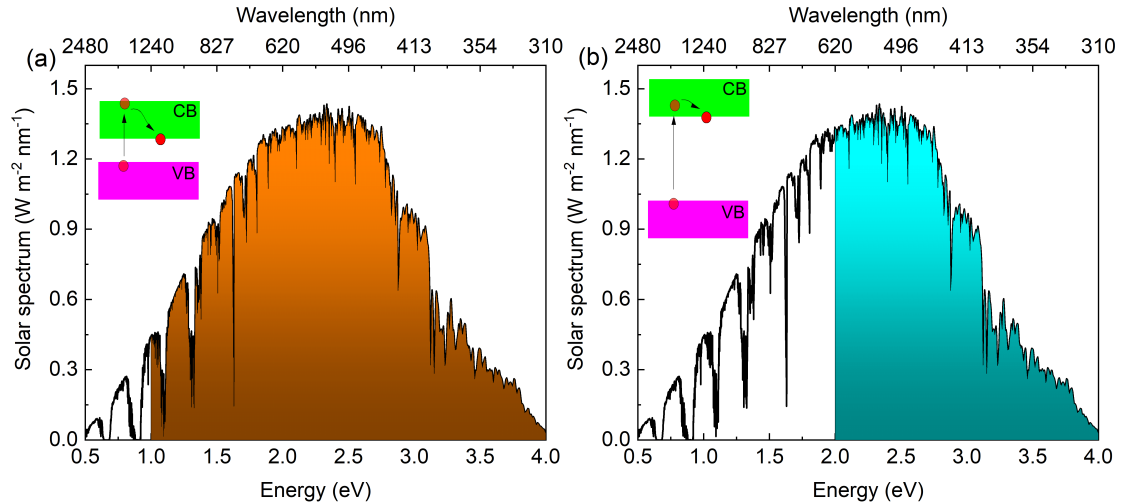
Figure 2.5: Absorption of the solar spectrum by a semiconductor with a band gap of (a) 1 eV and (b) 2 eV. Insets of the graphs show the extent of the thermalization in each case. The red circle represents an electron. VB and CB are the valence and conduction bands.

2.1.4 Radiative and non radiative recombinations

Some electrons that were generated in the p-type material will not be collected and will be lost through recombinations. Three types of recombinations are possible. The first one is the radiative recombination: when an electron and a hole recombine, a photon with an energy similar to the band gap is emitted. Because of its low energy, the photon has a low probability to be absorbed and thus it leaves the material (fig 2.6).

The second type is a non-radiative recombination that happens through defects. The presence of defects introduces new energy levels in the forbidden energy band. Thus, an electron in the conduction band can fall on one of the new energy levels and, if a hole jump on that level, they recombine (fig 2.6).

Non-radiative recombinations can occur through defect traps inside the crystal structure. However, this represents only recombinations without taking into account the pn junction. Indeed, many recombinations occur at the interface between the different layers. The source can be defects in the crystal due to broken bonds but also to extrinsic impurities from the environment or impurities that are rejected to the surface during the growth of the material.

Recombinations occuring in the p-type semiconductor are called bulk recombinations, while it is called interface remcombinations for the interfaces. It is possible to determine which type of recombinations is dominating in a solar cell by measuring the diode factor. This factor can be found via the measurement of the performance of the solar cell. The
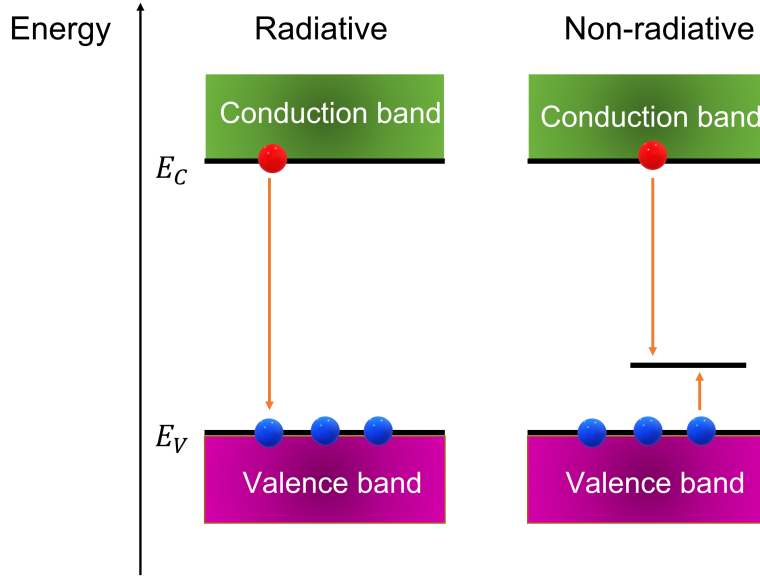
Figure 2.6: Radiative and non-radiative recombination processes in a semiconductor.

current density generated by the solar cell in the dark (without illumination) is given by

$$j_d = j_0 \left(exp \left(\frac{qV}{nk_BT} \right) - 1 \right) \tag{2.7}$$

where j_0, n, k_B and T are the diode saturation current density, the diode factor, the Boltzmann constant and the cell temperature. For an ideal diode, n=1. When the interface recombinations are dominant, n≥2. When 1<n≪2, the bulk recombinations (i.e. recombinations in the p-type semiconductor) are dominant. More details about the measurement of the current density will be given in section 3.6.1.

2.2   Buffer layers for Cu(In,Ga)(S,Se)$_2$ application

In this work, the Cu(In,Ga)(S,Se)$_2$ thin film technology is used to generate electricity. This material, also called CIGSSe, is the p-type material that is used to absorb light and form electron-hole pairs. As discussed earlier, a n-type material, called the buffer, is necessary to form a pn junction in order to separate these charge carriers. The structure of the solar cell will be discussed in this section and a literature review of the buffer layers used in this technology.

2.2.1   CIGSSe solar cell structure

The structure of the solar cell is shown in figure 2.7. The stack begins with a soda lime glass (SLG) substrate on which a molybdenum layer is sputtered (∼500 nm) and plays the role of the metallic back contact. SLG is preferred as a substrate for non-flexible

substrate because of its Na content. It was shown that Na can improve the efficiency of the solar cell when it is introduced during the growth of the absorber, which can occur because of SLG heating [10]. Mo is used as a back contact because of its high conductivity and ability to withstand high temperatures. Moreover, Na was shown to be able to diffuse through it [11]. However, Mo's surface is a highly recombinative layer and manipulating the absorber composition can be performed to mitigate it. This will be explained in the CIGSSe description below.

The p-type semiconductor, called absorber, is deposited on the Mo layer. Many deposition techniques [12], such as sputtering, evaporation as well as solutions processes can be used to deposit it. This layer is typically 2-3 μm. Indeed, in order to have a full absorption, 1 μm is required. However, the real thickness used is increased to minimize back side recombinations among others. When charge carriers are generated near the back contact, they can recombine due to interface defects. The chemical composition of the CIGSSe layer can be tuned to modify the band gap and to mitigate the back surface recombination.
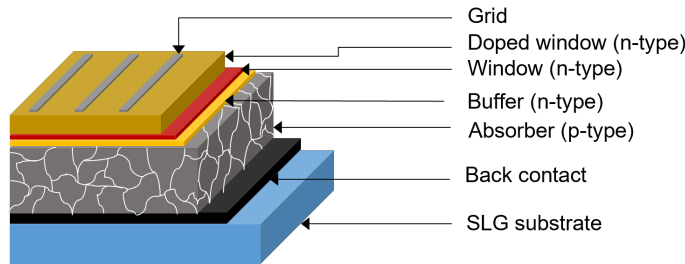
Figure 2.7: CIGSSe solar cell structure.

In the compound $CuIn_{1-x}Ga_xSe_2$, the band gap can be tuned by changing the ratio of In over Ga [6]:

$$E_g^{CIGSe}(x) = 1.04 + 0.65x - 0.26x(1 - x) \tag{2.8}$$

This equation is empirical and the extreme values are 1.04 eV for pure CISe and 1.68 eV for pure CGSe. This equation is true for CIGSe, i.e. sulfur free absorber. Ga increases the band gap, which is not strictly useful given that the band gap of pure CISe is near the ideal band gap to obtain the highest efficiency. However, Ga is incorporated in the material with a graded profile, i.e. low concentration at the front and high concentration at the back, in order to increase the band gap near the back contact. Indeed, as already stated, back side recombination can occur for charge carriers generated in this region. To circumvent this issue, a widen band gap can push the electrons toward the front and drag the holes toward the back of the cell (fig 2.8). This role is partially ensured by the $MoSe_2$ compound that naturally forms during the growth of the absorber but is usually insufficient.

The absorber used in this work also contains sulfur, which is usually concentrated at the front of the absorber [13]. Its effect is to increase the band gap of the material at the front as confirmed by the following relationship defining the band gap as a function of the chemical composition. In the case of the $\mathrm{Cu(In_{1-x}Ga_x)(S_ySe_{1-y})_2}$ compound, the band gap can be found through the following relationship [14]

$$E_g^{CIGSSe}(x,y) = 1.00 + 0.13x^2 + 0.08x^2y + 0.13xy + 0.55x + 0.54y \qquad (2.9)$$

The incorporation of S essentially shifts the valence band down, without influencing much the conduction band. It thus acts in the opposite way of Ga, i.e. it reflects the hole towards the back (fig 2.8) and therefore minimizes the recombinations [15].
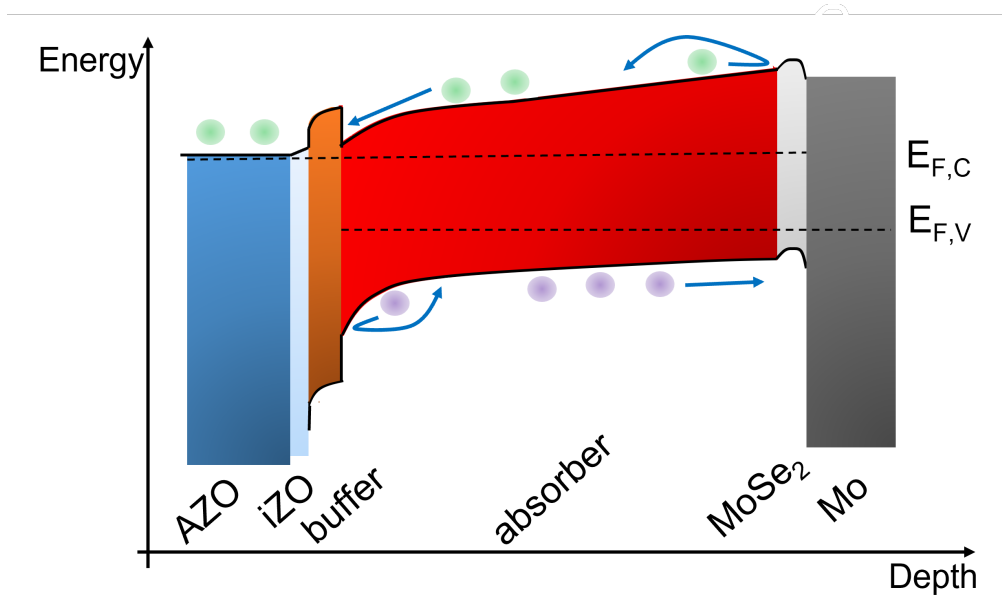
Figure 2.8: Band diagram of a CIGSSe solar cell. The green (purple) circles represents the electrons (holes). Diagram inspired by Fin Babbe thesis 2019.

The n-type material, called the buffer can be made from various materials such as CdS, $\mathrm{In_2S_3}$, Zn(O,S),... This will be discussed in section 2.2.2. The typical thickness of this layer is on the order of 20-70 nm. A wide band gap is desirable for this layer to avoid parasitic absorption of photons at short wavelengths (called the blue defect) corresponding to the buffer region (fig 3.25). Indeed, photons absorbed in this layer will not create charge carriers that can be collected and thus these photons are lost. The band alignment of this layer with the window layer and the absorber is critical in ensuring that electrons (holes) flow toward the front (back) of the cell [5]. The buffer also prevent damages to the absorber that can occur during the sputtering of the windows [16].

The intrinsic ZnO (iZO), which is the first window layer (50 nm thick), is a very resistive n-type material. It has a wide band gap (usually even wider than the buffer layer) to minimize the parasitic absorption. The second window is Al doped ZnO (AZO)

which is a wide band gap, n-type, highly conductive layer (400 nm thick) that enables the transport of the electrons. Finally, the front contact which is made of Nickel and Aluminium is deposited. It typically has a U shape to collect as much current as possible: it ensures that each part of the cell is less than 0.5 cm from the contact.

It should be noted that both the buffer and iZO are also used to prevent shunts in the solar cell. Indeed, it sometimes happens that openings are present in the absorber layer, which exposes the Mo back contact. If the AZO touches the Mo back contact, it forms an alternative path to charge carriers and it creates a shunt. If resistive layers are deposited on these openings, it reduces the likelihood of a shunt path [17]. It could be argued that iZO could be deposited directly on the absorber since it is resistive. However, the buffer layer shows essential properties that make it more suitable to be in direct contact with the absorber. Indeed, the buffer's lattice matches better with CIGSSe than the window. As already stated, the sputtering of iZO would damage the CIGSSe. And lastly, the buffer plays the role of intermediate between the absorber and the window in terms of band alignment: the bands would be misaligned if there was no buffer. In the next section, the buffers used in te CIGSSe technology will be reviewed.

2.2.2 Buffer review

As discussed in the previous section, a buffer layer is essential to ensure a good pn junction and protect the CIGSSe during the deposition of the windows. Many buffer materials (CdS, ZnS-based, $In(OH)_3$-based, In_2S_3-based, ZnSe-based, $ZnInSe_x$, In_xSe_y, ZnO, ZnMgO,...) have already been studied for CIGSe application. A thorough review can be found in [18].

In this section, the different materials used in this work as a buffer (CdS, In_2S_3, Zn(O,S)) for CIGSSe solar cells are reviewed. The focus will be put on the solution deposited buffers.

CdS

CdS was the most commonly used material for the buffer layer in CIGSe devices for decades. However, because of its toxicity and its low band gap corresponding to a parasitic absorption at short wavelengths, scientists started to work on alternative materials. The CIGSe world record until 2022 was obtained with a Zn(O,S) buffer [19] which is Cd-free and has a wide band gap. However, the new CIGSe world record contains a CdS buffer layer (unpublished at the time of the thesis writing) which shows that CdS is far from being outdated. It is thus of interest to carry on with the research on CdS and on the reduction of waste.

CdS is a n-type direct band gap semiconductor. It is most often deposited through chemical bath (CBD)[20] [21] [22]. The solution comprises ammonium hydroxide, cad-

mium salt and thiourea dissolved in water. Ammonium hydroxide is used to increase the pH, which prevents the precipitation of $Cd(OH)_2$ that originates from the hydrolysis of the Cd salt [23]. This will be discussed in more details in chapter 6. This process has been optimized through the years by tuning the salts concentration, bath temperature and deposition time [24][25]. It is important to note that the CBD CdS contains oxygen and the right compound is actually Cd(O,S).

CdS can also be deposited through vacuum processes. However, poorer performance for PVD deposited CdS (PVD-CdS) was found compared to CBD-CdS when used as a buffer on CIGSe (around 4% absolute drop in efficiency) [26]. The first significant difference lies in a larger open circuit voltage for CBD-CdS due to different interface recombinations [27]. This high recombination is associated with a higher defects contents in the buffer. It was shown that the lattices of CIGSe and CBD-CdS match well, while the lattices of CIGSe and PVD-CdS did not match and defects are present in the buffer due to this mismatch. Moreover, more Cd (Cu) diffuses from the buffer (absorber) to the absorber (buffer) in the CBD CdS. This means that an interfacial layer is formed and this leads to the improvement of the performance [27].

In order to decrease the waste, spin coating is was examined to deposit CdS. 500 times less solvents and 80 times less salts are used compared to laboratory CBD. The ink was made of cadmium acetate and thiourea dissolved in methanol. It was spin coated and annealed in air at 200°C for 10 min to form CdS. The layer was dense and smooth. The band gap was 2.5 eV which is slightly higher than the bulk band gap, i.e. 2.42 eV. The authors argued that quantum confinement was responsible for this increased band gap (will be discussed in chapter 7) [28]. Another work reported the spin coating of Cd(O,S) on Sb_2Se_3 [29]. The ink was made of cadmium acetate and thiourea as the work described above, however the solvents were ethoxyethanol and acetic acid. The oxygen content was tuned by controlling the thiourea concentration. Cd(O,S) was obtained after an annealing at 400°C for 5 min. Introducing oxygen led to a decrease in interface recombination. Spin coating of CdS is however not used for CIGSe so no report on its performance can be reported.

Only one work on inkjet printed CdS has been found and this work is unrelated to photovoltaics. Cadmium acetate and thiourea were dissolved in methanol:ethylene glycol solvent (95:5) [30]. The annealing procedure was carried out at 200°C for 60 min in a glove box to turn the precursor into CdS. The CdS is not pure, since some $Cd(SO_4)$ was found.

Even though inkjet printing can decrease the waste of the CBD CdS, it can be interesting to synthesize Cd-free buffer. Indeed, depending on the composition of CIGSSe, the VBM and CBM lies at different energy levels. In order to ensure good bands alignment, the VBM and CBM of the buffer have to be tuned, which has some limits if the same material is kept: indeed, doping can help in the tuning but it might be insufficient.

Moreover, the band gap of CdS is quite narrow (2.4 eV) which leads to parasitic absorption. The development of Cd-free buffers has gained interest and the following section describes In_2S_3.

In_2S_3

In_2S_3 is a material that has given high efficiency CIGSSe devices. A deep review on the impact of different deposition techniques on the properties of In_2S_3 films was done by Barreau [31]. The pure In_2S_3 single crystal has a direct band gap of 2.00 eV [32], however thin multicrystalline material shows deviation from this value. Moreover, the nature of the transition, i.e. direct or indirect, is still subject to discussion. This uncertainty comes from the position of the VBM. Indeed, simulated band diagram from density functional theory [33] shows that the VBM is located at the N point, while the CBM is at the Γ point, which means that the band gap is indirect with a value of 1.977 eV, similar to the experimental band gap of single crystal. However, at the Γ point, the value of the VBM is lower by only 0.089 eV compared to the N point. Since this energy difference is quite small, it can be considered that both the VBM and CBM are located at the Γ point and thus the band gap is direct with a value of 2.066 eV [33].

Various vapor phase deposition techniques are used for In_2S_3 such as thermal evaporation [34]. A direct band gap of the material was found as low as 2.0 eV [35]. It was shown that introducing oxygen into In_2S_3 could increase the band gap to 2.8 eV [36]. Atomic layer deposition (ALD) also leads to 2.8 eV [37] but oxygen is not responsible for the elevated band gap. It is argued that the size of the crystals are small enough to exhibit quantum confinement effect increasing the band gap. Another work with ALD showed a very wide band gap of 3.25 eV [38].

There is a growing interest into the solution deposition techniques and this will be the focus of the following review. Similarly to the CBD CdS, indium sulfide can be deposited through CBD. However, as for CdS, the material is not pure, i.e. $In(OH)_xS_y$ is formed [39]. Bayon et al. made a solution of $InCl_3$, thioacetamide (TA) and acetic acid (AcOH) [40]. In the solution, $In(OH)_3$ colloids are present and they precipitate on the substrate. They act as nucleation centers for the synthesis of indium sulfide, which explains the presence of $In(OH)_xS_y$ instead of pure In_2S_3. When increasing the bath temperature, the morphology goes from granular to strings of particles. When swapping AcOH with HCl, the morphology turns into a porous sponge-like structure. This shows that within a deposition technique, changing parameters can lead to different morphologies and properties of the indium sulfide. A CIGSe device with a CBD-$In(OH)_xS_y$ showed an efficiency of 14.9%, slightly lower than a CBD-CdS of 15.2% [41]. The film showed less parasitic absorption at short wavelengths compared to the CBD CdS. However, the collection at longer wavelengths was lower, finally giving a lower current than CdS. This lower para-

sitic absorption at short wavelength is coherent with the direct band gap of 2.75 eV found by Lokhande et al. [42] who added hydrazine hydrate, triethanolamine and ammonium chloride to the bath compared to Hariskos [41].

Spray pyrolysis is also often used to deposit buffer layers, in which, for example, $InCl_3$ and thiourea (TU) are used as metal and sulfur sources [43]. The band gap was found to be indirect, with values ranging from 2.2 eV to 2.4 eV by tuning the S amount in In_2S_x with 2<x<3.9. Sall et al. showed on the contrary that the band gap was independent of [S]/[In] in the ink and that this ratio did not influence much the final [S]/[In] ratio in the film [44]. Indeed, a [S]/[In] ratio in solution varying from 2.5 to 4.5 led to a constant [S]/[In] of 1.4 in the films. The band gap slightly varied from 1.57 eV to 1.63 eV. The crystallite size were large and constant with the [S]/[In] ratio (on the order of 120 nm). This shows that the band gap, the crystallite size and the final film [S]/[In] ratio barely depend on the initial [S]/[In] ratio in the solution. A CIGSe solar cell with the spray deposited In_2S_3 reaches 96% of the CBD CdS buffered device [45]. It was proposed that this lower efficiency is related to the oxygen contamination: the sample is heated to 200°C in air during the spray pyrolysis of In_2S_3 which leads to the introduction of oxygen that pushes the absorber copper to the bulk of the CIGSe.

Spin coating buffer layers is seldom discussed in the literature. The metal and sulfur sources are identical to the spray pyrolysis deposition discussed above, i.e. ($InCl_3$ and thiourea) but the solvent is changed (dimethylsulfoxyde (DMSO)) [46]. It was shown that the morphology is influenced by the [S]/[In] ratio in the ink: island shapes for a 1.5 ratio progressively disappear to form a continuous film for [S]/[In]=6. It was applied to CIGSe solar cell and led to best cell power conversion efficiency of 12% but it was not compared to a reference process. Another work [47] in which $In(NO)_3$ and thiourea dissolved in ethanol/ethylene glycol mixture showed that the best performing buffer on CIGSe has a [S]/[In] in the ink of 2. This device exhibits 102% of the CBD CdS buffered cell efficiency. However, a post annealing in H_2S was necessary which adds a toxic process to the synthesis of the layer. Contrarily to the literature reported earlier for In_2S_3, the decrease in parasitic absorption at short wavelengths is nearly negligible but no significant loss at longer wavelengths was found contrarily to what is usually reported.

Finally, inkjet printing is emerging as a new deposition technique for buffer layers because of its flexibility of patterning and its low waste. However, because of its novelty, publications are scarce on the subject. The literature review contains only the single publication following. In_2S_3 was inkjet printed on CIGSe [47] using the indium nitrate/thiourea ink discussed in the spincoating review. As for spin coating, a post annealing in H_2S was necessary to obtain 98% of the CBD CdS reference cell efficiency. When the annealing is performed in argon, the efficiency of the device is 86% of the reference cell.

In summary, the variation of band gap is associated either to a change in the chemical

composition (essentially the S content) but it was also proposed that the small size of the grain might be responsible for the higher band gap because of quantum quantization [48]. This will be further discussed in chapter 7. Moreover, the crystal properties strongly depend on the deposition technique. Some of these techniques such as ALD, spray pyrolysis, spin coating, CBD,... which require the use of precursor molecules often show the presence of residues such as oxygen, chlorine,... [49] [50]. However, the effect of chlorine residue is not discussed and its impact is unclear. Physical vapor deposition and sputtering [51] on the contrary lead to the least contaminated films. The increased band gap that is sometimes observed in non-CBD processes leads to less photons absorption at short wavelengths, however this gain is very often canceled by the lack of collection at long wavelengths, which might be due to a less doped buffer than the commonly CBD CdS [52]. The lower collection at long wavelengths could also partially be explained by the reflection losses. Indeed, it was shown that part of the photons are reflected by the cell before entering the cell when the buffer is In_2S_3 which means that the electron-hole pairs are not even generated and thus can not be collected [45].

Even though the band gap of In_2S_3 can be tuned in a wide range of energy, it can be simpler to change the buffer material. Moreover, the band alignment depends on both the buffer and the absorber, which means that In_2S_3 might not be suitable for every absorber compositions. Therefore, Zn(O,S) has attracted interest as an alternative buffer layer and is discussed in the next section.

Zn(O,S)

An important aspect of Zn(O,S) is its wide tunable band gap. The band gap of Zn(O,S) varies non-linearly between the band gap of ZnO and ZnS with x, where x is the sulfur content in $ZnO_{1-x}S_x$ [53]. Near the composition of ZnO (ZnS), the material has the properties of the pure material which is doped. For intermediate compositions, the band gap is a function of a ZnO and ZnS alloy. The band gap of zinc blende ZnO is 3.45 eV and ZnS is 3.84 eV. The lowest band gap is obtained for an approximate sulfur content of 0.4, i.e. 2.2 eV.

A Zn(O,S) buffer on CIGSe can help simplify the conventional layers stack. Indeed, typically, a CIGSe solar cell consists in glass/Mo/CIGSe/CdS/i-ZnO/Al:ZnO/contacts. Grimm et al. [54] showed that a sputtered Zn(O,S) based cell can work with a modified stack: glass/Mo/CIGSe/Zn(O,S)/Al:ZnO/contacts, i.e. the i-ZnO can be omitted. The efficiency of the Zn(O,S) based device was 97% of the CBD-CdS based solar cell. The parasitic absorption at short wavelengths clearly disappeared, hinting to a wide band gap (however the latter is not discussed).

As already discussed for In_2S_3, the properties of the material strongly depends on the deposition technique. Platzer-Bjorkman et al. [55] showed that ALD Zn(O,S) blocked

the current when the film was sulfur rich if the layer was not ultrathin and the open circuit voltage was low for an oxygen rich layer. This was found to be related to the band offset at the Zn(O,S)/CIGSe interface. The best Zn(O,S) buffered cell had 104% of the CdS buffered reference in this study.

Similarly to CdS, Zn(O,S) can be deposited through CBD. The solution is similar to CdS, i.e. a Zn salt and thiourea are dissolved in an alkaline solution. Bhattacharya et al. [56] synthesized a CBD Zn(O,S) on CIGSe with a record efficiency of 18.5%. It could be compared with a CdS buffered device, with an efficiency of 17.25%. However, this comparison is slightly biased by the fact that the Zn(O,S) device had an antireflective coating on top of the cell, while the CdS did not. Nevertheless, the parasitic absorption of CdS was overcome with Zn(O,S) thanks to a band gap of 3.8 eV. The time necessary for the deposition process is usually long (60 min) and effort has been put into reducing this time. Buffiere et al. [57] added H_2O_2 to the solution to decrease the deposition time. The band gap of the layer is 0.1 eV higher than the traditional CBD. H_2O_2 accelerates the formation of particles in the solution and thus the reaction rate. The deposition time is reduced to 2 min. The performance of the standard Zn(O,S) is 80% of the CdS buffer device, while the H_2O_2 Zn(O,S) is 82%, meaning that the fast method is as good as the standard CBD, but performs less well than the CdS.

Reducing the waste from CBD is an important goal. Zn(O,S) was inkjet printed on CIGSSe [58]. The ink consisted in zinc salt and thiourea in a mixture of water, ethanol and propylene glycol. Once inkjet printed, the ink was annealed at 250°C in air for 10 min. The band gap of the Zn(O,S) could be tuned with temperature, ranging from 3.8 eV to 4.2 eV, which is higher than pure ZnS and ZnO band gaps. This is related to quantum confinement effect as discussed in chapter 7. Such wide band gaps have already been found in other works where standard deposition techniques were used (CBD [59]) and is thus not purely related to inkjet printing. The efficiency of the best Zn(O,S) device is 118% of the efficiency of the CBD CdS buffered device.

In this work, In_2S_3, CdS and Zn(O,S) are studied. CBD CdS has historically performed well as a buffer layer in CIGSe. However, its toxicity is a real disadvantage and to decrease its impact, inkjet printable CdS was already suggested by one group. However, their ink contained methanol that requires the use of a fumehood and it was not applied solar cells. In this work, a new ink which can be used at industrial scale without requiring air purification apparatus is synthesized and deposited on CIGSSe cells to assess its performance as a buffer layer. To completely avoid Cd, an In_2S_3 buffer layer is cited as an alternative to CdS. It is shown in literature that it performs as well as the CBD CdS in a CIGSe device and can exhibit a wider band gap than CdS. A preliminary work already inkjet printed on CIGSe and gave good a good efficiency but the In_2S_3 layer was not deeply characterized and it required a toxic H_2S post-annealing treatment. Here, we will synthesize this buffer without the use of H_2S and study its properties in terms of

chemical composition, morphology and crystallography. It was shown in literature that [S]/[In] ratio in the ink can have impact on these different properties depending on the deposition technique. The effect of the [S]/[In] will be studied as well as the cell device performance of the buffers synthesized from these inks.

Zn(O,S) is a wide band gap semiconductor alternative to CdS, that is appreciated as a buffer layer thanks to the decrease in the parasitic absorption at short wavelengths within the solar cell. It was already inkjet printed and its band gap was found to be wider than the bulk counterpart. It is often claimed in literature that the wider band gap is due to a quantum confinement effect related to the nano-size of its constituent grains. is nanocrystallites. Unfortunately, this hypothesis is claimed but not proved. In this work, we will investigate the crystallite size and the band gap of the inkjet printed Zn(O,S) as well as In_2S_3 and CdS. The newly synthesized layers are characterized (chemical composition, crystallography, morphology,...) using the techniques described in the next chapter.

Chapter 3

Characterization techniques

This chapter describes the measurement techniques used in this work to characterize the inks and the morphology, crystal structure, chemical composition and band gap of the synthesized films. Lastly, the devices made with the inkjet printed buffers are characterized by measuring their performance.

3.1 Ink solution properties

In order to ensure that the inks are inkjet printable, their solution properties, i.e. surface tension and viscosity, are measured. Moreover, the interaction of these inks with the substrate are characterized using the contact angle measurement.

3.1.1 Goniometer

The machine is a Ossila contact angle goniometer. It enables the measurement of the surface tension via the pendant drop experiment as well as the contact angle of a liquid on a substrate as described in this section.

Pendant drop

The surface tension plays a key role in the printability of an ink. Various methods can be used to measure it such as direct measurement using a microbalance (Wilhelmy plate), measurement of the capillary pressure (maximum bubble pressure), analysis between the capillary and gravity forces (capillary rise) and analysis of gravity distorted drops (pendant drop) [60]. In the latter, a liquid drop pending from a needle changes shapes under gravity. The advantage compared to the widely used Wilhelmy plate measurement is the small liquid volume required, i.e. less than 25 μL for pending drop and 1 mL for Wilhelmy plate.

In order to determine the surface tension in the pendant drop experiment, the Laplace equation is used to establish the relationship between the difference in pressure ΔP and

the interfacial tension:

$$\Delta P = \gamma \left(\frac{1}{R_1} + \frac{1}{R_2} \right) \qquad (3.1)$$

where $\Delta P = P_{in} - P_{out}$, γ is the interfacial tension, R_1 and R_2 are the radii of the curvature of the drops as represented on figure 3.1a. If no force is applied on the drop, it assumes a spherical shape to decrease its surface to volume ratio. However, gravity acts on it through the hydrostatic pressure, adding to the inner pressure

$$\Delta P = \Delta P_0 + \Delta \rho g z \qquad (3.2)$$

where ΔP_0 is a reference pressure at z=0, $\Delta \rho$ is the density difference between the gas (air) and the liquid, g is the gravitational acceleration and z is the vertical height.

Equalizing eqs. 3.2 and 3.1 gives the Young-Laplace equation

$$\gamma \left(\frac{1}{R_1} + \frac{1}{R_2} \right) = \Delta P_0 + \Delta \rho g l \qquad (3.3)$$

Thanks to the symmetry of the drop, eq 3.3 can be expressed in terms of the cylindrical coordinates r, z and the tangent angle φ (fig 3.1b). The Young Laplace equation is then replaced by a set of differential equations respective to the arc length s [61]

$$
\begin{aligned}
\frac{d\varphi}{d\bar{s}} &= 2 - \mathrm{Bo}\,\bar{z} - \frac{sin\varphi}{\bar{r}} \\
\frac{d\bar{r}}{d\bar{s}} &= cos\varphi \\
\frac{d\bar{z}}{d\bar{s}} &= sin\varphi
\end{aligned}
\qquad (3.4)
$$

where the bar represents dimensionless variables through scaling by the radius of the drop at the apex R_0 and $Bo = \frac{\Delta \rho g R_0^2}{\gamma}$ is the Bond number often used to characterize fluids. These differential equations can be analytically solved solely in the case of a spherical drop, which happens only when the surface tension tends to infinity. In real case, these equations have to be solved numerically.

The first step is to determine the edge of the droplet. It uses the intensity gradient method in which the edge detection looks for large changes in pixel lightness over a limited number of pixels. If this gradient in lightness overpasses a certain threshold, an edge is detected. Then, the software fits a polynomial to the edge of the drop. The fit contains two main variables: the droplet radius R_0 and a fitting parameter which is the Bond number Bo. The latter characterizes the deviation of the droplet shape from a circle. The higher Bo, the lower the surface tension. Indeed, when Bo increases, the drop becomes more elongated, meaning a lower surface tension which allows more deformation from gravity (fig3.1c). For a constant Bo parameter, an increased drop radius (volume) implies a higher surface tension to maintain the same shape.
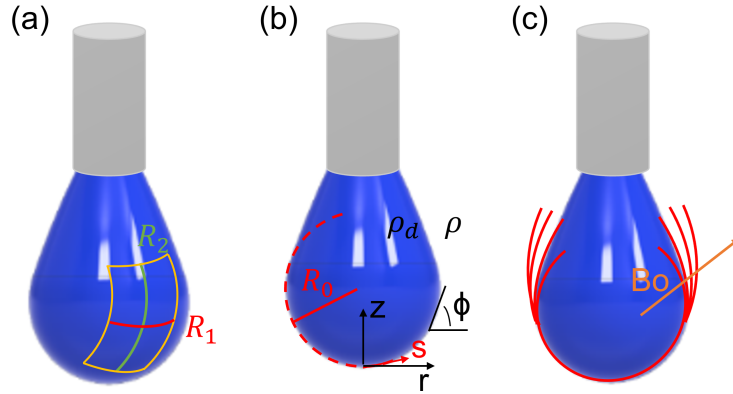
Figure 3.1: Pendant drop measurement. (a) Radii of the curvature of the drop in two directions (reproduced from [62]. (b)Parameters of the differential equations of Young Laplace equation (partially reproduced from [61]. (c) Influence of Bond number on the shape of the drop.

To determine the surface tension, $\Delta\rho$ must be known, i.e. the density of air and the density of the measured liquid. Moreover, the radius R_0 must be measured. This is achieved via a calibration of the image. The picture of a sphere with a known diameter is taken. The edge is then extracted and a curve is fitted. The diameter of the sphere in pixels is registered and is associated to the length provided to the software. Once the pixel-real size is calibrated, R_0 measured in pixel can be translated in real size (fig 3.2a). In between measurements, water was used to check the cleanliness of the needle. A clean needle should give the surface tension of DI water, i.e 72 mN/m (fig 3.2b). In the case of an unclean needle, the surface tension of water is found to be lower, i.e. 69.4 mN/m for example (fig3.2c). In this case, the syringe was continuously cleaned with water until the right value was obtained. Water was used as a verification because it does not leave residues and its evaporation rate is sufficiently low to enable a reproducible and trustworthy measurement (compared for example to ethanol).

Contact angle

The goniometer can also be used to measure the contact angle of a drop deposited on a substrate. This technique does not require any calibration, contrary to the pendant drop. In this experiment, a drop is deposited on a substrate and an image is acquired. The edge of the drop is extracted and the tangent to the drop at the three phases contact line is calculated. The contact angle should be measured as soon as the drop is deposited on the substrate. Indeed, when the liquid touches the substrate, the contact line is either not pined or pined. In the former case, the evaporation of the solvents leads to the shrinking of the drop with a constant contact angle. In the second case (i.e. the situation that occurs in this thesis), the evaporation of the liquid decreases the volume of the drop but

(a)

Calibration Diameter (mm) | 10,000
Milimetres per Pixel: | 0,0081

(b)

Surface Tension: 72.0 mN/m
RMS Error: 0.6
Radius: 1.2 mm
Bond Number: 0.2

(c)

Surface Tension: 69.4 mN/m
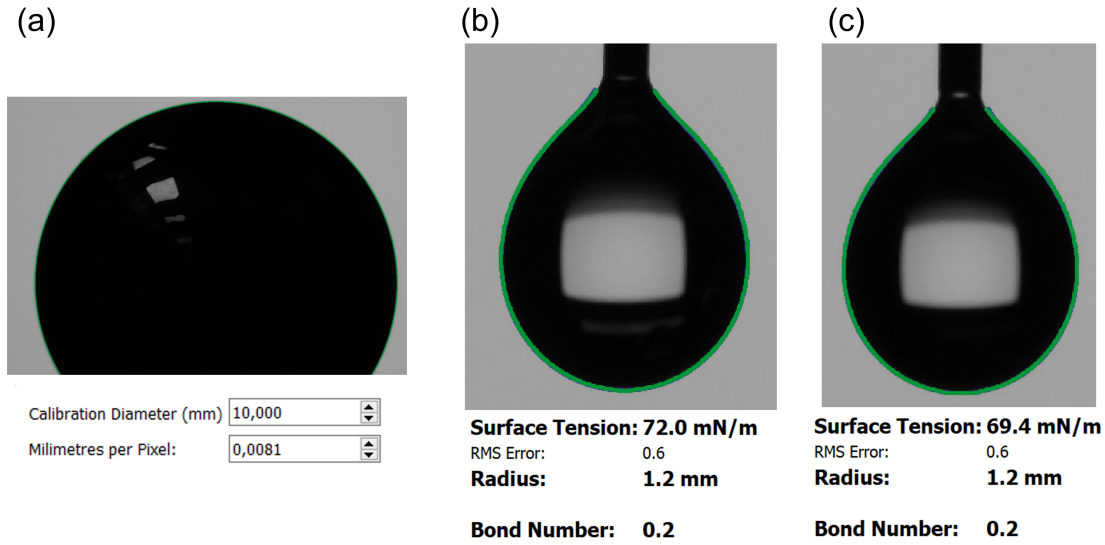RMS Error: 0.6
Radius: 1.2 mm
Bond Number: 0.2

Figure 3.2: (a) Calibration procedure for the pendant drop measurement. (b) DI water pendant drop with data associated to the measurement. (c) DI water pendant drop using an unclean needle.

the contact area with the substrate is constant. This leads to the flattening of the drop, i.e. the decrease of the contact angle. Figure 3.3a shows the contact angle (53°) of water on glass right after the deposition. After 2 minutes of evaporation, the contact angle of the drop decreases to around 38° (fig 3.3b). The left and right contact angle of this drop are different. Since they were similar at the deposition, it shows that the evaporation rate is different on both sides, i.e., the evaporation is faster on the left side. Different left and right contact angles is also an indication of an inhomogeneous substrate.

(a)

Left Angle: | 53.10°
Left RMS Error: | 0.58
Right Angle: | 53.21°
Right RMS Error: | 0.54
Average Angle: 53.15°

(b)

Left Angle: | 36.73°
Left RMS Error: | 0.47
Right Angle: | 40.16°
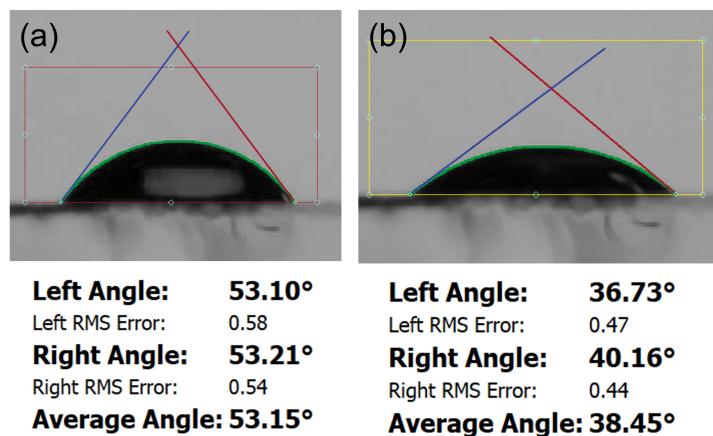Right RMS Error: | 0.44
Average Angle: 38.45°

Figure 3.3: (a) Contact angle of DI water on glass right after the deposition of the drop. (b) Contact angle of DI water on glass 2 minutes after the deposition of the drop.

3.1.2 Viscometer

The viscosity was measured using the Rheosense microVISC device where the liquid is pushed inside a rectangular glass flow channel and a monolithic silicon pressure sensor array measures the pressure (fig 3.4). The width of the slit is much bigger than its height. The pressure varies along the length of the channel. Because of its design, the edges of the slit have a negligible effect on the pressure drop and the flow can be considered as two dimensional.
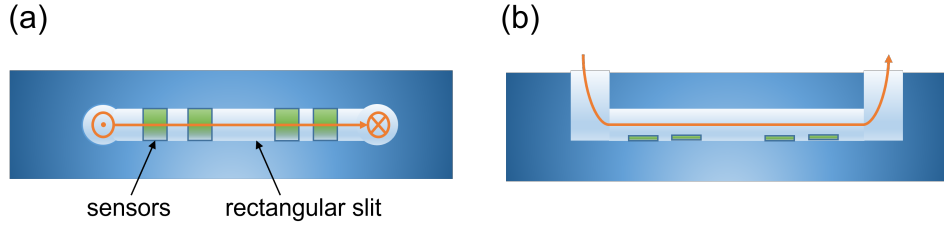

Figure 3.4: (a) top view and cross section image of the viscometer channel. The liquid flow is represented by the orange arrow.

The viscosity can be calculated from the following equations [63] [64]

$$
\dot{\gamma}_{app} = \frac{6Q}{wh^2}
$$
$$
\tau = -\beta \frac{wh}{(2w + 2h)} \tag{3.5}
$$
$$
\eta = \frac{\tau}{\dot{\gamma}_{app}}
$$

with $\dot{\gamma}_{app}$ the apparent shear rate, τ the shear stress, η the viscosity, Q the flow rate, w the width of channel, h the height of channel and β the slope extracted from a graph similar to figure 3.5 for the liquid measured.
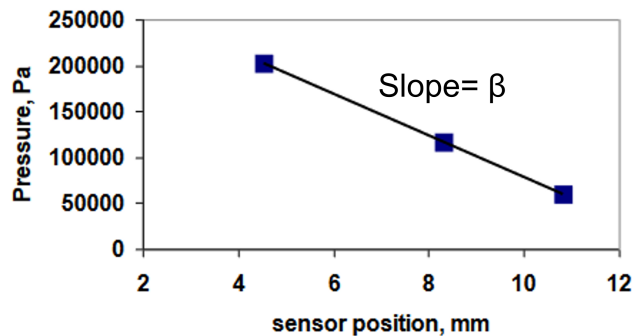

Figure 3.5: Pression variation along a rectangular channel in a Rheosense VROC device [64]. The slope of the linear regression is called β.

3.2 Morphology

The morphology of the thin films was characterized using the techniques described in this section. These techniques have different x-y resolutions as well as different depth resolution and thus give different information that will be exploited in this thesis.

3.2.1 SEM

Scanning electron microscopy (SEM) uses an electron gun to excite electrons in the material. The electron beam is typically 100 nm wide or less and the usual range of electrons acceleration voltage is 1 to 20 keV. Once the electrons penetrate the samples, they scatter elastically and inelastically and lose progressively their high kinetic energy. Samples have to be conductive to avoid overcharging on the surface. This charging often produces drift making the image blurry. In order to avoid it, the upper surface is bounded to the holder with copper tape.

Different signal can be collected from this excitation, such as Auger electrons, secondary electrons, back scattered electrons and X-Rays among others. These signals give information about the material at different depths (fig 3.6a). The volume of interaction, also known as the pear of interaction, depends on the accelerating voltage, the concentration of the atoms in the material and the atomic number. The higher the accelerating voltage, the bigger the pear of interaction (fig 3.6b). The higher the concentration and Z number, the smaller the volume of interaction. The buffer layer being thin (usually less than 100 nm), a low accelerating voltage enable to collect more signal from it. Secondary electrons originate from the surface or near-surface (around 10 nm) of the material . The incoming electron, known as the primary electron, hits an atom's electron elastically and ejects it (fig3.7a). This expelled electron is called secondary electron. The image gives the topography and the morphology of the sample. The ratio between secondary electrons (SE) and primary electrons (PE) is insensitive to the atomic number but it increases with a decreasing accelerating voltage (decreased pear of interaction).

Back scattered electrons (BSE) emerge from the interaction of the primary electron with the electromagnetic field of the nucleus of the atom. The electron is back scattered out of the material. The BSE depends on the atoms density. They produce an image with contrast related to the surface composition. Higher atomic number atoms make brighter signal on this image. Opposed to the SE, the number of BSE relative to the number of PE increases with the atomic number. This ratio is relatively insensitive to the accelerating voltage.

There exist two types of SEM guns: the thermionic emitter and the field emitter. The first one is associated to SEM, while the second is associated to FESEM. In SEM, the emitting filament is heat up to produce the electrons, while the FESEM uses a tip with a diameter small enough (around 100 nm) to concentrate an electric field and emit the
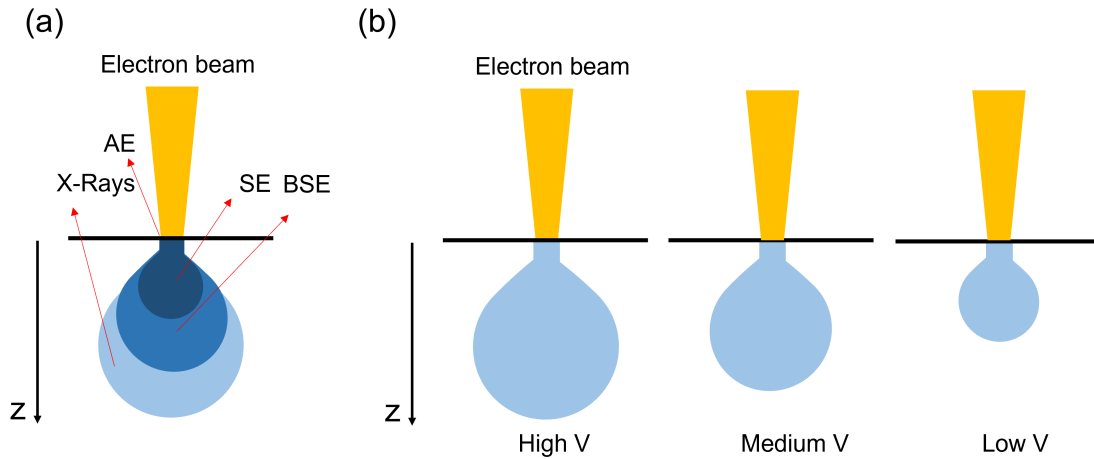
Figure 3.6: Pear of interaction of SEM. (a) Signal produced by SEM as a function of the penetration depth: Auger electron (AE), X-Rays, secondary electrons (SE) and back scattered electrons (BSE). (b) Influence of incoming electrons accelerating voltage (V) on the pear of interaction size.
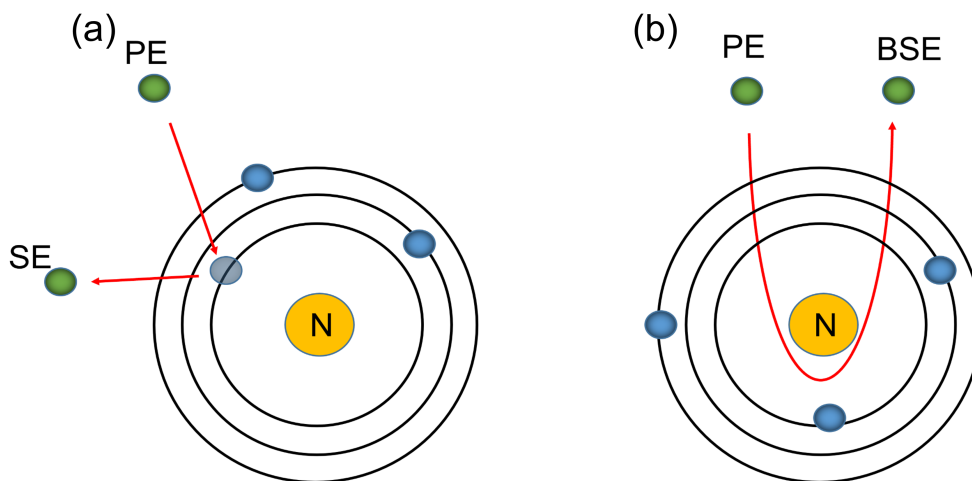

Figure 3.7: Generation by an incoming primary electron (PE) of (a) a secondary electron (SE) and (b) a back scattered electron (BSE).

electrons. FESEM has a higher resolution (around 2 nm) than SEM because of a thinner beam. Both SEM (SEM EVO10) and FESEM (Hitachi) were used for the measurements in this work.

3.2.2 FIB SEM

Focused Ion Beam SEM (FIB SEM) is very similar to SEM: the only difference is the use of ion beam instead of an electron beam to image the material. The source is a liquid metal (usually Ga) held in a reservoir. The liquid is in contact with a tungsten needle and flows down to a tip where a high extraction field is applied, pulling out the

Ga. Ga$^+$ ions are formed through ionization and accelerated down the column similarly to the standard SEM [65]. The preferred ion is Ga$^+$ because of its low melting point, making it liquid near room temperature and its low volatility, giving a long lifetime to the source, among others [66]. The focused ion beam is focused on the sample for two purposes: the milling of the material and the imaging.

Materials can be deposited using FIB-SEM. The desired material is brought near the sample in a gas phase (usually in the form of organomettalic molecules). The beam is then used to decompose the molecules resulting in the deposition of the desired metallic atoms on the surface while the organic part is dissociated in volatile fragments. The decomposition of the organometallic molecules is not perfect and some organic might be incorporated in the final layer. This technique was used in this work to deposit a conductive platinum layer for cross section imaging.

The range of travel for electron in typical SEM is around 1 μm for 15 to 20 keV, while it is much lower for heavy ions such as Ga for similar energy range: the distance for a target atomic number of 49 (indium) is around 16 nm and 34 nm for Z=16 (sulfur) [67]. The interaction produces therefore an image of the surface. When the ion enters the materials, it interacts with the target atoms and excites its electrons, creating secondary electrons called ion induced secondary electrons (iSE). They have advantages over the basic SE. The ion beam tends to form many more iSEs per incident ion than does an electron in SEM, giving a higher signal to noise ratio. However, the FIB-SEM tends to be a disruptive technique. The incoming gallium ions can implant itself in the target material altering its composition and structure. The implantation of these ions do not contribute a lot to the swelling of the material. However, the phenomenon known as amorphization resulting from the displacement of atoms during collision cascade, participates to the distortion of the crystalline structure [66].

Similarly to SEM, the charging of the sample is a concern. In order to avoid the charging, the sample was covered with 30 nm platinum protective layer be ex-situ sputtering (LEICA ACE 600) and the cross-section zone was coated with a 1µm in-situ platinum layer by ion beam induced deposition using gallium source of the FIB-SEM instrument (FEI Helios Nanolab 650) operating at 30 kV and 2 nA. The FIB-SEM measurement were performed in secondary electron mode using a 2 kV accelerating voltage.

3.2.3   HIM-SIMS

Helium Ion Microscopy with Secondary Ion Mass Spectrometry was measured using a NanoFab Helium Ion Microscope (ZEISS, Peabody USA) coupled with a SIMS system developed at LIST. This technique gives map of the chemical elements with a high space resolution as well as electron images. For the latter, a tungstene tip made of three atoms ionizes He gas that are accelerated with 20 kV toward the sample. The ionized He

generates secondary electrons in the sample that are collected at a low angle (fig 3.8). For the chemical maps, the gas is exchanged with Ne. The ions hit the surface and produce secondary ions by ionizing the elements of the materials. These ions leave the sample parallel to the incoming ions. They are then deflected and sorted based on their mass. Each mass is detected by a detector as shown on figure 3.8. The material's ions are either positive or negative and up to four ions can be detected at once. In the case of CIGSSe and In_2S_3, the positive ions that were used are Ga, In, Cu and Na. The negative ions are Se, O, Cl and CN. Nitrogen is hard to detect, except when it is present with C, explaining their coupling in the detection.
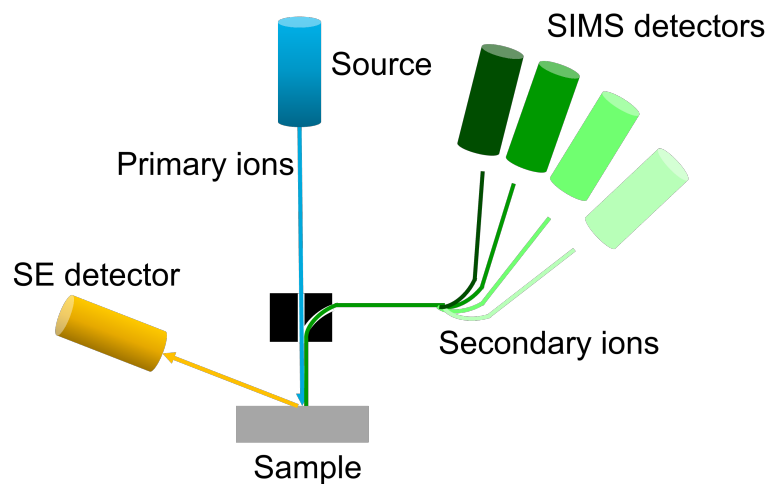
Figure 3.8: Sketch of HIM-SIMS measurement.

3.2.4 Profilometer

The profilometer uses a stylus to measure the height variation. Figure 3.9 shows that the tip (with a radius of 2 μm) is connected to a transducer through a stylus. The transducer increases and translates the mechanical signal into electronic signal. A force (ranging from 0.03 to 50 mg) is applied by the tip on the sample to perform a measurement which makes it a slightly destructive technique with sensible samples. The minimum measurable thickness is 10 nm, which is on the same scale as the buffer thickness (50 nm to hundreds of nm). The profilometer used in this work is the KLA Tencor P17.

Figure 3.9: Sketch of the profilometer tip

3.2.5 AFM

The working principle of atomic force microscopy (AFM) is similar to the profilometer: a tip is used to assess the topography of the surface. However, in AFM, an oscillation with a frequency equal or near the resonance frequency of the cantilever is imparted to the latter and the change in this oscillation either in term of amplitude (AM) or frequency (FM) is recorded. In this work, the FM mode was used and will be described in more details. The measurements were performed in non-contact mode. The interaction between the tip and the material is perturbed by attractive and repulsive forces. When the tip-material distance changes, the oscillation frequency changes (fig 3.10). A set-point, i.e. a fixed distance from the surface of the sample, is determined before starting the measurement and a certain oscillation frequency is associated to this set-point. When scanning the surface, a feedback system regulates the frequency of the cantilever to keep the shift in frequency (difference between the set-point frequency and cantilever frequency) constant. The movement of the cantilever is measured with a laser. More information can be found in [68].
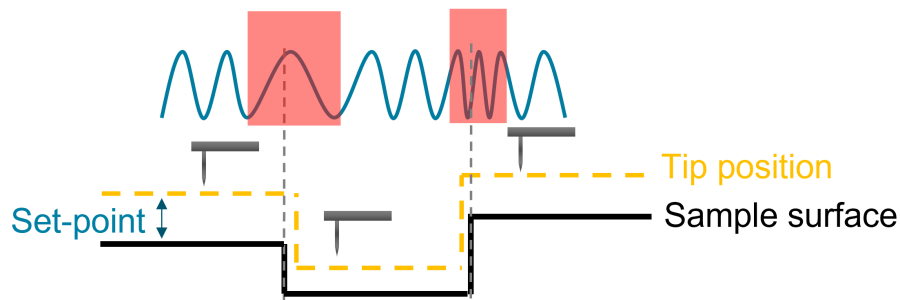

Figure 3.10: Sketch of frequency modulated AFM. The frequency of the oscillation is modified in the red areas when movement of the tip in the z direction is done.

The machine used is a Bruker MultiMode AFM with Nanoscope V controller (Digital instruments) in non-contact mode. The used tips are the 240-AC-PP probes from MikroMasch with a resonance frequency of roughly 70kHZ.

3.3 Crystallinity

The determination of the crystal structure of the synthesized materials was done by X-Ray and electron diffraction. The crystalline structure of a material can be expressed from the unit cell, i.e. the smallest set of atoms that can be reproduced to represent the whole crystal. This cell is defined by 3 lengths (a,b,c) and 3 angles (α, β, γ). Table 3.1 shows the seven crystal systems.

Crystal system	Lattice constant	Angles
Triclinic	a $\neq$ b $\neq$ c	$\alpha \neq \beta \neq \gamma \neq 90°$
Monoclinic	a $\neq$ b $\neq$ c	$\alpha = \gamma = 90°, \beta \neq 90°$
Orthorhombic	a $\neq$ b $\neq$ c	$\alpha = \beta = \gamma = 90°$
Tetragonal	a $=$ b $\neq$ c	$\alpha = \beta = \gamma = 90°$
Hexagonal	a $=$ b $\neq$ c	$\alpha = \beta = 90°, \gamma = 120°$
Trigonal	a $=$ b $=$ c	$\alpha = \beta = \gamma \neq 90°$
Cubic	a $=$ b $=$ c	$\alpha = \beta = \gamma = 90°$

Table 3.1: Seven existing crystal systems based on their lattice constants and angles.

3.3.1 XRD

X-Ray Diffraction (XRD) is used to find the crystallographic structure of a material. The wavelength of the X-Ray is similar to the interatomic distance in condensed matter. The incoming X-Ray are being diffracted by the plans of atoms. The constructive interference between these diffracted rays form peaks following the Bragg's law

$$2d_{hkl}sin\theta_B = n\lambda \tag{3.6}$$

where d_{hkl}, θ_B, λ are the interplanar spacing, the Bragg's angle, the wavelength of the X-Ray and n an integer. h, k and l represent the Miller indices. The target of the machine used is Cu with a characteristic radiation Cu K_α at 1.5418 Å. Figure 3.11a shows the $\theta - 2\theta$ configuration in which the X-Rays and the detector move in synchronization with an increasing θ angle (relative to the surface of the sample). This geometry is not well suited to the measurement of thin film because of its high penetration depth, leading to collection of signal mostly from the substrate. To bypass this issue, grazing incidence XRD (GIXRD) is often used to measure thin films. Figure 3.11b shows this configuration in which X-Rays have a very low constant incidence angle ω (0.5° to 2°), while the detector moves similarly to the XRD configuration. The X-Rays path inside the film is then increases, improving the signal to noise ratio. ω is usually taken bigger than 0.5° because a smaller angle might give a total reflexion which is a phenomenon exploited in X-Ray reflection (XRR). The machine used is a Bruker D8 Discover.

The cyrstallite size can be determined through XRD by measuring the full width at half maximum (FWHM), i.e. $2\theta_2 - 2\theta_1$ (fig 3.12). This technique can exaggerate the crystallite size because the larger crystallites increase the intensity while the smaller crystallites merge in the base of the peak [69]. The determination of the coherence length, which can be approximated as the crystallite size, from the FWHM is given by the Scherrer equation [70]
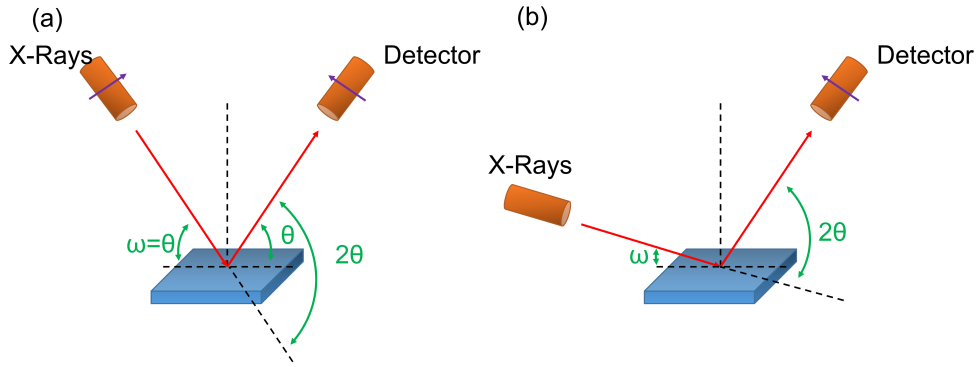
$$D = \frac{k\lambda}{\beta_{hkl}cos\theta} \tag{3.7}$$

Figure 3.11: Experimental setup for(a) $\theta - 2\theta$ configuration XRD and (b) a grazing incidence XRD, where ω is fixed.

where λ is the X-Ray wavelength, D the coherence length (crystallite size), β_{hkl} the FWHM of the peak located at $2\theta_c$, θ is θ_c and k is the Scherrer constant which is a dimentionless shape factor. The value is typically taken as 0.9 which corresponds to sherical crystallites. However, severe deviation from this value are observed when the shape varies [71].
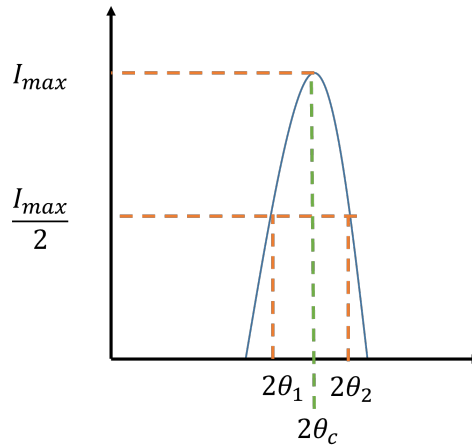
Figure 3.12: Definition of the Full width at half maximum (FWHM) of a diffraction peak. The width is defined by the difference between $2\theta_2 - 2\theta_1$ at half of the intensity of the peak. $2\theta_c$ is the center of the peak.

3.3.2 TEM, SAED and FFT

Transmission electron microscopy (TEM) enables the imaging of the material crystallites. Indeed, the wavelength of an electron decreases when its speed increases (i.e. accelerating voltage increases). When the wavelength decreases, the resolution of the microscope increases. The samples typically act as a grating, resulting in a diffraction pattern when interacting with the electrons. Most of the latters are not absorbed by the

material and they are scattered and unscattered when going through the sample. The non scattered waves go directly to the image plane through the focal plane of the lens without any interference occurring (fig 3.13a). The scattered waves interfere constructively or destructively at the focal plane following the equation $2dsin\theta = n\lambda$, where λ is the wavelength of the source, d is the spacing of the grating and θ is the scattering angle relative to the source direction. The electron wavelength (in nm) can be calculated using

$$\lambda = \frac{1.226}{\sqrt{E_0(1 + 0.978 \; 10^{-6}E_0}}$$

(3.8)

where E_0 is the electron energy in eV. The wavelength is thus small enough to image atoms. Finally, the scattered and unscattered waves recombine and interfere at the image plane. In order to increase the contrast of the imaging, the waves that are scattered at large angles can be filtered by an aperture before the image plane to prevent them from interfering with the unscattered wave (fig 3.13b). The elements that have a strong scattering effect appear then darker.

The diffraction pattern corresponds to the reciprocal lattice which is another repre-
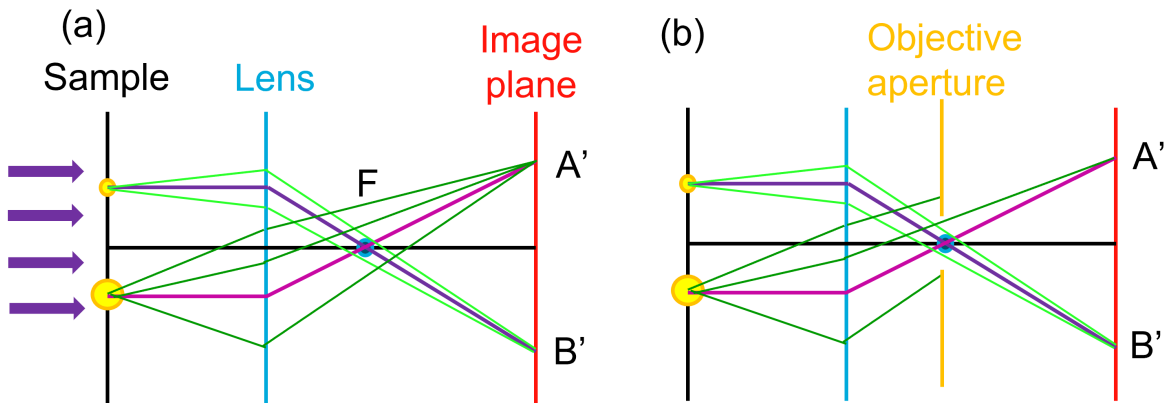

Figure 3.13: Formation of TEM image through scattering of electrons. (a) The unscattered wave (purple) directly go to the image plane via the focal plane, while the scattered waves (green) interfere at the focal plane. Scattered and unscattered waves finally interfere at the image plane. (b) Scattered waves at large angles are filtered through an aperture to increase the contrast. F is the focal plane.

sentation of the real space of atoms. The seven crystal systems shown in table 3.1 are described relatively to a set of vectors named $\overrightarrow{a}$, $\overrightarrow{b}$ and $\overrightarrow{c}$. When interpreting the (hkl) Miller indices in terms of a vector coordinates in the set of vectors, no direct relation can be found between this vector and the actual (hkl) plan except for the cubic system (fig 3.14) [72]. A new set of vectors can be created to give a meaningful relationship between the vector related to the (hkl) indices and the actual (hkl) plane. This set of vectors $\overrightarrow{a^*}$, $\overrightarrow{b^*}$ and $\overrightarrow{c^*}$, known as reciprocal basis vectors, follows the relation $\overrightarrow{a_i}\overrightarrow{a_j^*} \equiv \delta_{ij}$ and thus
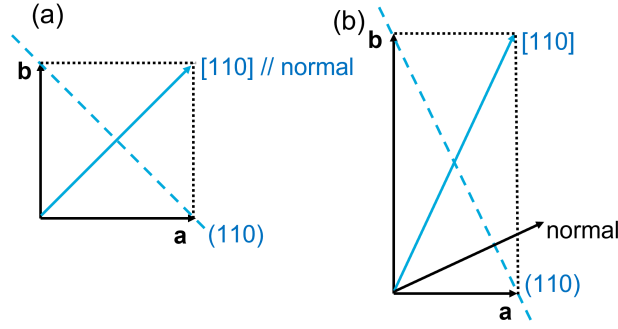
Figure 3.14: (a) The (hkl) Miller indices interpreted as coordinates in the set of vector is perpendicular to the (hkl) plane in a cubic system. (b) the vector is not perpendicular to the (hkl) plane in non cubic system. Figure reproduced from [72].

each vector can be written as

$$
\begin{aligned}
\mathbf{a}^* &= \frac{\mathbf{b} \times \mathbf{c}}{\mathbf{a} \cdot (\mathbf{b} \times \mathbf{c})} \\
\mathbf{b}^* &= \frac{\mathbf{c} \times \mathbf{a}}{\mathbf{a} \cdot (\mathbf{b} \times \mathbf{c})} \\
\mathbf{c}^* &= \frac{\mathbf{a} \times \mathbf{b}}{\mathbf{a} \cdot (\mathbf{b} \times \mathbf{c})}
\end{aligned}
\tag{3.9}
$$

The new lattice vector $\mathbf{g} = h\mathbf{a}^* + k\mathbf{b}^* + l\mathbf{c}^*$ is now perpendicular to the plane with (hkl) Miller indices. Moreover, the length of this vector is equal to the spacing between the lattice planes $|\mathbf{g}_{hkl}| = \frac{1}{d_{hkl}}$.

In the reciprocal lattice, the distance between the atomic planes d_{hkl} is represented by a single point at a distance $1/d_{hkl}$ from the lattice origin. The image formed by the diffraction points is called selected area electron diffraction pattern (SAED). When the number of crystals present is insufficient, the SAED pattern can not be formed. An alternative method to generate the diffraction pattern is the Fast Fourier Transform (FFT). It converts a signal from the original domain to the frequency domain. The TEM image is decomposed into sine and cosine functions. The frequencies of these functions is plotted with the associate intensity which corresponds to the repetition of the frequency to form the FFT image. This frequency representation corresponds to the reciprocal space, i.e. the diffraction pattern. It thus gives similar information to the SAED but the FFT is performed on a 2D image of a 3D object, while the SAED is directly performed on a 3D object, meaning that SAED includes information from both surface and bulk structures. The distance from the center of the diffraction pattern and a data point gives the atoms inter planar distance. In the case of regularly oriented crystals, the pattern is made of points (fig 3.15a), while when the crystals are randomly oriented in all direction, the points are replaced by a ring (fig 3.15b).

The sample preparation in TEM consists in the deposition of the inks and their
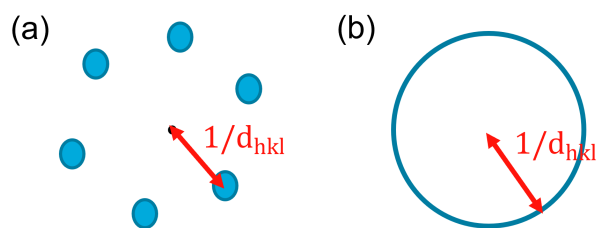
Figure 3.15: Sketch of a fast Fourier transform for (a) a regular crystal arrangement and (b) randomly orientated crystals.

annealing on TEM grids. In this work, the grids are holey carbon Ni grids. The frame and the mesh are made of Ni. An amorphous carbon layer is stuck on top of the mesh (fig 3.16a). This carbon layer contains holes (fig 3.16b). In the ideal case, the material should be deposited around this holes and it should stick out above the hole to enable the transmission of electrons through the material and the hole. In order to obtain enough transmission, the material should be very thin (ideally one atomic layer). The machine used is a Jeol Jem F200 operating at 200 kV.
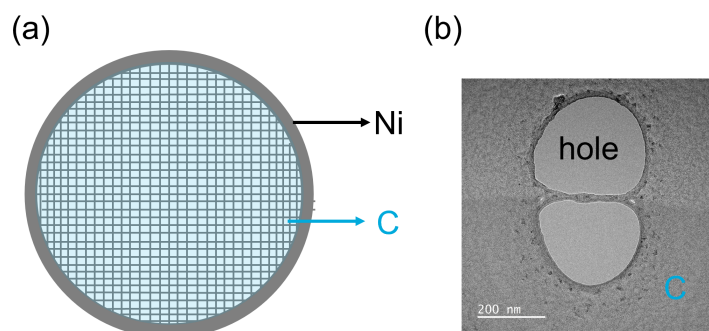
Figure 3.16: (a) Ni TEM grid with holey carbon layer. (b) TEM image of holey carbon.

3.4 Chemical composition

The chemical composition was obtained through the analysis of the electrons and X-Rays emitted by the material corresponding to XPS and EDX respectively as described in this section. The interaction of the light with the material, producing vibration of the bonds, also gives information on the chemical composition of the materials (Raman).

3.4.1 EDX

The energy dispersive X-Ray spectroscopy (EDX) is a method commonly used to determine the chemical composition of a sample. As discussed in subsection 3.2.1, the

37

primary electron interacts with the material and different signals can be collected. The SE and BSE are used for imaging of the sample, while the X-Ray gives information on the composition.

Figure 3.17a shows the working principle of EDS. A primary electron (PE) ejects an electron from an inner shell. An electron from another shell falls down on the available level and characteristic X-Ray of this transition is emitted. Figure 3.17b shows the characteristic X-Ray lines for transition from K, L, M and N shells. K lines are defined by a transition from the shell L, M or N shell toward the K shell. They are respectively called K_α, K_β and K_γ.
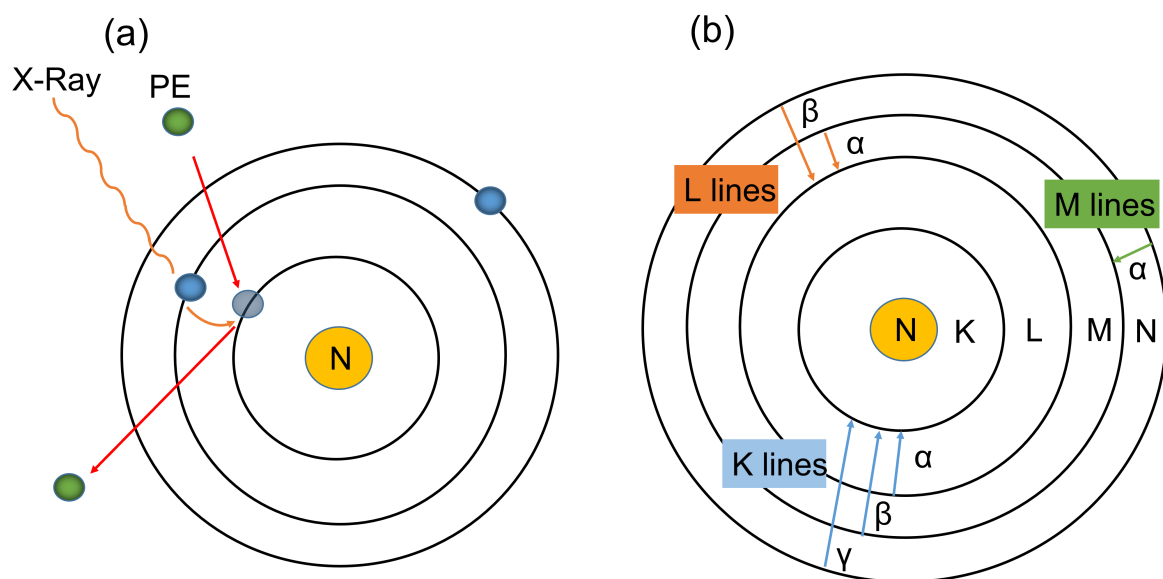
Figure 3.17: (a) Energy dispersive spectroscopy (EDX) of a material and (b) characteristic K, L, M and N X-Ray lines for transition between the shells.

Each atom has its own characteristic energies for the K, L and M lines, with their energy decreasing from K to M. Inside the family lines, such as K lines, the energy increases from α to γ, while the intensity of the signal decreases because a transition from n=2 to n=1 is more likely than n=3 to n=1. Since its intensity is higher, the K_α line is the most commonly used for the analysis of the composition.

The acceleration voltage has to be higher than the excitation energy and ideally this voltage is taken as twice the X-Ray energy to ensure a reasonable efficiency. The commonly used voltage in the SEM for EDX analysis is 20 kV. Taking into account voltage, the K_α line can be used for all atoms reported in table 3.2 except for Mo and Cd, for which the L_α has to be used. However, as discussed in the SEM subsection, the higher the accelerating voltage, the bigger the interaction volume. A CIGSSe absorber is thick enough (around 2 μm) so that the interaction volume is solely situated in this material. For a thin multi-layer sample, 20 kV gives signal from both the first layer and

the next layer. This is the case for a thin buffer layer deposited on glass or Mo-coated glass. In this case, the accelerating voltage can be decreased down to 7 kV, with which the K_α line can still be used for In, S, Cd, O, N, Cl and C, while the other atoms have to be measured through their L_α lines.

If a thin layer containing sulfur is deposited on Mo, the quantification is impossible because of the overlapping of the peaks. Indeed, the resolution of the machine is lower than the energy difference. Wavelength dispersive spectroscopy (WDX) is used to distinguish between overlapping peaks by measuring the x-ray signal as a function of a single wavelength thanks to a analytical crystal that can filter the wavelength. The position of the peak is thus exactly known for each element and the contribution from each element can be precisely measured. Even though this problem is easily overcome by the use of WDX, the measurement is still unreliable because EDX (or WDX) measurement is based on the assumption that the atoms that are detected are part of the same layer and relatively homogeneously distributed. However, in a bilayer system, this hypothesis turns out to be wrong. The chemical composition can thus be measured via these techniques by keeping in mind that it might be biased. The machine used is a SEM EVO10.

	K_α (keV)	L_α (keV)		K_α (keV)	L_α (keV)
Cu	8.040	0.930	Cd	23.175	3.133
In	3.286	0.368	Zn	8.630	1.012
Ga	9.241	1.098	O	0.525	
S	2.307		N	0.392	0.149
Se	11.207	1.379	Cl	2.621	0.183
Mo	17.441	2.293	C	0.277	

Table 3.2: X-Ray emission lines for the atoms encountered in this work [73].

3.4.2   XPS

X-Ray photoelectron spectroscopy is a ultra high vacuum technique where the sample exposed to X-Ray emits photoelectrons (fig 3.18a). An analyzer measures their kinetic energy (KE). The binding energy (BE) is then calculated from

$$E_B = h\nu - E_K - \varphi \tag{3.10}$$

where E_K and E_B are the kinetic and binding energies, h is Planck's constant, ν is the frequency of the X-Ray photon and φ is the work function of the spectrometer. E_B depends on the atom that emits the photoelectron and on its environment, meaning that a shift in E_B can be measured depending on the neighbouring atoms. Monochromatic Al K_α is used as a source. Its monochromaticity decreases the FWHM by a factor 2-4
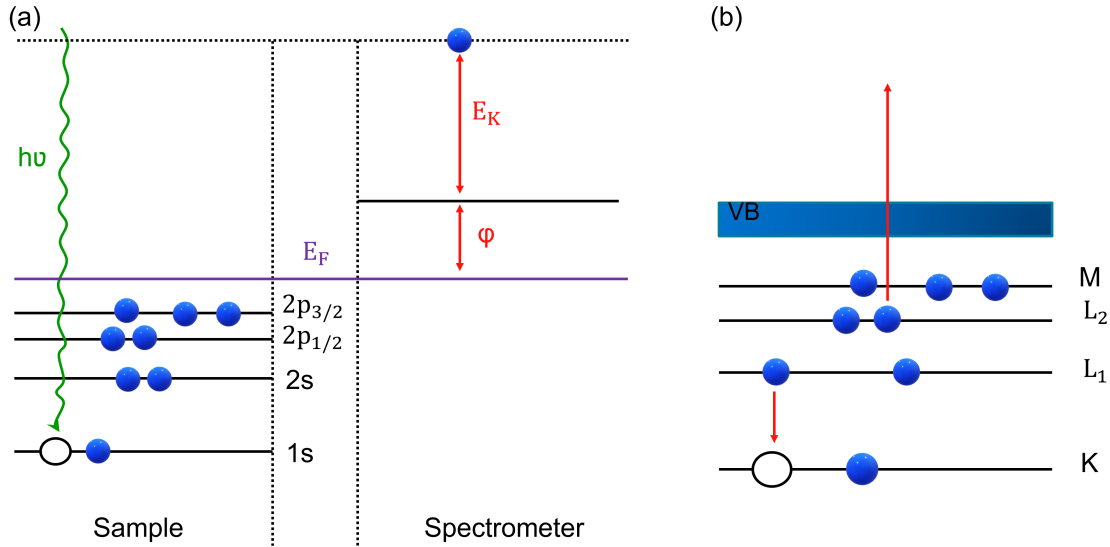
Figure 3.18: (a) Emission of a photoelectron from a sample exposed to X-Ray in XPS. E_F is the Fermi level. (b) Emission of an Auger electron KLL. VB is the valence band. Figure inspired by [74].

increasing the resolution of the spectrophotometer [74]. The X-Ray typically have an energy of 1-3 keV corresponding to a penetration depth of several microns. However, the deeper the photoelectrons are generated, the more likely the reabsorption of these photoelectrons. The signal is generally considered to be representative of the first 10 nm because photoelectrons can be collected without inelastic scattering. Auger electrons can also be emitted by the material. Indeed, in the model discussed earlier, the energy levels are considered to be unchanged before and after the emission of the photoelectrons. However, the E_B was found to be different from the theoretical values and this difference is related to the relaxation energy. This energy is related to the rearrangement of the electrons and their energy levels after the emission of the photoelectrons. This relaxation leads to the emission of an Auger electron (fig 3.18b).

XPS has some limitations. Films thicker than 10 nm require sputtering to analyze the full thickness. However, different artefacts such as preferential sputtering, oxidation state modification, ion doping, atoms mixing can occur. Moreover, charging of surface of insulating materials leads to peak shift and peak broadening. To avoid the charging, a flow of electrons in sent to the material to produce charge neutralizing. Another artefact originates from the carbon contamination due to the contact with air, which decreases the signal from the material. Two machines were used for the measurements. The first one is an Axis Ultra DLD with a monochromated Al k_α at 225 W. The second one is a thermofisher- Nexsa G2 with a monochromated Al k_α at 60 W.

40

3.4.3 Raman

In Raman Stokes scattering, a photon is sent on a material and interacts inelastically with the crystal lattice which creates a distortion of the electron cloud producing a virtual energy state. This interaction of the incoming photon, with an energy $h\nu_0$, with the crystal leads to its virtual absorption and the creation of a new photon with an energy $h(\nu_0 - \nu_{vib})$[75]. The energy difference between these two photons is called the Raman shift, often written in cm^{-1} unit. Raman scattering is characteristic of inelastic
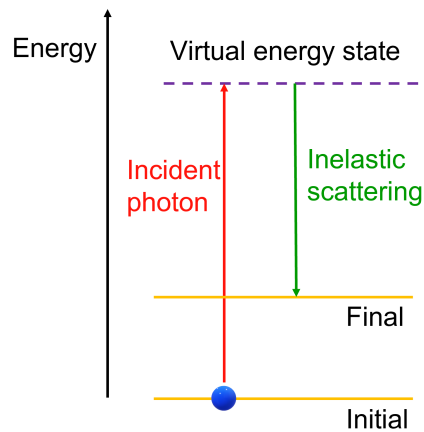
Figure 3.19: Sketch of Raman Stokes scattering process.

scattering. However, elastic scattering, know as Rayleigh scattering is more likely to happen than inelastic one. In the elastic process, the energy of the incoming photon and outgoing photon is identical. In order to remove the Rayleigh scattering component, the setup is equipped with a filter.

The frequency of vibration in Raman depends on the mass of the atoms excited and the strength of the bonds. For example, heavy atoms with weak bonds have a low Raman shift, while light atoms with strong bonds have a high Raman shift.

The machine used is a Renishaw inVia micro-Raman. Three lasers wavelengths were used: 442 nm, 532 nm and 785 nm.

3.5 Optical band gap

The band gap of the thin film was determined by using UV Visible spectroscopy. The machine used is a Lambda 950 Perkin Elmer photospectrometer. This technique enables to measure the transmittance (T) and reflectance (R) of a material. A monochromatic light is shined on the material, which if transparent, reflects and transmits light. The measurement of T and R is done through an integrating sphere. The latter is made of highly reflective material so that light can bounce inside it and be detected. In the

T measurement, the incoming light goes through the sample and is transmitted with scattering effects (fig 3.20a). Thanks to the integrating sphere, the scattered light in every direction is detected in the middle of the sphere thanks to the multiple reflection. If a standard detector was used, i.e. without integrating sphere, only the unscattered light would be detected and the transmission would be underestimated. The first spectralon (highly reflective material) (Sp1) is used to measure the reference beam. The referencing consists in measuring the transmittance while shining light into the sphere and also in the dark. These two measurements will correspond to the extreme of the scaling of transmittace, i.e. 100% and 0% T. The second spectralon, Sp2, is here to close the sphere. In R measurement, the sample replaces Sp2 and the light crosses the sphere, shines the sample (fig 3.20b) and is diffusely reflected by the sample. Reflections in the sphere ensures the collection of all the light by the detector as in the T mode [76]. The
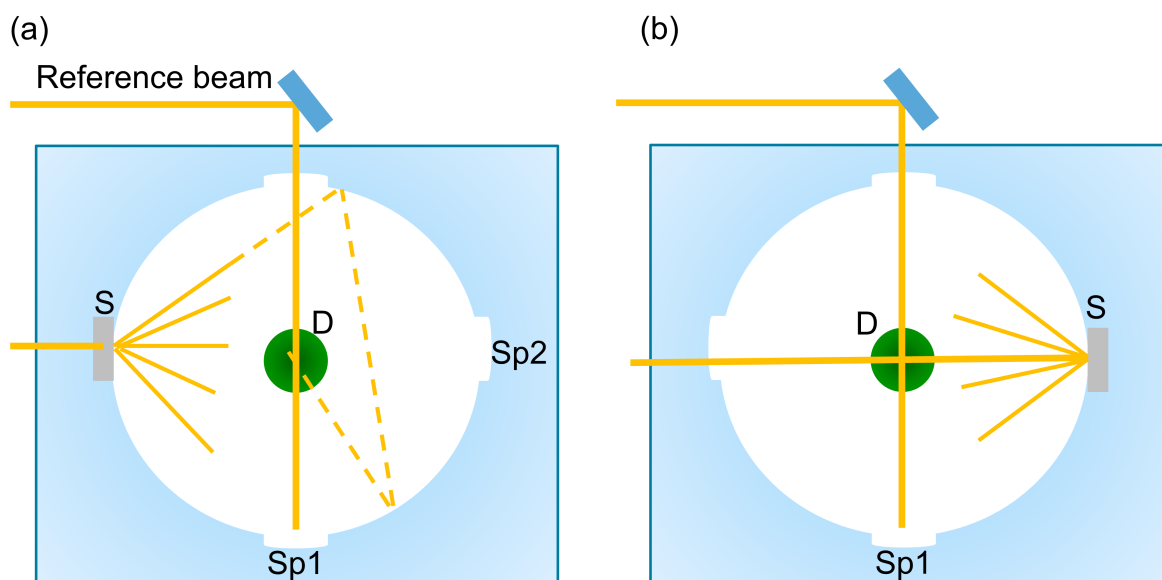
Figure 3.20: Measurement of (a) transmittance and (b) reflectance of a sample with an integrating sphere. S: sample, D: detector, Sp1 and Sp2 are Spectralon.

absorbance (A) of the material can be determined using $A + R + T = 1$. To determine the band gap, A should be translated into the absorption coefficient α. Many definitions exists for α and the one used in this work is given by

$$\alpha' = \frac{1}{d}ln\left(\frac{2T'}{-R^2+2R+T'^2+\sqrt{R^4-4R^3-2R^2T'^2+6R^2+4RT'^2-4R+T'^4+2T'^2+1}-1}\right)$$

where d is the thickness of the film, T' is the scaled transmission [77] and α' the corrected absorption coefficient. Indeed, the films are deposited on glass or quartz (1-2 mm thick) which is much thicker than the thickness of the films (50-150 nm). A significant amount of light is thus scattered by the substrate and do not enter the integrating sphere. The

T is thus scaled in order to have $A + R + T = 1$ far away from the band gap. Figure 3.21 shows the absorbance of a thin film deposited on glass with corrected and uncorrected T. Once T is corrected, A goes down to 0 far away from the band gap. Weiss et al. showed that the measurement was not affected by this scaling [77]. The absorption coefficient
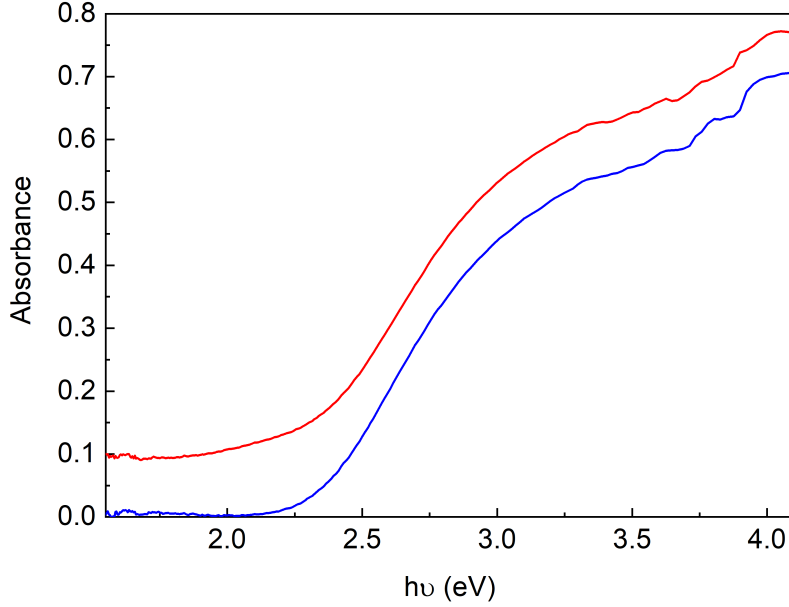

Figure 3.21: Absorbance of a thin film deposited on glass with uncorrected T (red) and corrected T (blue).

depends on the probability of the transition from the initial state to the final state and on the density of electrons in the initial state and the density of available states. Summing all the possible transitions leads to the absorption coefficient. Tauc [78] showed that the band gap can be found from α' through the following relationship

$$(\alpha'h\nu)^{1/n} = C(h\nu - E_g) \tag{3.11}$$

where C is a constant and E_g is the band gap. $n{=}1/2$ for allowed direct transition and $n{=}2$ for allowed indirect transition. The band gap can be extract from the plot of $(\alpha h\nu)^{1/n}$ versus $h\nu$ and do a regression in the linear part of the curve. The intersection with the x axis gives the band gap.

3.6   Performance of devices

Once the films have been characterized, their performance as n-type semiconductor have to be assessed. The films are deposited on p-type semiconductors and the solar cells are completed with the required layers. Then, their performance in producing electricity from light is measured.

3.6.1 JV

The measurement of the performance of a solar cell consists in applying a range of voltages to the cell illuminated with a AM 1.5 light as well as in the dark and the current flowing out of the cell, I, is measured. This current is most often expressed as a current density, i.e. the current divided by the area of the cell $j = I/Area$. Figure 3.22 shows typical JV curve in the dark and under illumination for a CIGSSe device. The current density of the cell in the dark is given by the equation

$$j_d = j_0 \left(exp \left(\frac{qV}{nk_BT} \right) - 1 \right) \tag{3.12}$$

with j_0, n, k_B and T the diode saturation current density, the diode ideality factor, the Boltzmann constant and the cell temperature. $n=1$ in the case of an ideal diode and is higher as soon as non idealities arises. The JV curve under illumination is the same curve shifted by the short circuit current density (J_{sc}) which is the current when the voltage is zero.

$$j = j_0 \left(exp \left(\frac{qV}{nk_BT} \right) - 1 \right) - j_{ill} \tag{3.13}$$

The open circuit voltage (V_{oc}) is the voltage when no current flows in the external circuit
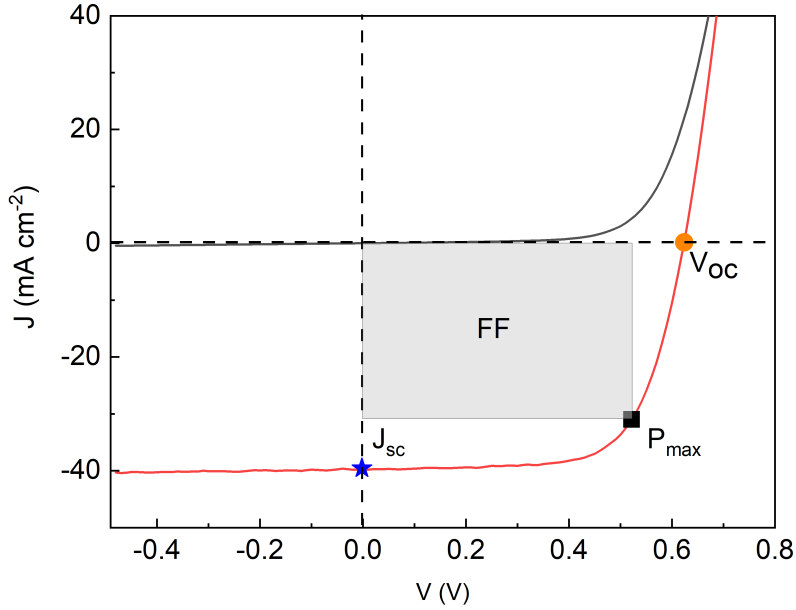
Figure 3.22: JV curves in the dark (black) and under illumination (red) of a solar cell.

and corresponds to the maximum voltage that the cell can deliver. It is given by

$$V_{oc} = \frac{nk_BT}{q} ln \frac{j_{ill}}{j_0} \tag{3.14}$$

The maximum power that can be obtained from the cell is given by $P_{max} = I_{max}V_{max}$

as shown on figure 3.22. In an ideal case, this point would be at the crossing of an horizontal line going through J_{sc} and a vertical line going through V_oc. However, this does not happen and the fill factor (FF) describes the squareness of the JV curve and is defined as the ratio between area of the grey rectangle of figure 3.22 and the rectangle with V_{oc} and J_{sc} edges.

$$FF = \frac{J_{max}V_{max}}{J_{sc}V_{oc}} \tag{3.15}$$

An empirical expression for FF is given by [79]

$$FF = \frac{v_{oc} - ln(v_{oc} + 0.72)}{v_{oc} + 1} \tag{3.16}$$

where $v_{oc} = \frac{q}{nkT}V_{oc}$ is the normalized open circuit voltage. The power conversion efficiency (η) of the solar cell is given by

$$\eta = \frac{J_{max}V_{max}}{P_{in}} \tag{3.17}$$

with P_{in} the power of the light irradiating the cell. It finally gives the equation used in this work to calculate the efficiency

$$\eta = \frac{J_{sc}V_{oc}FF}{P_{in}} \tag{3.18}$$

Non idealities generate power losses in the devices. They can be describes by n as already mentioned and the shunt R_{sh} and series resistances R_s. The shunt resistance gives information on the shunt path present in the cell. Every shunt path is an alternative path for the light generated current which reduces the current that flows through the cell junction which in turns reduces the voltage. The lower the shunt resistance, the more shunt path are present. The series resistance on the other hand is a parasitic resistance that reduces the fill factor and in extreme cases the short circuit current density as well. The lower the series resistance, the more ideal the cell. The FF is negatively impacted by the a high series resistance (R_s) and/or a low shunt resistance (R_{sh}) [79]

$$FF_s = FF_0(1 - R_s) \tag{3.19}$$

$$FF_{sh} = FF_0(1 - \frac{1}{R_{sh}}) \tag{3.20}$$

These expressions are useful to determine which series has more impact on the FF. An expression taking into account both resistances is more suited to determine the final FF [79]

$$FF = FF_0 \left\{ (1 - 1.1R_s) + \frac{R_s^2}{5.4} \right\} \left\{ 1 - \frac{V_{oc} + 0.7}{V_{oc}} \frac{FF_0}{R_{sh}} \left[(1 - 1.1R_s) + \frac{R_s^2}{5.4} \right] \right\} \tag{3.21}$$

The value of R_s and R_{sh} roughly correspond to the inverse slopes of the JV curve for voltages bigger than V_{oc} and around J_{sc} respectively. As a convention in this work, R_s was extracted from the illuminated curve and R_{sh} from the dark curve.

The current-voltage characteristics were measured with an AAA solar simulator under one sun illumination conditions.

3.6.2 PL

Photoluminescence is used during the processing of the cells to check the quality of the material and detect possible damage. This quality check is based on the quasi Fermi level splitting (qFLs) which corresponds to the highest possible V_{oc} that could be delivered by the cells. In practice, the voltage given by the cell is smaller than the qFLs because recombinations occur at the different interfaces of the cell. The measurement consists in shining a laser with an energy larger than the band gap of the material and measuring the photon flux emitted by the sample. Indeed, the laser excites the electrons that jump from the valence band (VB) to high energy levels of the conduction band (CB) (fig 3.23a), leaving holes in the valence band at various energy levels. Then, these electrons and holes thermalizes to the minimum of the CB and maximum of the VB respectively (fig 3.23b). Finally, the electron falls down to the VB, emitting a photon characteristic of the transition (fig 3.23c).
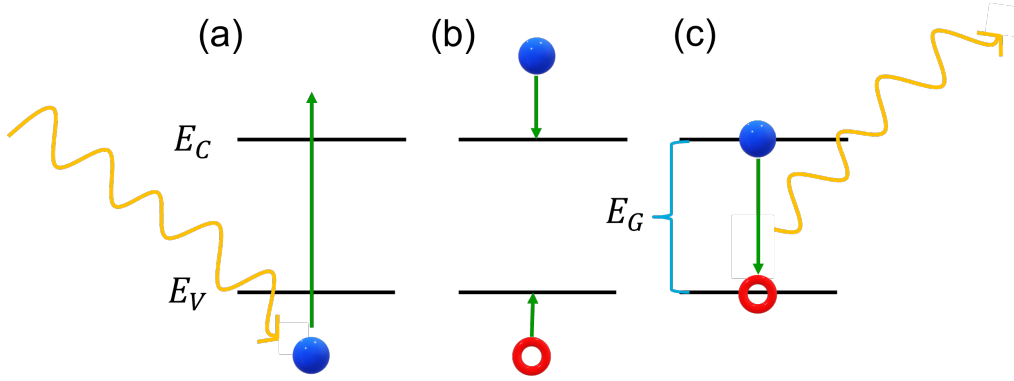
Figure 3.23: Sketch of the PL working principle. (a) Laser induced excitation of electron from VB to CB. (b) Thermalization of electron and hole. (c) Band to band recombination of electron and hole and emission of a photon.

The photon flux emitted from the material, Y_{PL} is given by

$$Y_{PL} = \frac{2\pi}{h^3 c^2} \frac{E^2 \, a(E)}{exp(\frac{E - \Delta\mu}{kT}) - 1} \tag{3.22}$$

where k, h, c, T are the Boltzmann constant, the Planck constant, the light velocity and the temperature respectively. $\Delta\mu$ is the qFLs and $a(E)$ is the absorptivity of the sample. $\Delta\mu$ does not represent the Fermi level splitting because the latter represent the

difference between the Fermi levels of the conduction and valence bands at equilibrium. However, in PL measurement, the laser produces an excitation that puts the system out of equilibrium and so $\Delta\mu$ represents the quasi Fermi level splitting.

Making the hypothesis that the absorptivity is 1 far above the band gap, equation 3.22 can be rewritten as

$$ln\left(\frac{Y_{PL}}{E^2}\frac{h^3c^2}{2\pi}\right) = \frac{\Delta\mu - E}{kT} \tag{3.23}$$

The qFLS is thus obtained as the intercept of a linear fit of the high energy wing of the curve shown on figure 3.24
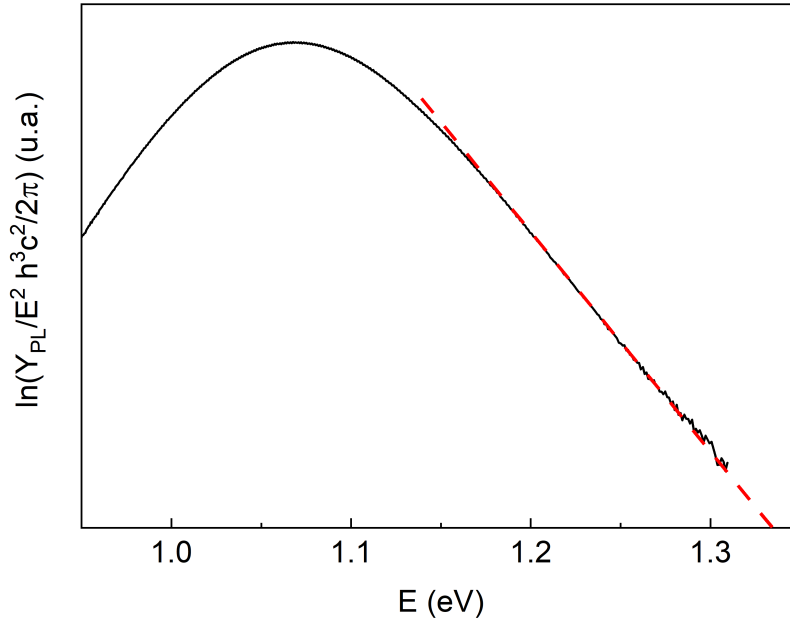
Figure 3.24: Extraction of the qFLS by the linear fitting of the high energy wing of the curve given by equation 3.23

3.6.3 EQE

External quantum efficiency (EQE) consists in the measurement of the current generated from an incoming light as a function of the wavelength of the irradiation. Figure 3.25 shows a typical EQE curve of a CIGSSe device with a CdS buffer. The scaling of the EQE curve can be interpreted as follow: 100 photons are sent onto the solar cell and the number of collected electrons is recorded. An EQE of 80% means that for 100 photons sent in, 80 electrons were collected. EQE is thus defined as

$$EQE(\lambda) = \frac{I_{ph}(\lambda)}{q\psi_{ph,\lambda}} \tag{3.24}$$

where q is the elementary charge and $\psi_{ph,\lambda}$ is the spectral photon flow incident on the solar cell which is determined by measuring EQE of calibrated references (Si and InGaAs).

Different losses prevent a 100% efficiency. At short wavelengths, the window has a parasitic absorption, meaning that photons that are absorbed there do not contribute to the current. A similar parasitic absorption is found in the buffer layer region. In this special case, the buffer is a CdS with a band gap of 2.4 eV. However, this absorption can be mitigated by choosing a material with a wider band gap such as Zn(O,S). At longer wavelengths, losses due to recombinations, reduced absorption and low diffusion length combine to reduce the efficiency. Over the absorption limit of the CIGSSe, no photon is absorbed and thus no current is generated. Reflection losses are also prevent some photons to enter the cell. If the measurement of the EQE is measured under short circuit
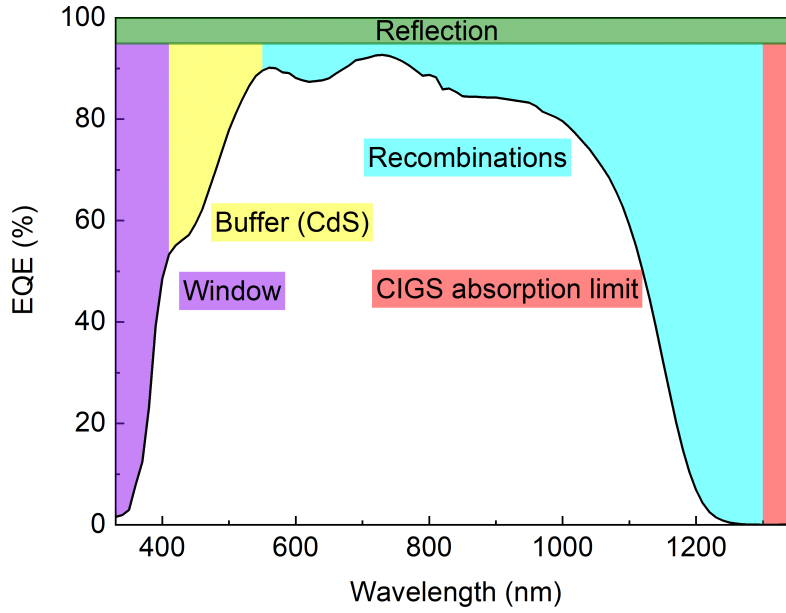
Figure 3.25: EQE curve with losses.

current condition, it can be used to measure the J_{sc} using the following relationship

$$J_{sc,EQE} = -q \int EQE(\lambda)\psi_{ph,\lambda}^{AM1.5}d\lambda \qquad (3.25)$$

where AM 1.5 corresponds to the light spectrum of the sun at our latitude (i.e. not equatorial). The derivative of the EQE can give information of the band gap of the CIGSSe and, if the absorption by the buffer is pronounced as in figure 3.25, the band gap of the buffer. The reader can find more information in [80].

EQE spectra were measured with a home-built system calibrated with Si and InGaAs references.

3.7 Substrates used for the different experiments

This section specifies the substrate that was used for each measurement. The Mo substrate is a 2 mm thick soda lime glass substrate coated with 500 nm of Mo sputtered in-house. The CIGSSe is an industrial (Avancis) absorber which composition can not be disclosed. The glass substrate is a 2 mm soda lime glass. The quartz substrate is 2 mm thick. For some measurements, multiple substrates are indicated in table 3.3. It means that the buffer was deposited on both substrates depending on the experiment.

	Substrate
Contact angle	Mo / CIGSSe
SEM	Mo / CIGSSe
FIB SEM	CIGSSe
Profilometer	Mo
AFM	Mo /CIGSSe
XRD	glass
TEM	TEM grids
EDX	Mo
XPS	Mo CIGSSe
Raman	Mo /CIGSSe
Band gap	glass / quartz

Table 3.3: Table of the substrates used with each measurement technique.

Chapter 4

Inkjet printing

This chapter describes every step from the ink formulation to the drying of the thin films containing the precursors of the semiconductors. First, the ink is formulated and the rheology is characterized to check its printability. Then, the interaction of the ink with the substrate is discussed and modeled to ensure a complete coverage of the thin layers. Finally, the drying process of the films is examined to generate a satisfying morphology (fig 4.1). In order to help the reader to understand the results, the chapter starts with the theory.
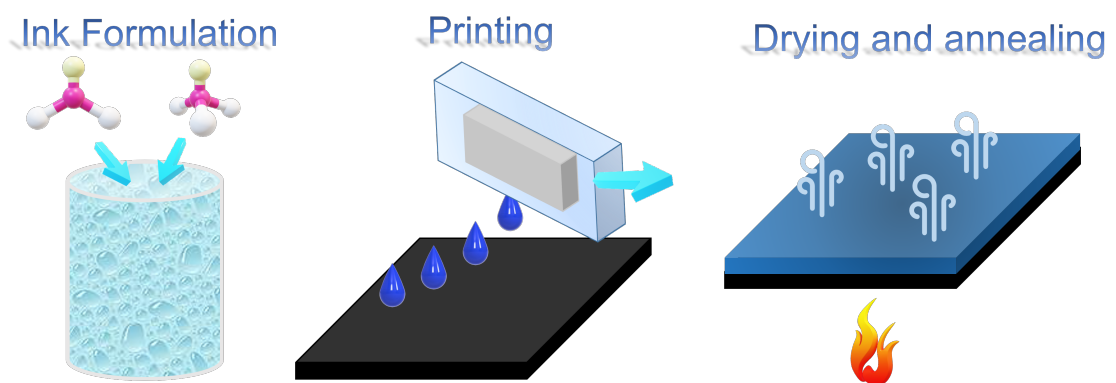
Figure 4.1: Sketch of the processing from ink formulation to the final film.

4.1 Theory

This section brings all the theoretical background required to understand the results presented in the next section. The basics of surface tension and viscosity of liquids is presented. Then, the inkjet printing method is explained. Finally, the wetting of the inks on the substrate and the evaporation of the solvents is discussed.

4.1.1 Surface tension

The surface tension is an alternative name to the surface free energy of the interface between a liquid and a gas. In a gas, molecules are far from each other and they nearly do not interact. When the gas is condensed into a liquid, molecules start to interact through the cohesive forces. In the liquid's bulk, molecules are fully surrounded by other molecules, putting them in the minimum energy state. At the interface between liquids or a liquid and another phase, molecules have less similar neighbours (fig 4.2). It creates an anisotropy in the cohesive forces: the interface molecules are strongly attracted by the interface and bulk molecules. The interface can thus be seen as a strong "wall" called surface tension (γ). Its strength depends on the molecular interactions inside the liquid. Both water and alcohols can form hydrogen bonds thanks to their OH group. Since water contains two available hydrogen atoms, the cohesion forces will be stronger than for ethanol which only has one available hydrogen atom. It results in surface tensions value at 20°C of 72 mN/m and 23 mN/m for water and ethanol respectively.
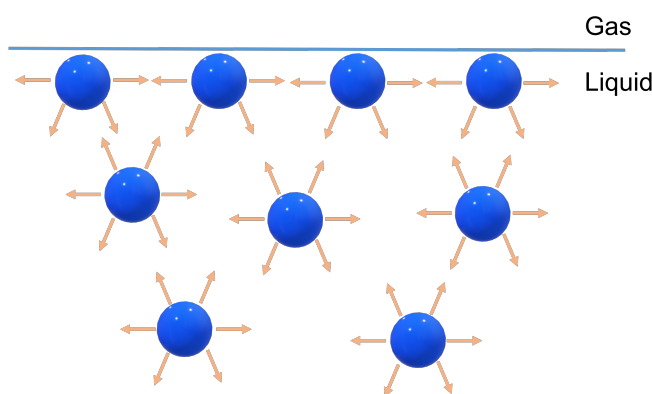
Figure 4.2: Schematic of molecules interactions leading to the surface tension at the interface between a liquid and a gas.

In the next subsections, the influence of temperature, solvents mixture and salts content on the surface tension will be discussed.

Temperature

The surface tension is temperature dependent. Heating the liquid increases the molecular movements and therefore the net force between the molecules is reduced. As a result, the surface tension is weakened. For instance, the surface tension of water and ethanol decreases by around 25% and 30% respectively by increasing the temperature to 100°C (fig A.1a in appendix A) [81] [82]. Moreover, results from these studies show that the variation in surface tension with temperature is not linear and depends on the liquid.

Solvents mixture

Liquids can be mixed in order to obtain a desired surface tension. However, the surface tension of a liquids mixture does not vary linearly with the increasing molar ratio between the host and guest liquids. Khattab et al. and others [83][84][85] showed that an increasing ethanol to water molar ratio decreases the surface tension of the mixture (fig A.1b). This decrease is very strong until a molar ratio of around 0.3 is reached and is relatively stable for higher molar ratio. This strong initial decrease can be explained by the interfacial mole fraction. It was shown by Raina et al. [86] that ethanol tends to seggregate at the interface, creating a disparity between the molar ratio at the interface and the total molar ratio. Moreover, the ethanol interfacial mole fraction is not increasing linearly with the ethanol molar ratio (fig A.1b). A very strong increase is observed at low ethanol mole fraction and then saturates. This trend at low molar fraction is in agreement with the strong decrease of the surface tension. This segregation has a consequence on stability of the solvents mixture: since ethanol segregates at the interface, it can evaporate more easily. The total ethanol molar ratio will thus change. A variation in the surface tension of the water ethanol mixture is then expected.

Influence of salts

The dissolution of salts in solutions also affects their surface tension. Weissenborn et al. measured the surface tension of aqueous solutions of electrolytes with various concentrations (c) of salts [87]. The variation of the surface tension was defined as $\Delta\gamma = \gamma - \gamma_0$ where γ and γ_0 are the surface tension of salts containing water and pure water respectively. $d(\Delta\gamma)/dc$ was reported for several salts depending on the nature of the ions. A positive value points to a depletion of solute at the gas/water interface, while a negative value indicates an adsorption of the solute at the gas/water interface. However, a negative value does not necessarily mean that both anion and cation are segregated at the interface. One of them may actually dominate the effect on surface tension. The same argument holds for a positive value. Weissenborn et al. found that small ions of high valency such as Mg^{2+}, called structure-making ions, are highly hydrated and increase the organization of water molecules by arranging them around itself. On the contrary, large ions of low valency, called structure-breaking ions, such as $(CH_3)_4N^+$ are weakly hydrated and do not promote water organization. For monovalent electrolytes, the surface tension can increase or decrease depending on the nature of the salts (fig 4.3a), while multivalents electrolytes increase the surface tension (fig 4.3b). In these studies, the surface tension variation was in the range -2 mN/m to 6 mN/m.

The surface tension of the inks used in this work are reported in table 4.1 (each ink will be explained later in this thesis). All values are equal within the error. For multivalent electrolytes, the variation in surface tension is nearly the error of our measurement for

52
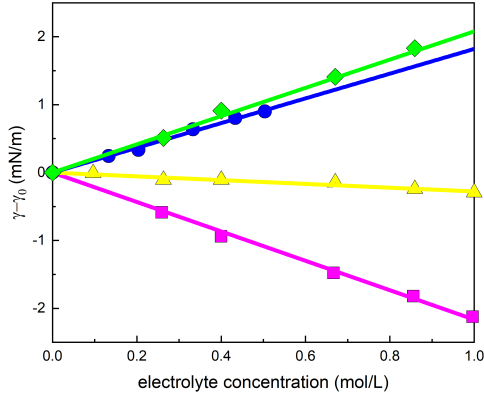
(a) Monovalent electrolytes. □ $HClO_4$, △ HCl , ◯ NaF , ◇ $NaCl$. Adapted from [87].
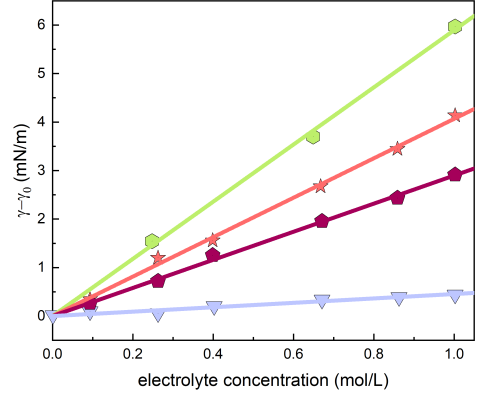
(b) Multivalent electrolytes. ◯ $LaCl_2$, ⋆ $MgCl_2$, ⬠ Na_2SO_4 , ▽ H_2SO_3. Adapted from [87].

Figure 4.3: Change in surface tension relative to water as a function of the concentration of the electrolyte.

concentrations lower than 0.8 M. For monovalent electrolyte with concentrations up to 1 M, the variation of surface tension is also within the error of our measurement. It is thus normal that all the surface tensions are similar since the effect of the different electrolytes is weak.

	Chemical species concentration (M)				
Ink name	$InCl_3$	$CS(NH_3)_2$	$Cd(CH_3COO)_2$	$ZnCl_2$	σ (mN/m)
solvent					34.7 ± 1.8
[S]/[In]=3	1.2	1.2			34.3 ± 2.2
[S]/[In]=1	0.4	0.4			33.9 ± 2.2
[S]/[In]=3 low c	0.1	0.3			33.3 ± 1.9
Cadmium acetate			0.8		33.5 ± 2.5
Thiourea		0.8			34.3 ± 2.2
[Zn]/[S]=1		0.4		0.4	32.8 ± 1.6

Table 4.1: Surface tension of some inks used to make In_2S_3, CdS and Zn(O,S).

4.1.2 Viscosity

Viscosity arises from the friction of molecules that are moving relatively to each other. The molecules moving in opposite direction can be represented by two surfaces of liquid as in figure 4.4. The upper surface is moving with a velocity v relatively to the lower surface. A linear gradient of velocity is present perpendicular to the upper and lower

surfaces. The resulting shear strain rate, $\dot{\gamma}$ is given by
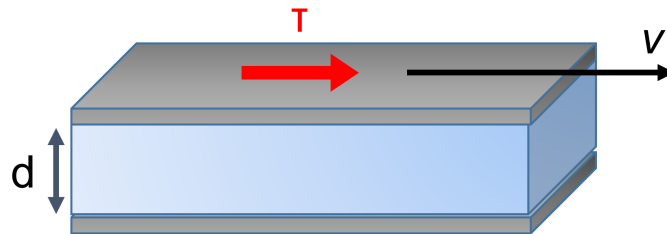
$$\dot{\gamma} = \frac{v}{d} \tag{4.1}$$

Figure 4.4: Shear strain of a liquid in movement.

where d is the spacing between the surfaces. The shear stress τ that is acting on the surfaces is proportional to the shear strain rate:

$$\tau = \eta\dot{\gamma} \tag{4.2}$$

where η is the dynamic viscosity of the liquid. If η is independent of the shear strain rate, the liquid is considered as Newtonian, while if it is dependent, it is called non Newtonian. Typically, liquids such as ethanol, water and propylene glycol are Newtonian liquids. Polymers or polymer solutions that have a long chain of atoms are non Newtonian liquids. Their viscosity is highly dependent on the shear strain rate. When the strain increases, the viscosity can either increase (shear thickening) or decrease (shear thinning) depending on the details of the individual systems. The most common phenomenon is the shear thinning.

In the next subsections, the influence of solvents mixture, temperature and salts content on the viscosity will be discussed.

Solvents mixture

In inkjet printing, solvents are often mixed to obtain a suitable rheology. A simple guess would be that the viscosity of a mixture is the weighed addition of the viscosity of each component. Taylor et al. studied the viscosity of water, ethanol and their binary mixture [88]. The viscosity of the latter was shown to deviate from a simple weighed addition rule. The viscosity deviation was defined as

$$\Delta\eta = \eta - (x_1\eta_1 + x_2\eta_2) \tag{4.3}$$

where η, η_1 and η_2 are the viscosities of the mixture, pure liquid 1 and pure liquid 2.

x_1 and x_2 are the mole fraction of liquid 1 and 2. Figure 4.5 shows that the viscosity of the water-ethanol mixtures increases with the mole fraction of water until a maximum is reached around $x_1 = 0.7$, then the viscosity decreases down to the viscosity of water. The deviation of the binary mixture viscosity as defined in equation 4.3 follows the same trend as the viscosity. It was shown that the viscosity deviation was correlated with the hydrocarbon chain length of the alcohol. Indeed, methanol showed a smaller deviation than ethanol, while propanol showed a larger deviation than ethanol. Since the hydrocarbon chains of the alcohols are hydrophobic groups, they tend to form micelles to minimize their interaction with water. The polar heads of the alcohols thus point outward and water layers are formed around it. The size of the micelle depends on the mole fraction of water: the larger the fraction, the smaller the micelle. These micelles are reponsible for the increase of viscosity in the binary mixture. The molecules in water layers around the micelle are known to have a different structure than in bulk water, leading to a higher viscosity [89]. The maximum of the deviation is simply linked to the size of the micelle: the smaller the micelles, the larger the volume of hydration layers and thus the larger the viscosity.
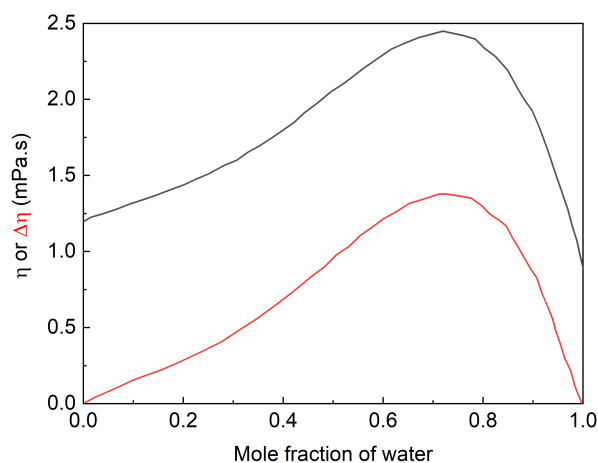
Figure 4.5: Viscosity η (black) and viscosity deviation $\Delta \eta$ (red) of an ethanol-water binary mixture. Data from [88].

Temperature

In liquids, the viscosity is dominated by the cohesive forces. As discussed for the surface tension, an increased temperature provides more energy to the molecules, which counterbalances the cohesive forces. The viscosity is thus decreasing with an increased temperature. Figure 4.6a shows the variation of the viscosity of water, ethanol and a water-ethanol binary mixture with temperature. The viscosity of water and ethanol is decreasing with temperature at a similar rate, while the rate is slightly faster for the

binary mixture with an ethanol mole fraction of 0.316 [90]. Figure 4.6b shows a similar graph for a water-propylene glycol binary mixture. The viscosity of pure propylene glycol decreases fast in the range 20 °C to 50 °C (40 mPa.s in 30°C), while water viscosity reduces by around 0.5 mPa.s. The binary mixture with a mole fraction of propylene glycol of 0.197 has a viscosity in the range of water but a decreasing rate with temperature similar to pure propylene glycol. Our ink (described in section 5.1) is a ternary mixture containing water, ethanol and propylene glycol. The viscosity of a ternary mixture is more complex. Studies on ternary mixtures are always related to specific liquids and the existing models are only applicable to these specific liquids. Moreover, experimental data are often used to calculate parameters of the model. This kind of analysis is however out of the scope of this thesis. The viscosity of the ternary mixture will also decrease with temperature and this property can be used to ease the printing. The conclusion of this study is that solvents mixture can be used to trigger the rheology of the ink by having a lower viscosity as well as a stronger response to temperature.
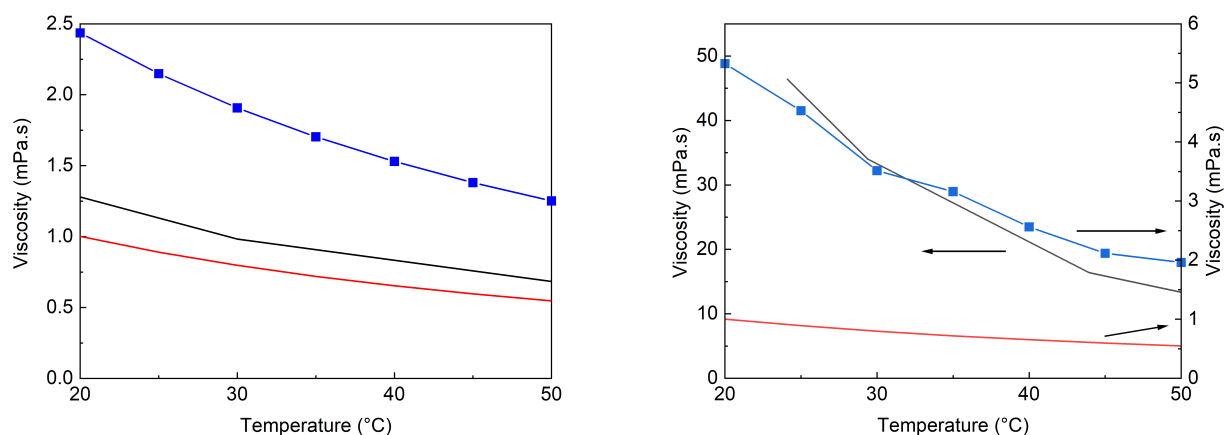
(a) Viscosity of water (red), ethanol (black) and water-ethanol binary mixture (blue/square) as a function of temperature at 20°C. The ethanol mole fraction is 0.316. Data from [91], [92], [90].

(b) Viscosity of water (red), propylene glycol (black) and water-propylene glycol binary mixture (blue/square) as a function of temperature. The ppg mole fraction is 0.197. Data from [93], [94],[91].

Figure 4.6: Viscosity of pure liquids and binary mixtures as a function of temperature.

Effect of salts

When salts are dissolved in water, they ionize. The ions have an effect on the viscosity of the solution. Dole et al. established a relationship between the viscosity of a water solution and the concentration of the salts known as the Jones-Dole equation [95]

$$\frac{\eta}{\eta_0} - 1 = AC^{1/2} + BC \tag{4.4}$$

where η, η_0, and C are the viscosity of the solution, the viscosity of water and the concentration of the salts (up to 1 M). A and B are interaction parameters that depend on the salts, temperature and solvent under consideration. A is related to the interionic forces between the electrolytes. Indeed, the ions tend to build a space lattice structure in the solution. Any disturbance trying to modify this arrangement will be counteract by the interionic forces. This induces an increase in the viscosity of the solution. This parameter has a positive value for all strong electrolytes (which are solutes that completely/almost completely ionize in solution) and is equal to 0 for non-electrolytes. B represents the ion-solvent interaction. It measures the order or disorder brought to the solvent structure by the ions. When B is positive, the ions are structure-making, while when B is negative, the ions are structure-breaking. Afzal et al. [96] showed that B tends to decrease proportionally to the increase in the entropy of hydration of the ions. They showed that highly hydrated cations such as Mg^{2+} and Ca^{2+} increase the viscosity, whereas the lowly hydrated ions will tend to decrease the viscosity. It was also shown that the temperature decreases the interaction between the solvent and the ions, leading to a decrease of the viscosity. Marcus et al. [97] did an extensive analysis of various electrolytes in order to determine their B parameter in water. The salts used in our solutions are $Cd(CH_3COO)_2$, $InCl_3$, $ZnCl_2$ and $CS(NH_3)_2$. The latter isomerizes in water following the chemical reaction [98]

$$CS(NH_3)_2 \; \rightleftharpoons \; NH_4^+NCS^-$$
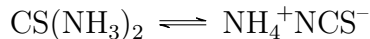
Table 4.2 shows the values of B for the ions present in our solutions. Given the low value of B, Cl^-, SCN^- and NH_4^+ are considered as not having any influence on the viscosity of the solution. All the other ions are structure making and increase the viscosity. Thus, thiourea is not influencing the viscosity of the solution. This analysis was performed

	Cd^{2+}	Zn^{2+}	In^{3+}	Cl^-	SCN^-	CH_3COO^-	NH_4^+
B	0.360	0.361	0.37	-0.005	-0.025	0.236	-0.008

Table 4.2: Parameter B from the equation of Jones-Dole (eq 4.4). Data from [97]

with pure water. The composition of our ink is however made of several liquids, namely water, ethanol and propyelene glycol. Saeed et al. [99] studied the viscosity change with the concentration of salts in a water-ethanol mixture. They also found that the viscosity increases with the concentration of salts, as well as with the ethanol/water ratio. Sonika et al. [100] also studied the ethanol-water system. They found that A and B were both positive for the studied salts (transition metal chlorides). A increased with the ethanol content, which indicates a significant solute-solute interaction. B decreased with the ethanol content, pointing to a decreased solute-solvent interaction. The value of the parameters can only be found via experimental analysis of viscosity data.

The case of our ink adds one more degree of complexity because of its ternary composition. Finding the value of A and B is out of the scope of this work. However, the Jones-Dole equation can be used to qualitatively explain the difference in the viscosity between the different inks reported in table 4.3. The viscosity of the solvent was around 3.85 mPa.s. After adding indium chloride and three time more thiourea, the viscosity increased by nearly 2 mPa.s. When, the concentration of both indium chloride and thiourea are divided by 3, the viscosity decreases to 1.5 mPa.s. However, when the concentration of indium chloride is kept constant and the concentration of thiourea is divided by 3, the viscosity nearly does not decrease. Moreover, the viscosity of the ink containing only thiourea is similar to the one of the solvent. The solution containing cadmium acetate has the highest increase in viscosity compared to the pure solvent. As mentioned earlier, Cd^{2+}, Zn^{2+}, In^{3+} and CH_3COO^- are structure making ions that increase the viscosity of the solution. Since thiourea has a weak B parameter, increasing its concentration does not have big effect on the viscosity. The higher viscosity of cadmium acetate, despite a similar B as indium can simply be explained by the higher concentration of cadmium acetate and the fact that both Cd^{2+} and CH_3COO^- influence the viscosity.

Ink name	Chemical species concentration (M)				η (mN/m)
	$InCl_3$	$CS(NH_3)_2$	$Cd(CH_3COO)_2$	$ZnCl_2$	
solvent					3.85 ± 0.08
[S]/[In]=3	1.2	1.2			5.80 ± 0.12
[S]/[In]=1	0.4	0.4			5.46 ± 0.11
[S]/[In]=3 low c	0.1	0.3			4.32 ± 0.09
Cadmium acetate			0.8		7.40 ± 0.15
Thiourea		0.8			4.09 ± 0.08
[Zn]/[S]=1		0.4		0.4	4.44 ± 0.09

Table 4.3: Viscosity of the inks used to make In_2S_3, CdS and Zn(O,S).

4.1.3   Drop-on-demand inkjet printing (DOD)

This section describes the working principle of the inkjet printer used in this thesis. In DOD inkjet printing, the ink is contained in a bag inside the cartridge and goes down to the nozzles through a channel (fig 4.7a). The nozzles are 18 µm squared holes evenly spaced (fig 4.7b). The droplets are ejected through nozzles thanks to a piezoelectric actuator that puts pressure on the liquid column held behind the printing nozzle [101]. In absence of a pressure pulse, the liquid stays inside the reservoir thanks to the surface tension of the liquid at the nozzle. When the pressure pulse reaches a certain threshold,

drops are ejected. The drops size is typically of the nozzle's size but it is possible to tune the size and velocity of the drop by managing the pressure pulse.

During the printing, the cartridge moves over the substrate from left to right (x direction). The printing in the y direction is performed by moving the substrate relative to the cartridge (fig 4.7c). A stand-off distance is always kept between the cartridge and the sample to avoid collision. Patterns can be created by controlling the deposition in both directions through the software. In the case of the printing of a film, it is possible to control its thickness by changing the drop spacing (DS), i.e. the spacing between the drops that are deposited on the substrate. A smaller DS, namely DS_1, gives a thicker film than a bigger DS, DS_2, because more inks is deposited on a given area (fig 4.7d).
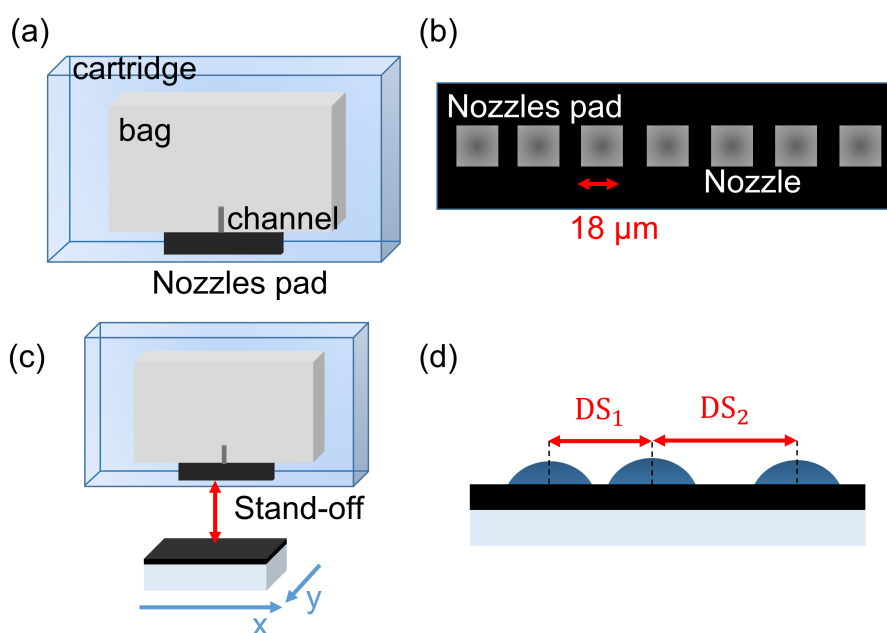
Figure 4.7: Schematic of (a) an inkjet printing cartridge and (b) its nozzles pad. (c) Schematic of inkjet printing process and (d) definition of drop spacing.

The ejection of the droplet is induced by sound waves that push the liquid through the nozzles. When a drop emerges from a nozzle, it does not detach right away from the liquid column. The drop is attached by a filament that is elongating with time (fig 4.8a). Once the filament gets to the critical thickness, it can either break only from the nozzle and form solely a main drop or it can break from the nozzle and the main drop and form a main drop and a satellite [102]. In good conditions, the satellite catches up with the main drop and only one impact occurs on the substrate. To ensure that this phenomenon can happen, a stand-off distance of up to 3 mm is taken from the substrate. However, this distance has to be minimized because horizontal air flow can drag the drop away from its initial vertical trajectory similarly to a leaf being blown by the wind (fig 4.8b). The shorter the travel, the smaller the deviation. A trade-off has to be found through

trial and error. If the rheology of the ink is not optimized, it might be impossible to get rid of the satellite droplets and multiple impacts are seen on the substrate because smaller droplets are more deviated than the main drop by air drags [102].
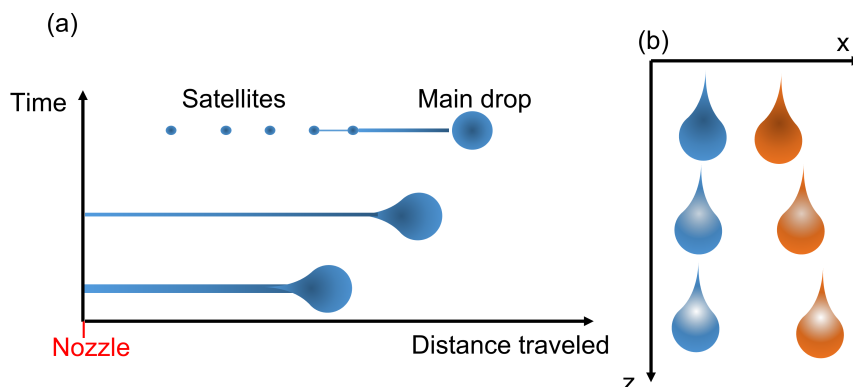

Figure 4.8: (a) Formation of a main drop and possible satellites from the break up of the liquid filament. (b) Horizontal deviation of a droplet falling vertically. In blue, an ideal vertical fall, in orange a deviated droplet due to wind blow.

Once the ejection of the drop is finished, the wave inside the column should be sufficiently damped in order not to produce interference. Hoath [103] showed that the residual oscillation can last up to 60 μs in a commercial printhead. If a new wave is added to the undamped wave, they will most probably have a phase shift, interfering constructively or destructively. Consequently, the second drop will not have the same speed, neither the same volume as the first drop. In order to damp the oscillation, the viscosity of the liquid as well as the jetting frequency have to be adjusted. Increasing viscosity will damp the movement of the liquid via frictions. When the viscosity is low, the jetting frequency, which is the frequency at which drops are ejected, can be adjusted to decrease the remaining oscillations of the liquid. The lower the frequency, the longer the time given to the liquid to damp the oscillations. This frequency can be as low as 1 kHz for the inkjet printer used (Fujifilm Dimatix 2850) and was set at 2.5 kHz in this work.

The actuation pulse that was used is shown in figure 4.9a. The ink is first kept at rest, then the voltage is rising until its maximum value in order to push onto the liquid column, the voltage is switch off afterward and the ink is again kept at rest until the next pulse. An image of the ejection of the drop is shown on figure 4.9b. From left to right, the drop is ejected with a tail (n°1), the tail is elongating (n°2), breaking into a satellite drop (n°3) that finally recombines with the main drop (n°4). Once the shape of the pulse is optimized for the ink, the voltage is adjusted for each nozzle in order to have a high velocity (to minimize the travel time in air) but also to remove all the potential satellite drops. It sometimes happens that the highest available voltage (40 V) turns out to be insufficient for the jetting of drops. This might be related either to a high

surface tension or a high viscosity. Increasing the temperature enables to decrease both parameters as discussed in sections 4.1.1 and 4.1.2. The head of the cartridge can be heat up to 60°C. However, the higher the temperature, the faster the evaporation of the high vapor pressure liquids such as water and ethanol, leading to the clogging of the cartridge (as thoroughly discussed in appendix A.1.2). The use of the heated head is thus useful but has its limits and a careful ink rheology synthesis should be first considered. Various possible issues that can be encountered with inkjet printing are detailed in appendix A.1.2.
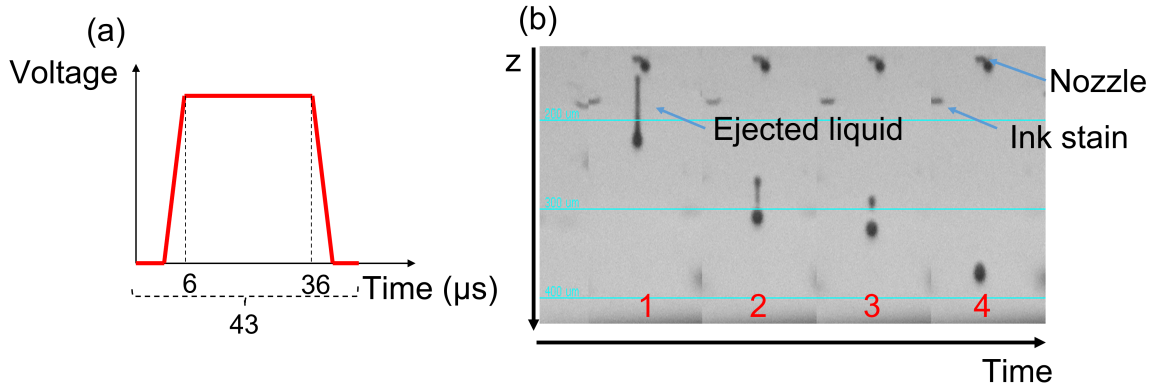
Figure 4.9: (a) Actuation pulse used for all inks and (b) Image of an ejected drop

4.1.4 Printability phase diagram

In order to ease the printing and obtain the best thin film quality, the rheology of the ink has to match the requirement of inkjet printing that will be detailed below. In an ideal case, the drops that are ejected should all be single drops (i.e. no satellites), have the same volume and travel vertically without disturbance. In order to determine the printability of an ink, characteristic physical numbers named Reynolds (Re), Weber (We) and Ohnesorge (Oh) numbers are used. The Oh number is barely encountered and its inverse, Z, is most often the characteristic number used. These numbers are defined as follow

$$Re = \frac{v\rho a}{\eta} \tag{4.5}$$

$$We = \frac{v^2\rho a}{\gamma} \tag{4.6}$$

$$Oh = \frac{1}{Z} = \frac{\sqrt{We}}{Re} = \frac{\eta}{\sqrt{\gamma\rho a}} \tag{4.7}$$

where ρ, η, γ and v are the density, the dynamic viscosity, the surface tension and the velocity of the fluid respectively and a is a characteristic length taken as the nozzle

diameter in inkjet printing. The Re number is the ratio of inertial forces to viscous forces. The We number is the ratio of the kinetic energy to the surface energy. The Oh number is the ratio of the viscous forces to the surface forces.

It was proposed by Reis et al. [104] that $1 < Z < 10$ for stable drop formation through numerical simulation. Duineveld [105] estimated the minimum velocity at which the ejected drop travels. It results from the balance between the force at the nozzle due to surface tension and the pressure created by the liquid inertia. This velocity v_{min} is given by

$$v_{min} = \sqrt{\frac{4\gamma}{\rho a}} \tag{4.8}$$

It can be translated into a minimum We number

$$We_{min} = v_{min}\sqrt{\frac{4\rho a}{\gamma}} > 4 \tag{4.9}$$

Another limitation is the splashing of the drop on the substrate. Stow et al. [106] showed that the splashing occurs when a drop impacts a substrate with a high speed. At the contact line of the drop with the substrate, a crown of liquid is formed and the liquid goes upward and outward. This liquid that is expelled from the drop makes splashing stains all around the drop. Ideally, the impact of the drop should be clear, i.e. one single impact without splashing. Stow et al. established the limit on the We and Re numbers to ensure it

$$We^{1/2}Re^{1/4} > f(R) \tag{4.10}$$

where $f(R)$ is a function of the surface roughness, which for flat surface is around 50. A printability phase diagram can be built from the aforementioned limitations (fig 4.10). The printability region is made of a narrow set of We and Re numbers. It is in between the instabilities defined by $1 < Z < 10$ which corresponds to too viscous liquids and liquids prompt to satellites formation. On the bottom of the graph is the lowest energy possible that needs to be imparted to the drop to enable ejection and on the top is the onset of splashing triggered by a high velocity.

Liu and Derby [107] did an extensive experimental analysis on the printability and developed an alternative printability diagram. They used Z as one of the characteristic number, which is independent of the velocity. Indeed, both We and Re numbers depend on the velocity which can not be known before the actual inkjet printing process. In order to predict whether an ink will be printable, the use of Z number is more informative. They did an extensive experimental analysis of the fluids printability with various Z (from 0.05 to 36.8) and We numbers (fig 4.11). They found that the velocity of the ejected droplet increased as a function of Z ($2 < Z < 14$) and stays quite constant for $Z > 14$. Without changing the fluid or the size of the nozzle, Z can be increased by either increasing the surface tension and/or decreasing the viscosity. However, the
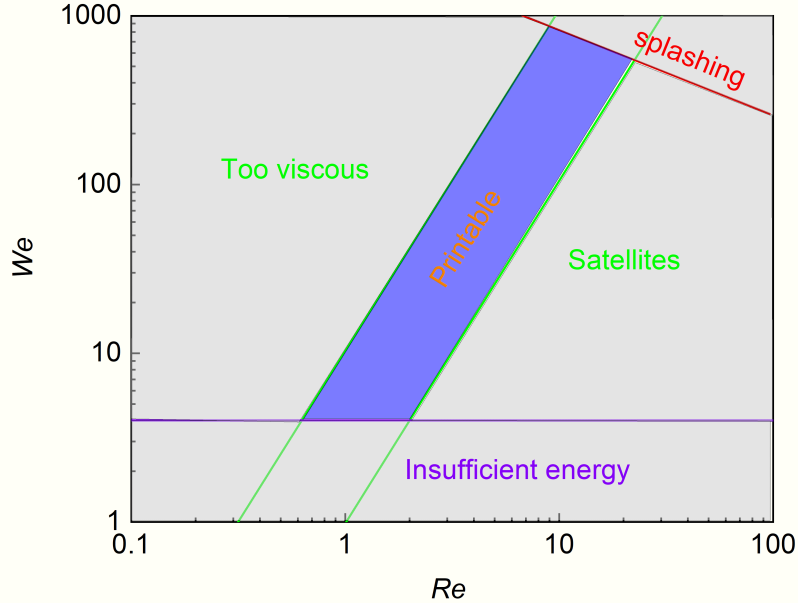
Figure 4.10: Printability diagram as a function of the We and Re number.

influence of the surface tension is not as pronounced as the viscosity because of its square root dependence. When Z increases (i.e. the viscosity decreases), the energy imparted to the liquid by the pressure pulse is less dissipated by friction, giving a higher drop velocity.

When the actuation pulse ejects liquid, different scenarios can occur. In the ideal situation, a single drop is ejected. As discussed previously, the formation of satellites is a common unwanted phenomenon. Once it is formed, it can either coalesce with the main drop or stay as an independent drop. In the worst case, several independent satellites are present. Figure 4.11 shows the conditions producing a single droplet, a coalescing satellite, a stable satellite and multiple satellites. A drawback of this graph is the use of We number which prevents to predict the printability without any doubt. However, a first verification of the printability can be done by checking if the Z number is in the right range.

For a constant Z, satellites starts to appear when a certain thresholds is reached in the We number. Increasing the We can be achieved by increasing the velocity. This means that passed a certain velocity threshold, the stand-off distance between the nozzle and the substrate given to the satellites to coalesce with the main drop is insufficient. Indeed, the small satellite is slowed down by air more drastically than the main drop. Moreover, the stand-off can not be elongated infinitely because of the perpendicular air drags deviating the main drop from its initial trajectory. This represents the upper limit of the velocity. This limit is found at a We number of 25 for $Z < 4$ based on the experimental data of Liu et al. [107] When $Z > 4$, this We threshold (i.e. satellite threshold) is decreasing with increasing Z (decreasing viscosity).

Z number also influences the number of stable satellites. Indeed, at low Z, only one
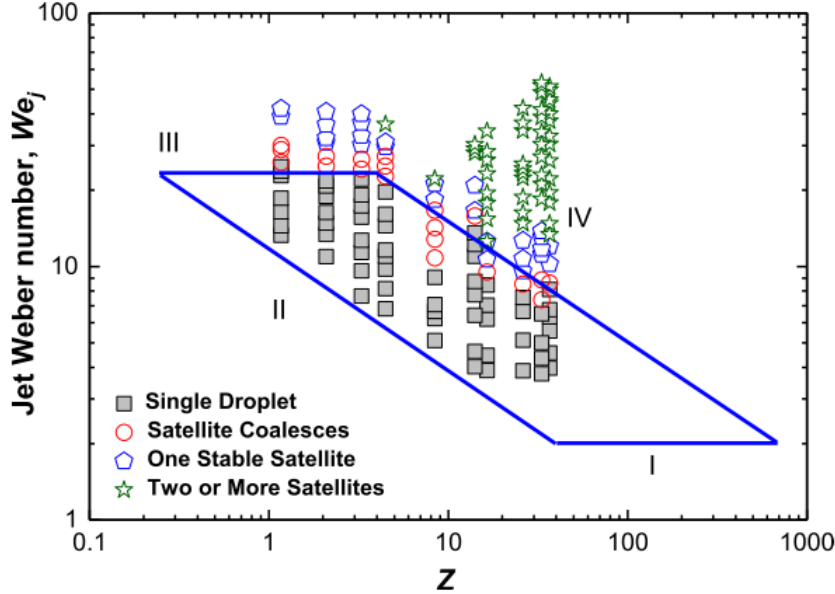
Figure 4.11: Printability phase diagram. The symbols are experimental data. The quadrilateral represents an hypothesized printability region found via extrapolation of experimental data. Figure copied from [107].

stable satellite could be obtained, while when $Z > 10$ the numbers of stables satellites increases. This observation does not imply that satellites do no exist at low Z, but that it might require a higher voltage than available in the piezoelectric actuator to create them. A tentative explanation of this change in satellites behaviour was done by Kim et al. [108]. The capillary number, defined as $Ca = We/Re = v\eta/\gamma$, represents the ratio of the viscous force to the capillary force. This parameter is useful in explaining the phenomenon taking place in the thread region, i.e. the neck between the filament and the main drop. Fluid is flowing out from the thread with time, making it thinner. During this process, capillary forces promote the thinning, while the viscous forces tend to resist to the thinning. When Z is large (i.e. starting from around $Z = 10$), the viscosity is low. The capillary forces take over the viscous forces, enhancing the break of the filament into several satellites.

Finally, the We lower limit is simply reached when no drop is ejected because the kinetic energy given by the pressure pulse is lacking compared to the surface energy. The quadrilateral shape on figure 4.11 represents the predicted printability region based on the extrapolation of the limits of the experimental data. For example, the region III is defined by the upper limit of $We < 25$ discussed above. The region II is the lower jettability limit, while region IV is the upper limit for $Z > 4$ and region I is taken as $We > 2$. This last limit is slightly different from the experimental data because of the restriction of the experiments: only a selected range of actuation voltages were tested. Other works showed lower inflight velocity than the one reported in the work of Derby et

al. which gives a lower We number. Duineveld et al. [105] found a Z number of 2, which is the limit that is reported in this figure.

In summary, the rheology of the ink, i.e. viscosity and surface tension, have to be tuned in order to have a Z number in the quadrilateral in figure 4.11. The We number can not be predicted because of the presence of the inflight velocity of the drop in the definition of the parameter. Thus, the figure is informative on the potential printability of the ink but can not give a definitive answer. In the next section, the process following the printing, i.e. the interaction of the ink with the substrate, is discussed.

4.1.5 Wetting

In the previous section, the essential rheology required to ensure a satisfying printability was discussed. Once the ink is ejected from the nozzle, it impacts the substrate and the interactions between the substrate and the ink will govern the spreading of the ink and ultimately, the morphology of the printed pattern. This section is dedicated to the study of the ink wetting.

Principle

The wetting refers to the spreading of a liquid deposited on a solid substrate. It can be characterized by the contact angle, defined as the angle between the substrate and the tangent to the liquid drop (figure 4.12). When the liquid spreads on the substrate, i.e. total wetting, the contact angle is 0°, whereas when the liquid keeps a round shape on the substrate, i.e. partial wetting, the contact angle is bigger. This angle is related to the forces acting at the triple line by the well known Young-Dupré law:

$$\gamma_{lv} \cos \theta = \gamma_{sv} - \gamma_{sl} \tag{4.11}$$

where γ_{lv}, γ_{sv}, γ_{sl} are the surface free energies between the liquid and the vapor, the solid and the vapor, the solid and the liquid, and θ is the contact angle.
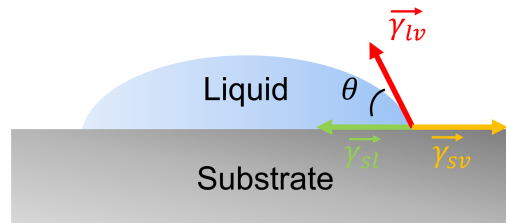
Figure 4.12: Contact angle (θ) of a drop deposited on a solid substrate, free energy between the liquid and the vapor (γ_{lv}), the liquid and the solid (γ_{sl}) and the solid and the vapor (γ_{sv}).

When a solid has a high surface free energy, the liquids tend to spread, whereas,

when the surface free energy is low, it does not. Substrates such as silicon and glass have a high surface energy. However, when some organic impurities are attached to the surface, the wettability decreases. This contamination from lab air makes the substrate improper in terms of wetting. In order to clean the substrates, different procedures have been used in literature, such a plasma cleaning [109], laser cleaning [110], ultra-violet (UV) ozone cleaning [111],... The latter turns out to be an efficient, convenient and inexpensive cleaning method for the cleaning of various substrates. During this process, organic impurities will be transformed into volatile compounds via the decomposition produced by the UV and the reaction with O_3. The details on the UV ozone process can be found in appendix A.1.3. Glass substrates, Mo-coated glass substrates and CIGSSe absorbers were used in this thesis. The first one was pre-cleaned with acetone, ethanol and deionized water before a 15 minutes of UV ozone treatment. The other two were directly treated with UV ozone treatment for 5 minutes. The choice of this duration will be explained in the section 4.1.5. Impurities that can not be removed via UV ozone treatment such as inorganic particles should be removed with a wet cleaning procedure that consists in dipping the sample in acetone, ethanol and deionized water successively when possible. Figure 4.13 shows a wet inkjet printed film, where impurities that were not successfully removed from the surface interact with the ink, preventing a correct wetting. The ink can either aggregates around the impurity or be repelled by it. The latter defect creates holes in the film, and in turn a potential pinhole in the solar cell.
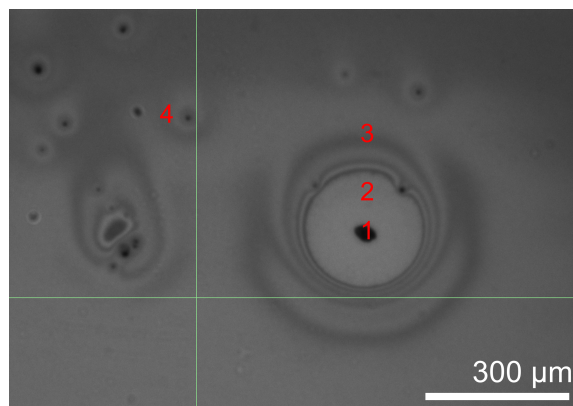
Figure 4.13: Optical image of disruptive residues in a wet inkjet printed film on Mo-coated glass. 1. residual impurity, 2. uncovered Mo, 3. ink covered Mo, 4. excess of ink due to impurity. The green cross is a referential from the inkjet printer and has no signification here.

Wetting model

Wettability is of utmost importance in order to form a continuous film on a substrate and should be checked before any experiment. To do so, the surface free energy of the solid has to be determined. The approach used here is based on the model of Owens-

Wendth-Rabel-Kaelbe (OWRK) [112]. Oss and Good [113] developed a more complex model taking into account the acid-base interactions. However, the OWRK model is considered as a sufficient approach in this work. As discussed earlier, the wetting of a liquid on a solid follows the well known Young law (eq 4.11). The early steps of this model was done for liquid-liquid interface and it was later extended to solid-liquid interface. To develop the model, Fowkes [114] hypothesized that the surface tension of liquids can be split into a dispersive (γ_d) and a polar (γ_p) components

$$\gamma_{lv} = \gamma_l^d + \gamma_l^p \tag{4.12}$$

Fowkes continued by assuming that two liquids in contact interact at their interface such that the interfacial regions are affected by the bulk attractive forces in each phase as well as the London dispersion forces across the interface, which can be approximated by a geometric mean $\sqrt{\gamma_1^d \gamma_2^d}$ (fig 4.14). In other words, the interfacial molecules of liquid 1 are attracted by the bulk molecules of liquid 1 (γ_1) and by the interfacial molecules of liquid 2 and this latter interaction follows a geometric mean ($\sqrt{\gamma_1^d \gamma_2^d}$). The same applies for liquid 2.
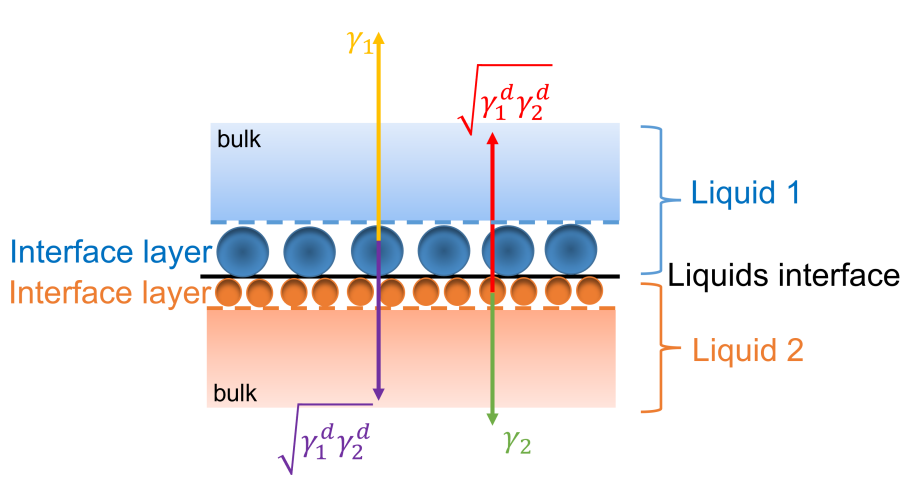
Figure 4.14: Forces acting on the interface of two liquids in contact. The rectangles represent the bulk molecules, while the beads are the interfacial molecules of each liquid.

This assumption was originally taken for similar molecules and it was later hypothesized that it can be applied most of the time to dissimilar molecules which have different volumes [115]. In the case of liquids having only dispersive interactions such as in hydrocarbons, the dispersion component felt in one liquid is given by $\gamma_1 - \sqrt{\gamma_1^d \gamma_2^d}$, while in the other liquid, this component is given by $\gamma_2 - \sqrt{\gamma_1^d \gamma_2^d}$. The surface tension at the interface between two liquids can thus be written as

$$\gamma_{12} = \gamma_1 + \gamma_2 - 2\sqrt{\gamma_1^d \gamma_2^d} \tag{4.13}$$

Owens et al. established a generalized expression for liquids having both dispersive and polar interactions [112]

$$\gamma_{12} = \gamma_1 + \gamma_2 - 2\sqrt{\gamma_1^d \gamma_2^d} - 2\sqrt{\gamma_1^p \gamma_2^p} \tag{4.14}$$

where the power factor p stands for polar contribution.

Fowkes further extended his model to the solids. Equations 4.12 and 4.13 can thus be written as

$$\gamma_{sv} = \gamma_s^d + \gamma_s^p \tag{4.15}$$

$$\gamma_{sl} = \gamma_s + \gamma_l - 2\sqrt{\gamma_s^d \gamma_l^d} \tag{4.16}$$

Taking into account both the dispersive and polar interactions in the solid and liquid, equation 4.16 can be written as

$$\gamma_{sl} = \gamma_s + \gamma_l - 2\sqrt{\gamma_l^d \gamma_s^d} - 2\sqrt{\gamma_l^p \gamma_s^p} \tag{4.17}$$

Introducing equations 4.15 and 4.17 into equation 4.11, the Young equation can be rewritten as

$$\gamma_{lv} \frac{1 + \cos(\theta)}{2\sqrt{\gamma_l^d}} = \sqrt{\gamma_s^d} + \frac{\sqrt{\gamma_s^p}\sqrt{\gamma_l^p}}{\sqrt{\gamma_l^d}} \tag{4.18}$$

where γ_{lv}, γ_l^p and γ_l^d can be found in literature for various liquid and the contact angle θ can be measured. γ_s^d and γ_s^p can be extracted by plotting the equation 4.18 with the y axis being the left hand side of the equation and the x axis being $\frac{\sqrt{\gamma_l^p}}{\sqrt{\gamma_l^d}}$. A linear regression gives $\sqrt{\gamma_s^d}$ as the intercept and $\sqrt{\gamma_s^p}$ as the slope.

This method was used to assess the wettability of the absorbers before the printing. The contact angles of dimethyl sulfoxide (DMSO), ethylene glycol, propylene glycol and water were measured on bare and 5 minutes UV ozone treated absorbers. The choice of the liquid probes is very important in order to have sufficiently spread data points and reliable measurements. The main aspects to take into account are

- the chemical interactions between the liquids and the substrate : the solid should not react chemically with the liquids.

- the volatility of the liquids: the three phases line of the drop pins to the substrate so that the drop can not move. When the solvent evaporates, the drop is deflating and the contact angle is decreasing. Fast evaporating liquids will have a fluctuating contact angle, which makes the measurement barely reproducible.

- the $\sqrt{\gamma_l^p}/\sqrt{\gamma_l^d}$ ratios: the different probes should have ratios sufficiently different to ensure the spreading of the data points. This will reduce the error on the extraction

of the polar and dispersive components of the solid free energy.

The polar and dispersive components given in literature are for pure liquids. However, our ink is made of a mixture of liquids. Therefore, a model is required to calculate the dispersive and polar components of the mixture. The surface tension of binary aqueous-organic mixture can be calculated based on the pure liquids characteristics. Connors et al. [116] established the following equation

$$\gamma_{mix} = \gamma_1 - [1 + \frac{bx_1}{1 - ax_1}]x_2(\gamma_1 - \gamma_2) \qquad (4.19)$$

where $\gamma_{mix}, \gamma_1, \gamma_2$ are the surface tension of the mixture, of the pure liquid 1 (water) and the pure liquid 2 (organic), x_1, x_2 are the mole fraction of liquid 1 and 2 and a and b are parameters specific to an organic-water mixture. The surface tension's dispersive component takes the form [117]

$$\gamma_{mix}^d = x_1^2\gamma_1^d + 2x_1x_2(1 - \delta_{12})\sqrt{\gamma_1^d\gamma_2^d} + x_2^2\gamma_2^d \qquad (4.20)$$

The simple geometric mean $\gamma_{mix}^d = \sqrt{\gamma_1^d\gamma_2^d}$ was not used because it does not take into account the effect of mixture composition. Eq 4.20 can be simplified by putting δ_{12} (which is an empirical fitting parameter, also called the binary interaction parameter) to 0

$$\gamma_{mix}^d = x_1^2\gamma_1^d + 2x_1x_2\sqrt{\gamma_1^d\gamma_2^d} + x_2^2\gamma_2^d \qquad (4.21)$$

This simplification only introduces an error of 2% compared to the full equation [117]. The polar component is easily found via the relation

$$\gamma_{mix}^p = \gamma_{mix} - \gamma_{mix}^d \qquad (4.22)$$

This formalism can be applied to water-ethanol and water-propylene glycol mixtures. In table 4.4, the fitting parameters and the free energy of the mixture as well as the polar and dispersive components are reported. These results will be further discussed in section 4.2.3.

The wetting model will be applied to the CIGSSe absorber in section 4.2.4 to evaluate the wetting of the inks.

4.1.6 Dewetting of a thin film

Dewetting refers to the spontaneous withdrawal of a liquid film on a surface. Even if the Young contact angle is smaller than 90° which corresponds to a partial wetting, a thin film can dewet [118]. Actually, the Young contact angle is characteristic of an equilibrium state, while dewetting occurs in metastable films. Dewetting is characterized

	Partition coefficient		Molar fraction		Surface tension (mN/m)		
	a	b	x_1	x_2	γ_{mix}	γ^d_{mix}	γ^p_{mix}
ethanol	0.963	0.897	0.62	0.38	26.3	20.8	5.5
propylene glycol	0.967	0.824	0.80	0.20	48.2	22.8	25.4

Table 4.4: Surface tension parameters of binary aqueous-organic mixtures at 25°C. Partition coefficients a and b are from [116] for ethanol and data for propylene glycol are obtained from a linear regression of data from [93] with eq 4.19. The surface tensions of the mixtures are calculated based on eq 4.19, 4.20 and 4.21

by three different regimes (fig 4.15). In the beginning, holes are created in the thin film by a rupture process. Then, these holes grow until they coalesce. Finally, the thin interface between the holes separate into small droplets. The dewetting phenomenon observed in
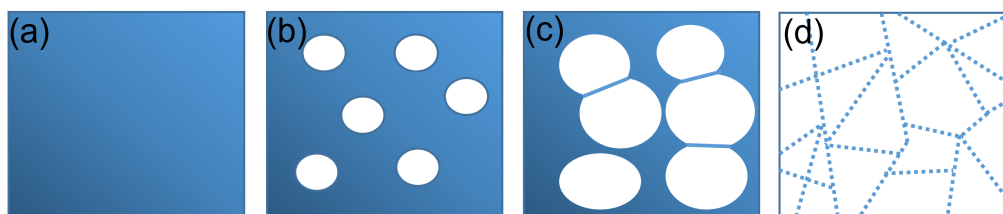
Figure 4.15: Stages of dewetting. (a) Continuous film, (b) nucleation of holes, (c) growth of holes, (d) splitting of holes interface into droplets.

figure 4.15 is due to heterogeneous nucleation. This type of dewetting is probably related to the presence of dust particles or inhomogeneities. It was already discussed that UV ozone is an effective cleaning process to remove organic molecules. However, non-organic particles have to be removed through wet cleaning using different solvents. This process is unfortunately not 100% efficient and each remaining particle can create a dewetting starting point.

Figure 4.16 shows the formation of fingers through the dewetting of a film starting from the edge. The ultimate stage of dewetting is the same as shown in figure 4.15d. A fast drying process as described in section 4.1.7 is a way to stop the liquid from flowing and thus circumvent the last stage of dewetting.

4.1.7 Evaporation and coffee ring effect

The last step of the processing is the annealing to turn the ink into the desired material. First, a drying step is necessary to ensure the formation of an ideal thin film. The drying has to be controlled in order to avoid inhomogeneities in the film. A very well-known drying issue is the coffee stain effect. Its appearance depends on three essentials conditions which are a non zero contact angle at the contact line between the liquid and
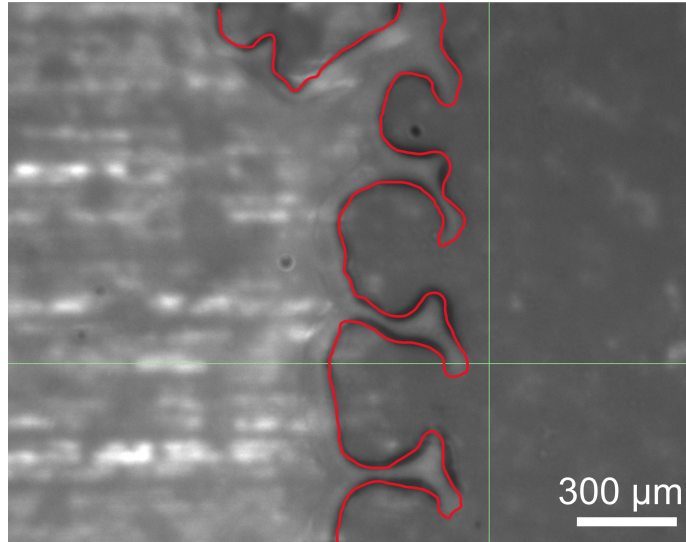
Figure 4.16: Dewetting of an inkjet printed film on quartz. The border (in red) of the film separate the film (on the left) from the uncovered quartz (on the right).

the substrate, the contact line is pinned and the solvent evaporates [119]. In the case of a non pinned liquid, the evaporation starts at the perimeter and the drop shrinks, preventing the formation of coffee stain effect but also reducing the size of the deposit compared to the size of the drop. In the case of a pined drop, it can not shrink and the liquid must flow to the perimeter to compensate for the evaporation. Moreover, in order to keep the spherical cap shape, the volume of liquid evaporated should decrease from the center to the perimeter of the drop. However, the evaporation is stronger at the edges. Thus, a liquid flow is necessary to maintain the balance. When the liquid flows toward the edges, it transports material that is being deposited and form the coffee ring (fig 4.17a). In the case of a printed line, the dried pattern is a dual-ridged profile.

In order to counteract this phenomenon, the driving force of the drying has to be modified. One possible mean is to use a mixture of solvents to generate gradients in the surface tension. This gradient will induce a Marangoni flow that prevents the accumulation of material at the contact line (fig 4.17b). In the Marangoni effect, the surface tension is lower at the edge than at the top of the drop creating a circulation of the material from the contact line to the top [120].

The knowledge addressed in this section will now be applied in the next section to discuss the results obtained on the rheology of the inks, the printability and the wetting of the films.

4.2 Results

In this section, the rheology of the inks used in this work is shown. Their wetting is studied using the wetting envelope model brought up in section 4.1.5. Finally, the drying
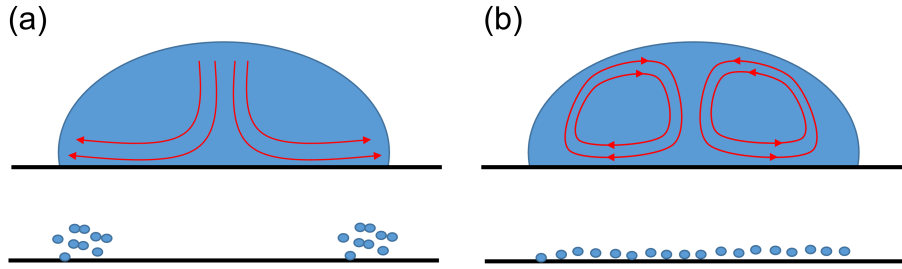
Figure 4.17: Material deposition from the evaporation of a drop. (a) Coffee stain effect. (b) Homogeneous deposition through Marangoni flow.

and annealing of the films is described.

4.2.1 Surface tension and viscosity

Table 4.5 shows the surface tension and viscosity of some of the inks used in this work. It was discussed in section 4.1.1 the influence of temperature, solvents mixture and salts content on the surface tension of the inks. Briefly, the solvents mixtures enables the fine tuning of the surface tension, while the temperature decreases it. The effect of salts was found to be negligible in our inks because of the low salts concentration. As a results, all the surface tensions of our inks are equal within the error. Similarly to surface tension, viscosity is influenced by temperature and solvents mixture allowing its tuning. Salts have a pronounced effect on viscosity contrarily to the surface tension as thoroughly discussed in section 4.1.2. This influence could be roughly explain by the Jones-Dole equation [95]

$$\frac{\eta}{\eta_0} - 1 = AC^{1/2} + BC \tag{4.23}$$

where η, η_0, and C are the viscosity of the solution, the viscosity of water and the concentration of the salts (up to 1 M). In a nutshell, the parameter B (table 4.6) could explain the increased viscosity. Indeed, the values of B was negligible for thiourea components and chlorine ion. The high viscosity of cadmium acetate could be justified by the added contributions of cadmium and acetate.

4.2.2 Printability phase diagram of the inks

The theory presented in section 4.1.4 is now applied to the inks used in this work. In order to ease the understanding, figure 4.18a shows the printability diagram with the effect of increase η, γ or v. The velocity keeps Z constant but increases We. η solely decreases Z. γ decreases We but increases Z, however this latter has a square root dependence on surface tension, meaning that We decreases more than Z increases.

| Ink name | Chemical species concentration (M) | | | | σ (mN/m) | η (mPa.s) |
	$InCl_3$	$CS(NH_3)_2$	$Cd(CH_3COO)_2$	$ZnCl_2$		
solvent					34.7 ± 1.8	3.85 ± 0.08
[S]/[In]=3	1.2	1.2			34.3 ± 2.2	5.80 ± 0.12
[S]/[In]=1	0.4	0.4			33.9 ± 2.2	5.46 ± 0.11
[S]/[In]=3 low c	0.1	0.3			33.3 ± 1.9	4.32 ± 0.09
Cadmium acetate			0.8		33.5 ± 2.5	7.40 ± 0.15
Thiourea		0.8			34.3 ± 2.2	4.09 ± 0.08
[Zn]/[S]=1		0.4		0.4	32.8 ± 1.6	4.44 ± 0.09

Table 4.5: Surface tension and viscosity of some inks used to make In_2S_3, CdS and Zn(O,S).

	Cd^{2+}	Zn^{2+}	In^{3+}	Cl^-	SCN^-	CH_3COO^-	NH_4^+
B	0.360	0.361	0.37	-0.005	-0.025	0.236	-0.008

Table 4.6: Parameter B from the equation of Jones-Dole (eq 4.23). Data from [97]

Taking one of the ink used in this work as an example (η=5.80 mPa.s, γ=34.3 mN/m,
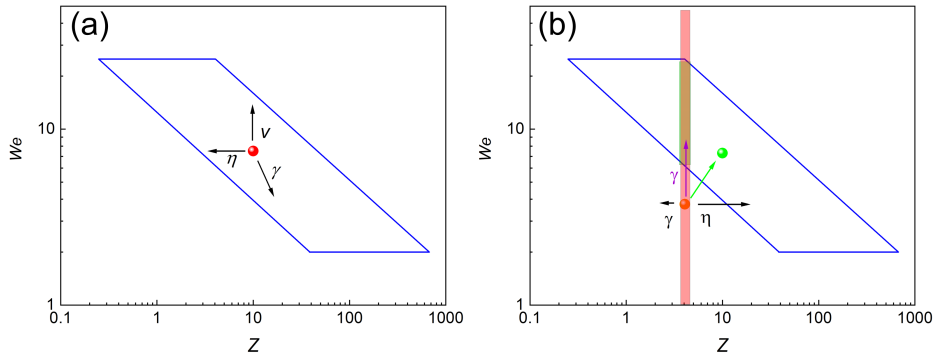
Figure 4.18: (a) Influence of increasing η, γ or v of a droplet on the position on the printability diagram. (b) Position of a droplet with η=5.80 mPa.s, γ=34.3 mN/m, a=18 μm , ρ=0.90 g/L (red sphere) on the printability diagram and the position after increasing the temperature (green sphere). The purple arrow stands for the effect of γ on We, while the black arrows represent the effect of γ and η on Z. The red area is the range of possible We corresponding to 2 m/s $<$ v$<$ 10 m/s and the green region is the allowed We for a stable printing with the same Z.

a=18 μm , ρ=0.90 g/L), the Z number is 4.1 (fig 4.18b). The Weber number depends on the velocity of the drop, which changes depending on the actuation voltage. For a theoretical range of velocity going from 2 m/s to 10 m/s, the We varies from 2 to 47 (red area). In order to have a satellites free jetting, the We number should be between 6 and 25 (green area). However, the upper limit of the actuating voltage of the used printer is

40 V which is not enough to produce the minimum We number meaning that the ink is in region II defined on figure 4.11. In order to bypass this issue, the temperature of the nozzles were increased to 40°C. It reduces the viscosity and surface tension, enabling an actuation voltage range of 25 to 40 V depending on the cleanliness of the nozzles. Indeed, the nozzles of a brand new head will eject at a lower voltage than a reused head. An optimization work has to be done before each printing. Figure 4.19 shows the printability diagram for 3 inks ([S]/[In]=3, Cadmium acetate and thiourea). At room temperature, none of these inks jets with the highest voltage (40 V). The head was thus heated to decrease the viscosity and the surface tension. The lower Z, the higher the temperature.
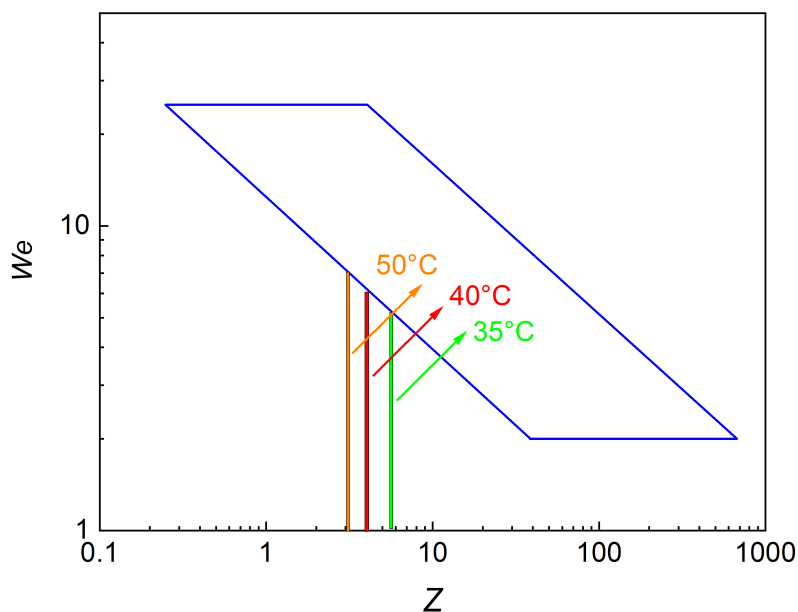
Figure 4.19: Printability diagram of 3 inks (Thiourea (green), cadmium acetate (orange) and [S]/[In]=3 (red)) before heating (areas) and after heating the head (arrows).

In summary, we could show that in terms of Z number, the inks are printable. However, the We number can only be determined experimentally. The inks actually have to be heated to enable the jetting even though the Z number is in the right range because the available voltage which control the We number is too low. By increasing the temperature, the We number increases and the voltage is high enough to eject drops.

4.2.3 Wetting of the inks

In this section, the influence of the inks salts content on the wetting of these inks is assessed in terms of time variation of the contact angle and initial spreading of the ink.

The contact angles of three inks were measured as a function of time on untreated Mo (fig 4.20(a)). The inks are [S]/[In]=3 (blue), [S]/[In]=3 low c (red) and [S]/[In]=1 (green) as reported in table 4.5. The contact angle is similar for all inks right after the

deposition. It then decreases rapidly during the first 2 minutes and decreases slowly for longer time. The angle of [S]/[In]=3 low c decreases faster than the other two which contain a higher In concentration. The trend seems to be exponential as highlighted by the fitting on fig 4.20(a). However, the inset showing a neperian logarithm of the contact angle is not linear. This means that the decay is actually not exponential. A double linear decrease seems more appropriate to describe the trend (fig 4.20(b)). The decrease until 2 minutes is similar for both [S]/[In]=3 and [S]/[In]=1 inks, while the slope of [S]/[In]=3 low c is steeper (table 4.7). The decrease is influenced by the indium concentration: the lower its concentration, the faster the decrease in contact angle. Figure 4.20(c) shows that the drop width is relatively constant over time. The contact angle can decrease either because of the evaporation of the drop or its spreading. Table 4.7 shows that the drop width was decreased by only 10% for the [S]/[In]=3 low c which means that the evaporation of the liquid is essentially responsible for the decrease in contact angle. The second region of figure 4.20(b) shows a different behaviour than region 1. The slopes (table 4.7) are much smaller than in the first region and are similar for all three inks, i.e. salts content independent. In summary, the significant evaporation happens in the first 2 minutes after deposition and is inversely proportional to the indium concentration in this time frame.
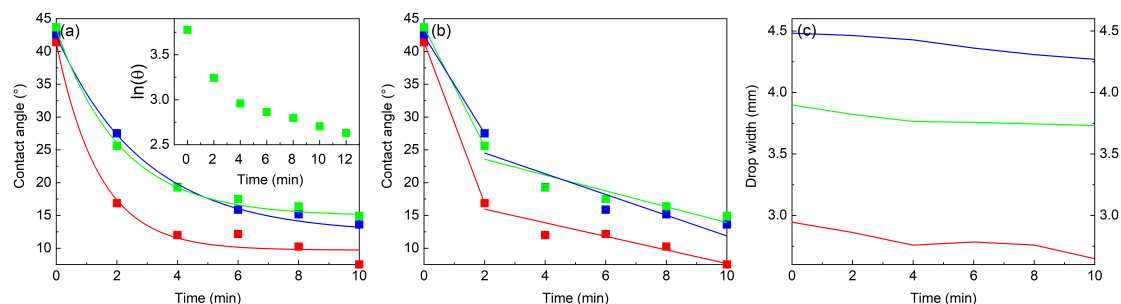
Figure 4.20: (a) Evolution of the contact angle of 3 inks ([S]/[In]=3 (blue), [S]/[In]=3 low c (red) and [S]/[In]=1 (green)) on non treated Mo as a function of time. An exponential curve is fitted to the data. The inset is a neperian logarithm of the contact angle as a function of time for [S]/[In]=3 low c. (b) Linear fitting of the data presented in (a). Two linear fitting are applied to each set of data. (c) Evolution of the drop width used to measure the contact angle as a function of time. The error bar is smaller than the symbol in (a) and (b). An error of 5% can be attributed to the measurements of (c) but it is not plotted for clarity.

The salts concentration also influences the spreading of a drop of constant volume. Figure 4.21a and b show inkjet printed [S]/[In]=3 ink with drops and a double line patterns, i.e. a line that was printed by printing successively 2 lines next to each other. The drops are made of a dark center region with a lighter ring. This could indicate the presence of coffee ring effect. This will be investigated in section 4.1.7. The double line also seems to be a double ridged bridge which is an outcome of coffee stain effect. A

	Intercept 1	Slope 1	Intercept 2	Slope 2	Relative variation drop width (%)
[S]/[In]=3	42.4	-7.5	27.7 ± 2.8	-1.6 ± 0.4	7
[S]/[In]=3 low c	41.4	-12.3	18.0 ± 1.3	-1.0 ± 0.2	10
[S]/[In]=1	43.7	-9.0	26.0 ± 1.9	-1.2 ± 0.3	4

Table 4.7: Parameters of linear regression in two regions from fig 4.20(b). Region 1 is until 2 minutes, region 2 is from 2 minutes to 10 minutes. Last column is the relative variation of the drop width after 10 minutes. No error on intercept 1 and slope 1 can be given because the linear fitting between two points is straightforward.

darker series of drops can be identified in the middle of the stripe. This is related to the issue with the angle of the cartridge described in the appendix A.1.2. Figure 4.21 c and d are the same patterns as figure 4.21 a and b for the ink [S]/[In]=3 low c, i.e. a lower concentration but the same [S]/[In] ratio. The drops diameter is bigger than for the more concentrated ink (130 µm for [S]/[In]=3 low c and 76 µm for [S]/[In]=3). The surface tension reported in table 4.5 are similar, excluding the influence of this parameter on the spreading. This spreading trend is in accordance with the contact angle trend of figure 4.20a. Based on the Young equation (4.11), the contact angle is defined by the balance between the free energies between the solid and the liquid γ_{sl}, the vapor and the solid γ_{sv} and finally between the vapor and the liquid γ_{lv}. We can safely hypothesize that γ_{sv} is constant and γ_{lv} was shown to be similar. The only free energy that can influence the spreading of the drop is thus related to the interaction between the solid and the liquid. Since the solvent composition is constant for all inks, the salts are found to be the influencing species. Thanks to this wider spreading, the double lines (fig 4.21d) does not show the darker drop stains in the middle of the line. Moreover, the coffee stain effect is not obvious in the drop pattern, while it seems to be present in the line pattern. This will be further investigated in section 4.1.7.

In a nutshell, the salts contents in the ink influences the evolution of the contact angle with time and also the initial spreading of the drop on the substrate. In the next section, the OWRK model is used to predict the wetting of a liquid on a given substrate.

4.2.4 Wetting envelope

Predicting the wetting of an ink on a substrate can help decrease the waste. Indeed, all the materials used in PV are precious and ideally, trial and error should be avoided. In this section, the modified Young equation derived in section 4.1.5 and reminded below, is used to establish the wetting of a liquid on CIGSSe. First, the solid free energy is determined using the following equation

$$\gamma_{lv}\frac{1+\cos(\theta)}{2\sqrt{\gamma_l^d}} = \sqrt{\gamma_s^d} + \frac{\sqrt{\gamma_s^p}\sqrt{\gamma_l^p}}{\sqrt{\gamma_l^d}} \qquad (4.24)$$
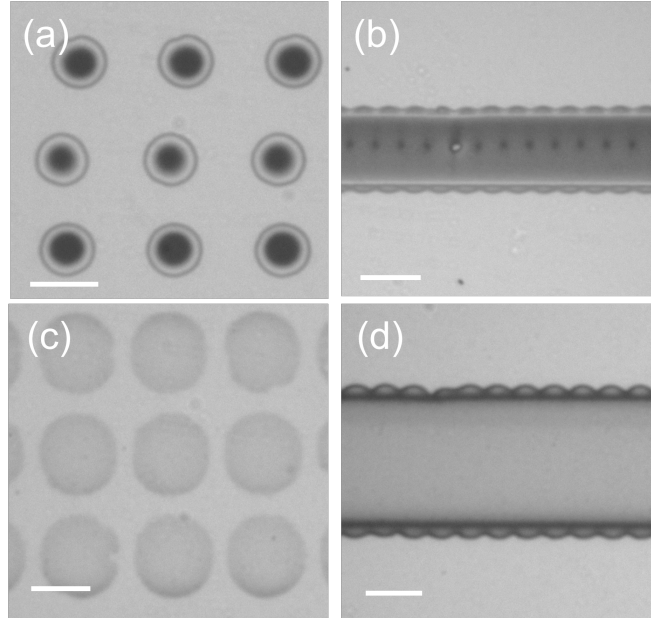
Figure 4.21: Optical image of inkjet printed drops (a),(c) and double line (b),(d). The first row represents the ink [S]/[In]=3 while the second row represents the ink [S]/[In]=3 low c. The scale bar is 100 µm. The pictures are taken just after the printing process.

where γ_{lv}, γ_l^p and γ_l^d can be found in literature for various liquid and the contact angle θ can be measured. γ_s^d and γ_s^p can be extracted by plotting the equation 4.24 with the y axis being the left hand side of the equation and the x axis being $\frac{\sqrt{\gamma_l^p}}{\sqrt{\gamma_l^d}}$. A linear regression regression gives $\sqrt{\gamma_s^d}$ as the intercept and $\sqrt{\gamma_s^p}$ as the slope.

Different liquids were deposited on CIGSSe substrates and their contact angles were measured. Table 4.8 shows that the contact angles of the liquid probes decreased with the UV ozone treatment applied to the CIGSSe, indicating a better wetting of the liquids on the surface.

	Contact angle $\pm$ 0.4 (°)				Surface energy	
	Dimethyl sulfoxide	Ethylene glycol	Propylene glycol	Water	$\gamma_s^d(\frac{mN}{m})$	$\gamma_s^p(\frac{mN}{m})$
Untreated CIGSSe	45.3	64.5	51.7	79.5	16.8 $\pm$ 0.7	10.4 $\pm$ 0.7
Treated CIGSSe	0	7.4	9.1	9.9	6.8 $\pm$ 0.9	67.9 $\pm$ 1.0

Table 4.8: Contact angle of liquid probes on untreated and 5 minutes UV ozone treated CIGSSe absorber and surface free energy of these surfaces. The measurement was perfomed a couple of seconds after the deposition to rule out any effect from evaporation.

Figure 4.22 is the plot of equation 4.24 based on the measured contact angles and liquids free energy components from table 4.9. The extracted free energy's polar and dispersive components of the untreated and UV ozone treated absorbers are shown in table 4.8. The untreated absorber have a surface more dispersive than polar. In order to have a good wetting of a liquid on a surface, the polar and dispersive components of both

the liquid and the solid have to be similar. Thus, polar solvents such as water poorly wets the absorber: it has a similar dispersive component as the absorber surface but the polar component is nearly 5 times bigger than the solid energy. After a 5 minutes UV ozone treatment, the solid free energy polar component drastically increased, while the dispersive component decreased, making it more compatible with water.
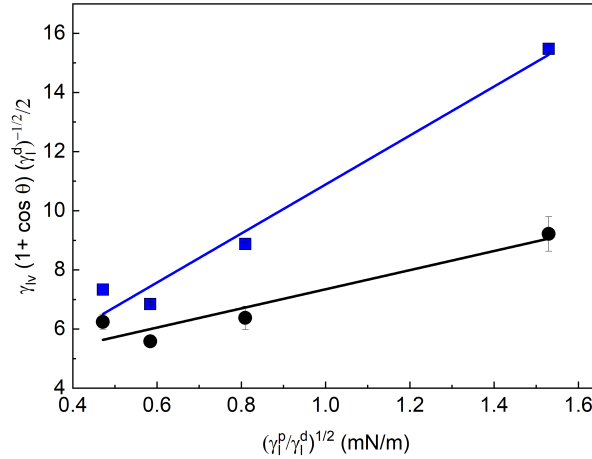
Figure 4.22: Plot of equation 4.18 based on the contact angles. Black circles and blue squares represent the untreated and UV ozone treated absorbers respectively. Solid lines are the linear regression of the associated data. The error on the data is the symbol size.

	Dimethyl sulfoxide	Ethylene glycol	Propylene glycol	Water	Ethanol
γ_l^d(mN/m)	36	29	26	22	19
γ_l^p(mN/m)	8	19	9	51	3

Table 4.9: Dispersive and polar components of liquid probes. Data from [121]

The formalism used to find γ_s^d and γ_s^p can be taken one step forward to enable the prediction of the wettability of solvents on a solid. Equation 4.24 can be rewritten as

$$\gamma_l^p \frac{1 + \cos(\theta)}{2} - \sqrt{\gamma_s^p}\sqrt{\gamma_l^p} = -\frac{1 + \cos(\theta)}{2}\gamma_l^d + \sqrt{\gamma_s^d}\sqrt{\gamma_l^d} \qquad (4.25)$$

The polar and dispersive components of the solid are known from the previous experiment. This simulation enables to find out which liquids will wet the surface with a certain angle. For example, for a full wetting, the contact angle is set to 0°. A script with a loop tests all possible values for the polar and dispersive components of the liquids and the data that verify the equation are saved. Figure 4.23(a) shows this set of data points, called the wetting envelope, with different contact angles (from 0° to 90°). The envelopes swells with an increasing contact angle, meaning that more liquids, i.e. with more diverse polar and dispersive components, fit inside the envelope, i.e. wet the surface. For

example, the data point n°1 in figure 4.23(a) is inside the 0° envelope, meaning that the virtual liquid 1 wets with a contact angle of 0°. Data point n°2 is inside the 60° envelope but outside the 30° envelope so the contact angle is in the range 30-60°. Data point 3 is outside all the wetting envelope, meaning that the contact angle is bigger than 90°. Figure 4.23b shows the 0° wetting envelope for an untreated and a 5 minutes UV ozone treated absorber. The wetting envelope of the untreated CIGSSe is quite restrained. Water and propylene glycol fall out of this envelope, meaning that none of them will wet the surface with a contact angle of 0°. Actually, their angle on the surface is 79° and 52°. Ethanol fully wets the surface with a 0° contact angle. After a 5 minutes UV ozone treatment, the wetting envelope is swollen compared to the previous one. Water nearly wets with a 0° contact angle and all the other liquids fully wet the surface.
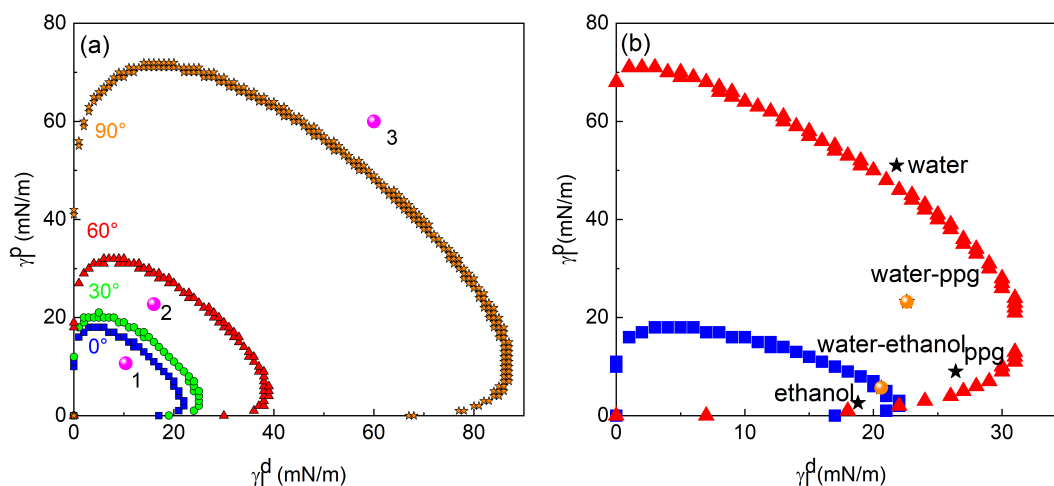
Figure 4.23: (a) Wetting envelopes with different contact angles. The data in pink are random data points to ease the understanding. (b) Wetting envelope of the untreated (blue) and 5 minutes UV ozone treated (red) CIGSSe absorber surface with a contact angle of 0°. The black stars represent the pure liquid polar and dispersive components. The orange spheres represents the polar and dispersive components of the aqueous-organic mixtures.

The wetting of pure liquids on the absorber was discussed. However, the ink contains water, ethanol and propylene glycol with 1:2:1 volume ratio. As shown in section 4.1.5, the surface tension parameters of aqueous mixtures can be calculated and are reported for water-ethanol and water-propylene glycol mixtures in table 4.10. Both water and ethanol have very similar dispersive component. The resulting dispersive component of the mixture falls thus in between these two values. The polar component in contrast, is very different between the two liquids. Even though the molar fraction of water is higher than the ethanol's, the polar component mixture is essentially equal to the polar component of pure ethanol. This means that the polar character of water is screened by ethanol in the mixture. In the case of propylene glycol-water mixture, the polar compo-

nent is somewhat in the middle between water and propylene glycol polar component, even though the mole fraction of water is 4 times bigger than propylene glycol. The polarity of water is screened by propylene glycol but not as much as in the ethanol's case. The dispersive component of the mixture is very similar to the ones from the pure liquids. Since the ink is made of the three liquids, an accurate model should take into account all of them. However, the models for ternary liquid mixtures are more complex with more fitting parameters and out of the scope of this thesis. The data for binary mixture can be nevertheless plotted on figure 4.23. The water-ethanol mixture wets completely the non treated absorber, while the water-propylene glycol mixture does not. After the UV ozone treatment, all binary mixtures wets the CIGSSe. We can thus expect to have a continuous film of ink on the treated absorber.

	water	ethanol	Propylene glycol	water-ethanol	water-ppg
γ_l^d(mN/m)	22	19	26		
γ_l^p(mN/m)	51	3	9		
γ_{mix}^d(mN/m)				20.8	22.8
γ_{mix}^p(mN/m)				5.5	25.4
γ_{mix}(mN/m)				26.3	48.2

Table 4.10: Dispersive and polar components of liquids used in the inks [121] and surface tensions of the mixtures calculated based on eq 4.19, 4.20 and 4.21

In summary, the surface free energy of the untreated and UV ozone treated CIGSSe were determined by using very small pieces, minimizing the waste. Wetting envelope were then modeled and the potential wetting of liquids was checked for both of these substrates. Once a satisfying coverage and wet morphology of the film is reached, the drying and annealing processes can be started and are discussed in the next section.

4.2.5 Drying and annealing

Figure 4.24a and c show the inkjet printed (using ink [S]/[In]=3) drops and line after the drying step which consists in 10 minutes drying at room temperature, followed by 5 minutes on a hot plate at 70°C. The diameter of the drops did not vary significantly during the drying step compared to the wet ink (shown on fig 4.21) (around 70 μm). The line pattern is affected by the gap inherent to multiple printing cycles discussed in appendix A.1.2. The drops and line have the same morphology after an annealing step at 250°C for 5 minutes (fig 4.24b and d). The optical images suggest that a coffee ring is present in both the drops and the lines. Figure 4.24e and f show profilometer 3D images of the annealed structures. The drop clearly exhibits a coffee ring effect with thick edges and thin center. The thickness of the edges is 60 nm, while the middle is

28 nm approximately. The 3D profile of the line shows different features. The first one is a coffee stain effect producing a double ridge structure with the edges being 179 nm thick, while the center is 90 nm thick in average. The second feature is the presence of three apparent stripes inside the main stripe due to the bigger gap in between printing cycles mentioned earlier. In a nutshell, the spacing between two printing cycle is similar/bigger than the drop size which creates a thinner film at the intersection between two cycles (fig A.3).
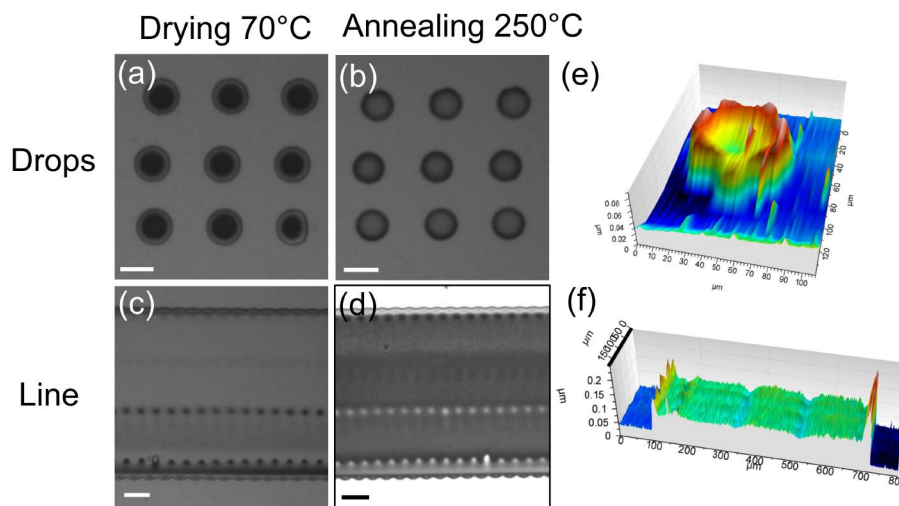
Figure 4.24: Inkjet printed patterns from ink [S]/[In]=3 dried at 70°C (first column) and annealed at 250°C (second column). (e) and (f) are the 3D profilometer images of (b) and (d). The scale bar is 100 μm.

The ink [S]/[In]=3 low c (which is the same ink as [S]/[In]=3 with a concentration divided by 4) shows smoother printing as discussed in section 4.2.3 (fig 4.21). The feature due to the abnormal drop spacing is not visible because the size of the drops is much bigger allowing a better overlapping of the drops/lines. After the annealing step (250°C for 5 minutes), the drops still do not seem to show coffee ring effect (fig4.25a), while the line shows darker edges (fig 4.25b) related to coffee ring effect as confirmed by the 3D profilometer image (fig 4.25c). The 3D topography of the drop was not measurable through profilometer because of its very low thickness. Since a strong coffee ring effect occurs in both the high and low concentration inks, this effect is confirmed to be solely driven by the solvents. Extensive studies have been performed on the coffee ring effect and possible solutions to prevent it. Having a mixture of solvents to produce a Marangoni effect is one of them as discussed earlier. However, the mixture of water, ethanol and propylene glycol is insufficient to prevent completely the coffee ring effect. Printing in a vapor rich environment is known to reduce the evaporation rate and control the coffee ring, however, this can not be used in our printer because of its metallic and electronic components. The fast heating of the sample can be used [122]. It was shown that a

fast heating could counteract the diffusion of material toward the edges by having a fast descending membrane that would have a capture-effect. Indeed, when the sample is dried quickly, the upper liquid-air interface goes down very rapidly and catches the material like a net to finally drag it down to the substrate. A film inkjet printed on a substrate heated at 60°C is shown on figure 4.26. The substrate was heated to enable the fast drying as soon as the material is printed to create the fast descending interface. The coffee ring effect can unfortunately be seen on the top, left and right corners meaning that the dynamic of the coffee ring effect can not be counteract by heating the substrate or that the temperature was not enough to have a fast descending interface. The temperature of the printer can not be further increased so this method had to be rejected.
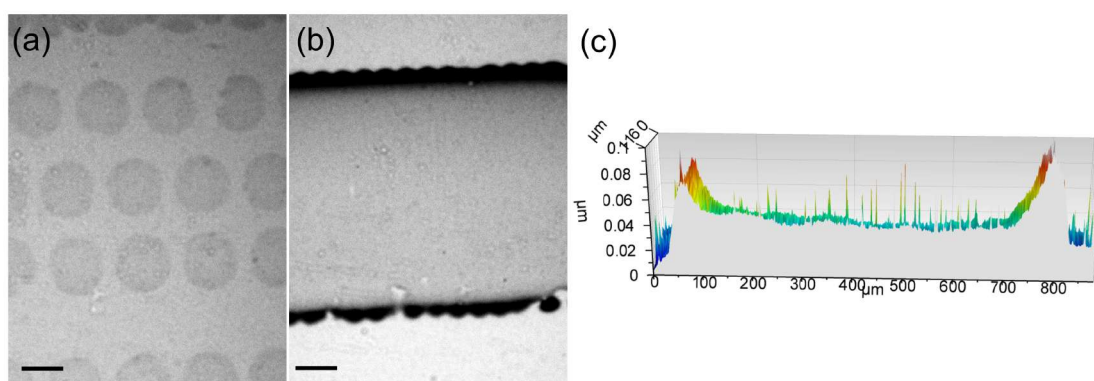
Figure 4.25: Optical images of annealed (a) drops and (b) line of ink [S]/[In]=3 low c. The coffee ring effect of the line is confirmed through the profilometer map (c). The scale bar is 100 μm.

Figure 4.26: Inkjet printed film on a substrate heated at 60°C and further dried and annealed with the standard procedure described earlier.

The goal of this thesis was to inkjet print thin films. The coffee ring effect is not a huge concern since it only creates a different thickness between the edges and the rest of the film. Indeed, in our solar cells, the edges are always isolated from the rest of the device. However, another concern regarding the morphology is shown on figure 4.27. It shows the evolution of a film macro-morphology from the wet to the annealed state. The wet film already shows some inhomogeneities in thickness for both low and highly concentrated inks as attested by optical interference. The dried films seems to be more homogeneous while the annealed films show very different macroscopic morphology. The annealed low concentration film is thicker on the left hand side because of the coffee ring effect. The

highly concentrated ink, on the contrary, shows much more inhomogeneities than the coffee ring effect. Indeed, several wave fronts can be noticed. This structure is actually already present after the drying even though it is unclear in this figure. This wave fronts are thus related to the drying step and become more obvious with the annealing step. The source of these wave fronts is still unclear but it shows that the evaporation of the ink starts at the bottom left corner.
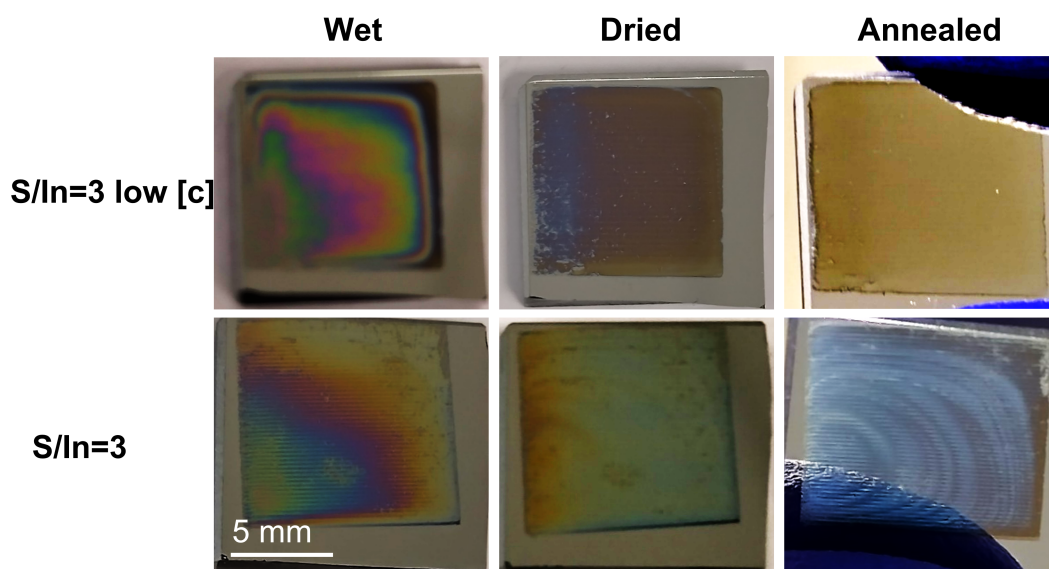
Figure 4.27: Evolution of inkjet printed films morphology through the drying and annealing processes for the inks [S]/[In]=3 and [S]/[In]=3 low c. The scale bar is the same for all the images.

The drying stage also has an influence on the micro-morphology of the film. Figure 4.28 shows the SEM images of [S]/[In]=3 ink based film dried at 3 different temperatures (70°C, 180°C, 250°C) and further annealed at 250°C except for the sample already dried at 250°C. The low magnification images (fig 4.28a, c, e) are called macro-morphology, while the high magnification images (fig 4.28b, d, e) are called micro-morphology. The macro-morphology varies significantly with temperature. The 70°C film looks rough and homogeneous, while the 180°C film has elongated structures all over the surface. The 250°C shows similar elongated structures but scattered. The micro-morphology images enhances the difference between these processes. The low temperature looks very porous and homogeneous, whereas the mid temperature has a double layer organization: elongated shapes as the top layer and a porous structure similar to the low temperature film as a bottom layer. The high temperature shows a porous network that seems to be made up of small round particles with bigger holes than the low temperature film. This structure resembles very much to the last stage of dewetting shown on figure 4.15 in section 4.1.6.

The interface between the buffer and the CIGSSe is known to be delicate and a source
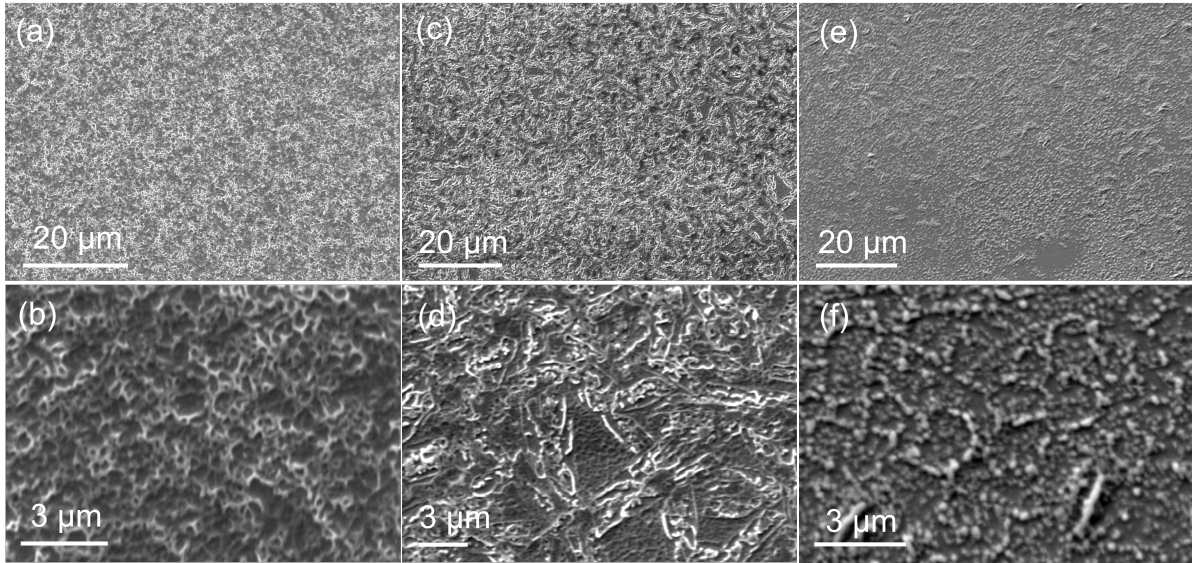
Figure 4.28: Low (first row) and high magnification (second row) SEM images of [S]/[In]=3 based film dried at (a), (b) 70°C; (c), (d) 180°C; (e), (f) 250°C.

of recombinations. It is however difficult to judge which layers might create more defects at the interface because of their rough morphology. Since the layer will be deposited on CIGSSe, the influence of the heating process has to be taken into account at the drying stage. High temperatures are known to be detrimental for the CIGSSe [123][124] and the lowest drying temperature was chosen to avoid putting the CIGSSe under too much stress.

This low temperature processing was tried with one of the ink having [S]/[In]=1.5 with no particular reason of focusing on this ink (which will be discussed in the next chapter). Three different drying procedures were tried and they were all followed by an annealing at 250°C: room temperature drying for 3 hours (fig 4.29a), 70°C for 5 minutes right after printing (fig 4.29b) and room temperature for 10 minutes and then 70°C for 5 minutes (fig 4.29c). The film dried right away at 70°C shows a rough morphology with islands-like shapes. The morphology of the other processed films is more dense and similar. For a gain of time and to increase the repeatability, the process in which the sample is first dried at room temperature and then at 70°C is chosen for the drying of the samples in this thesis.

Once the film is dried, it can be annealed to turn the precursor film into the desired material. This step is performed in a metallic annealing box that can be put under vacuum or filled with a gas (nitrogen or air). The temperature and annealing times are specific to the material that are formed and mentioned in the according chapters. The heating rate is always 30°C per minute with a starting temperature of 100°C. The cooling is done naturally down to room temperature. The hot plate that is used has fluctuation of temperature up to 20°C, meaning that it heats up at a higher temperature than required and then goes down. These fluctuations might make the results barely reproducible.
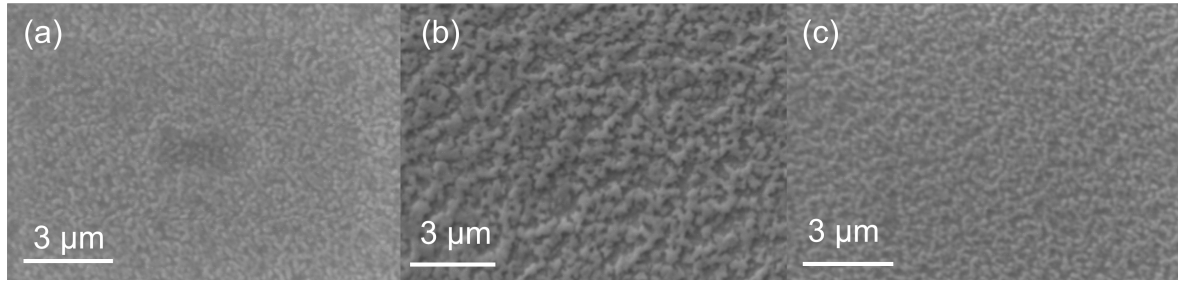
Figure 4.29: SEM images of In$_2$S$_3$ films using three different drying processes (followed by an annealing at 250°C). (a) room temperature for 3 hours, (b) 70°C for 5 minutes right after printing, (c) room temperature for 10 minutes and then 70°C for 5 minutes.

Thanks to the metallic box, the excess energy is distributed over the whole box and the fluctuation is partially damped.

4.3 Summary

The printability of an ink highly depends on its rheology and interfacial properties. The surface tension and the viscosity were measured and the printability was assessed by comparing with a printability phase diagram from literature. The viscosity of the inks was influenced by the salts' nature and concentration, while the surface tension was similar for all inks. Temperature was sometimes applied to the nozzle of the cartridge to adapt the viscosity and the surface tension and ensure a stable printing, i.e. the ejection of a single drop.

The wetting of the ink on the substrate was studied by observing the coverage of the substrate by the ink. It was shown that the bare substrates free energy, i.e. pristine Mo coated glass and CIGSSe, mismatched with the free energy of the ink, leading to a high contact angle. To increase the wetting, the substrates were treated with UV ozone. The latter modified the free energy of the substrate and allowed a better match of the free energies. The wetting envelope model enabled to verify the free energy match between the substrate and any kind of solvent. Finally, the drying and annealing of the wet thin films was studied and ideal conditions were found: drying in air for 10 min, followed by 5 min at 70°C and annealing for 5 min at 250°C.

Chapter 5

Indium sulfide buffer layer

In the previous chapter, it was shown that a careful ink synthesis is essential to ensure a good wetting of the buffer layer on the substrate. Moreover, optimal drying and annealing processes were determined.

The next step is to assess the effect of different absorber coverage, inks composition in terms of solvents mixture and salts content and the annealing temperature. The chapter will first starts with the inks description used to carry out the mentioned studies. Then, a quick proof of concept of the formation of In_2S_3 from the aforementioned ink is presented. Thanks to the highly versatile inkjet printing, a precise deposition of the material enable to vary the coverage and study its impact on the solar cells.

Once the coverage leading to the highest efficiency is determined, the macro-morphology of the buffer layer is changed by adding propylene glycol to the ink which smoothed the film. However, the carbon residue often found in solution processes is known to be detrimental for the solar cells because it acts as non-radiative recombination centers. The effect of this addition of propylene glycol on the thin film properties and on the cells efficiency will thus be assessed.

Another ink component that can be modified is the salts content. The stoichiometric ratio in In_2S_3 is 1.5. However, the precise salts content in the ink to maximize the efficiency of the cell is not known and different [S]/[In] ratio as well as the pre-synthesis of S-In bond is studied to determine their impact on film quality/purity and cells efficiency.

It is often discussed in literature that heat treatment applied to solar cells can have positive impacts on the performance of the cells. However, when this temperature is too high, the performance degrades. Different annealing temperature will be applied to the solar cell to turn the ink into In_2S_3 and the properties will be compared.

Lastly, UV ozone has been mentioned as a way to improve the wetting of the ink. However, an alternative path to obtain a continuous layer exists, i.e. decreasing the concentration of the ink and the drop spacing. We investigate this processing and compare it with the UV ozone used in all the other studies.

5.1 Inks synthesis

Multiple inks were synthesized to enable the following studies all involving indium chloride and thiourea (TU). Some of them require the pre-synthesis of a complex that can be written as $In(TU)_3Cl_3$ (shown in fig 5.1). This complex was synthesized similarly to [125] with small differences in the processing.[1] In order to check the quality of the synthesized product, the crystallographic structure was recorded and compared to literature. The powder was redissolved in water and the mixture was deposited on glass and dried. Figure 5.1 shows the XRD spectra of the synthesized product as well as the reference from Otto et al. [125]. A difference can be seen both in peaks position and intensity. This can be due to the difference in the processing for the measurement. Indeed, Otto et al. synthesized the powder and then recrystallized it to form a single crystal, giving a high purity, while in this work no purification process is used and the crystallization process is fast (drying on a hot plate). This process probably create preferential growth. Otto et al. determined the crystal structure to be triclinic with $a = 8.4842$Å, $b = 10.5174$Å, $c = 13.1767$Å, $\alpha = 111.1870°$, $\beta = 98.0870°$, $\gamma = 97.889°$.

To further check that the synthesized powder coincides with the literature and to find
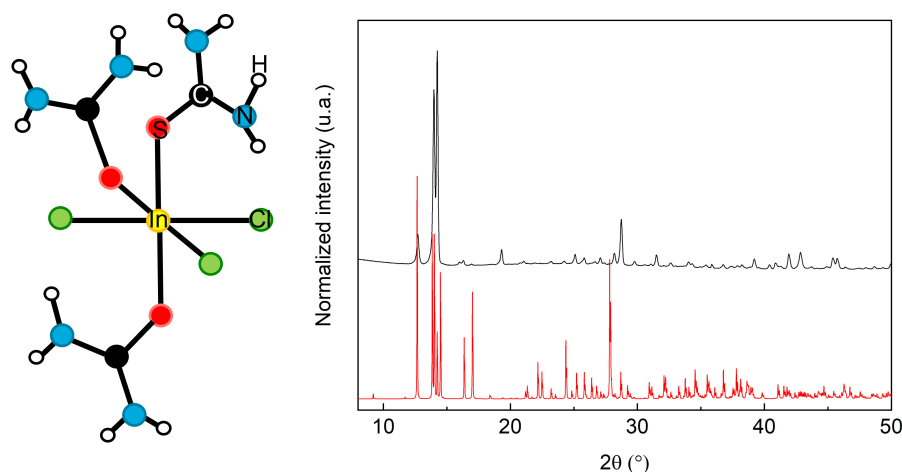
Figure 5.1: Chemical structure of the complex molecule and XRD of the complex powder redeposited on glass substrate through solution dissolution (black). The reference from [125] is presented in red.

the lowest temperature at which the annealing can be carried out to form In_2S_3, thermogravimetric analysis (TGA) was performed on the powder. The first decomposition starts around 220°C and finishes at 250°C followed by a second decomposition step until 330°C. The annealing was performed only until 400°C because the application of the In_2S_3

---

[1]0.21 mol of thiourea (Alfa Aesar, ACS, 99% min) were first dissolved in 100 mL of water under stirring. Then, 0.063 mol of anhydrous indium(III) chloride (Alfa Aesar, anhydrous, 99.999%) were added. When the solution became clear, it was heated to 80°C to form tristhioureaindium(III) chloride $(In(TU)_3Cl_3)$ which appears as a white precipitate. It was filtered and washed with acetone and stored in vacuum.

is on a photovoltaic device, which limits the allowed annealing temperature (section 5.7) [124]. A pure In_2S_3 product is not obtained at 400°C which is already much higher than the annealing temperatures used in this work. The decomposition curve has the same shape as the reference [125] but is shifted. This may be related to a different temperature calibration. Moreover, the decomposition curve is nearly identical in air and in Ar, meaning that the annealing medium does not influence the decomposition temperature of the compound. Interestingly, Otto et al. found that the mass loss at 700°C (72.8%) was higher than the expected mass loss (69.8%) indicating the unexpected evaporation of volatile indium species. A complete analysis of the evaporated species can be found in [125]. Thanks to this thorough analysis, it was found that the chemical reaction to form In_2S_3 starts with the decomposition of two neighbouring thiourea molecules in the melt at 225°C:

$$2\,SC(NH_2)_{2(l)} \longrightarrow CS_{2(g)} + 2\,NH_{3(g)} + H_2NCN_{(l,g)}$$
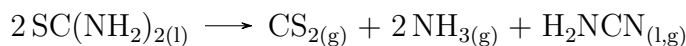
Indium chloride then reacts with CS_2 to form indium sulfide. The general reaction at 240°C is thus as followed

$$2\,InCl_3 + 3\,SC(NH_2)_{2(l)} \longrightarrow In_2S_{3(s)} + 3\,H_2NCN_{(l,g)} + 6\,HCl_{(g)}$$
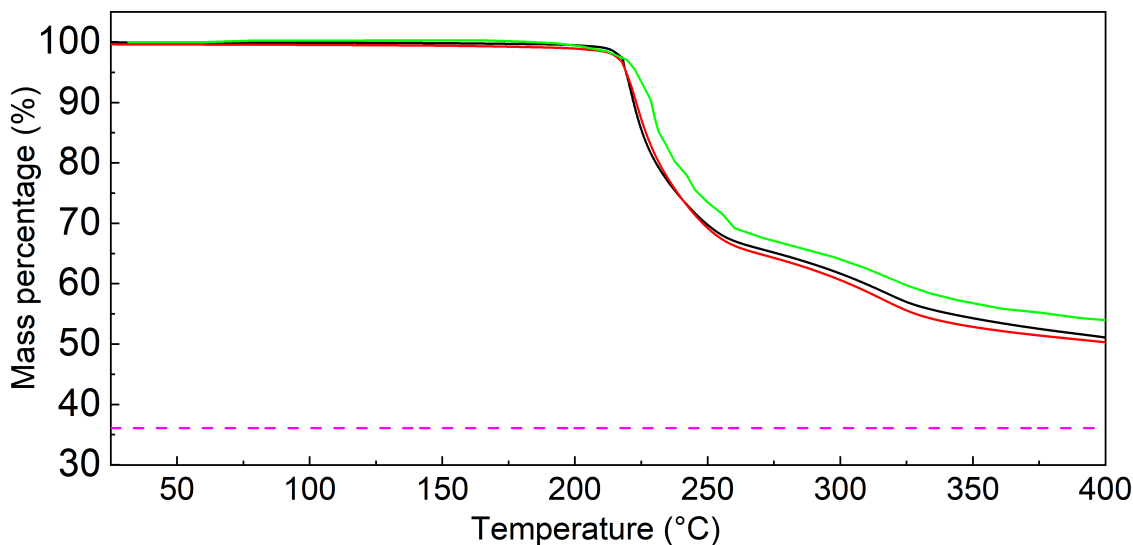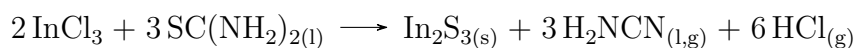
Figure 5.2: TGA of $In(TU)_3Cl_3$ powder. The annealing was performed in air (black) and in argon (red). A reference curve (green) for product synthesized by Otto et al. [125] and annealed in air. In dashed pink, the mass loss corresponding to residue free In_2S_3.

This temperature (240°C) is actually related to the decomposition of 15 mg of powder which is considered as a bulk condition. In the real conditions, the typical amount that is annealed is 0.15 mg deposited on a large surface (6 cm^2) which might alter the starting decomposition temperature.

The inks composition used in this chapter are reported in table 5.1. The solvents composition was varied to improve the morphology of the buffer and ease the printing process. The presence of carbon residue related to the introduction of ppg will be discussed. Different salts configuration and concentrations will also be compared.

	water	ethanol	ppg	In(TU)$_3$Cl$_3$	InCl$_3$	TU
Surface coverage	3	1		0.8		
Propylene glycol	1	2	0 to 1	0.8		
Complex No Complex	1	2	1	0.4	0.4	1.2
Sulfur to indium ratio	1	2	1		0.4	0.4 to 1.2
Temperature	1	2	1		0.4	1.2
UV ozone	1	2	1		0.4/ 0.1	1.2/0.3

Table 5.1: Composition of the inks in each study section. Liquids volume are in mL and salts contents are in M.

5.2 Proof of concept

As mentioned in chapter 4, the formation of inkjet printed buffer layers requires several steps which are shown on figure 5.3. First, the ink is formulated as described in section 5.1. Then, it is inkjet printed on the substrate. Finally, the ink is turned into In$_2$S$_3$ using different annealing steps. Each step will be studied in the different sections of this chapter.
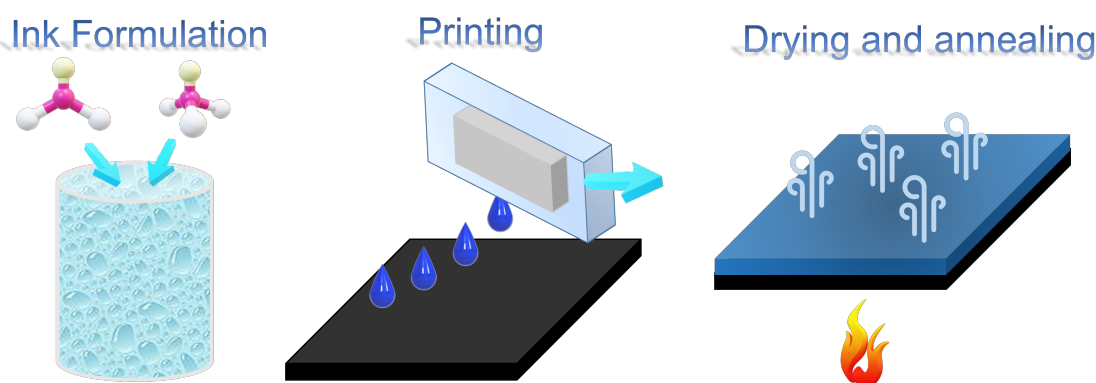
Figure 5.3: Sketch of the processing from ink formulation to the final film.

As a proof of concept that In$_2$S$_3$ can be formed following the discussed procedure, figure 5.4 shows a brief analysis of one of the formed material that will be discussed in details later in the chapter.

The SEM image shows that the morphology is porous and this will be discussed later. XPS measurement indicates a below stoichiometric [S]/[In] ratio, which is expected to be 1.5. This could be due to preferential sputtering of S. The film contains foreign atoms related to air contamination and residues from thiourea and $InCl_3$ molecules, i.e. C, N and Cl. The Mo is already present at the front because of the porosity of the layer. The O which is found in considerable amount is not bonded to In, as confirmed by the XRD data. Indeed, the extraction of lattice parameters shows that it is very similar to the literature reference (section 5.5). The crystallite size extracted from the FWHM of the XRD is 6.9 nm, which will be shown to be small. Raman confirms that the crystallites are small. Indeed, the signal consists in a large asymmetrical peak. When comparing with literature, several peaks are required to account for the total signal. If the material had bigger crystallites, these peaks would not or weakly overlap.
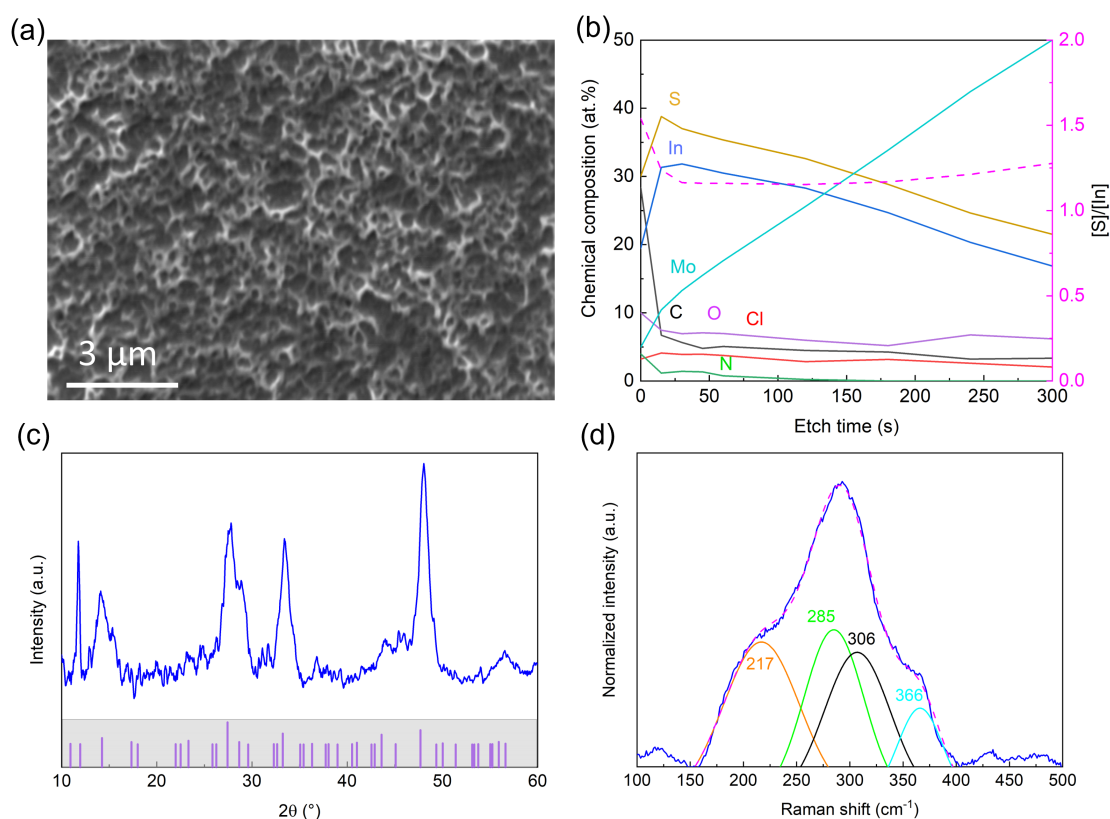
Figure 5.4: Characterization of the In_2S_3 formed from the ink [S]/[In]=3. (a) SEM image, (b) Chemical composition from XPS, (c) crystal structure from XRD (ref PDF4+ 00-025-0390) and (d) Raman spectrum. The peaks fitted are from [126] [127].

In summary, the compound synthesized using the aforementioned inks is indeed In_2S_3. In the next section, the coverage of the absorber by the buffer layer is discussed. Indeed, inkjet printing is a versatile deposition technique that enables the precise deposition of material. It is thus possible to vary the covering and assess the impact on the efficiency of the solar cells.

5.3   Surface coverage

In order to form a pn junction on the whole surface of the CIGSSe, the buffer should entirely cover the surface. This condition depends on the coverage of the ink which is driven by the spreading of the drops. As shown on figure 5.5a, the deposited drops on a pristine absorber are separated from each other because the diameter of the drops (21 μm) is smaller than the drop spacing (35 μm), leading to a surface coverage of 37%. UV ozone treatment was used to treat the surface of the CIGSSe to increase its wettability [128]. After 30 s of UV ozone treatment (fig 5.5(b)), the contact angle is decreased and the diameter of the drops is now 25 μm, giving a surface coverage of 53%. After 120 s of UV ozone treatment (fig 5.5(c)), the droplet diameter is around 46 μm (bigger than the drop spacing) and the ink is fully covering the absorber although stripes and dots related to the fast drying of the ink are still visible. Indeed, the solvents mixture is mainly water in this study. The coffee ring effect is very strong in aqueous solutions so the precipitating salts aggregate at the contact line. As a result, this phenomenon gives rise to an oscillation in the film thickness perpendicular to the printing direction. As shown in the sketch of figure 5.5, the coffee ring effect produces high edges which overlap in the continuous film and form a high bridge. The effect of this macroscopic non uniformity will be discussed in section 5.4.

The small agglomerates circled in red on figure 5.5 are attributed to the absorber since they are also present without any buffer (figure 5.5(d)). Their size (10 μm is in accordance with $CuSe_x$ particles shown in literature [129]). KCN etching is known to be able to remove this phase. However, this treatment was not applied to the samples before taking the SEM image of the bare absorber. In order to improve the efficiency of the devices, absorber went under KCN etching before the deposition of the buffer.
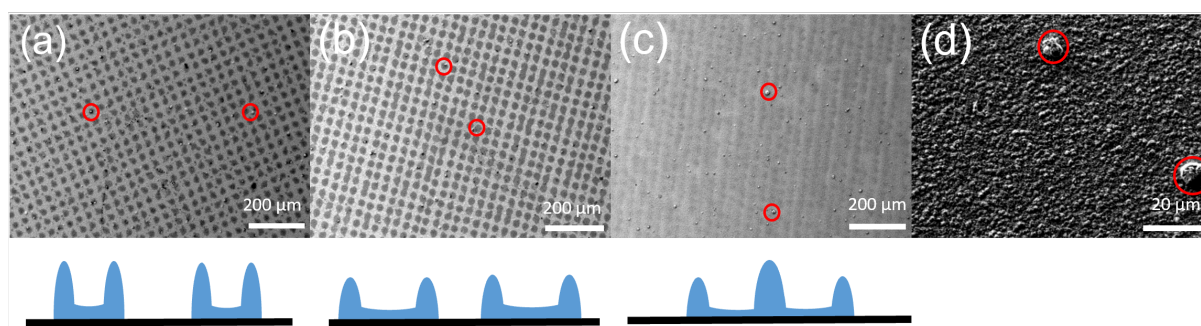
Figure 5.5: Low magnification SEM top view of annealed In_2S_3 layer deposited on CIGSSe absorber with (a) 0 s, (b) 30 s and (c) 120 s of UV ozone treatment on the CIGSSe surface. (d) is a higher magnification SEM top view of the bare CIGSSe. Agglomerates in the red circles are attributed to the absorber. A sketch of a cross section image of two neighbouring drops as a function of the UV ozone treatment is shown under the low magnification SEM images. This figure is modified from published work [130].

FIB-SEM cross section (figure 5.6) shows that the buffer layer seems to mostly cover the absorber. However, consequent holes can be seen in the buffer. This holes are actually due to the porosity of the layer. This will be discussed in section 5.6. The thickness of the film is varying and can be as thick as 120 nm. The particles present on the CIGSSe cross section originates from the redeposition inherent to gallium milling. Indeed, the sputtered particles leaving the material in the gas phase can condense back onto the solid phase when getting in contact with a solid surface [66].
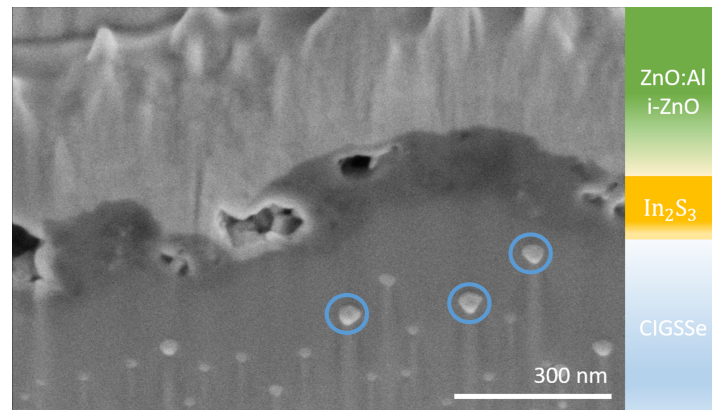
Figure 5.6: Cross section FIB-SEM image of a complete device with a 120s UV ozone treatment. The white particles circled in blue on the absorber layer are a redeposition effect inherent to gallium milling.

The presence of an oxide layer on CIGSSe surface is considered as detrimental for the absorber [131]. UV ozone treatment is used to make the surface hydrophilic, however, the formation of oxides are also very likely. The chemical composition of the CIGSSe surface was measured with high resolution XPS before and after a 5 minutes UV ozone treatment[2]. Figures 5.7a and b focus on the range of binding energies 283-293 eV where the C1s peak is situated. The carbon peak fitting is difficult because it strongly overlaps with the Se LMM peak (green dashed line). The carbon contamination found are in C-(C-H) (hydrocarbons), C-O, C=O and O=C-O (carboxyl) phases. The majority phase is hydrocarbons, while the other phases are in nearly negligible amounts both before and after the UV ozone treatment. The intensity of the carbon signal is divided by two after the UV ozone treatment, corresponding to an actual decrease of the carbon content from 29% (before) to 19% (after treatment). The presence of carbon after the treatment is partially due to atmosphere contamination. Indeed, after the ozone treatment, the sample is transferred in air to the XPS machine.

As expected, the oxygen content increased from 23% to 47% (not shown) and points

---

[2]the time of the treatment is longer than 120 s because the absorber is different. Indeed, the whole experiment was based on an absorber from industry called A, while this specific experiment (XPS) was done on absorber from Avancis which requires a longer UV ozone time to ensure a continuous layer. The effect of UV ozone treatment is supposed to be similar on both types of absorber
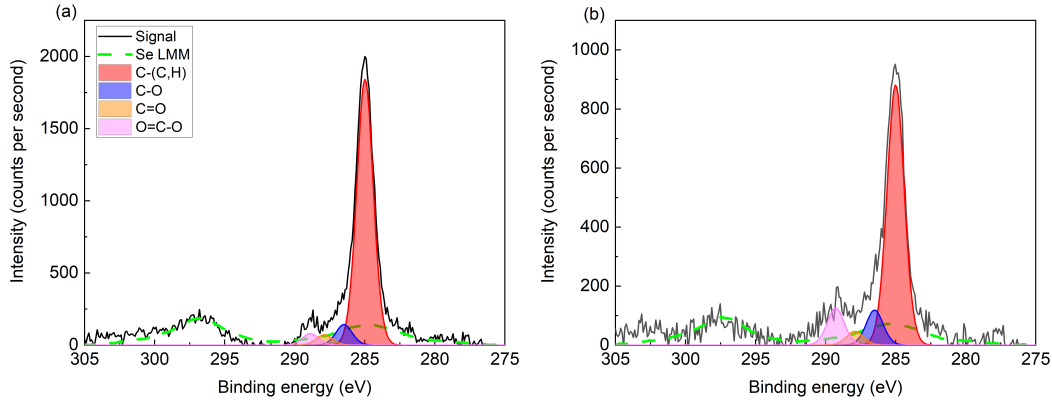
Figure 5.7: High resolution XPS of the carbon phases on the surface of CIGS of (a) untreated and (b) 5 min UV ozone treated CIGSSe absorber. y axis scale is divided by 2 in (b) compared to (a).

to the incorporation of oxygen on the CIGSSe surface. The formation of oxides with the different atoms present in the CIGSSe is shown on figures 5.8 and 5.9. The gallium is found in the Ga(S,Se) as well as in Ga_2O_3 phases before the treatment. A Ga(S,Se)-O mixed phase is the majority after the UV ozone treatment. The copper is found in sulfide/selenide phase Cu-(S,Se) as well as in the detrimental $CuSe_x$ commonly found in CIGSSe, which hopefully represents only a quarter of the phases. After the treatment, a pronounced $Cu(OH)_2$ phase appears and accounts for more than half of the Cu phases. Indium is present in both chalcogenide phase and oxide phase before and after the treatment. The oxide phase goes from one quarter to half of the phases due to the treatment.

As already shown, Se is found in Ga, Cu and In phases which can be summarized as CIGSSe and $CuSe_x$ phases. A small SeO_x is already present before the treatment and its content dramatically increases after the ozone treatment as shown on figure 5.9. The sulfur composition is difficult to evaluate because of its overlap with Se and Ga peaks. Nevertheless, it is found solely in CIGSSe phase before the treatment. After the ozone, sulfur oxide SO_x appears but its quantification is hard given the numerous peaks overlapping.

The Na peak (not shown) increased after the UV ozone treatment which might be due to the thinning of the contamination layer but also to the heating of the sample that promotes the diffusion of sodium. In short, the surface of the absorber before the ozone treatment was rich in carbon and some elements were already found in oxides phase. After the UV ozone treatment, the carbon contamination decreased and the amount of oxides phases increased.

These results can be put in perspective by comparing with a previous study on the impact of UV ozone treatment on CIGSSe absorber [128]. After 90s of treatment, the signal of O1s increased ($\times$ 2.6), while the C1s decreased ($\div$3). In our study, the oxygen
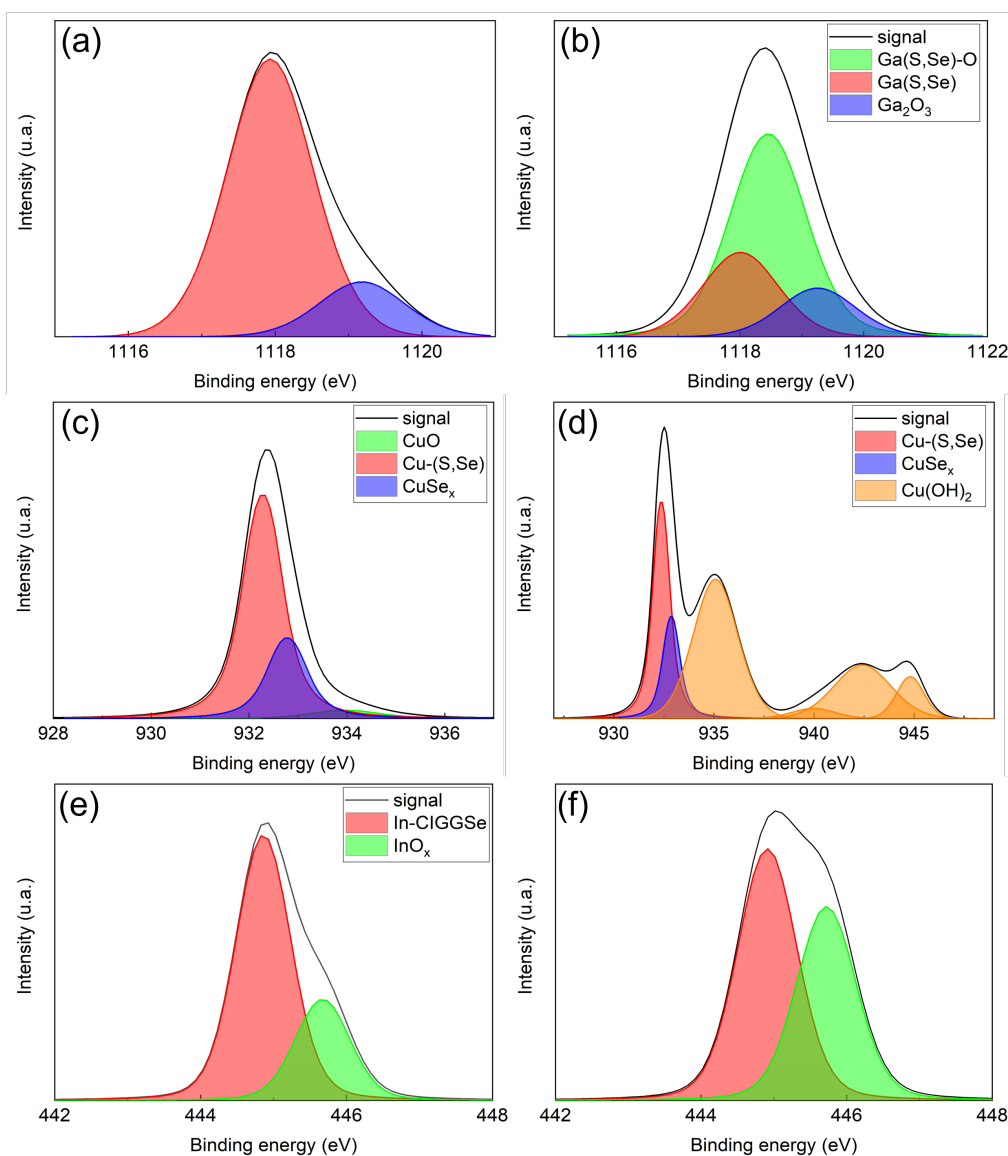
Figure 5.8: High resolution XPS of (a), (b) the Ga phases, (c), (d) the Cu phases and (e), (f) the In phases. The first column is before the UV ozone treatment and the second column is after the treatment.

content was increased by a factor of 2, which is similar to the reference study but the carbon was decreased by a factor of 1.5 only. This might be due to the time between the UV ozone treatment and the loading in the machine. The oxygen variation indicated the formation of metal oxides and hydroxides, while the decrease in the carbon impacted the amorphous carbon and hydrocarbons but barely the carbonates and carboxyl, similarly to our measurements. It was shown that all the intensity of peaks related to the absorber atoms (including Na) increased because of the reduction of the adsorbates layer. Indium oxides, already present before treatment, increased and accounted for 50% of the overall indium signal. The Cu $2p_{1/2}$ peak did not change in shape but its intensity increased. The Se 3d revealed two phases on the pristine sample: a chalcopyrite environment and a Cu-Se one. After 90s of treatment, a third component, namely Se-O appeared. Sulfites

94
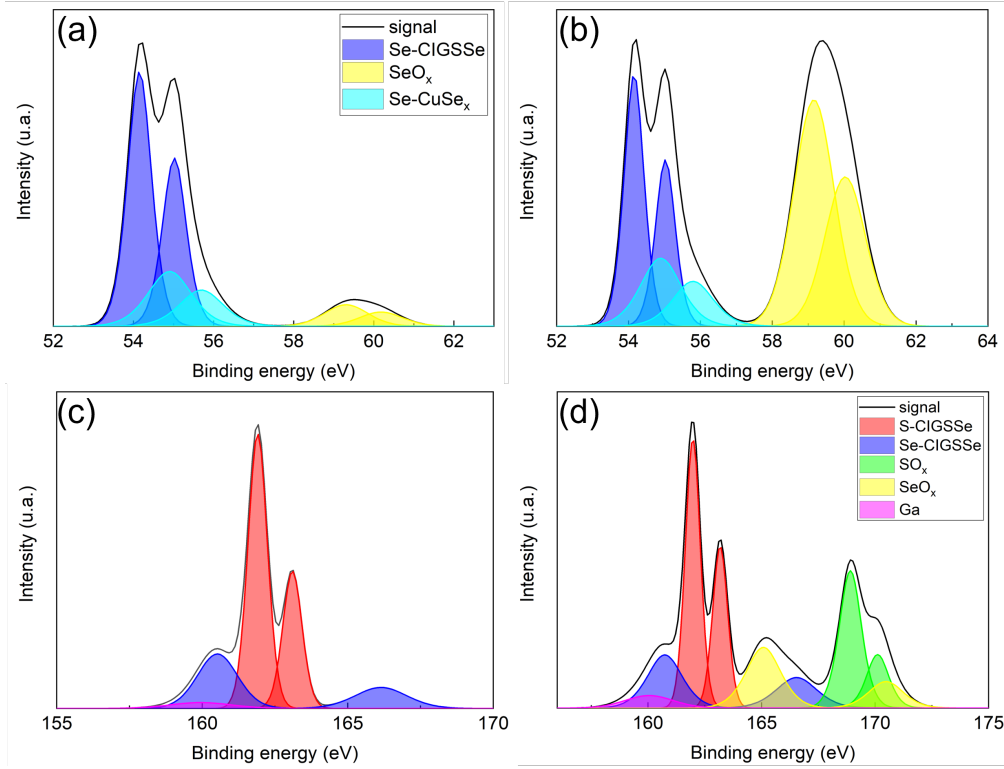
Figure 5.9: High resolution XPS of (a), (b) the Se phases and (c), (d) the S phases. The first column is before the UV ozone treatment and the second column is after the treatment.

and sulfates were also detected. Similar findings were observed for a 20 minutes UV ozone treatment. The Na 1s was however reduced in intensity. It was hypothesized that volatile Na compounds were formed and gave rise to a pseudo rinsing step. Moreover, the Cu $2p_{1/2}$ peak changed its shape significantly, indicating the formation of CuO. Interestingly, no $Cu(OH)_2$ was detected in this study whereas a very strong peak was present in our measurement. No gallium oxides were measured because Ga was not present at the front surface, contrarily to our study.

The effect of UV ozone treatment in our work is thus comparable to literature. The carbon contamination is indeed decreased but the formation of oxides is strong and possibly leads to degradation of CIGSSe. Indeed, a study showed that absorbers in contact with air show degradation in their quality. The minority carrier lifetime decreases by more than 2 orders of magnitude when the absorber is kept in air for 24 hours [132]. The degradation in nitrogen is dramatically slowed down compared to air storage [133]. The lifetime of a sample stored in air for 1 day is similar to the one of a sample kept in nitrogen for 14 days. The degradation can be assumed to be related to the oxidation of the surface either because of oxygen or water. This degradation in the lifetime implies a decrease in the open circuit voltage. The loss in V_{oc} was up to 150 meV after 24h of storage in air [132]. A decrease in the open circuit voltage might be expected in our samples.

Figure 5.10 shows the JV characteristics of the devices as a function of the surface coverage of the buffer layer (which depends on the UV ozone treatment time). The open circuit voltage increases from less than 400 mV for a buffer free device to more than 570 mV for a fully covered device. It can be explained by the fact that the absorber is damaged by the sputtering of the window layers when it is not protected by the buffer layer. The V_{oc} of the fully covering In_2S_3 is even higher than the reference cell with a chemical bath deposited (CBD) CdS buffer. The latter has been used for decades as a reference cell in CIGS community and usually gives decent efficiency. Unexpectedly, no loss in V_{oc} is observed due to the 120 s UV ozone treatment.
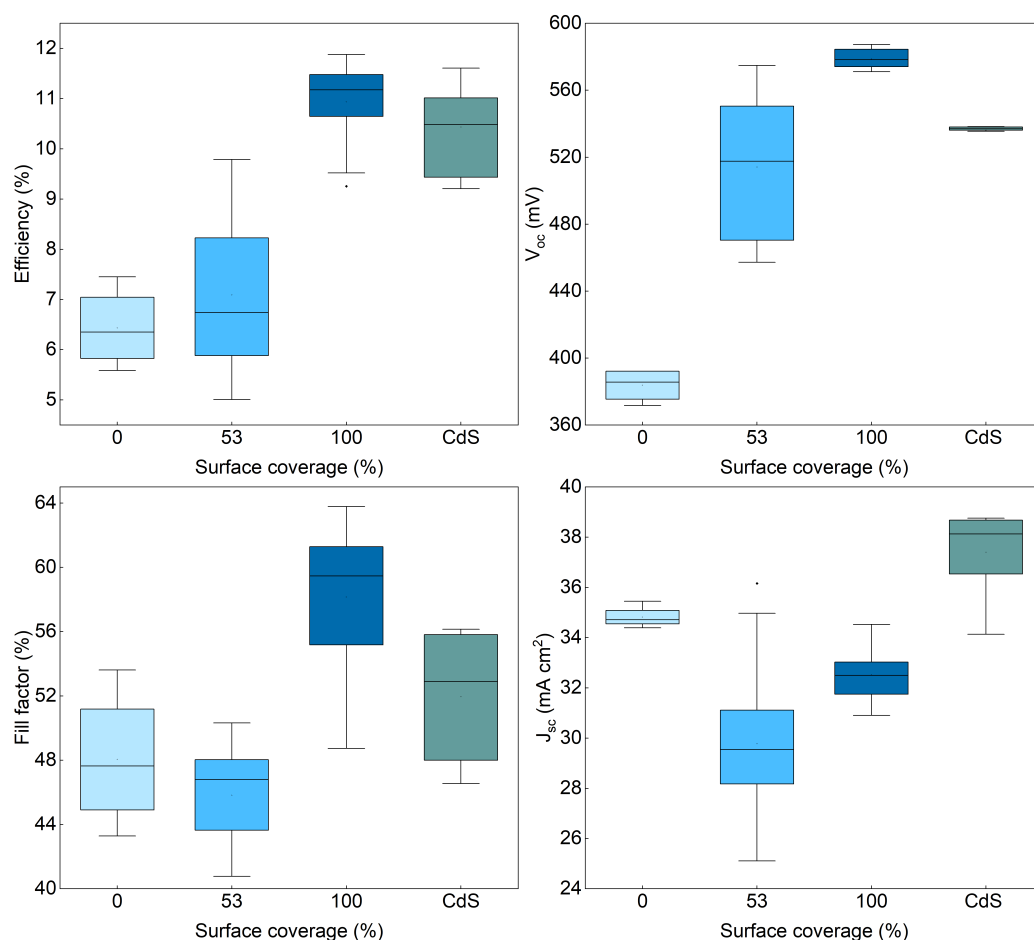
Figure 5.10: Optoelectronic properties of 16 cells: efficiency, open circuit voltage (V_{oc}), fill factor (FF), short circuit current density (J_{sc}). Data are in blue represent the In_2S_3 with different surface coverage. Data in green represents a reference with a CBD CdS buffer layer. Figure modified from [130]

The fill factor is around 63% for the best fully covering buffer and lower for the uncovered and partially covering layer and it surpasses the reference cell. It means that a fully covering layer is required to have the highest FF. However, even the highest FF is still low, which can be explained by the parasitic resistances. Indeed, the best cell has

FF=63%, J_{sc}=32.6 mA cm^{-2}, n=1.93 and V$_{oc}$=571 mV which correspond to an ideal FF (i.e. without parasitic resistances) of 72% based on equation 3.16. However, once taking into account the R_s=1.73 Ωcm^2 and R_{sh}=733 Ωcm^2 using equation 3.21, the FF drops to 63% which is the measured value. The most detrimental resistance is the series resistance: using eq 3.19, the FF drops to 67% solely because of the series resistance. When solely taking into account the effect of R_{sh} (eq 3.20), the FF drops to 70% which corresponds to a loss of 2%. Even though the series resistance has more influence, the shunt resistance is also important to take into account to explain the decrease in the FF. The resistances for all devices are reported in appendix B. In short, the shunt resistance is increasing with the surface coverage. On the opposite, the series resistance does not seem to be correlated with the coverage.

The short circuit current density is high without buffer, then decreases with a partial covering and finally increases again for a full coverage. Moreover, the device parameters of the partially covering buffer are more spread than in the other coverage levels. It shows that the characteristics are highly influenced by the homogeneity of the buffer. The short circuit current density was further examined with external quantum efficiency (fig 5.11). The blue defect at short wavelength is present in all curves except for the buffer free
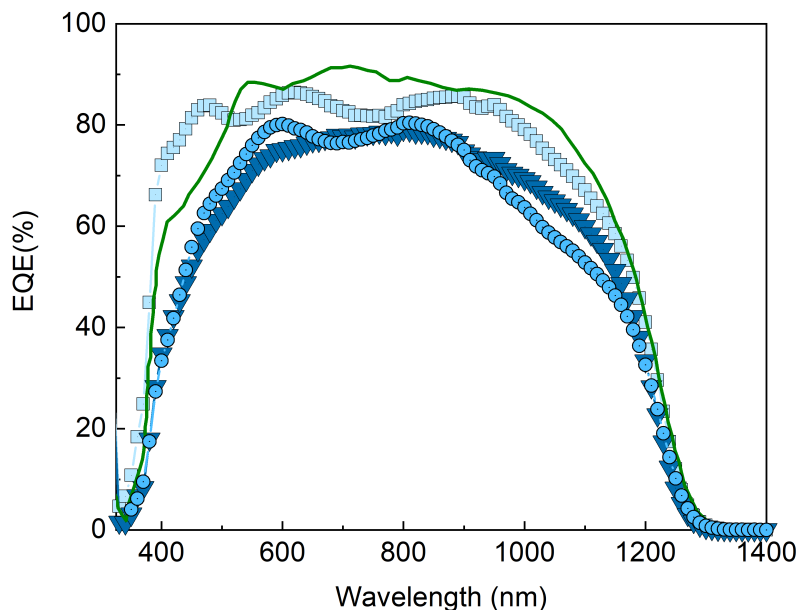
Figure 5.11: External quantum efficiency (EQE) of devices with different percentage of In$_2$S$_3$ buffer coverage (squares: 0%, circles : 53%, triangles: 100% and a reference cell with a CBD CdS (solid line).

device. This loss in EQE is due to parasitic absorption into the buffer: photons absorbed in this layer do not generate carriers that can be collected. This phenomenon is typically encountered for CBD CdS that has a band gap around 2.42 eV. The band gap of the In$_2$S$_3$ was found to be 2.5 eV using Tauc plot on a thick (> 1 μm) inkjet printed In$_2$S$_3$. This

blue defect is slightly different for the fully covering compared to the partially covering In_2S_3. The latter can indeed be seen as a combination of a uncovered (in-between drops) and covered with a thick layer (drops) device.

The EQE with partially and fully covering In_2S_3 are lower independently of the wavelength compared to the reference. This indicates a lower pn junction quality due to interface recombinations. The partially covered In_2S_3 shows a decrease at longer wavelength, hinting to a lack in collection at the back. This might be related to the quality of the absorber which was several years old.

The conclusion of this study is that a fully covering buffer layer is essential to get high efficiency and this can be achieved by treating the CIGSSe surface with UV ozone treatment prior to the ink deposition.

5.4 Solvents mixture investigation to increase the wetting

In the previous section, it was shown that the macroscopic morphology of the fully covering film was wavy (fig 5.5) because of the coffee ring effect which is very pronounced in aqueous solutions, as well as the fast evaporation of the solvents. Moreover, this fast evaporation produced clogging at the nozzle and very short lifetime of the cartridges. In order to improve the macro morphology and to mitigate the clogging, the coffee ring effect and the evaporation rates need to be decreased. The solvents mixture was modified, by adding propylene glycol (ppg) which is a low vapor pressure solvent. Ppg is expected to have different advantages: decrease in the drying rate of the mixture because of the high boiling point of ppg, less pronounced coffee ring effect thanks to Marangoni flow and easiness of printing. The slow drying will enable the drops and lines to stay wet longer and merge together to form a smooth film. The water:ethanol ratio was also modified to influence the coffee ring effect through Marangoni flow.

By introducing 0.5 mL of ppg, the film presents less oscillations in thickness (fig 5.12(b)) than the ppg free film (fig 5.12(a)). When adding 1 mL of ppg, the film is macroscopically smooth and free from consequent thickness oscillations (fig 5.12(c)). Figure 5.12(d) shows the morphology of a device with a CBD CdS buffer layer. Its morphology is very similar to the smoothest In_2S_3.

Inks containing ppg have already been used for the deposition of CIGSe. It was observed that ppg leaves carbon residues after the annealing of the material [134]. The introduction of carbon containing molecules are often necessary for example, when using the inkjet printing technique and several coatings are required to reach a thickness of 1 to 2 µm. This carbon residue is thought to be responsible for the lower efficiency than the hydrazine-based absorber which are residues free [135]. The arguments often raised
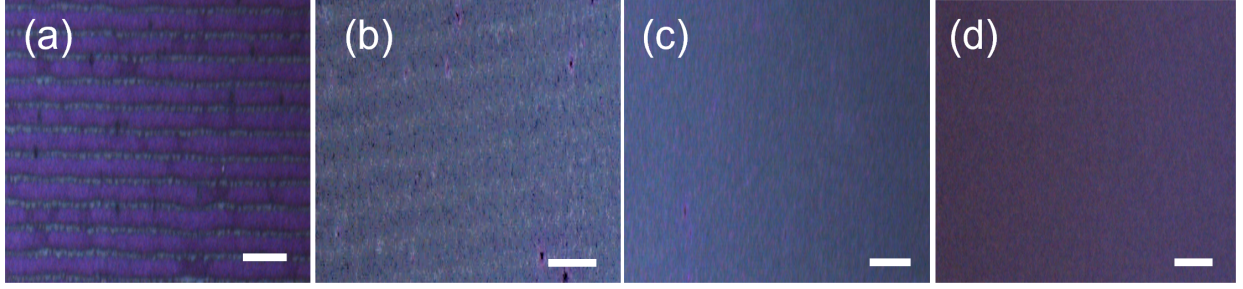
Figure 5.12: Optical microscope image of completed devices with In_2S_3 buffer from ink containing (a) 0 mL of ppg, (b) 0.5 mL ppg and (c) 1 mL of ppg. (d) is a device with a chemical bath deposited (CBD) CdS buffer. The scale is 0.1 cm.

are the non-radiative recombinations occurring at the numerous interfaces between the grains and the low diffusion length [136]. This residue is also supposed to induce a higher series resistance of the device [137]. Similar detrimental effects can be expected in the case of the buffer layer.

To quantify the carbon content in the buffer layer as a function of the ppg concentration, In_2S_3 precursor inks with different ppg contents as shown in table (5.2) were printed on CIGSSe and annealed at 250°C for 5 minutes. The amount of carbon residue was

	water	ethanol	ppg	$In(TU)_3Cl_3$
0 mL	1	2	0	0.8
0.5 mL	1	2	0.5	0.8
1 mL	1	2	1	0.8

Table 5.2: Composition of the inks used in to assess the carbon content. Liquids volume are in mL and salts contents are in M.

measured through XPS. Figure 5.13a shows that a high content of carbon is present on the surface of the films and then decreases down to 0 for the ppg containing ink after the sputtering of the out-most layer. It actually represents the contamination from the atmosphere that arises between the production of the films and the introduction in the machine. The carbon content does not decrease down to 0 before 2 min of sputtering for the ppg free film. Figure 5.14 shows the evolution of the morphology of a rough film after sputtering at 45° relative to the normal to the surface. The thickness is not etched homogeneously because of the variation in the thickness of the film. The photoelectrons are emitted from both the thinnest (buffer bulk) and the thickest part (buffer surface) of the film, which are supposed to be carbon poor and carbon rich respectively. The broadening of interface for rough film is a well known phenomenon in XPS.

To determine whether 120 s of sputtering corresponds to the full thickness of the buffer, the Ga signal from the CIGSSe was measured. Figure 5.13b shows that Ga is present at the front of the bare absorber. It can thus be expected to find Ga before 120 s

of sputtering if the whole buffer is sputtered. The signal of Ga is not detected before 150 s of sputtering for a In_2S_3 buffered CIGSSe. We can thus conclude that the films seem to be carbon free and recombination centers linked to this residue should not be encountered.
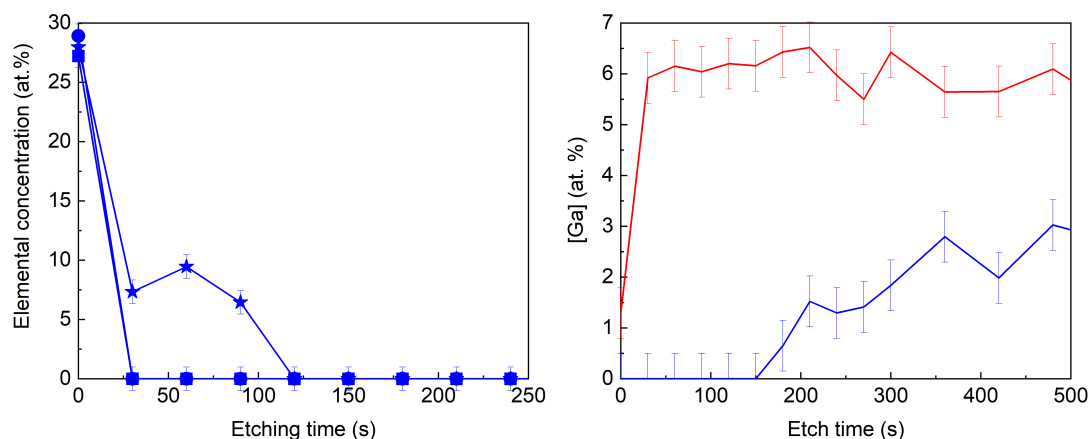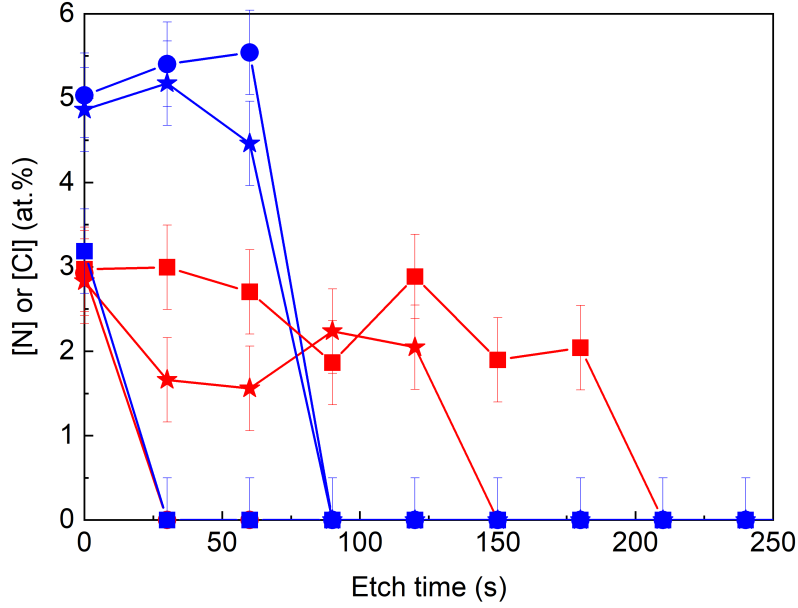

Figure 5.13: (a) XPS measured carbon content in In_2S_3 films made from inks containing 0 mL (stars), 0.5 mL (circle) and 1 mL (square) of ppg. (b) Ga content from XPS of bare CIGSSe (red) and In_2S_3 buffered CIGSSe (1 mL ppg). The line is drawn to guide the eye.
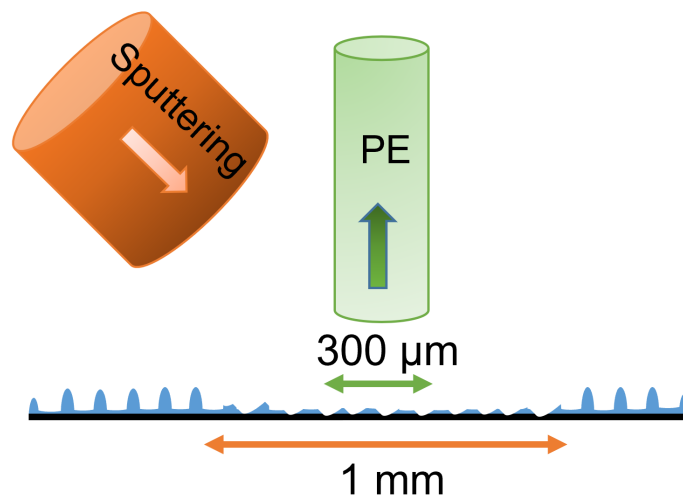
Figure 5.14: Schematic of sputtering of wavy films. The sputtering is done at 45° relative to the normal and the photoelectrons (PE) are acquired along the normal to the surface of the sample. The etching width is 1 mm while the width of the analyzed area is 300 µm to avoid edge effects. The width of the stripes is around 50 µm, meaning that several stripes are analyzed simultaneously.

100

Since the In_2S_3 are carbon free, any improvement in the device performance can directly be associated to an improved morphology. The hypothesis is that a smoother film will lead to better devices because a rough interface between CIGSSe and the buffer bring inhomogeneities that might be detrimental to the cell. JV measurements (fig 5.15) show that the efficiency of the devices increases with the amount of ppg added to the ink. The homogeneity also increases as proved by the smaller distribution of the data.
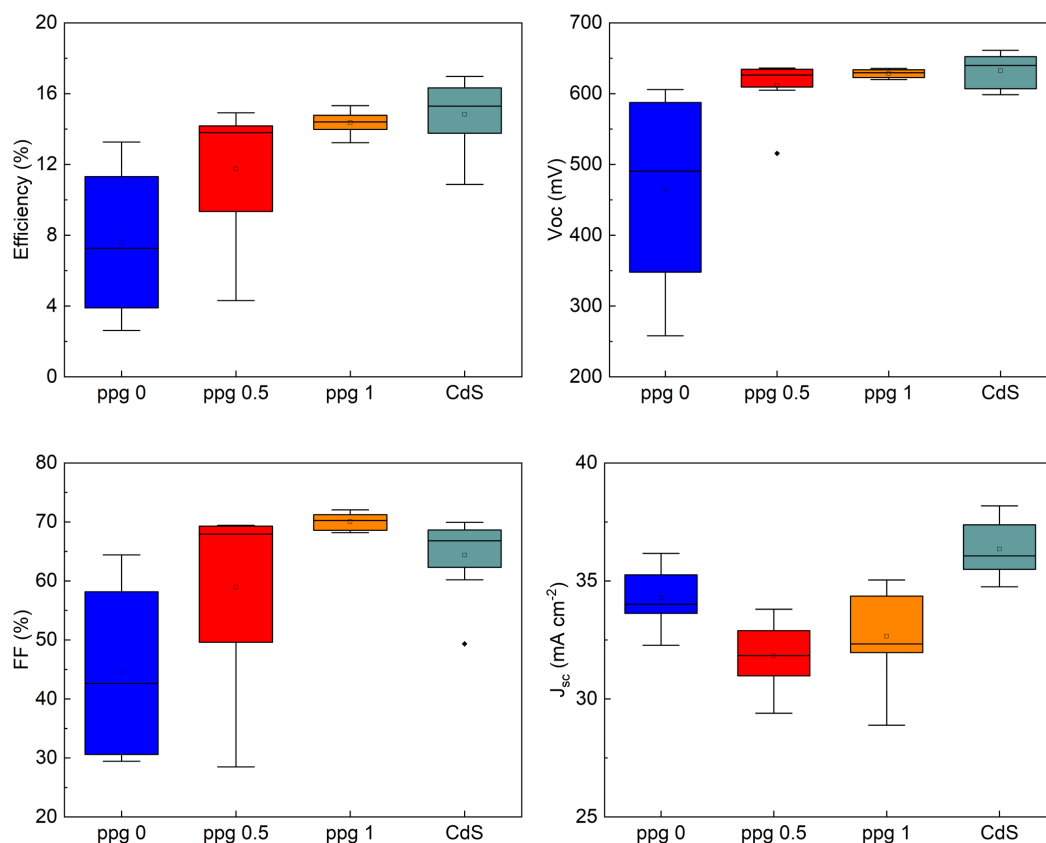
Figure 5.15: Optoelectronic properties of 8 cells: efficiency, open circuit voltage (V_{oc}), fill factor (FF), short circuit current density (J_{sc}). The amount of ppg in the ink is increased from left to right. Data in green represents the reference device with a CBD CdS buffer layer.

The V_{oc} of the ppg free has a huge variance (more than 300 mV), whereas both of the ppg containing sample have a V_{oc} comparable to the CBD CdS reference. The FF increases steadily with the addition of ppg. The 1 mL ppg has a tight distribution and even surpasses the FF of the reference cell. The low FF for ppg free is controlled by the parasitic resistance. Indeed, a low efficiency cell (4.3%) has an ideal FF (without parasitic resistances, eq 3.16) of 45%, while with the low shunt resistance (15 Ωcm^2), it is 27% (eq 3.20) which is similar to the measured value of 29%. In the case of a high efficiency cell (13.2 %), the ideal FF is 65% which does not change when taking into account the high

shunt resistance (2437 Ωcm^2). The series resistance (0.2 Ωcm^2) slightly decreases the FF to 64% (eq 3.19) which is the measured value. In short, the V$_{oc}$ and FF increases with the smoothing of the buffer layer.

The j$_{sc}$ decreases with the introduction of ppg. To understand this trend, EQE was measured (fig 5.16). The blue defect which is present in the reference spectrum is less pronounced on the indium curves. Both the ppg free and the 1 mL containing inks give a similar EQE. The 0.5 mL ppg curve is lower at all wavelengths, indicating recombination at the interface, however its source is unclear. The EQE of the reference is higher for wavelengths longer than 500 nm, indicating a better collection of charge carriers than the In$_2$S$_3$.
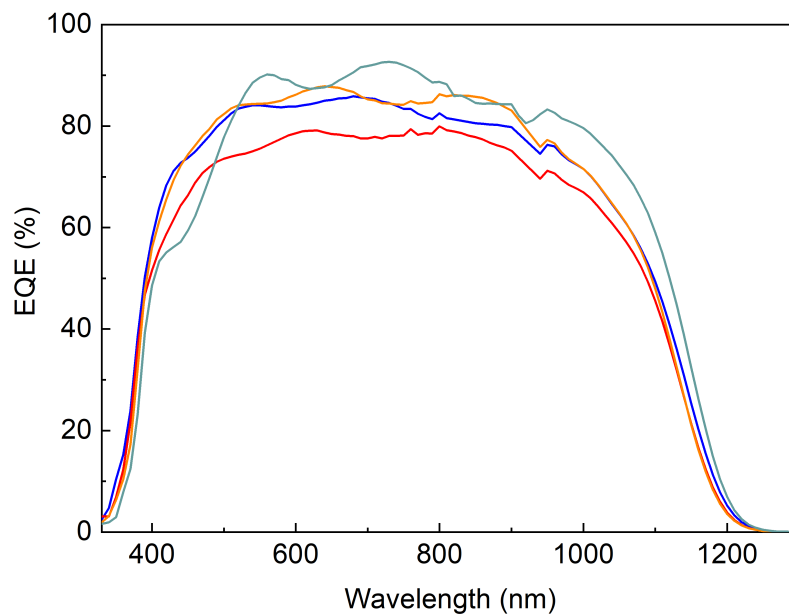
Figure 5.16: EQE of best devices containing 0 mL (blue), 0.5 mL (red) and 1 mL (orange) of ppg. The reference cell with CBD CdS is in green.

The lower charge carriers collection might be related to the doping of the buffer layer. Indeed, the space charge region gets narrower with a low doping. The doping of In$_2$S$_3$ is difficult to control since it is related to the annealing step. Indeed, a slight variation in the annealing profile can influence the evaporation of nitrogen and chlorine. Figure 5.17 shows that the nitrogen and chlorine contents decrease right after the first sputtering run and seems to reach 0%. However, the detection limit of the machine is 0.5 at.%, so it is hard to determine the foreign atoms content. Nevertheless, if the doping of the buffer is low, the small space charge region in the absorber might explains the lower collection found in the EQE.

The diffusion of some atoms can be expected from the CIGSSe to the buffer and inversly because of the heat treatment after the buffer deposition. Figure 5.18a shows the XPS measured copper to indium ratio of a bare absorber and an absorber covered with the

Figure 5.17: XPS measured nitrogen (blue) and chlorine (red) content in In_2S_3 films made from inks containing 0 mL (stars), 0.5 mL (circle) and 1 mL (squares) of ppg. The line is drawn to guide the eye.

indium sulfide buffer with 1 mL of ppg. The [Cu]/[In] ratio of the bare absorber is pretty constant over the depth measured, whereas this ratio clearly increases progressively for the buffered sample. Interestingly, the "bulk" [Cu]/[In] ratio of the buffered sample does not reach the same "bulk" ratio of the bare absorber. It could thus be hypothesized that the Cu diffuses towards the buffer. Laurencic et al. [138] measured Raman spectroscopy on CIGSe absorbers with an indium sulfide buffer layer to study the evolution of the ordered vacancy compound (OVC), known as $CuIn_5S_8$ phase. This compound that may form when the phase is Cu poor, can already be present in the CIGSe without buffer. When the In_2S_3 buffer layer is deposited and a thermal treatment is applied to the stack, Cu can diffuse from the CIGSe to the buffer, reducing the Cu content in the absorber, creating or increasing the OVC.

It was shown that the OVC Raman peak increases relatively to the CIGSe peak when comparing the bare CIGSe and the buffered one [138]. Figure 5.18b shows the Raman spectra of the bare and buffered CIGSSe. The main peaks of CIGSSe are visible on both spectra around 278 cm^{-1} corresponding to A1 (Se-Se), 212 cm^{-1} for B2/E mixed mode and 290 cm^{-1} for A1(S-S). The modes A1(Se-Se) and A1(S-S) represent the vibration of Se or S anions in the x-y plane with the cations at rest. B2/E mixed mode represents the vibrations of anions and cations together. A supplementary peak is found at 128 cm^{-1} and is associated to $CuInSe_2$ phase. No OVC peak is found on the bare absorber spectrum. Several peaks of In_2S_3 are found on the buffered CIGS spectrum with two of them partially overlapping with CIGSSe peaks: 179, 199 and 336 cm^{-1} [126]. The OVC that was absent

on the bare CIGSSe is present but small for the buffered sample, indicating Cu diffusion from the absorber to the buffer and the formation of OVC. Since this OVC is weak, the pronounced widening of the interface buffer/CIGSSe from 0 s to 1500 s in XPS is probably unrelated to the OVC but rather to a pronounced porosity that will be discussed in the next section.
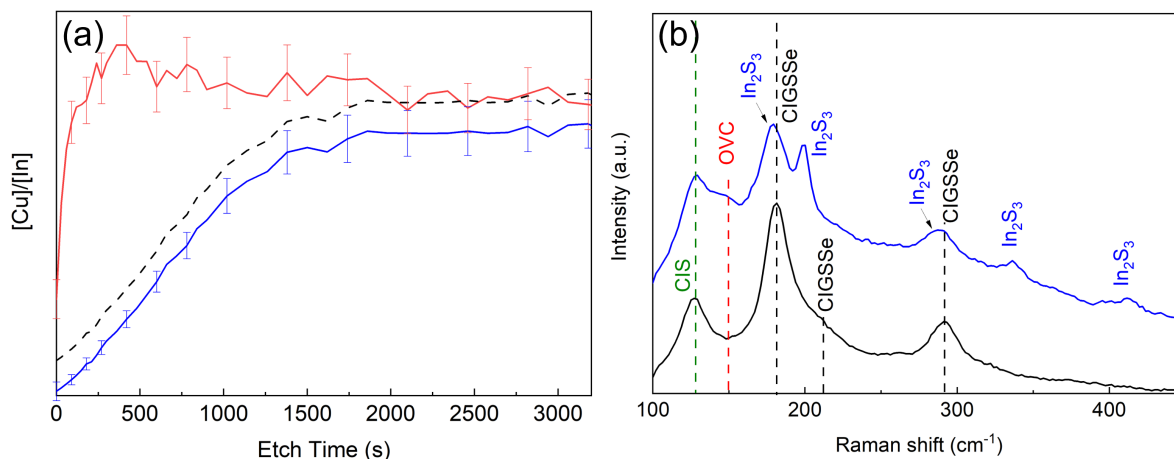
Figure 5.18: (a) [Cu]/[In] ratio measured through XPS on In_2S_3 buffered (ppg 1 mL) (blue) and bare absorber (red). The dashed line represents a virtual sample with a buffer where the bulk ratio is identical for the bare and buffered CIGSSe. (b) Raman measurement on bare (black) and buffered (blue) CIGSSe. The red (black) dashed line represents the position of the OVC (CIGSSe). The referencing of the peaks (green dashed lines) is from [139][140]. The wavelength of the laser is 442 nm.

5.5 Complex/No Complex

The purity of the In_2S_3 film is of high importance to form a good pn junction and avoid non-radiative recombination. It was shown in section 5.4 that N and Cl residues are present in the film. Nevertheless, the resulting devices showed good efficiencies. These were based on the use of a compound called $In(TU)_3Cl_3$ in which an In-S bond is pre-formed. Wu et al. argued that the pre-formation of an indium-sulfur bond in solution should avoid the formation of oxides in the context of synthesizing the semiconductor CISe [141]. This statement led to the following study comparing an ink with this pre-formed complex and a simpler ink where $InCl_3$ and thiourea are directly mixed into the ink (table 5.3). The synthesis of this compound ($In(TU)_3Cl_3$) was already discussed in section 5.1.

In order to determine if any difference is present between the two chemistries, Raman spectroscopy was measured on solutions containing $InCl_3$, thiourea, the addition of these

	water	ethanol	ppg	$In(TU)_3Cl_3$	$InCl_3$	TU
Complex	1	2	1	0.4		
No Complex	1	2	1		0.4	1.2

Table 5.3: Composition of the Complex and No Complex ink. Liquids volume are in mL and salts contents are in M.

molecules and the $In(TU)_3Cl_3$ complex, the dried films obtained from these inks as well as the complex powder (fig 5.19, table 5.4). The thiourea solution shows three main peaks: 734 cm^{-1} corresponding to the symmetric stretching of C=S bond, 482 cm^{-1} for the symmetric bending of the N-C=S and 436 cm^{-1} for the symmetric bending of N-C-N. These values are shifted compared to literature [142], i.e. 411 cm^{-1} for the N-C-S, 469 cm^{-1} for the N-C=S and 740 cm^{-1} for the C=S bonds. These literature data are measured on dried thiourea, while our measurement is made on a solution which might influence the vibration of the bonds. The aqueous $InCl_3$ shows a large single peak at 299 cm^{-1} (symmetric stretching mode) which corresponds to the overlapping of two peaks 289 cm^{-1} and 301 cm^{-1} [143].
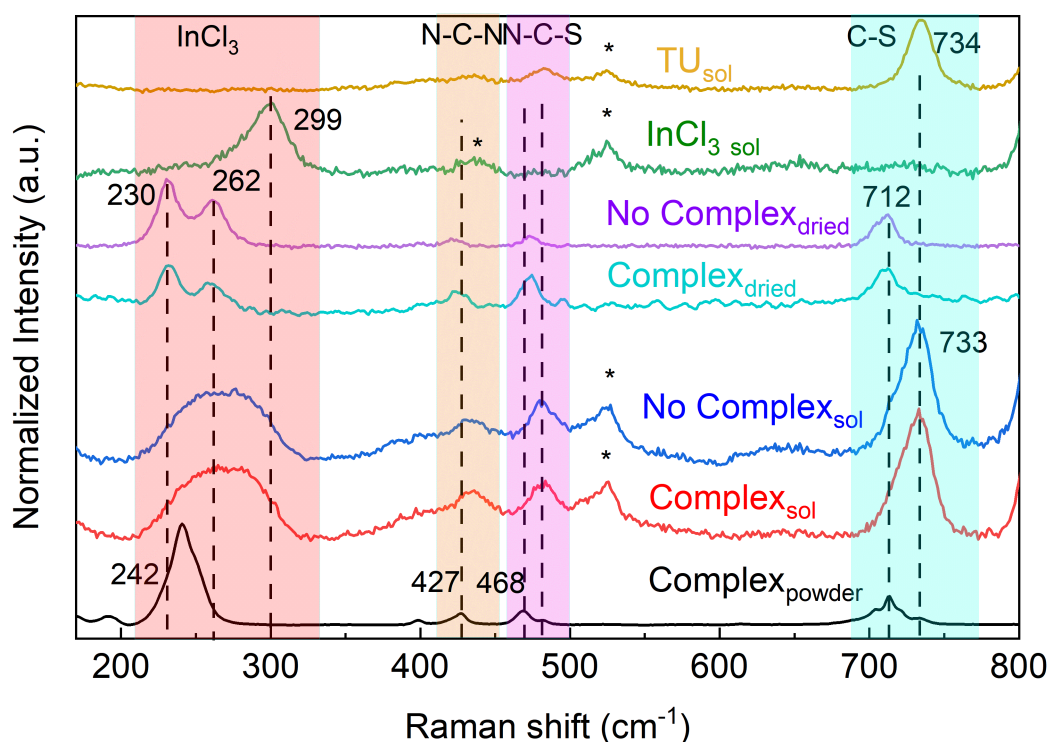
Figure 5.19: Raman spectrum of $In(TU)_3Cl_3$ powder (black), complex in solution (0.4 M) (red), No Complex in solution (0.4 M $InCl_3$, 1.2 M TU) (blue), film of dried complex (cyan) and dried No Complex (purple), $InCl_3$ in solution (0.4 M) (green), TU in solution (1.2 M) (yellow). The star corresponds to a peak from the solvents.

The spectrum of the complex powder shows multiple peaks. The one at 712 cm^{-1} is shifted compared to literature value of pure thiourea (740 cm^{-1}) indicating weakening

	InCl$_3$	N-C-N	N-C-S	C-S
Dried TU		411	469	740
InCl$_3$	289.2/ 300.9			
TU$_{sol}$		436	482	734
InCl$_{3sol}$	299			
No Complex$_{dried}$	230/262	423	473	712
Complex$_{dried}$	232/259	424	473	711
No Complex$_{sol}$	266	432	481	733
Complex$_{sol}$	266	433	482	734
Complex$_{powder}$	242	427	468	712

Table 5.4: Raman's peaks position for thiourea, InCl$_3$, Complex and No Complex solutions, Complex and No Complex dried films and Complex powder.

of the C-S bond which is coherent with the formation of a metal-sulfur complex. A red shift of approximately 30 cm^{-1} was observed for tris thiourea zinc acetate complex [142], which is similar to the shift observed in our material. The N-C-S peak (468 cm^{-1}) is similar to the dried thiourea, even though it is found to have a blue shift of around 10 cm^{-1} in literature for other complexes. The N-C-N peak (427 cm^{-1}) is blue shifted compared to pure thiourea. The peak related to InCl$_3$ is situated at 242 cm^{-1} and is red shifted by more than 50 cm^{-1} compared to the indium chloride solution indicating a serious weakening of the bond and confirming the presence of an interaction with other atoms. The complex dissolved in solution shows a different Raman spectrum with shifts in all peaks. The thiourea related peaks are blue shifted and correspond to the thiourea in solution, while the indium related peak position is 262 cm^{-1} and is wide (the FWHM is doubled compared to the InCl$_3$ only solution). This shift translates into a strengthening of the In-Cl bond, i.e. a likely decrease of the sulfur-indium bond. This peak seems to encompass both the peak present in the complex powder and the indium in solution, pointing to the presence of multiple chemical environments in the solution. The solution consisting in the simple dissolution of thiourea and indium chloride in the solvents mixture gives an identical Raman spectrum as the complex solution spectrum meaning that the molecules are in the same chemical environment as in the complex solution. This could imply that the pre-synthesis of a complex powder does not have any advantage over the simpler process.

The complex and No Complex inks were printed on Mo and dried at 70°C for 5 minutes to remove the solvents and both Raman spectra are very similar. A red shift of 20 cm^{-1} is observed for the C-S bond compared to the ink. The InCl$_3$ peak is divided in two partially overlapping peaks at 230 and 262 cm^{-1} which clearly shows the presence of multiple chemical environments. The first peak corresponds to a strong In-S complex that is even more pronounced than in the complex powder as attested by the red shift. The second peak is blue shifted compared to complex powder but red shifted relative to the

indium chloride solution and it probably represents a less strong complex. In summary, the complex powder does have a different spectrum than indium chloride and thiourea dried or in solution, confirming the presence of a sulfur-indium interaction. However, once dissolved in the solvent, the interaction is visible only in the indium chloride peak which is probably an indication of the weakening of the S-In complex and the widening of this peak might indicate the presence of multiple chemical environments. The complex seems to form again in the printed dried film as attested by the position of the C-S peak of thiourea but the multiple chemical environment are again visible in the indium chloride peak that is divided in two peaks probably corresponding to strong and less strong complex. No difference is observed between the complex and No Complex chemistries in terms of ink or dried film showing that the pre-synthesis of the complex is apparently unnecessary.

The dried films showed some inhomogeneities and the data discussed in figure 5.19 were taken in the majority phase to ease the understanding. However, figure 5.20 shows an optical image of the dried film where blue stains in a yellow phase (majority phase) can be observed. The Raman spectra do show a difference in the double peak of indium chloride: these peaks seem to merge together in the blue stains, while they are distinct in the majority yellow phase. This could indicate that the yellow phase has nearly two distinct chemical environment while the blue stains contains multiple environments. These inhomogeneities are however not found in the annealed films.
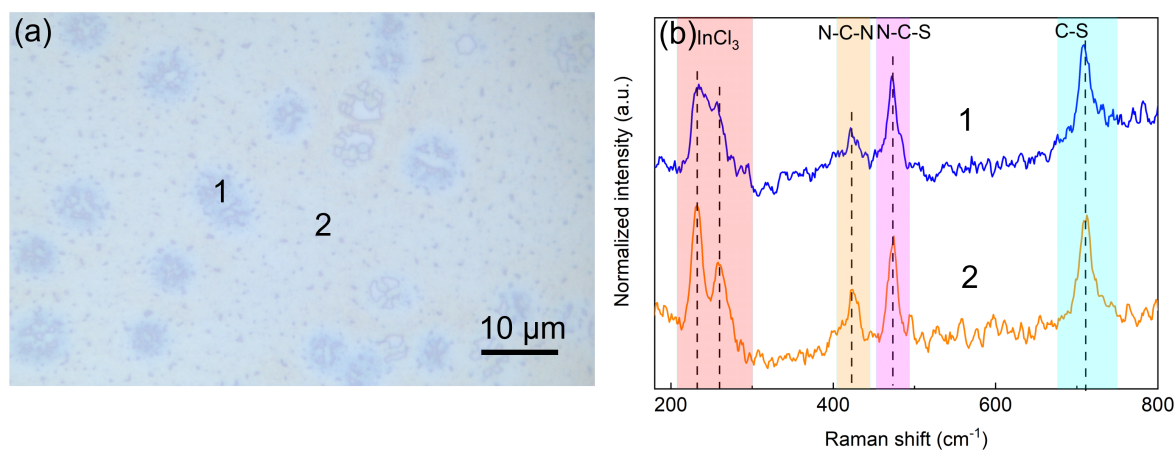
Figure 5.20: Optical image (a) and Raman spectra (b) of a complex dried film. Spectrum 1 and 2 correspond to the blue stains and the yellow phase respectively.

The Raman spectra of the In_2S_3 films resulting from the complex and No Complex dried films annealed at 250°C for 5 min are shown in figure 5.21. The peak is broad because of the low crystallinity of the film (this will be further discussed in the XRD measurement below). It consists in the overlapping of several peaks. However, the determination of the peaks present is quite difficult because of the width. A tentative peak position determination is 217, 285, 306 and 366 cm^{-1} These peaks are associated

to tetragonal β-In$_2$S$_3$ phase [126] [127]. Both the complex and No Complex spectra are similar even though the complex maximum seems to be slightly shifted and narrower than the No Complex.
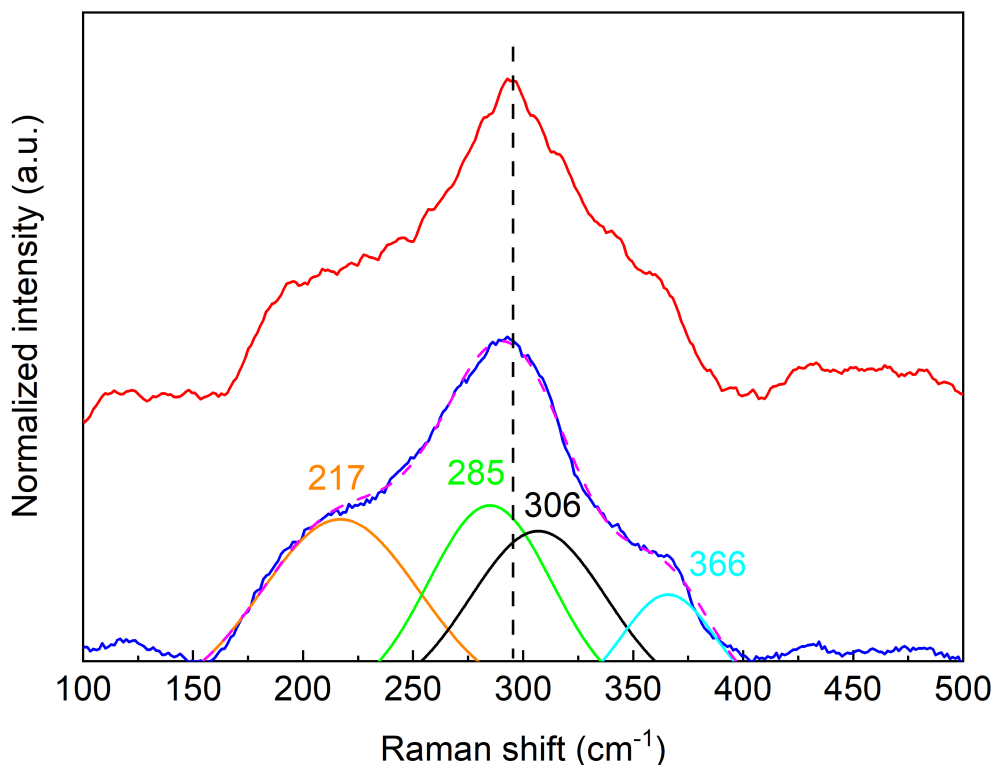
Figure 5.21: Raman spectra of In$_2$S$_3$ from complex (red) and No Complex (blue) inks, multiple peaks fitting (from orange to light blue) and the cumulative curve from the peak fitting (pink).

GIXRD confirms the tetragonal β-In$_2$S$_3$ crystalline structure for both complex and No Complex based In$_2$S$_3$ (fig 5.22). A PVD indium sulfide grown at 285°C (substrate temperature) was taken as a reference sample to compare the degree of crystallinity of the synthesized films. Both complex and No Complex show similar spectra but different from PVD which is probably due to a preferential growth. Table 5.5 shows the (2212) peak position for the three samples. The peak position (48.05°) is identical for complex and No Complex but higher than the PVD reference (47.87°). The PDF4+ card 00-025-0390 gives a peak position at 47.70°. The difference in peak position might be due to the incorporation of oxygen. Indeed, oxygen is smaller than sulfur which shrinks the unit cell size, i.e. inter planar distance (d spacing). XRD and Raman measurements point to a tetragonal structure in which the unit cell parameters are defined as followed (table 3.1): $a=b\neq c$, $\alpha = \beta = \gamma = 90°$. The unit cell parameters are reported in the same table for the Complex, No Complex and PVD films calculated from the equation

$$\frac{4\sin^2\theta}{\lambda^2} = \frac{h^2 + k^2}{a^2} + \frac{l^2}{c^2} \tag{5.1}$$
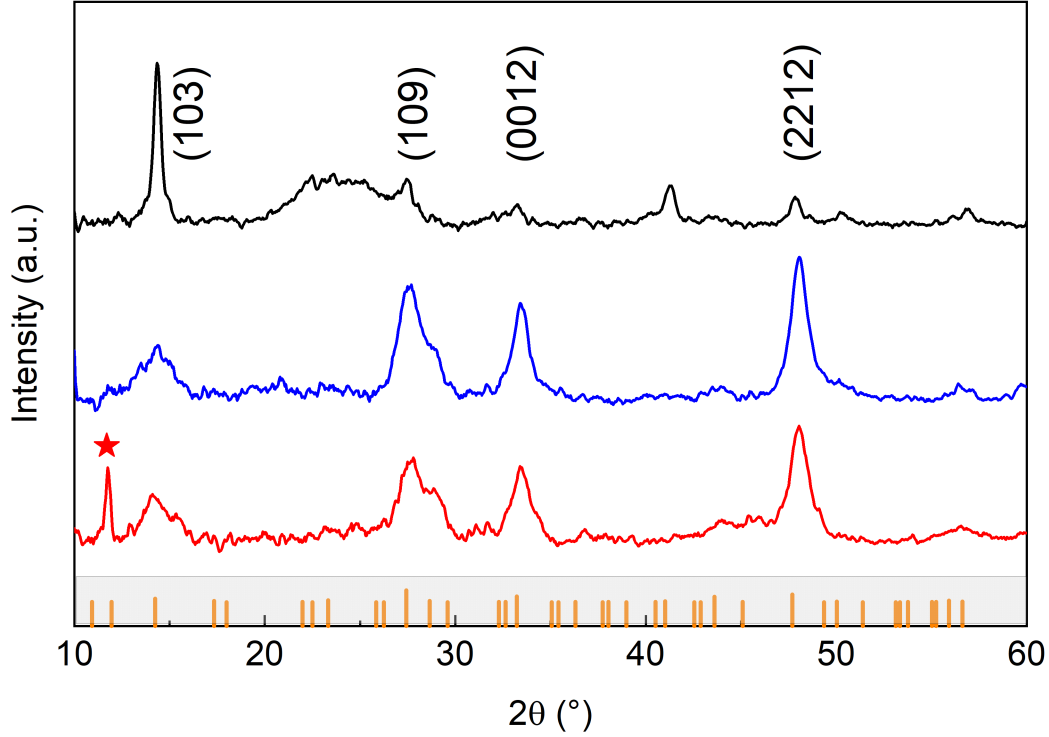
Figure 5.22: GIXRD of complex (red) and No Complex (blue) based In_2S_3 film annealed at 250°C for 5 min and PVD deposited In_2S_3 (black). The main peaks are labelled. The peak labelled with a star is an unknown peak. The reference is PDF4+ 00-025-0390.

where λ is the XRD wavelength (1.5406Å), θ is the Bragg's angle and h, k, l are the Miller indices. The obvious shift reported on the (2212) peak actually needs to be put in perspective. Indeed, the a, c and volume (V) of the unit cell have a relative deviation of around 1% compared to the literature values (a=7.619 Å, c=32.329 Å, $V = 1877$Å^3). This relative difference is actually within the error of the measurements and data processing, and can not be undoubtedly attributed to the replacement of sulfur by oxygen.

The full width at half maximum (FWHM) of the (2212) peak (table 5.5) is identical inside the error for Complex and No Complex materials and is nearly double the FWHM of the PVD reference. The coherence length (an approximation for the crystallite diameter) obtained through Scherrer equation (3.7) is nearly identical for both Complex and No Complex (6.5 nm) and is about half of the PVD's (11.7 nm). This disparity in crystallites size can be understood as a difference of energy supplied during the growth of the material: PVD provides more energy to the sample than the hot plate heating process used to anneal the printed samples. The small size of the crystals in inkjet printed In_2S_3 and their associated band gaps will be further discussed in chapter 7 in which quantum confinement relates the size of the crystal to the band gap.

In summary, the vibrational properties of the dried and annealed films for both the Complex and No Complex inks were shown to be similar. The same observation was made for the crystal structure of both In_2S_3. The next property of the materials that is

	2θ of (2212) peak (°)	FWHM(°)	Coherence length (nm)	a (Å)	c (Å)	V (Å^3)
Complex	48.05 ± 0.01	1.11 ± 0.03	6.50 ± 0.14	7.69	32.10	1899
No Complex	48.07 ± 0.01	1.05 ± 0.02	6.88 ± 0.13	7.58	32.15	1849
PVD	47.87 ± 0.01	0.62 ± 0.03	11.68 ± 0.55	7.67	32.26	1899

Table 5.5: Crystallographic data from XRD data of In_2S_3 films from complex and No Complex inks annealed at 250°C for 5 min and PVD In_2S_3.

compared is the micro-morphology.

AFM showed a porous morphology for the In_2S_3 layers with deep holes that might go down to the substrate (fig 5.23). Some features appear very bright and look like standing wall, separating darker regions which look less prominent (intermediate dark) or very deep hole (extreme darkness). In an ideal case, the buffer should be dense and smooth. Indeed, non-radiative recombinations often occur at interfaces.
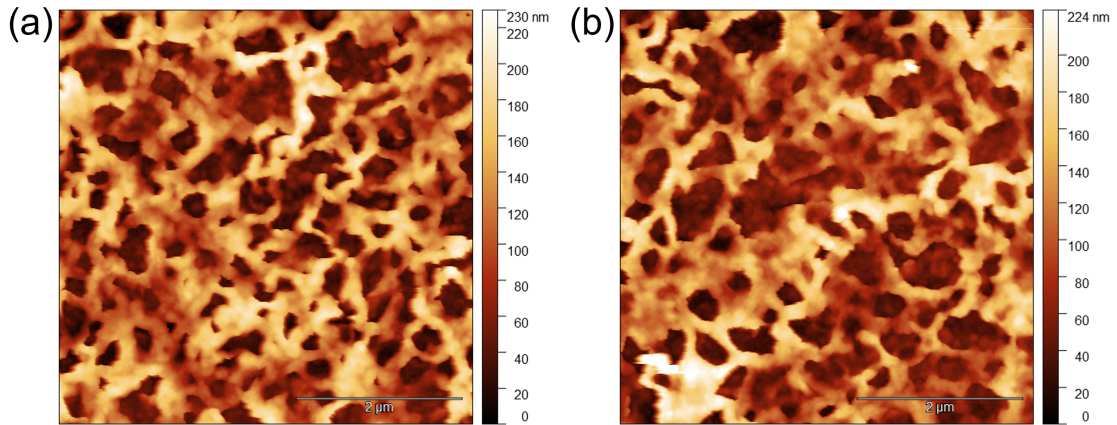
Figure 5.23: AFM images of complex (a) and No Complex (b) based In_2S_3 deposited on Mo coated glass and annealed at 250°C for 5 min.

With the current morphology, the interface between the buffer and the window layer is much bigger than between two smooth layers, increasing the likelihood of non-radiative recombinations. Moreover, CIGSSe sometimes contains holes down to the Mo. If the AZO layer touches the Mo, a shunt path is created. The buffer is usually deposited to fill these holes. However, if the buffer is porous down to the CIGSSe, the holes of CIGSSe might stay open and be filled with AZO. Nevertheless, both Complex and No Complex show an identical porous morphology and its origin will be further discussed in section 5.6. This morphology is unrelated to the deposition technique (inkjet printing). Indeed, Wang et al. [47] inkjet printed and spin coated indium sulfide and did not report any porous structure. However, several differences exist between their ink and the one used in this work as shown in table 5.6. It will be shown in section 5.6 that the solvents are not responsible for the porous morphology. The important difference between these inks

110

is thus in the salts nature, their concentrations and [S]/[In] ratio (1.5 for Wang and 3 for this work). The [S]/[In] ratio will be examined in section 5.6.

	Complex	No Complex	Wang et al.
water	1	1	
ethanol	2	2	9
propylene glycol	1	1	
ethylene glycol			1
$In(TU)_3Cl_3$	0.4		
$InCl_3$		0.4	
TU		1.2	1.5
$In(NO_3)_3$			1

Table 5.6: Complex and No Complex and Wang's [47] inks composition. Liquids volume is in mL and salts amount is in M.

XPS measurements did not show any difference between the In_2S_3 from the complex and No Complex inks. The distribution of the [S]/[In] and [Cu]/[In] were identical to the previous XPS measurements and can be found in the appendix B. No clear evidence of a difference in chemical composition or crystallographic structure was found for the Complex and No Complex based In_2S_3. They were thus inkjet printed on CIGSSe, annealed at 250°C for 5 min and the performance of the devices was studied.

The performance of the CIGSSe solar cells with a buffer layer based on the Complex and No Complex inks is reported on figure 5.24 as well as a reference with a Zn(O,S) buffer sputtered by Avancis. The reference cell was completed with AZO and contacts, while the other cells were finished with iZO, AZO and contacts. The efficiency of both Complex and No Complex are statistically identical and very similar to the reference. The open circuit voltage of the In_2S_3 buffered solar cells is higher than the reference. The quasi Fermi level splitting (qFLs) of these cells was measured before and after the buffer deposition to assess the impact of the deposition and annealing processes. The qFLs of the bare absorbers were around 660 meV respectively and decreased to around 650 meV after the deposition. A difference of 10 mV is actually quite small and is often considered to be part of the error so if a degradation occurred after the annealing, its effect is not significant. When comparing the qFLs with the V_{oc} of the complete cell, a decreased of 10 meV is again recorded for the complex, that might be considered as the measurement error or originate from non-radiative recombination at the buffer/absorber interface or at the windows interfaces. In the case of the No Complex, this drop is around 20 meV, which is not within the error, and it clearly points to a recombination loss.

The fill factor of the complex has a wider distribution indicating a possible inhomogeneity. A similar spread is found in the shunt and series resistances (shown in appendix
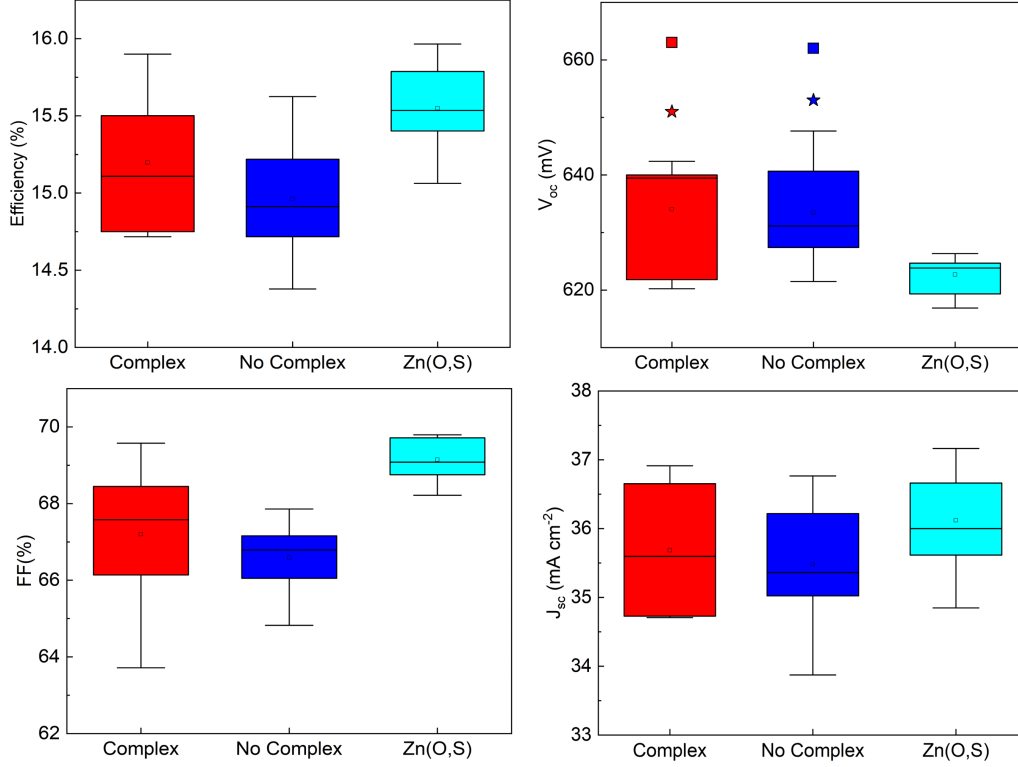
Figure 5.24: Optoelectronic properties of solar cells with an In_2S_3 buffer layer from the complex (red) and No Complex (blue) inks and a reference with a $Zn(O,S)$ buffer layer sputtered by Avancis. The squares and the stars in (b) represents the qFLs before and after the deposition of the buffers.

B fig B.3). However, these variations could not be explained by a morphological change: when checking multiple subcells (fig 5.25), more defects are found on the No Complex sample (fig5.25b) which contradicts the FF trend. Moreover, the $Zn(O,S)$ reference showed a shunt resistance 4 times smaller and a higher series resistance than the In_2S_3 buffer but still have a higher FF. Regarding the short circuit current density, the spreading is within the error of the area measurement. The performance parameters of the record cells for each buffer is shown in table 5.7. The efficiencies are quite similar for all samples.

	Efficiency (%)	V_{oc} (mV)	FF (%)	J_{sc} mAcm^{-2}	$J_{sc,EQE}$ mAcm^{-2}
Complex	15.9	640	68	36.3	36.3
No Complex	15.6	631	67	36.8	36.1
Zn(O,S) Avancis	16.0	624	69	37.1	37.0

Table 5.7: Record cells performances for complex and No Complex based In_2S_3 buffered solar cells and the reference with Avancis $Zn(O,S)$.

EQE measurement (fig 5.26) shows no parasitic absorption due to the buffer for the Complex and No Complex, while a blue defect is present for the $Zn(O,S)$, meaning that the band gap of this layer is not as high as usually encountered [58]. The EQE spectrum
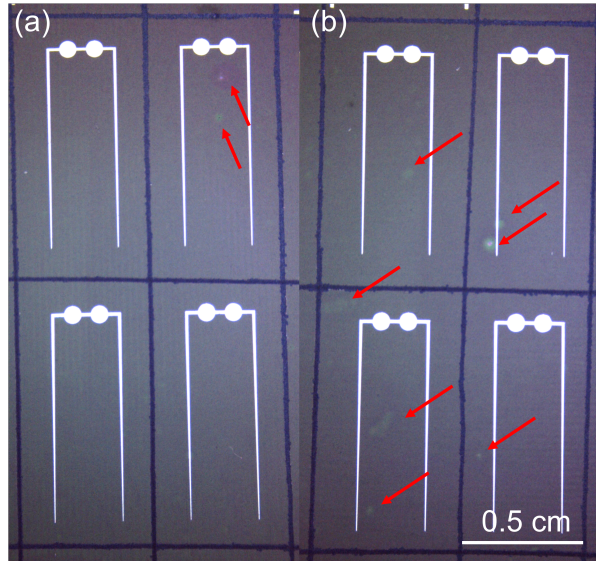
Figure 5.25: Optical image of multiple subcells with an In_2S_3 based on (a) complex ink, (b) No Complex ink. The red arrows point toward defects in the macro-morphology.

of Zn(O,S) cells shows oscillations in the region 500 nm - 800 nm that are related to the interference of light between the different layers. These phenomenon is absent in the In_2S_3 samples, proving that the layers are rough, damping any possible interference. The In_2S_3 and Zn(O,S) spectrum do not overlap on the long wavelength edge because of a slightly different band gap, i.e. 1.09 eV for Complex/No Complex and 1.07 eV for Zn(O,S) as shown on figure 5.26. The J_{sc} calculated from the EQE of Complex, No Complex and Zn(O,S) are shown in table 5.7. It shows that the current was slightly overestimated essentially for the No Complex.

In conclusion, no significant difference was found between the Complex and No Complex chemistries. The pre-synthesis was found to be unnecessary in our ink system. It was also shown that the In_2S_3 in a CIGSSe device gave similar efficiency as an industrial Zn(O,S) deposited buffer [3]. An optimization of the thickness of the buffer is shown in appendix B on figure B.4 and the thickness used in the previous results was found to be optimal.

Room for improvement was also found in the annealing medium. Even though the oxygen was not found in significant amount in the XPS measurement when annealing the sample in air, a change in the annealing medium was found to improve the efficiency of the device (fig 5.27). The mean efficiency is higher for the annealing in nitrogen compared to air. This improvement is found in V_{oc}: the distribution is tighter in nitrogen and centered at 660 mV, whereas the mean is around 635 mV for air annealing. The qFLs of the bare absorbers were similar. After the processing, both samples showed a similar qFLs loss. However, the V_{oc} is even lower compared to the qFLS for the air annealed sample, while

---

[3]Applying a light soaking of the complete devices could improve the efficiency by 1 or 2%.
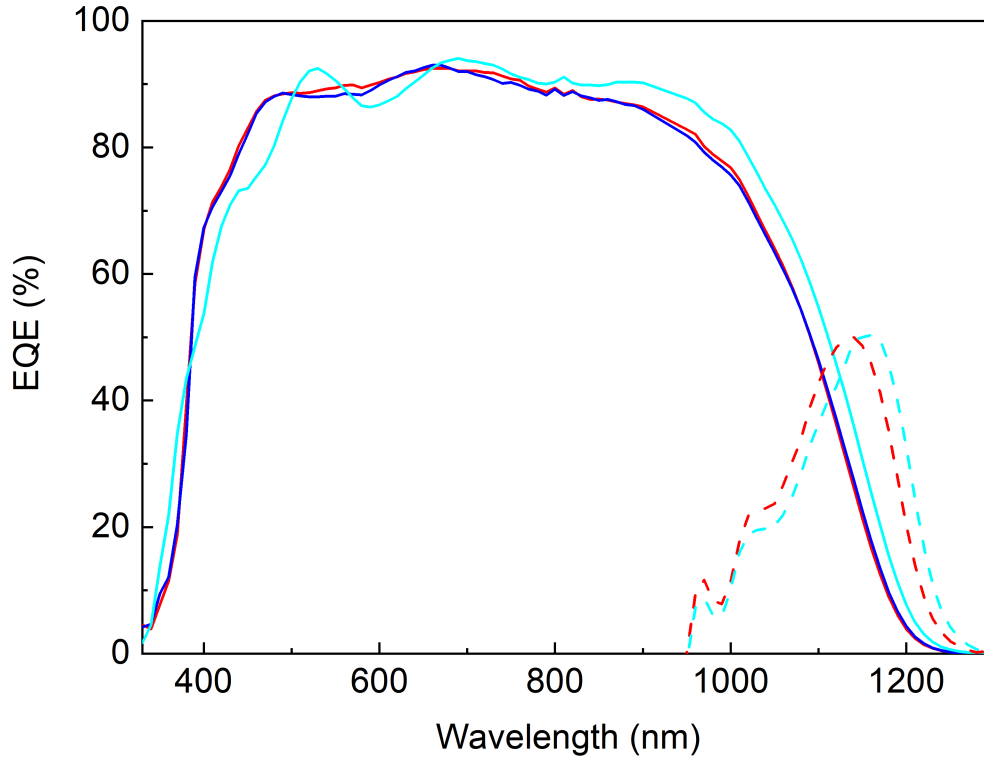
Figure 5.26: EQE of record cells with a complex (red), No Complex (blue) and Zn(O,S) (light blue) buffers. The dashed curve represents the derivative of EQE relative to the photon's energy $dEQE/dE$ enabling the finding of the band gap of the absorbers.

it is similar for the nitrogen one. An anomaly is even noticed: the qFLs is smaller than some V_{oc} of the cell. This might be related to the approximation used to find the qFLS from the generalized Planck law: it is hypothesized that the CIGSSe light absorption is complete (100%) which might be a wrong assumption. The FF is also higher in average for the nitrogen sample. Based on equation 3.16, the maximum mean FF is 73.1 % for the air and 73.8 % for the nitrogen samples without taking into account the resistance losses. The series resistance is higher for the nitrogen sample which should drive the FF to lower values and is in contradiction with the current results. The trend in shunt resistance is in accordance with FF but the values are so high that it does not affect the FF significantly. The trend in FF is thus unrelated to the resistances. Nevertheless, the mean FF value for air is 68% and 70% for nitrogen which is actually a small difference. Only the J_{sc} is found smaller for the nitrogen sample. The annealing in nitrogen is a good candidate to increase the efficiency of the cells.

5.6 Varying the sulfur to indium ratio in the ink

Since the pre-synthesis of a complex was not proven to be essential, a new degree of freedom can be explored in the In_2S_3 ink, i.e. the sulfur to indium ratio. An excess
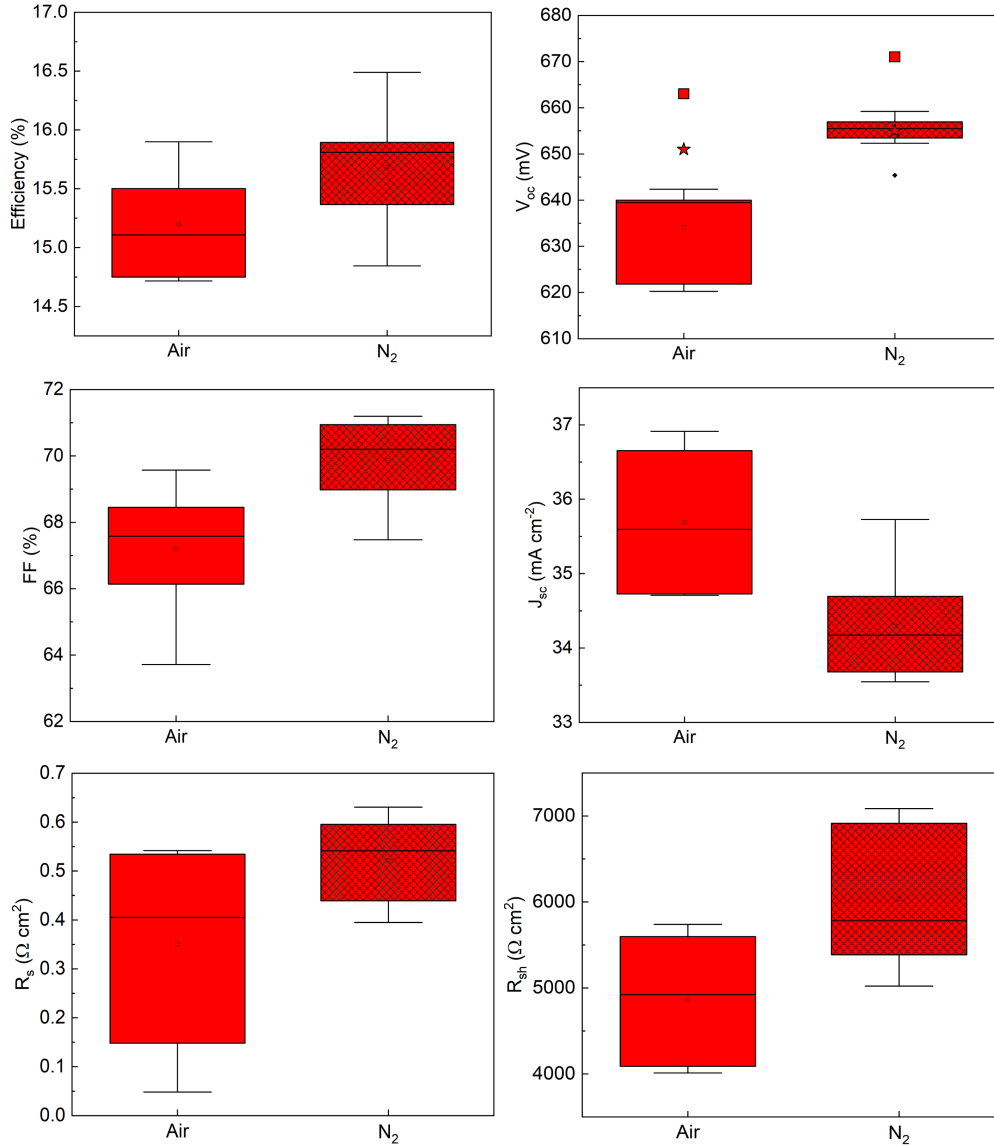
Figure 5.27: Optoelectronic properties of solar cells with an In_2S_3 buffer layer from the complex ink annealed in air and in nitrogen: efficiency, V_{oc}, FF and J_{sc}. The squares and stars in V_{oc} represents the qFLs before and after the deposition of the buffers respectively.

of sulfur was used in the previous section to prevent the incorporation of oxygen in the lattice. Indeed, In_2S_3 films deposited through CBD, which is often the preferred solution deposition technique, contain oxygen. The formation of $In(OH)_3$ is unavoidable due to the hydrolysis of In^{3+} in aqueous solution. The resulting material is $In_x(OH,S)_y$ rather than pure In_2S_3 [42]. Barreau et al. synthesized a CBD deposited In_2S_3 with a [S]/[O]=2.5 and showed that the main contribution of oxygen was In−O bonds [144].

In order to form a pure In_2S_3, a minimum [S]/[In]=1.5 ratio seems to be necessary. However, even though the CBD In_2S_3 contains oxygen, it performs decently as a buffer layer for CIGSe [41]. The [S]/[In] ratio was thus varied from sulfur rich ([S]/[In]=3 and 2) to sulfur poor ([S]/[In]=1) as well as the stoichiometric ratio ([S]/[In]=1.5) to determine

the ideal ratio with our ink system (table 5.8 for inks composition). The first two inks are expected to form an In_2S_3 without oxygen or with a very low content, while the third ink is expected to make $In_x(O,OH,S)_y$. The stoichiometric ratio should ideally form pure In_2S_3 as the sulfur rich inks, however, the smallest variation in the ratio due to human handling might drive this ink toward sulfur poor or sulfur rich ink.

	$InCl_3$ (M)	TU (M)
[S]/[In]=3	0.4	1.4
[S]/[In]=2	0.4	0.8
[S]/[In]=1.5	0.4	0.6
[S]/[In]=1	0.4	0.4

Table 5.8: Composition of the inks with various [S]/[In] ratios.

5.6.1 Morphology

The impact of the [S]/[In] ratio on the morphology at each step of the processing was recorded. Figure 5.28 shows SEM and EDX images of dried and annealed films deposited on Mo from the ink with [S]/[In]=3. The dried film shows a dense structure with small features creating roughness on the surface (fig 5.28a,b). The EDX mapping shows an homogeneous distribution of indium and nitrogen which are characteristic of indium chloride and thiourea (fig 5.28c,d). The ratio [In]/[N] seems to be homogeneous (fig 5.28e). The mapping of sulfur is not reported because the film was deposited on Mo coated glass and Mo and S peaks overlap in EDX, making quantification impossible. The In_2S_3 annealed film (fig 5.28f) morphology showed an irregular porous structure with holes size ranging from 0.1 to 1 µm. The important contrast is related to local charging which might either be related to a phase separation or to the morphology since In_2S_3 film is resistive. It could be hypothesized that thiourea molecules form agglomerates that evaporate during the annealing, creating this porosity. However, the atoms were found to be homogeneously distributed. It was also confirmed that the porosity was uncorrelated to the total concentration of the ink. Indeed, decreasing the concentration of each molecule by a factor of four still created a porous morphology (appendix B). The morphology was discussed for films deposited on Mo coated glass. However, the actual application requires the deposition on CIGSSe that might produce a different morphology.

The In_2S_3 buffer was deposited on CIGSSe and figure 5.29 shows that the morphology of the buffer is similar on CIGSSe as on Mo. The holes size is varying from 100 nm to 500 nm which is smaller than on Mo. The thickness of the wall (already shown in AFM measurement in section 5.5) is typically of 100 nm. This porosity can be found all over the sample (fig 5.29c). Some features (hightlighted in red) of the CIGSSe seem not to be covered or barely covered when comparing the bare CIGSSe and the covered CIGSSe.
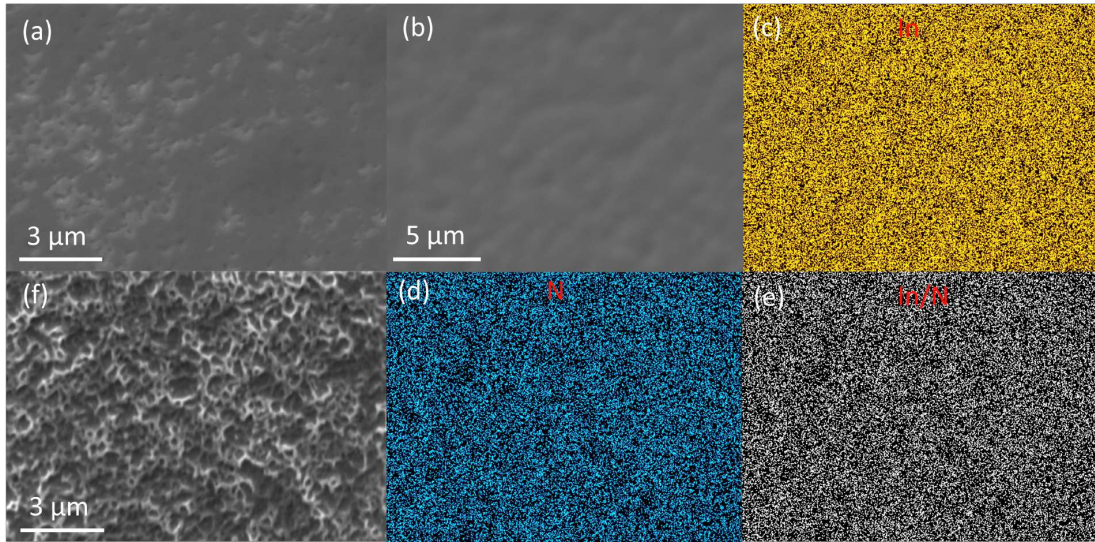
Figure 5.28: Inkjet printed film based on [S]/[In]=3. (a)SEM (7kV) and (b) SEM (20kV) images of dried film. (c) Indium (d) nitrogen and (e) [In]/[N] EDX (20kV) elemental mapping of dried film. (f) SEM image of the annealed film. The dried film was gold coated (1-5 nm) to prevent its degradation due to heating during measurement.

The presence of uncovered CIGSSe could create shunt in the films and is a subject of concern.
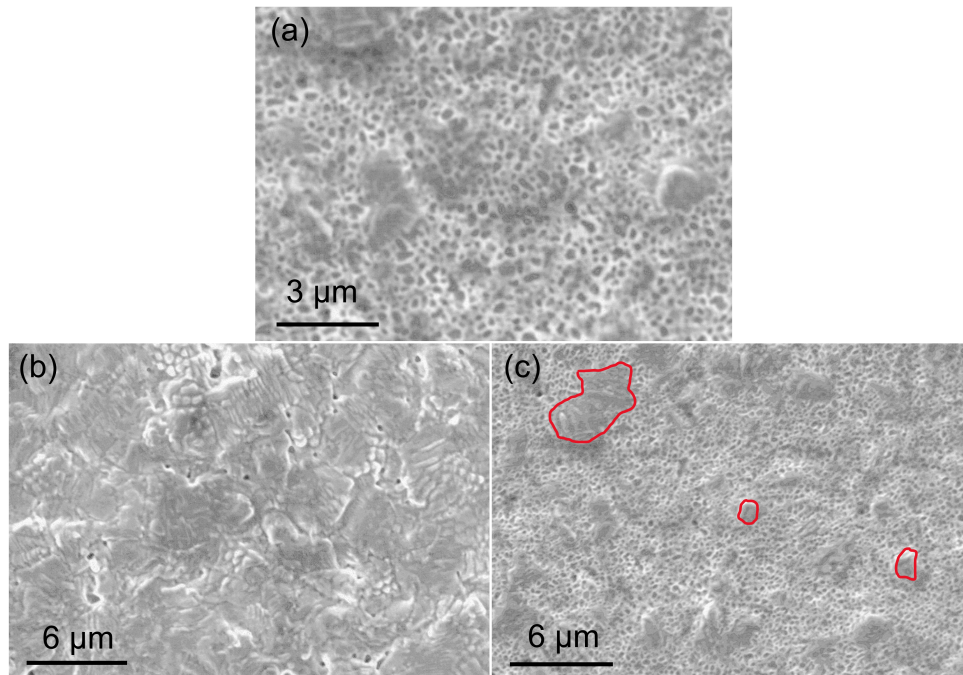
Figure 5.29: SEM images (7kV) of an inkjet printed In_2S_3 film from the ink with [S]/[In]=3. (a)high magnification of the film deposited on CIGSSe, (b) low magnification of bare CIGSSe and (c) low magnification of the film deposited on CIGSSe. Highlighted regions are some of the features of the CIGSSe that seem to be barely covered by the film.

In order to determine whether the apparent holes in the film are open down to the CIGSSe or a thin In_2S_3 layer is present, HIM-SIMS was measured on a bare CIGSSe and a buffered CIGSSe. Figure 5.30 a to d shows the contaminations (O, CN and Cl) on the bare absorber. The oxygen is found homogeneously on the surface (the contrast is due to morphological effects). This O is due to the UV ozone treatment as well as natural oxide formation in air. C and N are also present due to air contamination. The chlorine content has two sources. The first one is that Cl is nearly always observed on samples via HIM-SIMS. The second is that this bare absorber is actually part of the same absorber piece as the buffered one. They were thus annealed together in the close metallic pot. During the chemical reaction, $HCl_{(g)}$ is released and can condense back onto the bare CIGSSe. Figure 5.30 e to g shows the same measurement performed a second time, i.e. on a fresh surface. All the signals decreased proving that O, C, N and Cl are indeed surface contaminations.
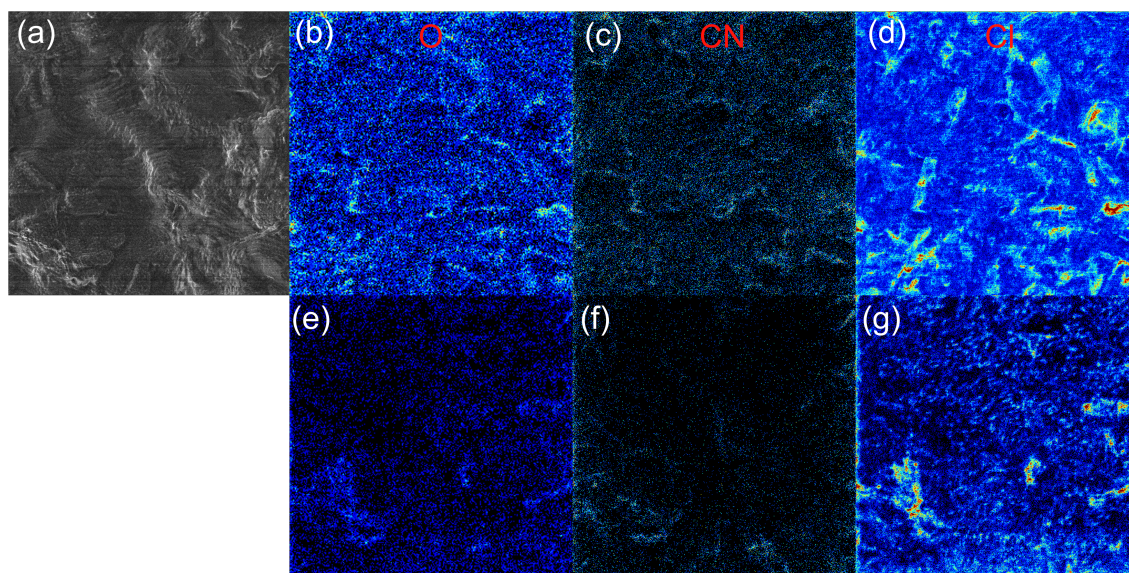
Figure 5.30: HIM-SIMS of bare CIGSSe. (a) Electron image (b), (c) and (d) are O, CN and Cl maps. (e), (f) and (g) are O, CN and Cl maps measured on a fresh surface (i.e. after the measurement of (b), (c) and (d). Each image is 10 μm by 10 μm.

Figure 5.31 shows the buffered CIGSSe. Several CIGSSe regions look uncovered as shown by the light grey textured areas and the porosity of the buffer (in-between the uncovered areas) is still visible. The Ga map shows bright signal in the uncovered regions, confirming the absence of buffer. The In map is homogeneous given that In is present in both CIGSSe and In_2S_3. The Cl signal which is characteristic of the buffer since it originates from the $InCl_3$ salt. It is cleary shown that the uncovered areas are nearly free from Cl. The regions are in light blue but figure 5.30d shows that Cl is already present on the bare absorber. In the buffer region, the signal is higher showing that In_2S_3 is found. The porosity is visible in the Cl map and the signal is similar to the uncovered CIGSSe. It can thus be concluded from this measurement that the CIGSSe is uncovered

both in large areas but also within the porosity. The CN signal shows that the buffer contains slightly more of these contaminations than the bare absorber. The oxygen, on the other hand, is homogeneous, proving that oxygen is not/weakly incorporated in the buffer. Knowing that the buffer does not cover entirely the CIGSSe raises a question: is the device shunted? The observation of with SEM of the surface of the buffered CIGSSe over large scale did not lead to the discovery of pinholes. Moreover, the CIGSSe is made of hills and valleys in terms topography. It is hypothesized that the pinholes are mostly present in the valleys. The buffer was shown to cover the valleys, meaning that it would cover most of the pinholes. The solar cells should thus not be tremendously influence by shunting.
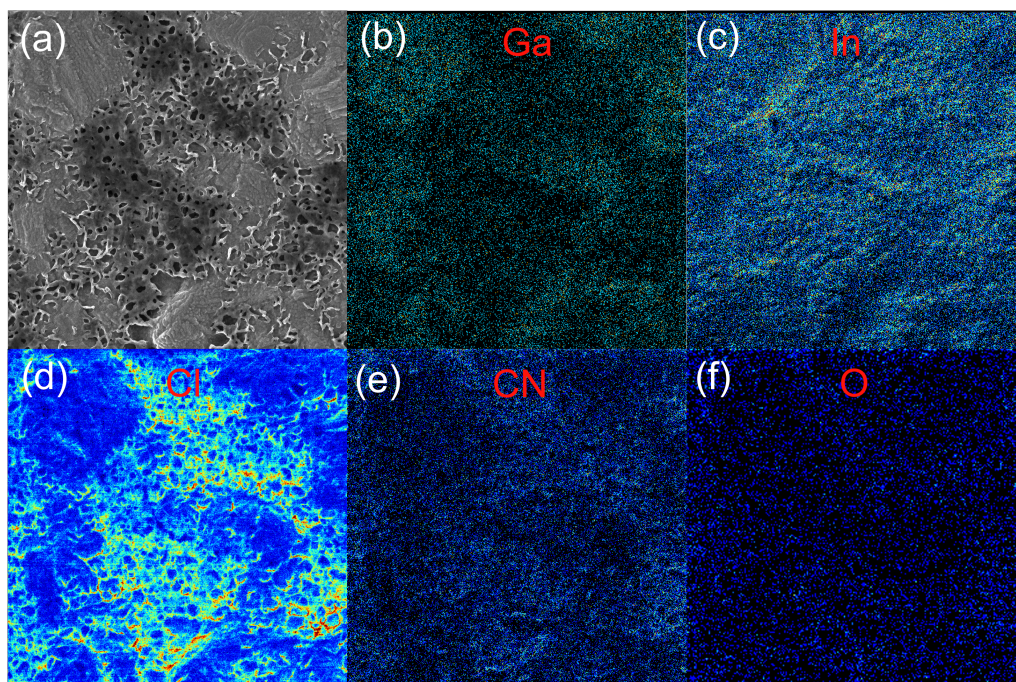
Figure 5.31: HIM-SIMS of buffered CIGSSe. (a) Electron image, (b) to (f) are Ga, In, Cl, CN and O maps. Each image is 10 μm by 10 μm.

A comment can be added to the HIM-SIMS analysis about the Na content (fig 5.32). The map of Na on the bare absorber shows a homogeneous distribution. After the buffer deposition and subsequent annealing, the Na content is also homogeneously distributed. However, the buffer does not intrinsically contain Na which proves that Na diffused from the glass to the front surface. This Na could influence the properties of both the CIGSSe and the buffer and could be further studied in a later work.

Figure 5.33 shows the SEM and EDX images of the dried and annealed film with [S]/[In]=2 ratio deposited on Mo. The dried film looks dense but rougher than for [S]/[In]=3. The EDX mapping show an homogeneous distribution of indium, nitrogen and [In]/[N] except for the holes with the ring shape. The center of the latters have the same composition as the film, while a ring can be seen with a lower signal, indicating the
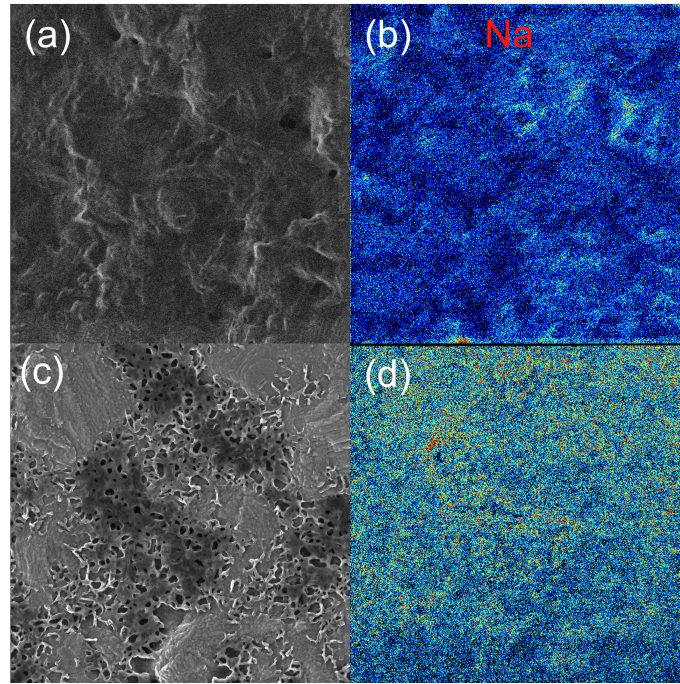
Figure 5.32: Electron image (a), (c) and HIM-SIMS (b), (d) of bare absorber and buffered CIGSSe respectively. Each image is 10 µm by 10 µm.

absence of the chemical species or their presence in very low amount. The morphology after the annealing is porous but contrarily to the [S]/[In]=3, the size distribution of the holes is much tighter (around 0.5 µm) and their shape looks more regular.
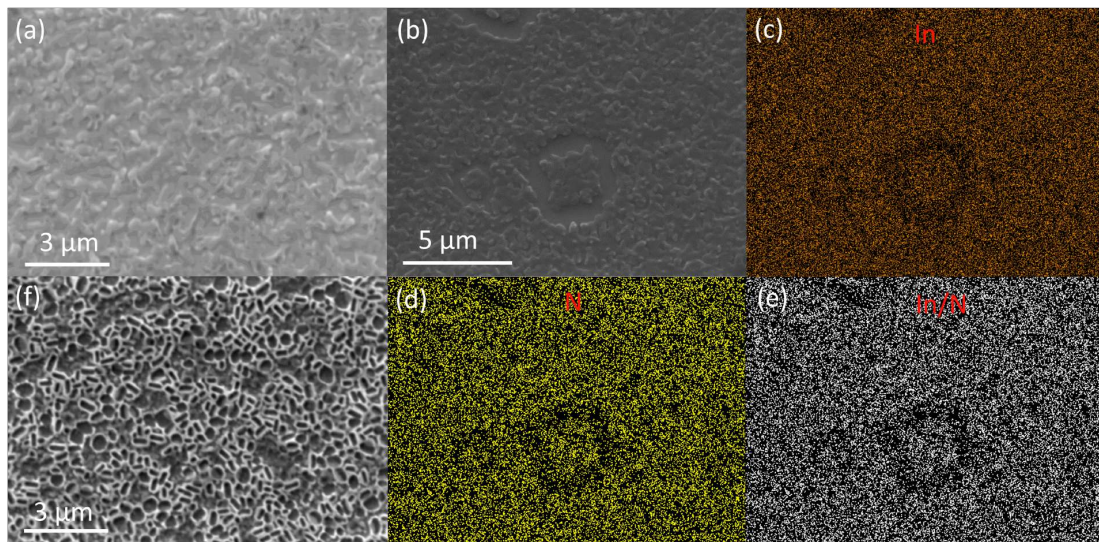
Figure 5.33: Inkjet printed film based on [S]/[In]=2. (a)SEM (7kV) and (b) SEM (20kV) images of dried film. (c) Indium (d) nitrogen and (e) [In]/[N] EDX (20kV) elemental mapping of dried film. (f) SEM image of the annealed film.

The morphology of the buffer on CIGSSe was found to be completely different. Figure 5.34a shows that the buffer is mostly dense. A small area with porosity is highlighted but this kind of region is very rare. Some features of the CIGSSe are not or barely covered by

120

the buffer (fig 5.34b). The typical facetting of CIGSSe is even visible in the highlighted regions. This was discussed for [S]/[In]=3 through HIM-SIMS and it was shown that CIGSSe is indeed exposed. However, the pinholes were still mostly covered. The dense morphology of this buffer is supposed to be ideal for a good quality cell. However, the quality of the junction does not only depend on morphology and the actual performance of the cell will be discussed later.
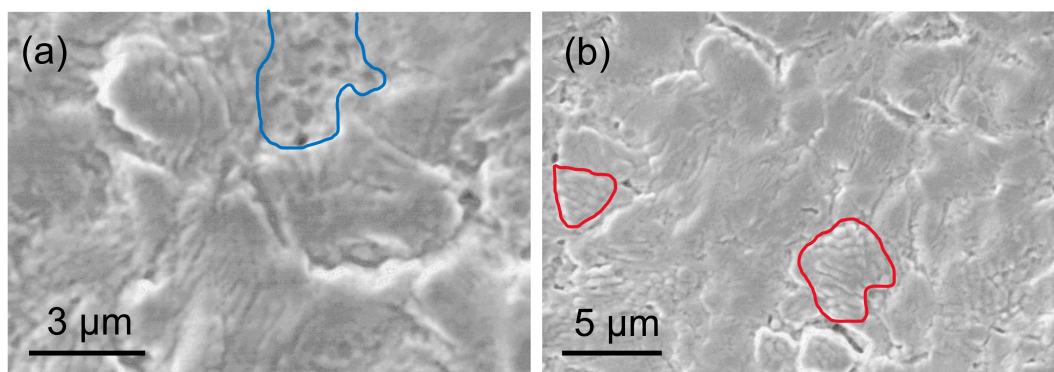
Figure 5.34: SEM images (7kV) of an inkjet printed In_2S_3 film from the ink with [S]/[In]=2. (a)high magnification of the film deposited on CIGSSe and (b) low magnification of the film deposited on CIGSSe. Highlighted regions in (a) show some apparent porosity in the buffer and show in (b) some of the features of the CIGSSe that are not or barely covered by the buffer.

The [S]/[In]=1.5 ratio showed an unexpectedly complex behaviour. The sample showed two kind of morphologies as shown on figure 5.35 a and b. Flowers-like shapes (fig 5.35a) are found on the surface, separated by a smoother region (fig 5.35b). Inset of figure 5.35a shows a zoom on one of these flowers. Figure 5.35 d to f show the EDX data: the flowers show a stronger signal than the in-between smoother material, which could be due to a stronger chemical concentration or simply a morphological difference. Both nitrogen and chlorine are found in these two features, however, their ratio shows the same morphology pointing to a phase separation. Indeed, by doing the ratio between the two elements, the influence of the thickness is removed. Since the ratio [Cl]/[N] is more intense on the flowers, it means that they contain more indium chloride. This inhomogeneity will be further studied with Raman.

The region in-between the flowers look reasonably dense after the annealing of the film (figure 5.35c). The flower-like structure turns into features with a black center and white tentacles (fig 5.36a) after the annealing. The dense morphology mentioned earlier is only visible outside of these regions. The white tentacles have a partially dense structure with a brighter contrast, while the darker center has a dendritic shape. The EDX indium mapping of a feature shows a clear increase of contrast in the white region and a slightly lower contrast in the darker region. It could be argued that the lower contrast is related to
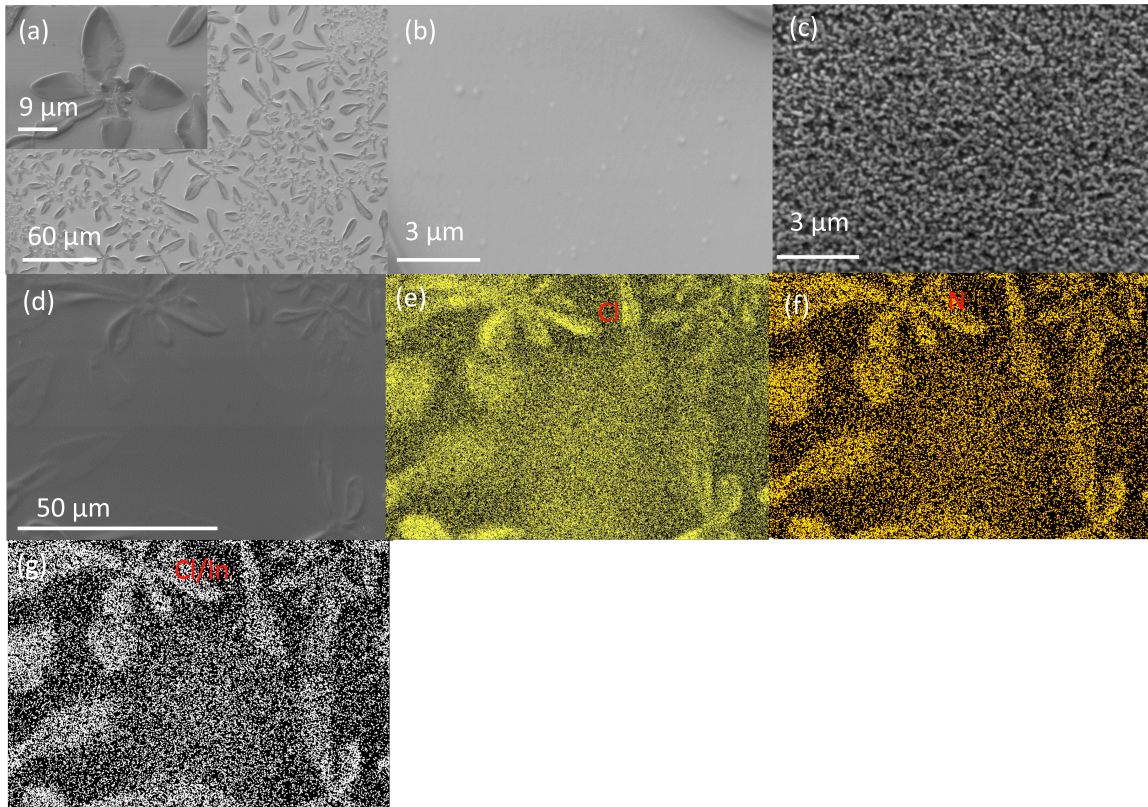
Figure 5.35: Inkjet printed film based on [S]/[In]=1.5. (a), (b)SEM (7kV) (d) EDX (20kV) images of dried film. (e) chlorine (f) nitrogen (g) [Cl]/[N] EDX elemental mapping of dried film. (c) SEM image of the annealed film.(c) SEM images of annealed film morphology in-between the flowers.

the thickness difference. Figure 5.37 shows a 3D mapping of one feature. The large blue region corresponds to the smooth part of the film while the green region is the tentacles and the dark blue is the center. The green region is clearly thicker than the smooth film and the dark blue is thinner. The signal collected from EDX is thus more or less intense depending on these thicknesses. However, the mapping of [In]/[N] shows that the higher contrast is still present which is probably related to a phase separation.

The morphology of [S]/[In]=1.5 is different on CIGSSe. Figure 5.38a shows that the morphology of the buffer is dense, however, facets from CIGSSe are observable, which as discussed for [S]/[In]=3 has a low impact on the shunting. On the other hand, the big features with tentacles were not noticed. Figure 5.38b exhibits a region with a different contrast (highlighted in blue) which is of a similar size to the shapes found in the film deposited on Mo. These are very rarely observed in the film deposited on CIGSSe and the correlation between the shapes found on Mo and on CIGSSe is very hard to confirm. The buffer seems to be more homogeneous on CIGSSe which is the application of interest in this work.

When decreasing the ratio to [S]/[In]=1 (fig 5.39), the dried film looks dense and smooth, rarely showing some prominent features. The chemical distribution of indium
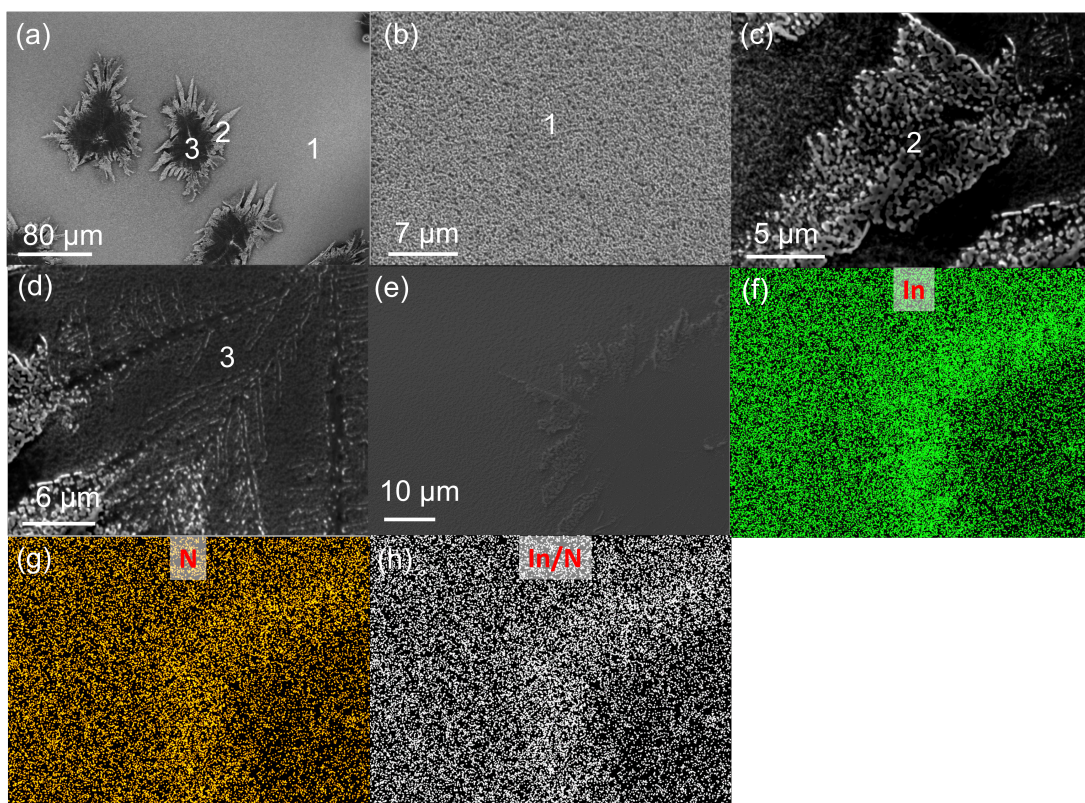
Figure 5.36: Annealed inkjet printed film based on [S]/[In]=1.5. (a), (b), (c) and (d) SEM images(7kV). (e), (f), (g), (h) are the EDX (20kV) image, indium, nitrogen and [In]/[N] mapping of a feature. Numbers 1, 2 and 3 on (a) refers to images (b), (c) and (d).
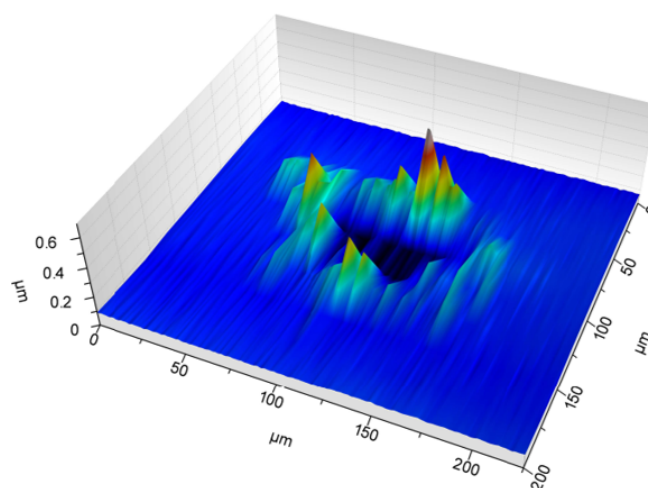
Figure 5.37: Profilometer map of a feature in the annealed film from the ink [S]/[In]=1.5.

and nitrogen is homogeneous except in the prominent circular shapes that seems to show a higher concentration of In. However, the [In]/[N] map (fig 5.39e) does not show prominent features at the same position. The annealed film is still dense but rougher than the dried film. Figure 5.40 shows the morphology of the buffer on CIGSSe. When comparing the bare absorber (fig 5.40a) with the buffered CIGSSe (fig 5.40b), the characteristic features
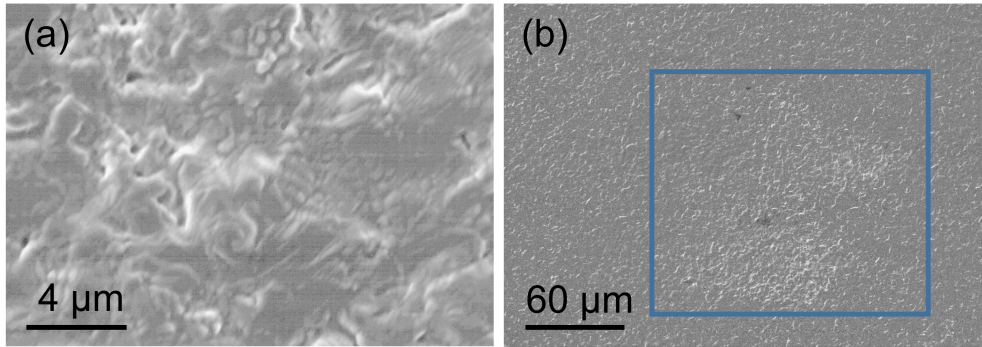
Figure 5.38: SEM images of an inkjet printed In_2S_3 film from the ink with $[S]/[In]=1.5$. (a)high magnification of the film deposited on CIGSSe (7kV) and (b) low magnification of the film deposited on CIGSSe (10kV). Highlighted region in (b) shows a feature that can be rarely seen.

of CIGSSe are smoothed after the deposition of the buffer indicating that the CIGSSe was covered by the buffer. In summary, the morphology of the buffers were very different on Mo for the various ratios but once deposited on CIGSSe, the topography looked dense and similar for all ratios, except for $[S]/[In]=3$.
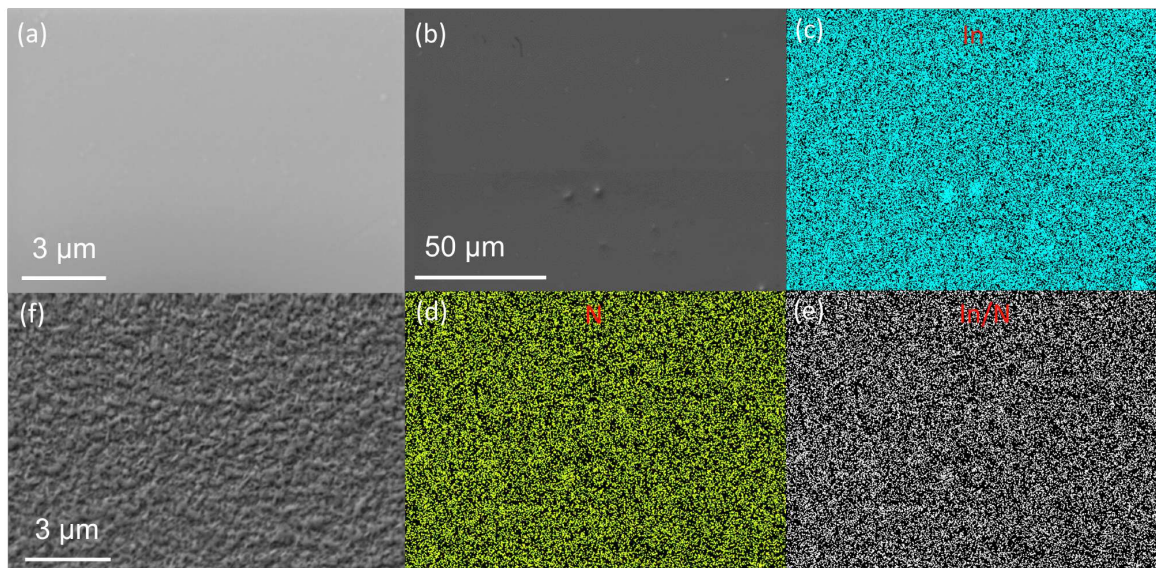
Figure 5.39: Inkjet printed film based on $[S]/[In]=1$. (a)SEM (7kV) and (b) EDX (20kV) images of dried film. (c) Indium (d) nitrogen and (e) $[In]/[N]$ EDX elemental mapping of dried film. (f) SEM image of the annealed film.

Since the dried films are dense and EDX did not show any agglomerates, the formation of porosity is probably a process that happens in the solid state. Figure 5.41 shows a SEM image of the gold covered dried film with $[S]/[In]=3$. The electron beam set at 10 kV hit the surface in the middle of the figure for 20 minutes. When compared to the pristine material (fig 5.41b), the morphology is different: the dense structure is exchanged with formation of holes and hills. It could be argued that the change in morphology is simply
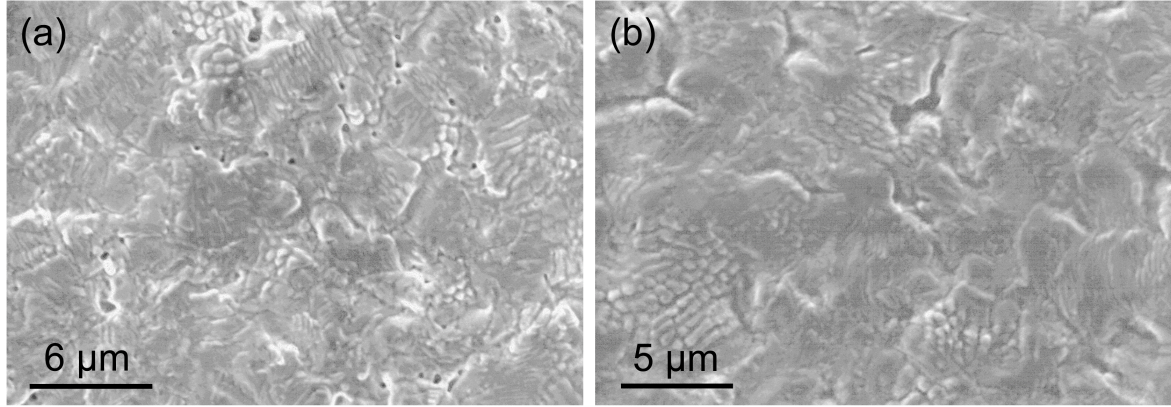
Figure 5.40: SEM images (7kV) of an inkjet printed $In_x(O,S)_y$ film from the ink with [S]/[In]=1. (a)Bare CIGSSe and (b) CIGSSe coated with the buffer.

due to evaporation of remaining solvents. Figure 5.42 shows the Raman spectroscopy of the solvents mixture and the dried film with [S]/[In]=3. The solvent shows several peaks that can be attributed to water, ethanol and propylene glycol except the peak at 525 cm^{-1} that could not be attributed to any of these solvents. The spectrum of the dried film does not show any of the peaks reported for the solvent proving that all the solvent was removed during the drying step. Two peaks (at 435 and 1091 cm^{-1}) might falsely be attributed to the solvent in the dried film. However, the dashed lines show that the peaks positions are different. This morphology (fig 5.41) that resembles the porous annealed film is produced by solid state dewetting. This process occurs similarly to the liquid state dewetting, where holes nucleates and grow. Ultimately, islands are formed if the energy given to the constituents is sufficient to ensure their mobility. The film reaches a temperature that enables dewetting but this temperature is not necessarily the melting temperature of the constituents. The Young equation applies similarly to the liquid case discussed in chapter 4.

$$\gamma_s = \gamma_i + \gamma_f cos\theta \tag{5.2}$$

where $\gamma_f, \gamma_i, \gamma_s$ and θ are the energy per unit area of the island, the island-substrate interface, rigid substrate and the contact angle. If $\gamma_s > \gamma_i + \gamma_f$, the film is stable and does not dewet [145]. If this condition is not satisfied, the film will dewet if the kinetics allows. Changing the energy of the substrate has a complex effect given that both γ_s and γ_f are modified and it is hard to predict the change in behaviour by changing the substrate energy. It can nevertheless explain the change in porosity when varying the [S]/[In] ratios and keeping the same substrate. Indeed, the energy of the dried film, i.e. γ_i, depends on [S]/[In] ratios. The variation of this ratio changes both γ_i and γ_f but not γ_s. This equation can also explain the change from porous to dense structure when changing the substrate. The surface energy of Mo and CIGSSe were determined using the

method of subsection 4.1.5. The total free energies are 74.6 mN/m and for 51.6 mN/m for CIGSSe and Mo respectively. Satisfying the condition for stability is thus harder for Mo than CIGSSe and dewetting is promoted on Mo which explains the change from porous to dense film for [S]/[In]=2 deposited on Mo or CIGSSe. The porosity was also found to decrease for [S]/[In]=3 when deposited on CIGSSe.

This work showed that decreasing the [S]/[In] ratios improves the stability of the dried film independent of the substrate and decreased dewetting. Moreover, it was found that CIGSSe had an energy that promoted the stability of the film and the porosity appeared only for [S]/[In]=3.
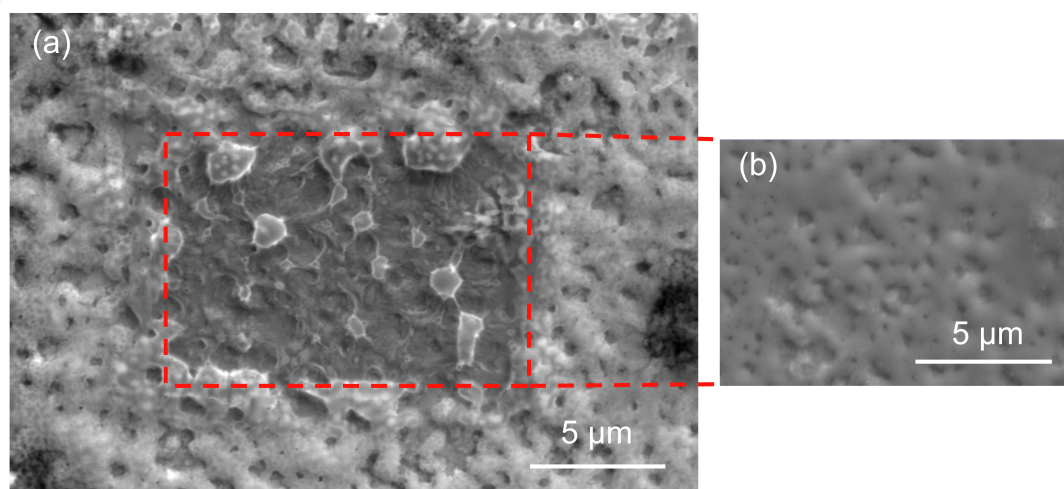
Figure 5.41: FE-SEM images of [S]/[In]=3 film dried at 70°C. (a) film after 20 minutes with the electron beam at 10kV. The middle part is where the beam hit the sample. (b) morphology of the middle part of (a) after 1 minute with the electron beam at 10 kV.

5.6.2   Investigation of S-In coordination

It was shown in section 5.5 that $InCl_3$ and TU coordinate in solution and in the dried films at different degrees. This coordination might be influenced by the [S]/[In] ratio and is studied here. Raman spectroscopy (fig 5.43) was measured on inkjet printed films dried at 70°C to check the potential formation of metal-sulfur complex structures as in section 5.5. The [S]/[In]=3 ratio was already discussed in the latter section. It shows a double peak for the indium chloride molecule (in the region 200-300 cm^{-1}) indicating the presence of two chemical environments that were interpreted as complexing with thiourea molecules at different degrees. The C-S peak of thiourea was also shifted compared to the pure thiourea solution. The [S]/[In]=2 shows a similar spectrum with a double peak for the indium at the same positions as the [S]/[In]=3 and the same shift for the C-S peak. When decreasing the ratio to 1.5, the double peak turns into a single wide peak similar to the spectrum of the complex/No Complex in solution shown in figure 5.19 revealing the
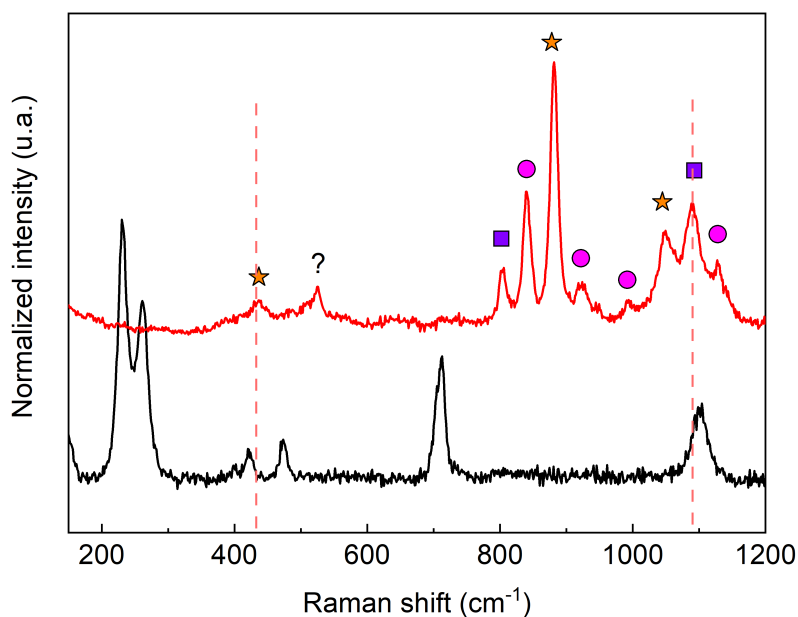
Figure 5.42: Raman spectra of the solvents mixtures (red) and the dried film with [S]/[In] (black). The stars, squares and circles represent ethanol, water and propylene glycol respectively. The dashed lines are a guide to the eye to ease the understanding of the description in the main text.

presence of multiple chemical environments. The thiourea peak seems to be slightly red shifted compared to the higher sulfur content. The same spectrum is found for [S]/[In]=1.

The films with [S]/[In]=2 and 1.5 shows some inhomogeneities that might give a different Raman signal. Indeed, the [S]/[In]=2 shows two different morphologies on image 5.44a: the Raman spectra (fig 5.44b) are hopefully similar showing that the chemical composition/environment is the same and that only the crystallization is different. For [S]/[In]=1.5, the different morphologies already noticed in the SEM images (fig 5.35) are also studied with Raman. Figure 5.44c shows that the signal is different from figure 5.43 which corresponds to the smooth part of the film. The flower shapes shows the double peak for the indium chloride indicating a different chemical environment: the smooth part has more different chemical environments than the flowers.

Figure 5.45 shows Raman spectra of the annealed films. The sulfur rich inks formed an In_2S_3 crystal that was already discussed in section 5.5. The [S]/[In]=1.5 shows additional peaks compared to the sulfur rich samples at 404 and 482 cm^{-1}. These peaks are even more prominent for [S]/[In]=1 and are related to the introduction of oxygen that will be further discussed in the XRD measurement.

In summary, the In-S coordination forms for all [S]/[In] ratio in the dried films. However, there are essentially two environments for [S]/[In]$\geq$2, while the number of chemical environments is higher for the [S]/[In]$\leq$1.5. Moreover, the annealed films with [S]/[In]$\leq$1.5 show two additional peaks in Raman corresponding to oxides.
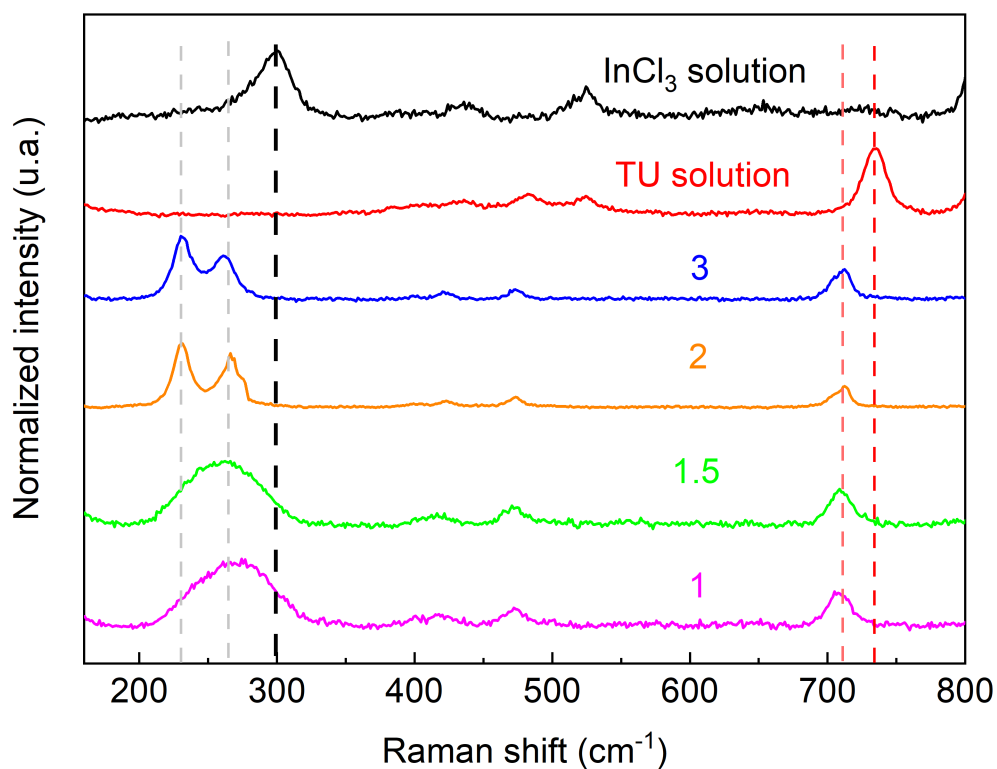
Figure 5.43: Raman spectra of dried films with [S]/[In]=3 (blue), 2 (orange), 1.5 (cyan) and 1 (pink). Solutions of In_2S_3 (black) and thiourea (red) are plotted as a comparison.
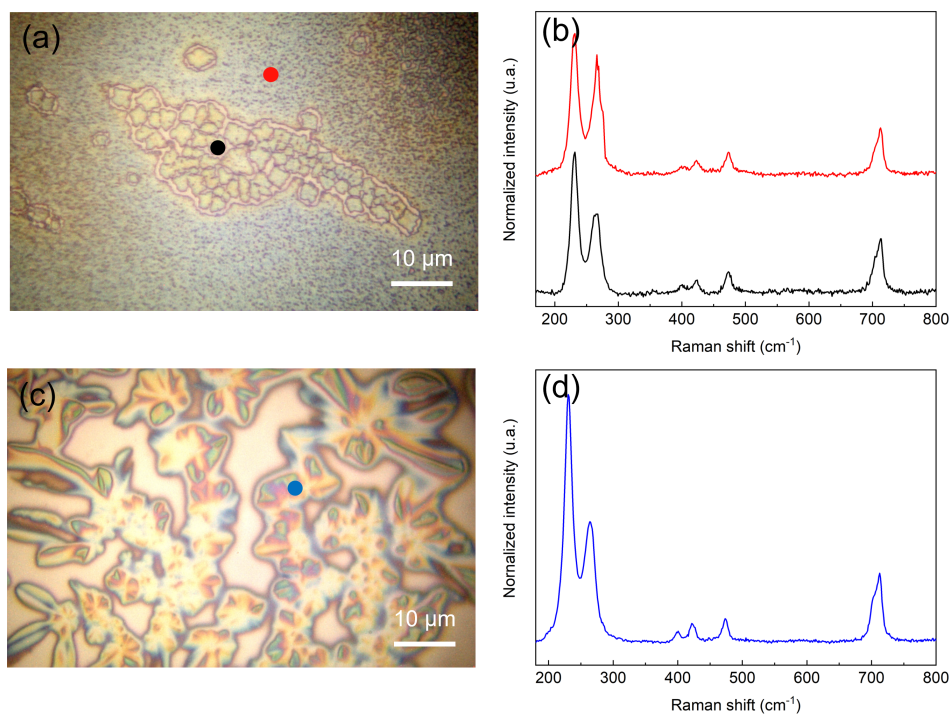
Figure 5.44: Optical images and Raman spectra of dried films with [S]/[In]=2 (a),(b) and [S]/[In]=1.5 (c), (d).
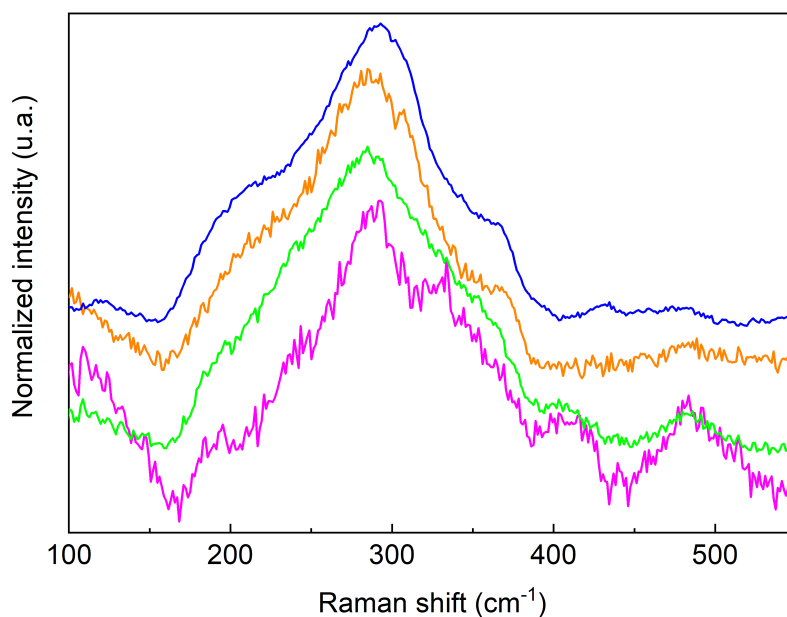
Figure 5.45: Raman spectra of $In(O,S)_x$ from inks with [S]/[In]=3 (blue), 2 (orange), 1.5 (green) and 1 (pink).

5.6.3 Crystallography

GIXRD measurements confirmed the formation of a tetragonal β-In_2S_3 for all the [S]/[In] ratios (fig 5.46). A comparison with literature shows a slight shift in the peaks position for all [S]/[In] ratios, even when the provided sulfur is in excess.
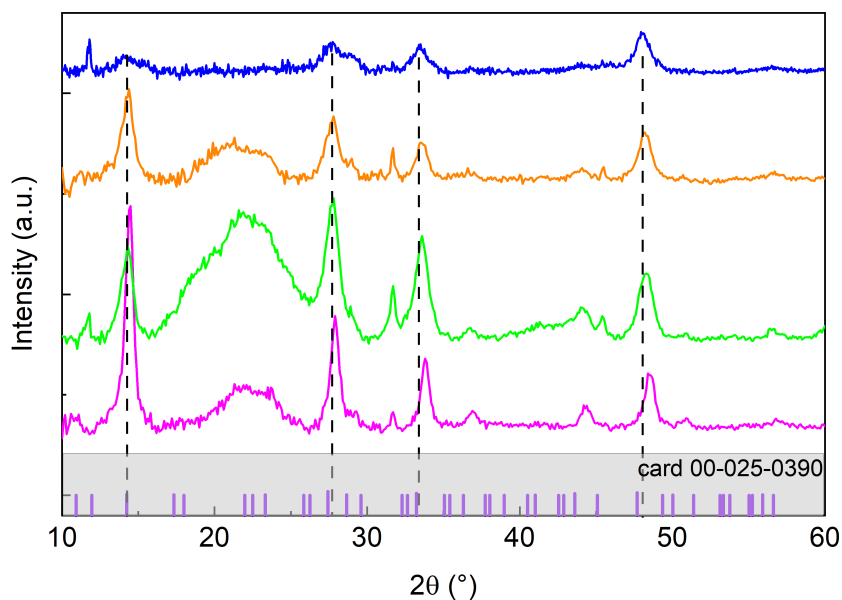
Figure 5.46: GIXRD of In_2S_3 films from inks with [S]/[In] ratios of 3 (dark blue), 2 (orange), 1.5 (green) and 1 (pink).

Using equation 5.1, the lattice constants have been calculated based on (109) and (0012) peaks respectively around 27° and 33°. Table 5.9 shows the lattice parameters for

all [S]/[In] ratios. The volume of the unit cell is found smaller for all ratios compared to the literature reference. The difference is relatively low for the sample with excess sulfur, while this difference is higher for the stoichiometric and sulfur poor samples, indicating a higher introduction of oxygen in the lattice. Kim et al. [43] deposited In_2S_x with x varying from 2.0 to 3.9 through spray pyrolysis. They found that the unit cell parameters slightly increases with the sulfur content similarly to this work.

[S]/[In]	a (Å)	c (Å)	V (Å^3)	$(V_0-V)/V_0$ (%)
3	7.583	32.157	1849	1.5
2	7.545	31.990	1822	2.9
1.5	7.483	32.009	1792	4.5
1	7.500	31.790	1788	4.7
Literature reference	7.619	32.329	1877	0

Table 5.9: Unit cell parameters of $In_x(O_y,S_{3-y})$ films obtained from inks with different [S]/[In] ratios. Literature reference is PDF4+ card 00-025-0390 of In_2S_3.

The coherence length can be calculated using the Scherrer equation (eq 3.7). Figure 5.47 shows that the crystallite size (approximated by the coherence length) decreases with an increasing sulfur content. The crystallite size is found to be smaller than literature [146] where the grain size is 15.9 nm for [S]/[In]=1.5 which is nearly the double of the grain size in this work. Otto et al. showed even bigger crystallite size for [S]/[In]=3 (52 nm) for a film deposited through chemical spray pyrolysis at 230°C. Moreover, the trend in coherence length is shown to be similar to the variation of the unit cell volume.
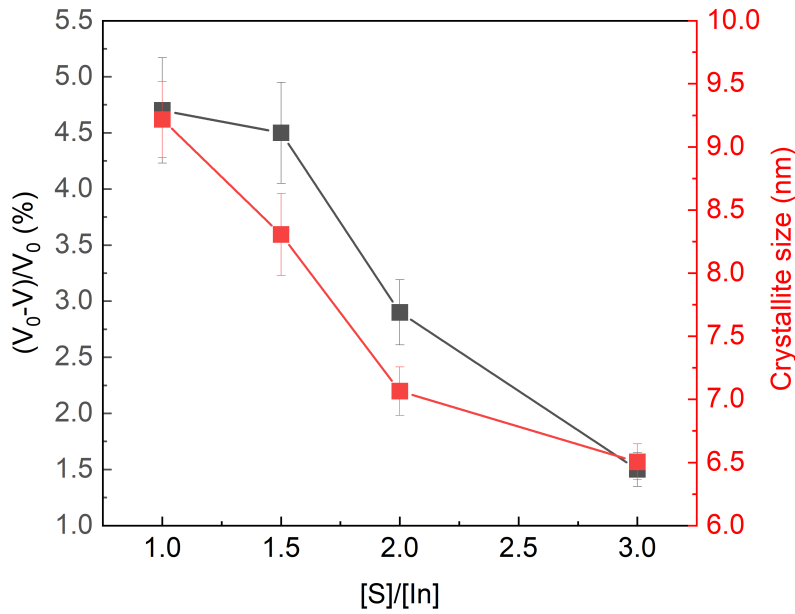
Figure 5.47: Variation of unit cell volume as percentage compared to literature (black) and crystallite size (red) of samples with [S]/[In]=3, 2, 1.5 and 1.

5.6.4 Chemical composition

The chemical composition of the In_2S_3 films deposited on Mo and annealed with varying [S]/[In] ratios was determined with XPS. Figure 5.48a shows the [S]/[In] ratios as a function of the depth of the films. The front surface (0 s of etching) has a higher ratio than the rest of the film. The composition of the surface is actually hard to determine because of the numerous contaminations from air, making the front ratio hardly reliable. The [S]/[In] ratios then seem to be constant over the thickness of the films. The ratio is identical within the error for initial [S]/[In]=3 and 2 and decreases a bit for initial [S]/[In]=1.5, while the initial [S]/[In]=1 is significantly different to the others. It can be noted that the measured [S]/[In] are different from the initial [S]/[In] and even the expected [S]/[In]. Indeed, the initial [S]/[In]=3, is expected to give [S]/[In]=1.5 in the annealed film and is actually 1.2. This can actually be explained by the preferential sputtering of sulfur in XPS. The evolution of XPS [S]/[In] with initial [S]/[In] is shown on figure 5.48d. It has a fast increase until the stoichiometric point and then slows down and start to saturate.

The oxygen content was already investigated through Raman and XRD. It was shown that [S]/[In]=1.5 and 1 contained more oxygen than [S]/[In]=3 and 2 for which the O content was nearly 0. Figure 5.48b does not show any trend in the oxygen content with the initial [S]/[In]. The analysis of the oxygen content is actually hard because the Mo signal was detected very early in the measurement and it turns out to be severely oxidized. The fitting of the In peak pointed to an In_2S_3 phase for all [S]/[In]. XPS is not the ideal technique to determine the presence of an indium oxide phase and the reader should refer to the XRD and Raman measurements.

The chlorine content is found to be deeply related to the excess of sulfur in the initial [S]/[In] and constant over the depth of the film (fig 5.48c). The sulfur rich ([S]/[In]=3, 2) inks showed a lower Cl content in the annealed films than the stoichiometric and sulfur poor ([S]/[In]=1.5, 1). The chlorine content is around 20% of the In for the sulfur poor and 10% for the sulfur rich. Figure 5.48d shows the mean chlorine content for each [S]/[In] in solution. No smooth transition between the chlorine rich and chlorine poor samples is observed contrarily to the XPS [S]/[In].

Buecheler et al. [147] tested different [S]/[In] ratios using ultrasonic spray to deposit indium sulfide. They found that the samples with excess sulfur (i.e. [S]/[In]=4, 3, 2) showed a polycrystalline structure through XRD, while the sulfur poor (i.e. [S]/[In]=1) did not show any distinct peak, contrarily to our work. They argued that the grain size in the layer was too small or the sulfur deficit prevented nucleation and thus crystallization. No other phase such as In_xO_y were detected in any of the films. XPS showed that the chlorine content was nearly doubled for the [S]/[In]=1 compared to [S]/[In]=3, analogously to this work. No other element than In, S and Cl was detected, while our
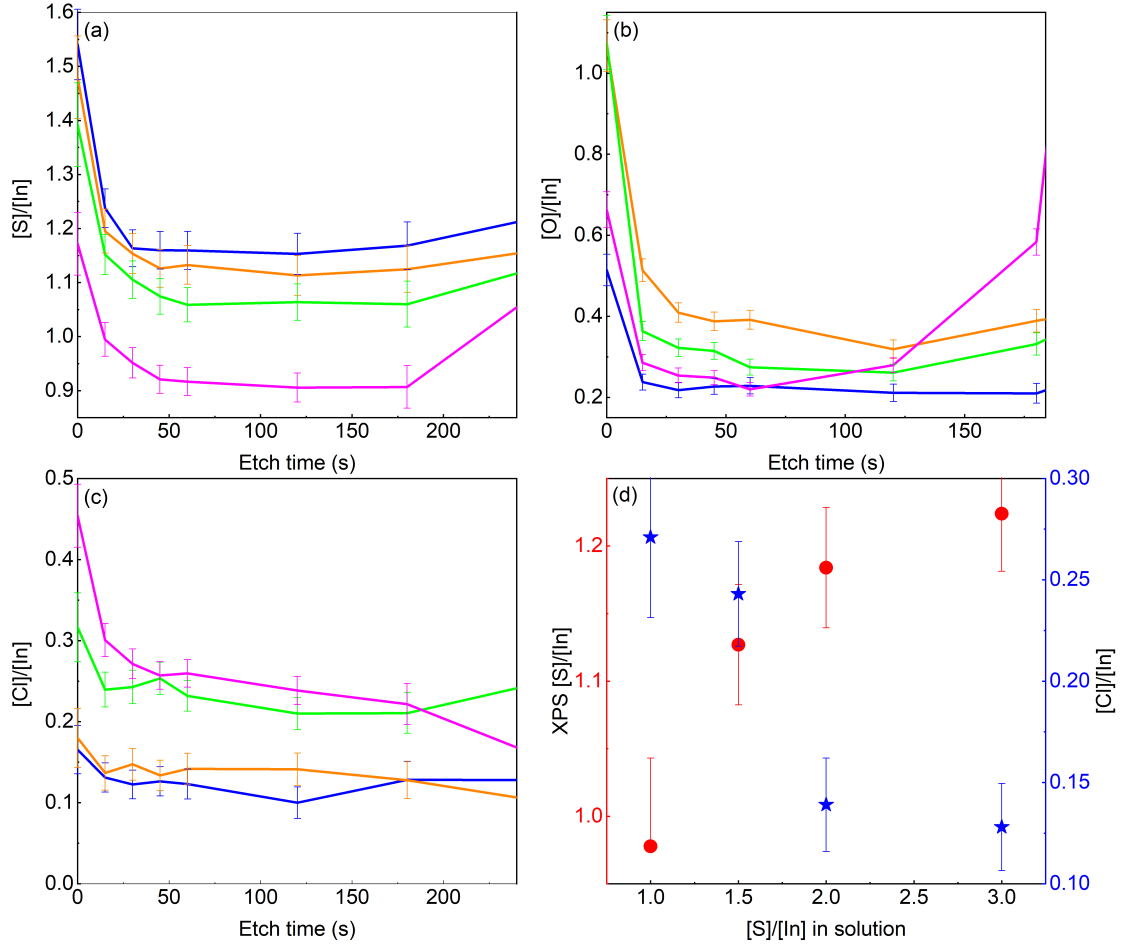
Figure 5.48: Chemical composition from XPS measurements of In$_2$S$_3$ annealed films deposited on Mo with varying initial [S]/[In] ratio: 3 (blue), 2 (orange), 1.5 (green) and 1 (pink). (a) Depth profile of [S]/[In] ratio. (b) Depth profile of normalized O content ([O]/[In]). (c)Depth profile of normalized Cl content ([Cl]/[In]). (d) Variation of mean XPS measured [S]/[In] and [Cl]/[In] with initial [S]/[In].

work also showed N but its content is similar to the detection limit of the machine and is thus not discussed.

5.6.5 Band gap

The band gap of the films were tentatively extracted using UV VIS spectroscopy. Transmittance and reflectance were measured on films deposited on a quartz substrate. The nature of the transition, i.e. direct or indirect, is still uncertain for In$_2$S$_3$ as discussed in section 2.2. Bhattacharyya et al. [148] developed a formalism to determine the nature of the transition as well as the band gap of a semiconductor based solely on the reflectance data without using a Tauc plot. This development starts from the definition of the absorption coefficient α [149]

$$\alpha = \frac{A}{h\nu}(h\nu - E_g)^m \tag{5.3}$$

where A is a constant, E_g is the band gap and m is characteristic of the transition. The value of m can be 0.5, 2, 1.5 or 3 for allowed direct, allowed indirect, forbidden direct or forbidden indirect transitions respectively. Taking the logarithm of this equation gives

$$ln\alpha = lnA - lnh\nu + mln(h\nu - E_g) \qquad (5.4)$$

Its derivative enables to find m and E_g

$$\frac{d(ln\alpha)}{d(h\nu)} = -1/h\nu + m/(h\nu - E_g) \qquad (5.5)$$

Equation 5.5 suggests that the plot of $dln\alpha$ versus $h\nu$ should show a divergence at $h\nu = E_g$. After the calculation of E_g, m can be determined from the slope of the plot of $ln(\alpha h\nu)$ versus $ln(h\nu - E_g)$. The extraction of the band gap using the divergence as suggested did not work with our data: no clear divergence was observed. However, transmittance data were used in this work. Bhattacharyya et al. showed that the determination of the band gap was less precise using transmittance data. Indeed, the plot of $ln\alpha$ as a function of $h\nu$ showed a sharp fall at the band gap for a $CuInSe_2$ based on reflectance data, while this fall was less sharper with the transmittance data.

Barreau et al. [150] met the same problem in their study of In_2S_3. They defined their band gap as the maximum of the peak found in the plot of $d(ln\alpha)/d(h\nu)$ versus $h\nu$ as an alternative. Figure 5.49a shows this plot for [S]/[In]=2 and 1. The band gap were found to be 2.64 eV and 3.08 eV for [S]/[In]=2 and 1 respectively by fitting a gaussian on the peak. Once the bang gap is determined, the plot of equation 5.5 gives m, the slope of the linear fitting (fig 5.49b). The value of m is around 0.7 which does not correspond to the possible values cited. However, as already mentioned, calculations based on transmittance are not as precise as reflectance and a coefficient of 0.7 (will be further discussed in chapter 7) can be associated with 0.5 which is the nearest value. Barreau et al. also found a direct band gap with a value of 2.7 eV. Our material is thus determined to be a direct band gap semiconductor.

As a comparison, a Tauc plot for direct band gap semiconductor was plotted and the band gap was extracted for all [S]/[In] ratio (fig 5.49c). The band gaps obtained through a linear fitting are 2.9 eV, 2.7 eV, 2.9 eV and 3.1 eV for [S]/[In]=3, 2, 1.5 and 1 respectively. The slopes are different which shows that the semiconductors formed are not identical. The band gap of the sulfur rich sample decrease with a decreasing sulfur content while it is found to increase for the stoichiometric and sulfur poor films. This latter increase can be related to the oxygen content. Indeed, the general band gap of bulk In_2O_3 is 3.7 eV so the band gap of $In_x(O,OH,S)_y$ film increases with decreasing sulfur content.

The use of Tauc plot has long been a subject of concern because of its sensibility to measurement and analysis conditions such as the fitting range. Indeed, the choice of the
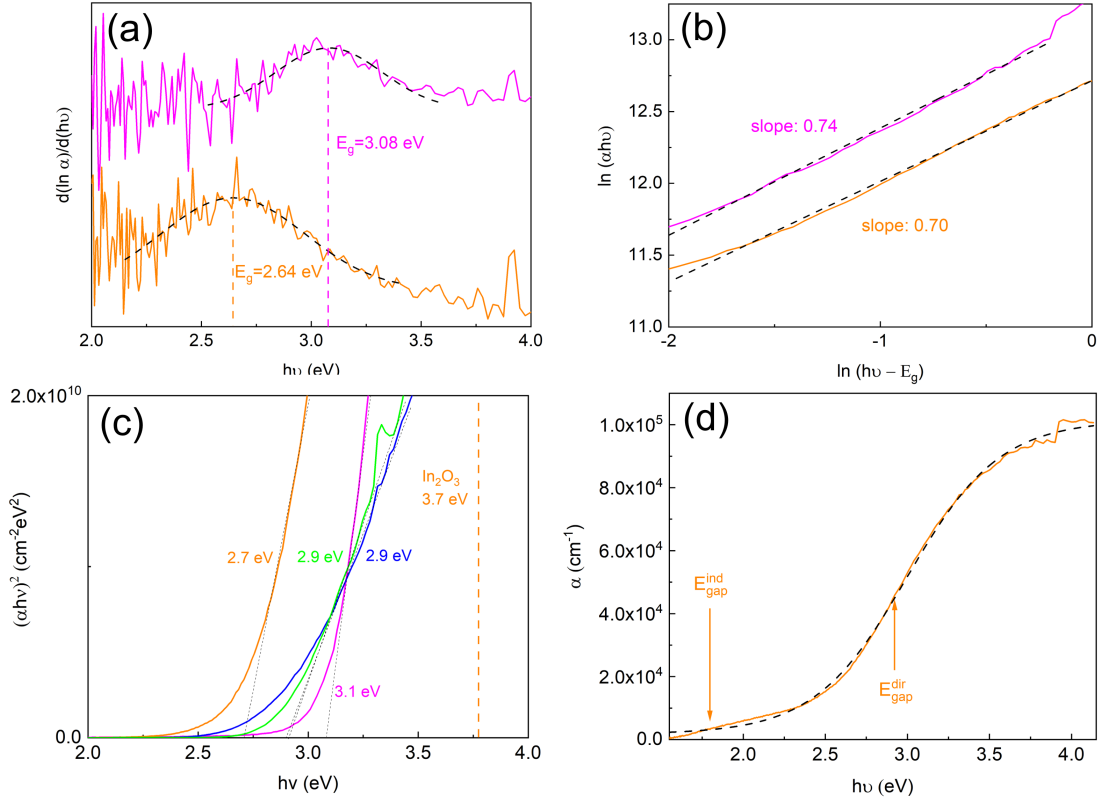
Figure 5.49: (a) Plot of $\frac{d(ln\alpha)}{d(h\nu)} = f(h\nu)$ of the film with [S]/[In]=2 (orange) and 1 (pink). (b) Plot of $ln(\alpha h\nu)$ versus $ln(h\nu - E_g)$. (c) Tauc plot for direct band gap semiconductor for [S]/[In]=3 (blue), 2 (orange), 1.5 (green) and 1 (pink). (d) Absorption coefficient of In_2S_3 film with [S]/[In]=2 (orange) using reflectance and transmittance data. Boltzmann fit of $\alpha(E)$ (dashed line). The direct and indirect band gap calculated from the Boltzmann fit are indicated with arrows.

fitting range was found to seriously influence the extracted band gap. Zanatta developed a new analysis to extract the band gap from reflectance and transmittance data and to minimize the error [151]. The absorption coefficient is fitted with a Boltzmann curve with the following expression

$$\alpha(E) = \alpha_{max} + \frac{\alpha_{min} - \alpha_{max}}{1 + exp[\frac{E-E_0^{Boltz}}{\delta E}]} \tag{5.6}$$

with α_{min}, α_{max} are the minimum and the maximum of the absorption coefficient, E_0^{Boltz} is the energy at which the absorption coefficient is halfway between α_{min} and α_{max} and δE is related to the slope of the curve. The band gap is then given by the following formula

$$E_{gap}^{Boltz} = E_0^{Boltz} - n_{dir-ind}^{Boltz}\delta E \tag{5.7}$$

where $n_{dir}^{Boltz} \sim 0.3$ and $n_{ind}^{Boltz} \sim 4.3$. It was argued that a good R^2 was not necessarily a synonym of a good fit and that its quality should be assessed by the error on each of the

aforementioned parameters and it should be checked that the fit mostly follows the data curve. Zanatta showed that using a Boltzmann fitting enables to use any expression of the absorption coefficient without impacting the value of the band gap. Figure 5.49d shows the Boltzmann fit for [S]/[In]=2. The fit follows the data quite well and the error on the parameters are reasonable (table 5.10). The direct and indirect band gaps extracted with the Boltzmann method for all [S]/[In] ratios are reported in the latter table. The direct band gap is around 3 eV for [S]/[In]=3, 2 and 1.5, and is higher for [S]/[In]=1, i.e. 3.49 eV. Since In_2S_3 can also be considered indirect, these band gaps are also reported. It is found to steadily increase from 1.9 eV to 2.4 eV with decreasing sulfur content. The direct band gap values are higher than the reported ones from the Tauc plot. However, the Boltzmann approach is more trustworthy for several reasons: as already mentioned, any expression can be used to calculate the absorption coefficient, the fitting does not require to choose a fitting range and is not sensitive to measurement problems or inappropriate spectrum correction [151]. Indeed, it was shown that an upward or downward shift by 10% or a compression or stretching of the data by 10% did not lead to a change in the band gap.

[S]/[In]	3	2	1.5	1
$\alpha_{min}(cm^{-1})$	488 ± 94	1767 ± 148	1492 ± 58	2327 ± 220
$\alpha_{max}(cm^{-1})$	54472 ± 279	101407 ± 369	47269 ± 144	159681 ± 2284
E_0^{Boltz} (eV)	3.077 ± 0.004	2.998 ± 0.003	3.034 ± 0.002	3.571 ± 0.001
δE (eV)	0.279 ± 0.004	0.281 ± 0.003	0.172 ± 0.002	0.266 ± 0.005
$E_{gap,dir}^{Boltz}$ (eV)	2.99 ± 0.01	2.91 ± 0.01	2.97 ± 0.01	3.49 ± 0.01
$E_{gap,ind}^{Boltz}$ (eV)	1.87 ± 0.02	1.79 ± 0.02	2.29 ± 0.03	2.42 ± 0.02

Table 5.10: Boltzmann fit parameters of $\alpha(E)$ and extracted direct and indirect band gap for [S]/[In]=3, 2, 1.5 and 1 .

Another issue that has not been discussed yet is the porosity of the film. Indeed, some of the films were shown to be porous which probably influences the reflectance, transmittance and thickness of the film. The reflectance and transmittance are obviously distorted by the fact that light is not reflected by the pores and is more transmitted by the latters. We can thus expect a lower reflection and a higher transmission of the light in a porous material. Moreover, the thickness is hard to determine given that the film is not smooth, nor dense. The uncertainties in all these parameters make the absorption coefficient pretty unreliable and a new model would be required but out of the scope of this thesis. As a default choice, the Tauc plot and the absorption coefficient are still used but all the values should be interpreted with care.

In summary, the direct band gap of In_2S_3 is found to be pretty stable for [S]/[In]=3, 2 and 1.5 with a value around 2.9 eV, while it is significantly higher for [S]/[In]=1 with a value of 3.5 eV. An indirect band gap was also reported and its value lies between 1.8 and 2.4 eV for the different ratios.

5.6.6 Devices performance

JV results of devices with an In_2S_3 buffer from inks containing a [S]/[In] ratio of 3, 2, 1.5 and 1, as well as a reference cell with an industrial Zn(O,S) buffer are shown on figure 5.50. The efficiency of the devices with a sulfur rich ink, i.e. [S]/[In]=3 and 2, is similar to the reference device. The V_{oc}, J_{sc} and FF are all similar to the reference cell. The [S]/[In]=2 has higher V_{oc}, FF and similar J_{sc} than [S]/[In]=3. The performance of the best cells are reported in table 5.11. The [S]/[In]=2 outperforms the Zn(O,S) reference in efficiency (0.5%) thanks to a higher V_{oc} (improvement of nearly 30 mV) and similar FF and J_{sc}. The increased V_{oc} might be related to a better band alignment. The quasi Fermi level splitting was measured before and after the deposition of the buffer. It decreased by around 10 meV after the deposition process and annealing, which is inside the error of the qFLs extraction and does not necessarily prove that the absorber was degraded. The qFLs are equal to the best performing cells for both [S]/[In]=3 and 2. This means that no band alignment issue that would produce serious recombination at the pn junction are present in these samples. The thickness of the buffer with [S]/[In]=2 was varied and showed that the thickness used in the above mentioned result was not optimized. A thicker buffer gave similar efficiency but with a tighter distribution which is desirable. A thinner film on the other hand was shown to be detrimental for the cell. The details are shown in appendix B.

[S]/[In]	Efficiency (%)	V_{oc} (mV)	FF (%)	J_{sc} (mAcm^{-2})
3	15.6	631	67	36.8
2	16.5	651	69	37.0
1.5	4.2	664	27	23.3
1	0.4	627	28	2.5
Zn(O,S)	16.0	624	69	37.1

Table 5.11: Record cells performances for [S]/[In] ratio of 3, 2, 1.5 and 1 based In_2S_3 buffered solar cells and the reference with Avancis Zn(O,S).

The stoichiometric ratio [S]/[In]=1.5 and sulfur poor [S]/[In]=1 buffered devices show very low JV parameters (fig 5.50). The efficiency are respectively 4.2% and 0.4% for the record devices. The V_{oc} of [S]/[In]=1.5 is higher than the qFLs which is impossible and might actually be related to an error introduced when using an approximation. Indeed, the determination of the qFLS uses the generalized Planck law where the absorbance is hypothesized to be 1. However, when this assumption is wrong, i.e. when the absorption is not 100%, the qFLs is underestimated. Apart from this anomaly, the V_{oc} is still similar to the qFLs and to [S]/[In]≥2 and Zn(O,S) reference cells. The [S]/[In]=1 shows a very large spreading of the data (over more than 200 mV) and the qFLs is slightly higher than the best V_{oc}. This distribution is hard to explain because no macro-morphology difference is observed on the solar cell. The FF factor is low for both [S]/[In]=1.5 and 1
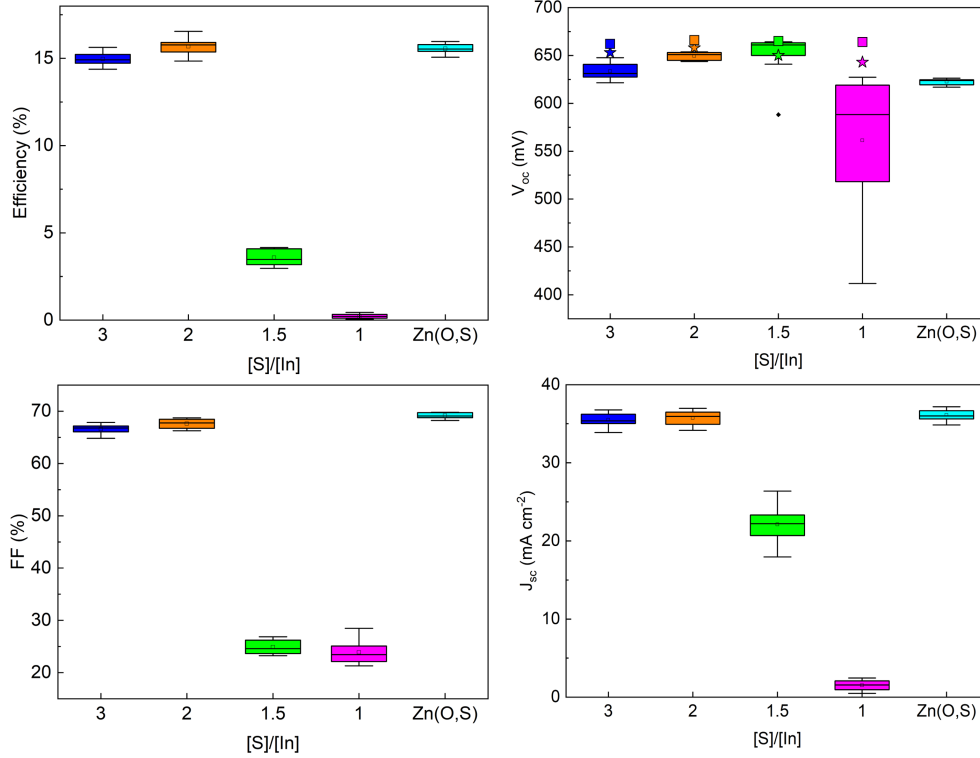
Figure 5.50: Optoelectronic properties of 8 cells with an In_2S_3 buffer from inks containing a [S]/[In] ratio of 3, 2, 1.5 and 1, as well as a reference cell with an industrial Zn(O,S) buffer. The squares and stars on the V_{oc} graph represents the qFLs before and after the buffer deposition.

ratios.

Interestingly, the shunt resistance extracted from the dark curve shows similar values for all ratios (appendix B figB.7). However, a good fitting of the diode model for [S]/[In]=1.5 and 1 was not possible in the illuminated conditions. Indeed, the JV curves have unconventional shapes for [S]/[In]=1.5 and [S]/[In]=1 (fig 5.51) which are very different from the typical curve obtained for [S]/[In]=3 and 2 and the Zn(O,S). The J_{sc} of [S]/[In]=1.5 is more than 10 mAcm^{-2} lower than the sulfur rich cells in average. The J_{sc} of [S]/[In]=1 is nearly 0 mAcm^{-2}.

Figure 5.52 shows the EQE of the best devices. The Zn based buffered sample shows a shoulder at short wavelengths indicating a parasitic absorption but shows good collection at longer wavelengths (above 90%). Oscillations are typical effect of light interference in the layers stack. The J_{sc} extracted from the EQE is 37.0 mAcm^{-2} which corresponds to the J_{sc} measured through JV. The [S]/[In]=3 does not show pronounced oscillation confirming the roughness and high thickness that damp the interference effect. The parasitic absorption at short wavelengths is less pronounced and is related to the AZO layer. As discussed in section 5.5, the band gap of the absorber is slightly different to the reference which explains the lower collection around 1200 nm. The [S]/[In]=2 shows
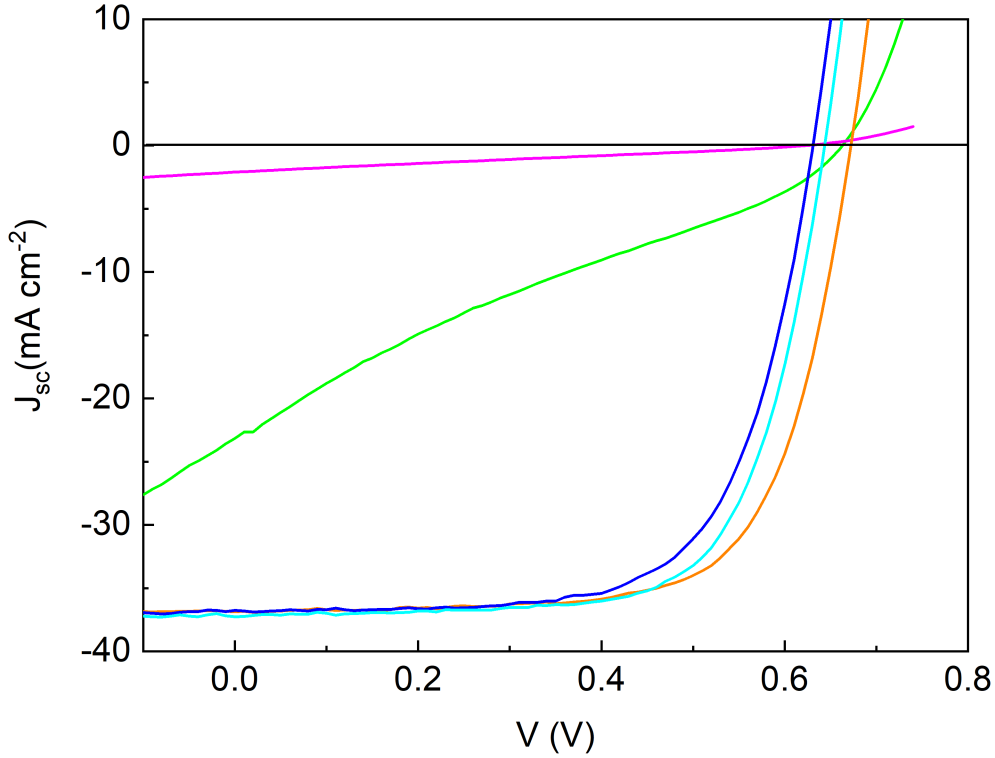
Figure 5.51: JV characteristics of CIGSSe devices with In_2S_3 buffer with [S]/[In]=3 (blue), 2 (orange), 1.5 (green) and 1 (pink) and with a industrial Zn(O,S) buffer (cyan).

oscillations which confirms the dense and smooth morphology of the buffer on CIGSSe shown in SEM. The collection at intermediate wavelengths (visible range) is as high as the reference cell and is 7% lower from 700 nm to 1100 nm indicating a lack of collection at the back which might be explained by a smaller depletion region due, for example, to a lower doping of the buffer compared to the reference cell.

The collection is reduced at all wavelengths for [S]/[In]=1.5 compared to the reference cell. The extracted J_{sc} is 31.9 mAcm^{-2} which is much higher than the IV measured J_{sc} (23.3 mAcm^{-2}). This means that there is a barrier for the photocurrent. Indeed, the small current generated from EQE can easily pass this barrier while the high current under the AM 1.5 illumination (JV) is blocked [5]. The EQE of [S]/[In]=1 clearly shows that the pn junction is defective.

Two hypothesis were contemplated to explain the low efficiency of the cell with [S]/[In]=1. The first one is an insufficient thickness of the buffer even though the shunt resistance is quite high: the calculated thickness for DS 40 μm is 42 nm for pure In_2S_3. When the drop spacing is decreased to 30 μm, the calculated thickness is 75 nm. Figure 5.53 shows the performance of the solar cells. The efficiency did not significantly improve with a thicker buffer. The V_{oc} and FF even decreased, while the J_{sc} slightly increased but the data distribution is very wide.

EQE (fig 5.54) of two different cells on the same device shows two very different
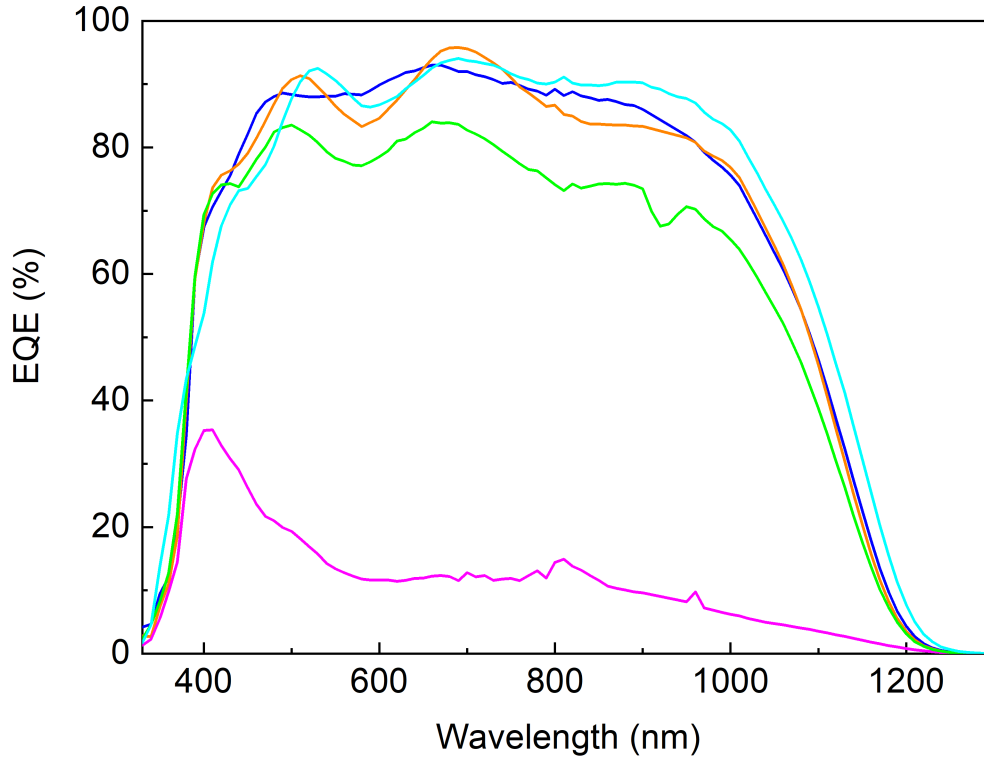
Figure 5.52: EQE of best devices with an In_2S_3 buffer from inks containing a [S]/[In] ratio of 3 (dark blue), 2 (orange), 1.5 (green) and 1 (pink), as well as a reference cell with an industrial Zn(O,S) buffer (cyan). The drop around 900 nm in the green curve is a measurement artefact.

behaviours for the DS 30: the best performing cells for this thicker buffer gave a decent EQE, while the worst cell showed a similar behaviour to the thinner buffer layer (DS 40) and the pn junction looks defective. Figure 5.55 shows an optical image of the cell. Two zones with different colours can be observed. The upper cells are pink while the other cells are greenish. This difference was not observable on the bare absorber, nor directly after the printing of the buffer. However, after the drying and annealing steps, these differences appeared. It has obviously effects on the quality of the pn junction even though its nature can not be explained. Nevertheless, the general behaviour is the defective pn junction and the outliers are actually the best performing cells. The J_{sc} extracted from these two regions are 33.6 mAcm^{-2} and 11.6 mAcm^{-2} for the best and worst performing cells.

The second hypothesis explaining the low efficiency is the detrimental effect of the introduction of oxygen in the buffer layer during annealing. The efficiency (fig 5.53) dramatically increases when the sample is annealed in nitrogen, increasing from around 1% efficiency to 12%. The distribution of V_{oc} is tight and slightly higher than the cells annealed in air. The measured qFLs is lower than the measured voltage which is physically impossible and has already been discussed previously. The FF is doubled but the distribution is wider than the air samples. The J_{sc} is significantly increased and has a
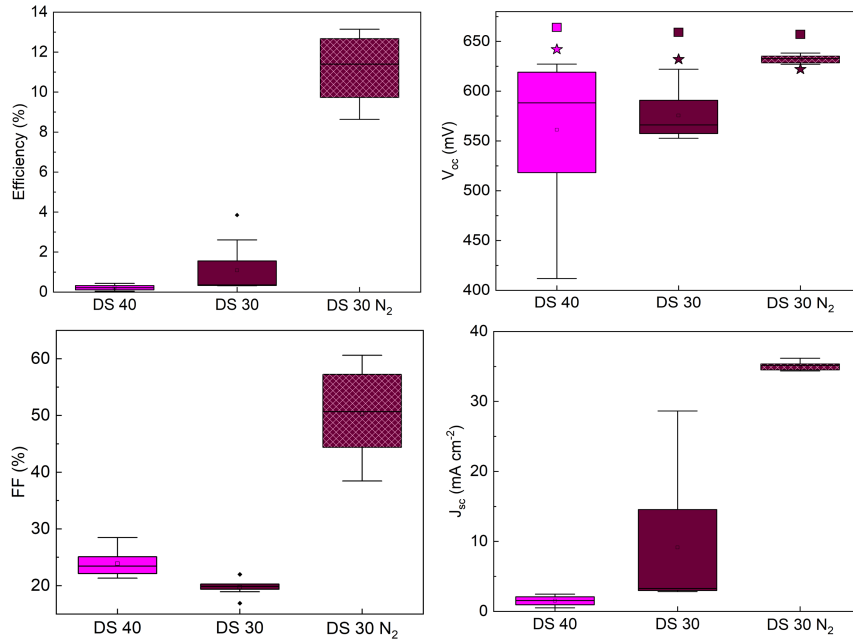
Figure 5.53: Optoelectronic properties of 8 cells with varying $In(O,OH,S)_x$ buffer thickness from inks containing a [S]/[In]=1. A sample annealed in nitrogen is also plotted. When not mentioned, the annealing medium is air. The star squares and stars on the V_{oc} graph represent the qFLs before and after the buffer deposition.
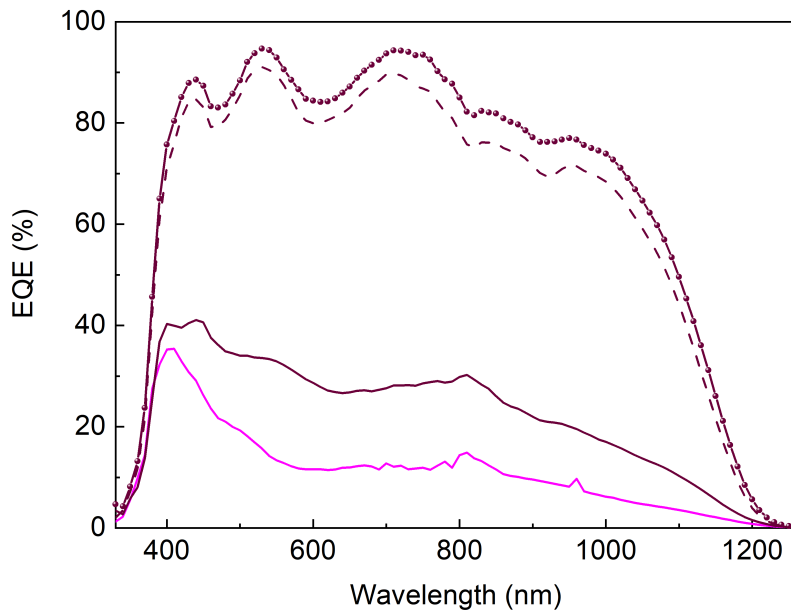

Figure 5.54: EQE of best devices with an In_2S_3 buffer from inks with [S]/[In]=1 with different drop spacing and annealing medium (air=solid line, nitrogen=line+symbols). DS 30 best performing cell (dashed dark pink), DS 30 worst performing cell (solid dark pink), DS 30 annealed in nitrogen (symbol dark pink) and DS 40 (light pink).

value similar to [S]/[In]=3 and 2. The EQE (fig 5.54) shows a lack of collection at the long wavelengths which has been discussed previously. Oscillations related to interference
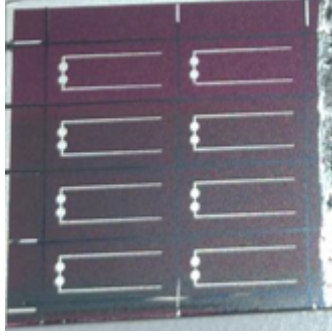
Figure 5.55: Optical image of the device with an In_2S_3 buffer with [S]/[In]=1 and DS 30.

are present meaning that the buffer is probably thin and smooth. The blue defect is also absent for this [S]/[In] ratio. Interestingly, the curve is similar to the best performing cells (outliers) for the air annealed sample. However, the low efficiency of the air annealed device can not be attributed to the O content. Indeed, XPS measurements (not shown) did not point to any significant difference in the composition of the films annealed in air and in nitrogen. The reason behind the improvement of the efficiency of the nitrogen annealed sample is still unknown.

It can be concluded that an excess of sulfur in the ink is essential if the buffer is annealed in air. The improvement in efficiency when annealing [S]/[In]=1 in nitrogen seems to be promising for [S]/[In]=1.5 if the low efficiency is also related to the annealing in air. The data can be found in appendix B. The annealing in nitrogen showed an improvement of around 1 % in efficiency and was thus not successful. The bad performance of this device is not understood yet.

A similar work has been performed by Wang et al. [47]. The ink consisted in a mixture of ethanol and ethylene glycol and indium nitrate and thiourea salts. Inks with [S]/[In]=3, 2, 1 were spin coated and the films were dried at 150°C in air for 1 min and then annealed in a furnace at 225°C for 10 minutes in 5% H_2S containing Ar atmosphere. The highest efficiency was obtained with [S]/[In]=2, even outperforming the reference device with a CdS buffer layer (12.8% against 12.5%). Similarly to this work, this ratio outperformed the other ratios and the [S]/[In]=1 was the worst device (10.4%). The V_{oc} and the FF are the highest for [S]/[In]=2 and the lowest for [S]/[In]=1 similarly to this work (using the device results for the nitrogen annealed [S]/[In]=1). A slightly decreasing J_{sc} with increasing [S]/[In] ratio is found in their work while the current is highly dependent on the [S]/[In] ratio in our work. The SEM cross section images showed a rough buffer layer but the morphology was not commented regarding a potential porosity of the layer and a direct link between the results of their and our works is difficult to make.

5.7 Temperature

The annealing temperature used in all the previous studies was 250°C. In order to optimize the annealing temperature, the CIGSSe and buffer (from the ink [S]/[In]=3) stack was annealed at 280°C and 310°C. The analysis of the chemical composition did not shown pronounced difference between the annealing temperatures. Figure 5.56 shows the XPS data for the buffer deposited on CIGSSe and annealed at 250°C and 310°C only. The residues content is very similar for both samples. Most of them are removed after the first sputtering cycle meaning that they are essentially contamination from the atmosphere. The temperature does not seem to have a significant influence on the impurities content. The [S]/[In] content is found to be around 1.5 in the region determined as the buffer layer. Within the error, no difference is found in the buffer layer region between the two temperatures. A difference is observed in the absorber region which might be due to a different absorber initial composition or to the preferential sputtering of sulfur. The [Cu]/[In] trend is similar for both annealing temperatures within the error. As discussed in section 5.4, the progressive increasing [Cu]/[In] ratio is due to Cu diffusion and to porosity of the buffer.
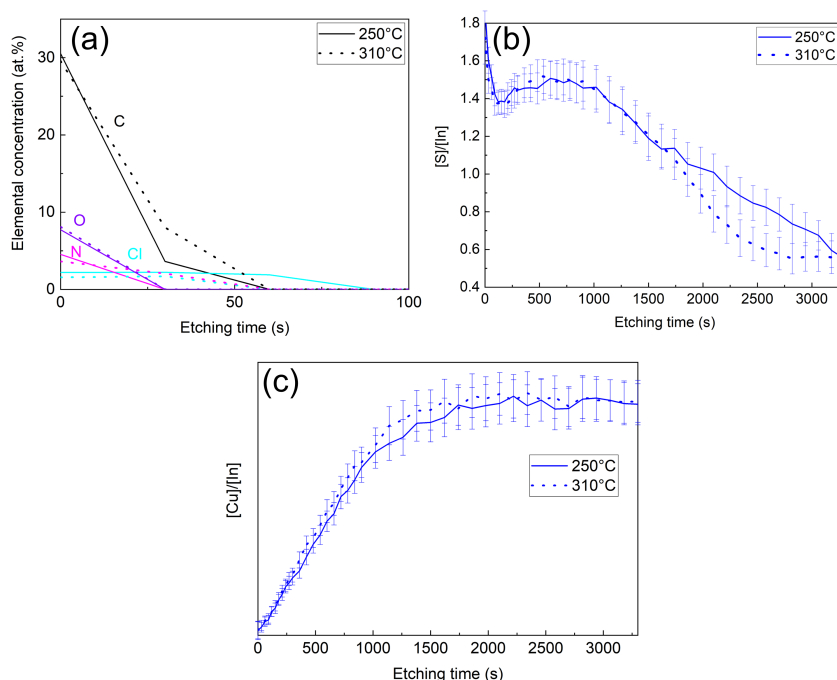
Figure 5.56: Chemical composition from XPS of In$_2$S$_3$ films annealed at 250°C and 310°C. (a) Residues content (C, Cl, N and O), (b) [S]/[In] and (c) [Cu]/[In].

Figure 5.57 and table 5.9 show the crystallographic data of the film annealed at different temperatures. The (2212) peak position does not change much with temperature. The peaks width decreases with temperature implying an increase in the coherence length, i.e. in the crystallite size. The unit cells parameters decrease with temperature and the

unit cell volume of the 280°C film is nearly identical to the literature value. This volume decrease with an increased annealing temperature could be due to the introduction of oxygen in the lattice.
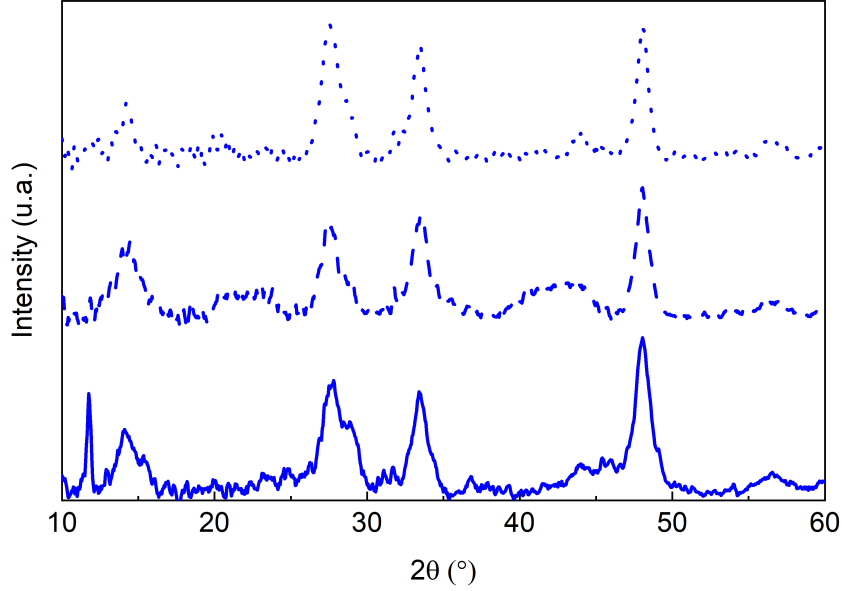

Figure 5.57: GIXRD spectrum of In_2S_3 annealed at 250°C (solid line), 280°C (dashed line) and 310°C (dot line).

	Coherence length (nm)	a (Å)	c (Å)	V (Å^3)	$(\frac{V_0 - V}{V_0})$ (%)
250°C	6.50 ± 0.14	7.69	32.150	1899	-1.1
280°C	7.27 ± 0.13	7.63	32.09	1868	0.5
310°C	7.93 ± 0.17	7.46	42.14	1788	4.7
Literature reference	N/A	7.619	32.329	1877	0

Table 5.12: Unit cell parameters of In_2S_3 films annealed at 250°C, 280°C and 310°C. Literature reference is PDF4+ card 00-025-0390 of In_2S_3.

The performance of the cells annealed at different temperatures are reported in figure 5.58. As soon as the temperature is increased, the efficiency decreases. It is unrelated to the V_{oc} that shows a relatively constant average value over the different annealing conditions. The voltage loss is even the most pronounced for the 250°C sample rather than for the 310°C. The FF decreases with temperature (T). The series resistance (not shown) is low and similar for all T (0.6 Ωcm^2), while the shunt resistance measured in the dark (not shown) is high and similar for all T (4000 Ωcm^2). However, the shunt resistance measured on the illuminated devices (not shown) decreases with the annealing temperature, meaning that the shunt paths are activated by illumination which can explain the decreasing FF. The J_{sc} varies slightly between the different conditions but shows the same data distribution.
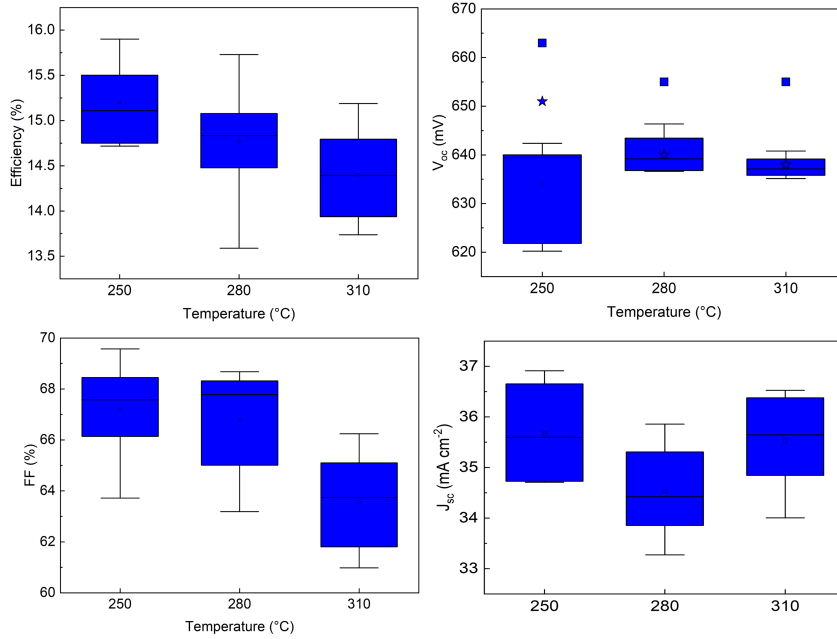
Figure 5.58: Optoelectronic properties of 8 cells with In_2S_3 buffer from the ink containing a [S]/[In]=3 annealed in air at 250°C, 280°C and 310°C. The star squares and stars on the V_{oc} graph represent the qFLs before and after the buffer deposition.

Figure 5.59 shows that the collection at all wavelengths decreases with an increasing annealing temperature. The J_{sc} are 36.3, 35.7 and 35.1 mA/cm^2 for 250°C, 280°C and 310°C respectively. This is different from the best devices J_{sc} measured in JV probably because of an error on the measurement of cells areas. The trend given by EQE confirms the one in efficiency. The ideal annealing temperature is thus 250°C.

5.8 Is the UV ozone treatment necessary?

The use of UV ozone has been extensively explained in chapter 4 and in section 5.3. In order to have a continuous film, UV ozone was applied to the substrate to increase the wetting and this was associated to a low contact angle of the liquid on the substrate and an increased spreading of the ink. Another way to ensure the full coverage of the CIGSSe by the buffer layer without ozone treatment is the decrease of the concentration of the ink and of the drop spacing. Indeed, since on prisitine absorber, the spreading of the drop is small, the drop spacing has to be decreased to ensure the overlaping of the drops. However, to keep a reasonable thickness for the buffer, the ink concentration should be decreased.

The concentration of the ink was divided by four and the DS was set to 20 µm, i.e. half of the usual DS. Figure 5.60 shows profilometer maps of inkjet printed drops and lines on UV ozone treated and non treated molybdenum substrates. The treated substrate decreases the contact angle of the liquid and a coffee ring is found for the drop
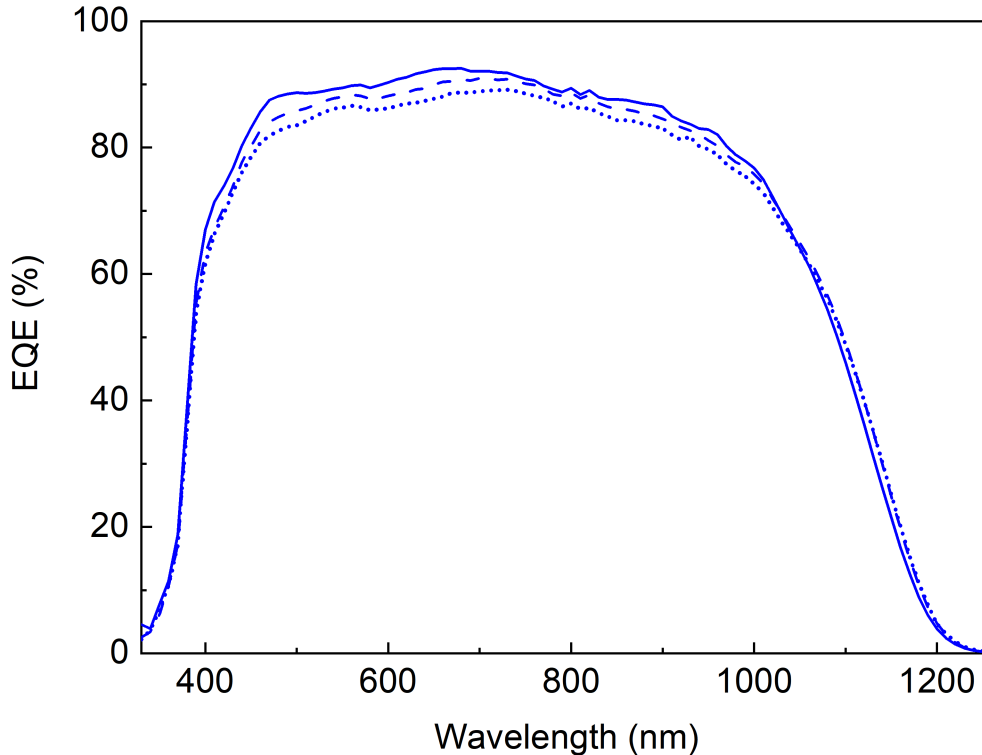
Figure 5.59: EQE of best devices with an In_2S_3 buffer from ink with [S]/[In]=3 annealed at different temperatures: 250°C (solid line), 280°C (dashed line) and 310°C (dot line).

(fig 5.60a) and a double ridged line (fig 5.60b). For the same ink concentration on a non-treated substrate, the drop did not show any coffee ring effect (fig 5.60c, d). The material is concentrated in the middle of the feature and the edges have a low thickness. Hertaeg et al. [152] showed that a low contact angle tends to promote the coffee ring effect. Simulations and experiments showed that the formation of the coffee ring depends on both the initial volume fraction of particles in the droplet and its contact angle. The simulations showed that a volume fraction of polystyrene particles lower than 0.15 led to a coffee ring effect independently of the contact angle (up to 25°). From an initial volume fraction of 0.3 onward, no coffee ring effect was found. In between, these conditions, for a fixed volume fraction, a higher contact angle would cancel the coffee ring effect whilst a low contact angle would promote it. Experimental data did not fully agree with the simulations in terms of volume fraction threshold. However, the transition from a coffee ring to the absence of it by tuning the contact angle was confirmed.

Figure 5.61 shows the micro-morphology of the annealed In_2S_3 films for a low and high contact angle. The low contact angle based film shows the typical morphology seen in this work for [S]/[In]=3. When the contact angle is increased, the morphology looks denser but still contains holes. This morphology looks more adapted to be used as a buffer layer. This change in morphology can be explained by the solid state dewetting addressed earlier (section 5.6.1). The dewetting is controlled by the Young equation (eq
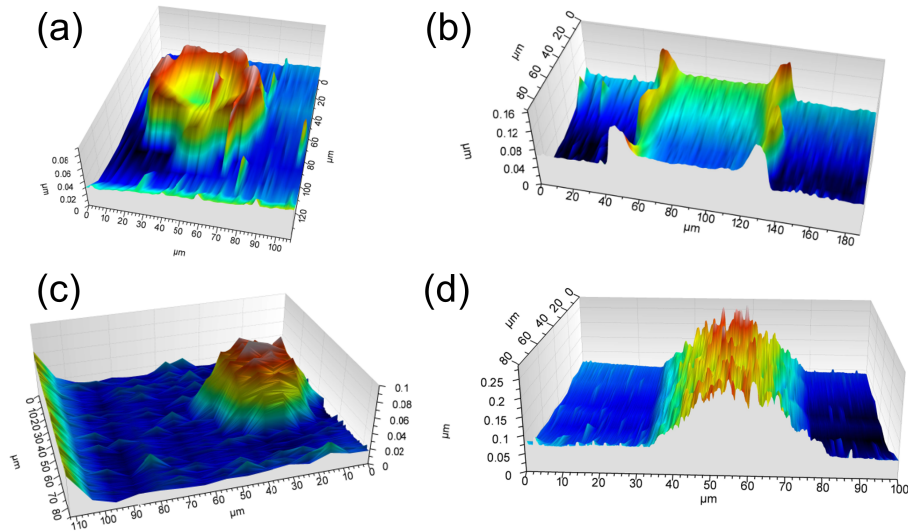
Figure 5.60: Profilometer maps of annealed inkjet printed features on Mo with a low contact angle (a) drop (b) line and with a high contact angle (c) drop (d) line.

5.2). When no UV ozone is applied, the surface energy of the Mo (γ_s) is lower than with the treatment. However, the condition for a stable film is $\gamma_s > \gamma_i + \gamma_f$. The higher the surface free energy of the substrate, the less likely the dewetting. If γ_s decreases, the dewetting is thus more likely. Nevertheless, γ_i is also modified by the UV ozone treatment. Since the dewetting decreased when the UV ozone was not applied, it means that both γ_s and γ_i changed favorably.
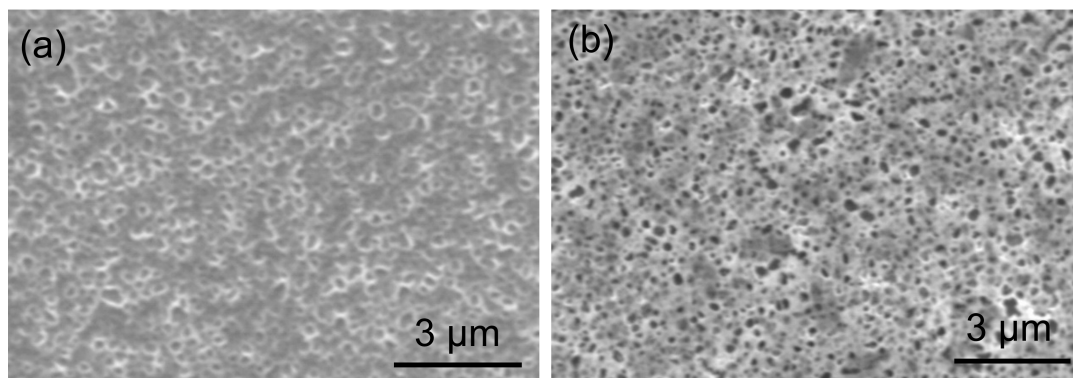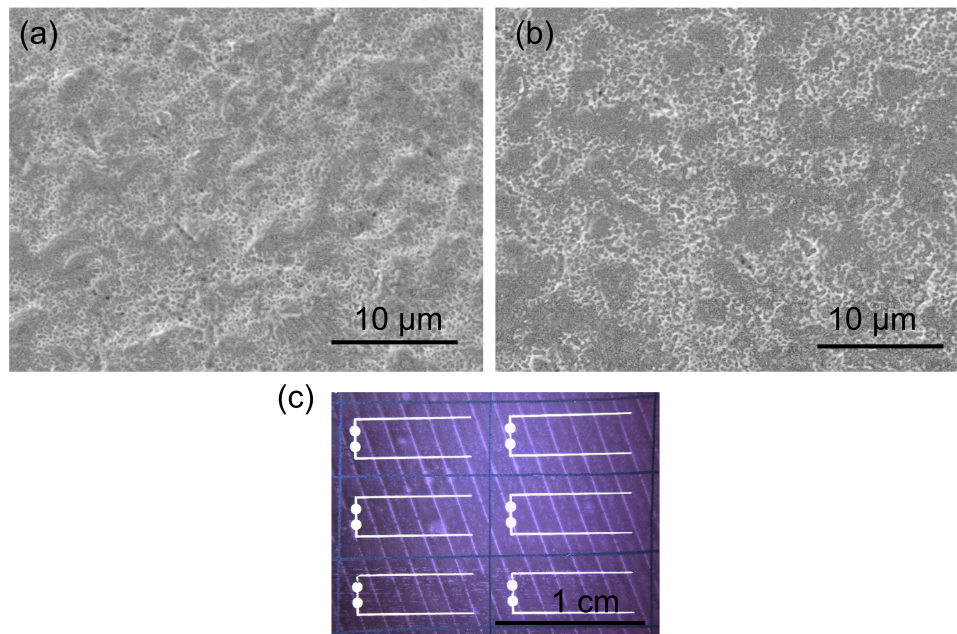

Figure 5.61: SEM images of In$_2$S$_3$ from the ink with [S]/[In]=3 inkjet printed on Mo with (a) 5 min UV ozone treatment and (b) without treatment.

Figure 5.62 shows that the buffer's morphology on both treated and non treated CIGSSe is porous and the size of the pores are bigger without ozone so no improvement in the morphology is obtained. The biggest disadvantage encountered without UV ozone treatment is the macroscopic morphology of the solar cell. Indeed, the UV ozone treatment makes the surface more hydrophilic and enables to overcome perturbation that

would create holes in the film. When the surface is not treated any kind of disturbance might produce defects in the film. Figure 5.62c shows an optical image of a complete cell without UV ozone treatment. Oblique stripes are present on the surface and are free from buffer material which means that shunt paths might be present or that sputtering damage can occur during iZO deposition. These stripes originate from the packaging of the wafers: plastic bags with stripes features that were touching the absorber layers. Smaller defects that can not be observed on this image were also present in the buffer.

Figure 5.62: SEM images of In_2S_3 from the ink with [S]/[In]=3 inkjet printed on CIGSSe with (a) 5 min UV ozone treatment and (b) without treatment. (c) image of a complete cell without UV ozone treatment on the CIGSSe prior to inkjet printing.

Figure 5.63 shows the performance of the devices with and without UV ozone treatment. The efficiency of the non treated cell is lower by around 2%. This loss is related to a loss in the V_{oc} and in J_{sc}. The qFLs of the non treated cell before the deposition of the windows was similar to the treated cell. Since the same material is formed, no band alignment issue can be mentioned here. The only reasonable explanation is the damages made on the CIGSSe during the sputtering of the window layer as discussed in section 5.3.

Figure 5.64 shows that the loss in J_{sc} is due to a lack of collection at all wavelengths which might be related to losses at the interface due to recombinations following the damage of CIGSSe surface. A parasitic absorption is more pronounced for the non treated sample. This can be interpreted as a thicker buffer in some regions due to the liquid dewetting in other regions that increase the parasitic absorption. Oscillations related to interference are not present meaning that the samples are either rough or thick. The FF is very similar with a wider spread of the data for the non treated sample confirming
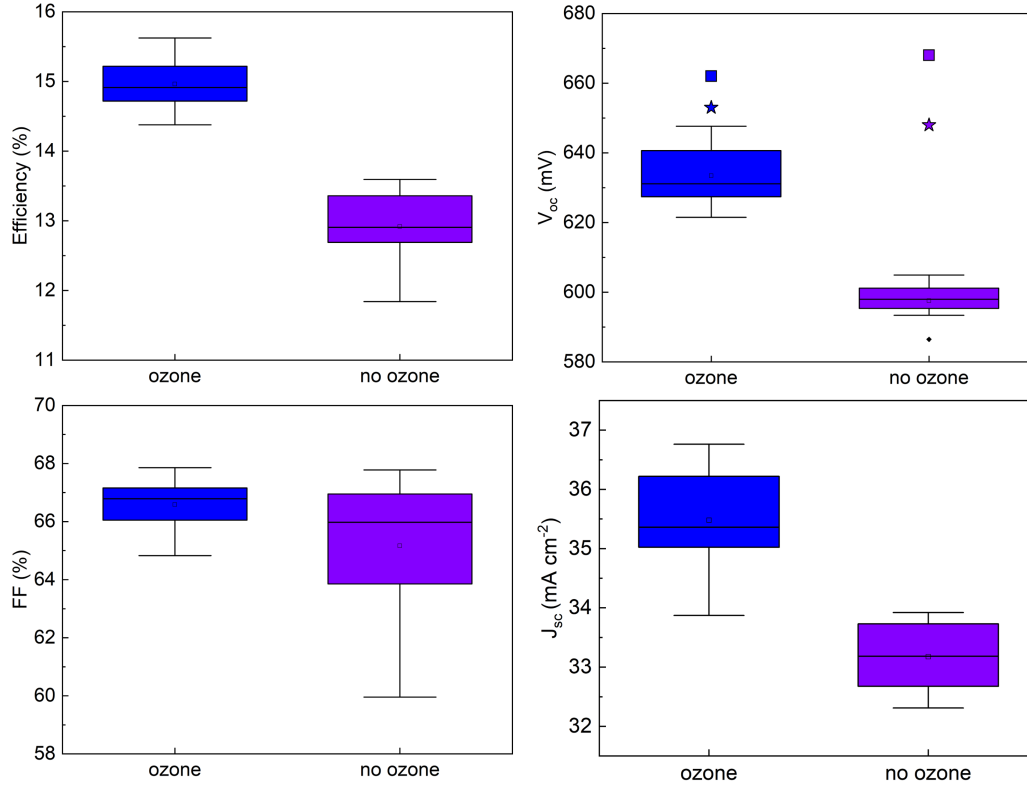
147

Figure 5.63: Optoelectronic properties of 8 cells with In$_2$S$_3$ buffer from the ink containing a [S]/[In]=3. The CIGSSe was either treated with UV ozone treatment before the printing or left pristine. The star squares and stars on the V$_{oc}$ graph represent the qFLs before and after the buffer deposition.

inhomogeneities.

In summary, the UV ozone treatment ensures that the number of pinholes is as low as possible and is currently essential for our inkjet printed layers. However, this process can be replaced by another process that increases the hydrophilicity without inducing damage to the absorber such as a gentle Ar$^+$ plasma treatment [128].

5.9 Summary

In this chapter, the In$_2$S$_3$ buffer layer morphology, chemical composition, crystallography, optical properties and performance in a device were determined.

The surface coverage of the absorber by the buffer layer was shown to be important: a full coverage of the absorber led to the highest power conversion efficiency of a device. A partial coverage allowed the formation of defects at the absorber surface due to the iZO sputtering damage which decreases the V$_{oc}$.

Inks with an increasing propylene glycol (ppg) content were synthesized and the performance of the buffers was assessed. The highest content of ppg (25% of the ink volume)
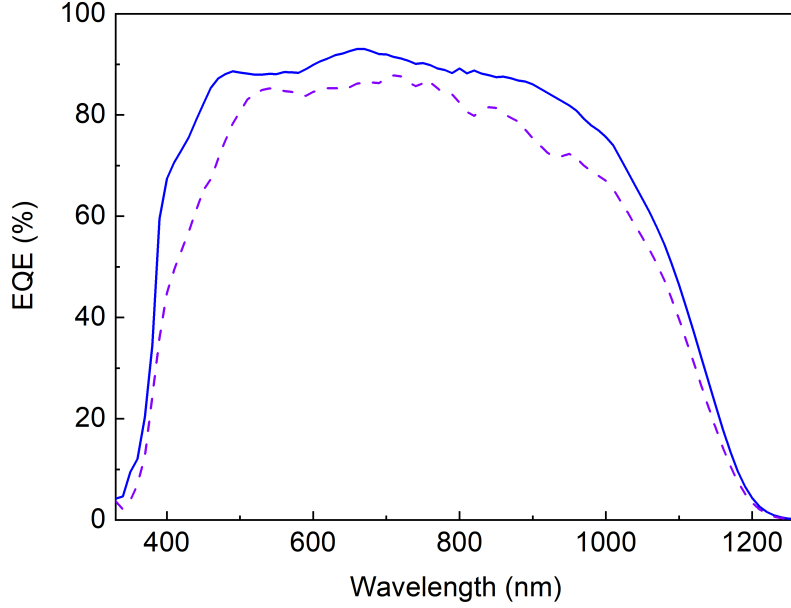
Figure 5.64: EQE of best devices with an In_2S_3 buffer from ink with [S]/[In]=3 on CIGSSe with (solid line) and without UV ozone (dashed line).

led to the highest device efficiency with this buffer. The improvement in efficiency was attributed to the smoothing of the macro-morphology of the buffer. Moreover, the presence of a detrimental carbon residue related to the possible decomposition of ppg was ruled out.

The source of indium and sulfur in the ink were indium chloride and thiourea (TU). Literature claimed that the pre-formation of a In-S bond (called Complex) was necessary to prevent the formation of indium oxide during the annealing. The Raman spectra of an ink containing the complex and an ink simply made of the salts were shown to be identical: a complex between the $InCl_3$ and TU was visible in both cases. In other words, this complex spontaneously forms in solution. The annealed films formed from these inks were also similar in terms of composition and crystallinity. Moreover, they perform similarly in a device and nearly as well as a reference device with a Zn(O,S) buffer.

It was shown in the literature that the [S]/[In] ratio in the ink could sometimes influence the final properties of the In_2S_3 buffer depending on the ink and the deposition technique. We synthesized inks with [S]/[In]=3, 2, 1.5 and 1 and characterized the buffer layers. The In_2S_3 morphology was significantly porous for [S]/[In]=3. It was denser by decreasing the [S]/[In]. This behaviour was attributed to solid state dewetting resulting from an energy mismatch between the dried buffer and the substrate. The performance as a buffer layer highly depended on the [S]/[In]. The sulfur rich inks, i.e. [S]/[In]=3 and 2, performed as well as the reference cell with a Zn(O,S). The [S]/[In]=2 even outperformed the reference cell by 0.5% thanks to an increased V_{oc} of 30 mV. The devices with a buffer made from inks with [S]/[In]=1.5 and 1 had a low performance and showed abnormal JV

curves.

Finally, the highest annealing temperature of the solar cell was shown not to have severe impact on the efficiency of the devices. Indeed, devices annealed at 250°C and 310°C showed a mean difference of 0.5% in efficiency.

Chapter 6

Cadmium sulfide buffer layer

The CdS buffer is known to be toxic and alternative Cd-free buffers have gained interests. However, CdS is still used as attested by the new CIGSSe world record (23.6%) obtained with a CdS buffer (not published yet). The previous CIGSSe record solar cell obtained in 2019 was 23.35% with a Zn(O,S) buffer layer [19] which shows that alternative buffers do gain interest even though CdS is sometimes still preferred. Moreover, the studies on the Cd-free buffer layers are very often compared with CdS devices. The toxicity of cadmium can not be mitigated, however, this toxicity can have a very low impact by decreasing the amount used to form the thin film. Indeed, a typical deposition technique for CdS is the chemical bath which typically requires 200 mL of solvents (with a basic pH) to process four samples. As a comparison, the deposition using inkjet printing of four CdS thin films would require 50 000 times less solvents and 2100 times less material. In short, if an inkjet printable CdS can be made, it would have a lower impact on the environment and could be used without making compromise with the wish of photovoltaics to make green energy. In this chapter, we will investigate the inkjet printing deposition route for CdS, the properties of the synthesized films and the performance of the cells with this buffer layer.

New solution deposition processes have already been investigated such as spin coating and inkjet printing. Patel et al. dissolved cadmium acetate and thiourea in methanol [28]. However, methanol is toxic for human and not allowed to be handled out of a fumehood which ruled out this ink for this work. Ramos et al. [30] used cadmium acetate and thiourea in a methanol: ethylene glycol mixture (ratio 95:5). This ink was also ruled out because of methanol.

In this chapter, an inkjet printable CdS buffer was developed to allow its use while decreasing its detrimental environmental impact. The benign mixture of water:ethanol 3:1 was used with a cadmium acetate concentration of 0.8 M and thiourea 0.8 M. However, the solution was shown to be unstable. Figure 6.1 shows the inks with concentration from 0.1 M to 0.4 M. The solutions were clear when prepared but turned to yellow after one day corresponding to a precipitate of CdS. This reaction resembles chemical bath deposition
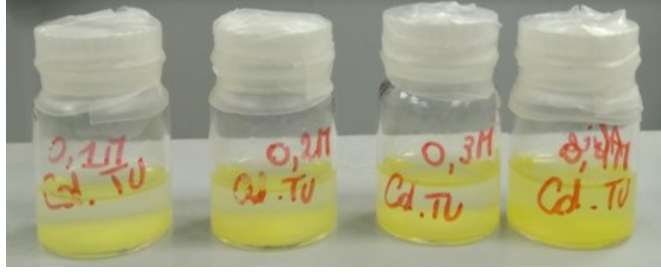
Figure 6.1: Solutions of cadmium acetate and thiourea in the solvent mixtures 3:1 water:ethanol with an increasing concentration: 0.1 M, 0.2 M, 0.3 M and 0.4 M from left to right.

in which cadmium sulfate (for example) and thiourea are added to an ammonia solution. The following equation represents the different steps of the reaction [23]. The first step corresponds to the decomposition of the cadmium source in the basic solution
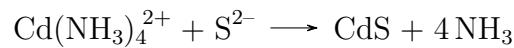
$$CdSO_4 + 2\,NH_4OH \longrightarrow Cd(OH)_2 + (NH_4)_2SO_2$$
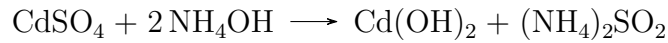
The second step is the formation of an intermediate complex

$$Cd(OH)_2 + 4\,NH_4OH \longrightarrow Cd(NH_3)_4^{2+} + 2\,OH^- + 4\,H_2O$$

The third step is the decomposition of thiourea in the basic solution

$$(NH_2)_2CS + 2\,OH^- \longrightarrow CH_2N_2 + 2\,H_2O + S^{2-}$$
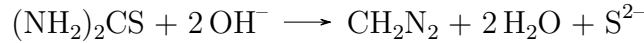
Finally, the intermediate complex and the decomposed thiourea react to form CdS

$$Cd(NH_3)_4^{2+} + S^{2-} \longrightarrow CdS + 4\,NH_3$$

The basic pH of the solution is extremely important. It prevents the precipitation of the intermediate complex $Cd(OH)_2$ and decreases the concentration of the free Cd^{2+} ions in the bath. The formation of the intermediate complex is necessary to ensure a slow reaction with S^{2-} and thus an homogeneous deposition of the CdS. Our ink does not contain any ammonia which makes the chemical reaction different from the CBD deposition. The ink is made of water and ethanol, cadmium acetate and thiourea and has a pH of 5. The source of this acid pH is thiourea. Indeed, the ink containing only cadmium acetate has a neutral pH, while the ink with thiourea only has a pH around 5. This can be explained by the following reaction of thiourea in water [98]

$$SC(NH_2)_2 \rightleftharpoons NH_3 + HNCS \rightleftharpoons NH_4^+ + NCS^-$$

The second equilibrium is pushed to the right because HNCS is a strong acid [98]. Then, the NCS$^-$ reacts with the free Cd^{2+} which are numerous since the solution is not alkaline and CdS is formed. This solution can be used for fast processing techniques such as spin coating. However, inkjet printing requires a long time stability because of its low use

152

of material that makes the cartridge usable for several months. This precipitate did not occur in solution for the In_2S_3 because an intermediate complex was found in Raman measurement. It is hypothesized that this complex was stable enough to prevent the reaction to occur.

In order to circumvent this precipitation issue, the cadmium acetate and thiourea were separated into different cartridges and printed successively onto the CIGSSe. The processing of the sample is shown in figure 6.2. The UV ozone treatment on the CIGSSe was applied in this study since it was proven to be necessary in chapter 5. The sample was dried for 10 minutes in air and 5 minutes at 70°C on a hot plate after the printing of each layer to ensure a good morphology. This drying step in between the layer was found to be mandatory. Indeed, if the second layer was printed on a semi-dried first layer, a bulging instability appeared and the morphology was seriously impacted. An annealing step was used to turn the precursor into CdS following the proposed reaction

$$Cd(CH_3COO)_2 + SC(NH_2)_2 \longrightarrow CdS + residues$$
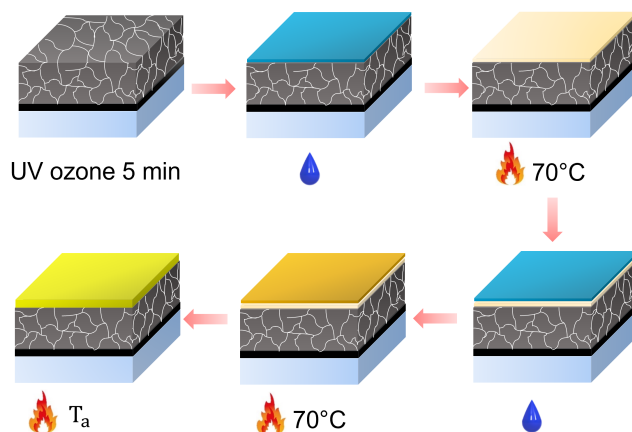
Figure 6.2: Inkjet printing of the CdS buffer layer. The processing steps are as follow: the absorber is treated with UV ozone for 5 minutes, the first layer is printed, the sample is dried at 70°C, the second layer is printed, the sample is dried at 70°C and finally annealed at the required temperature T_a.

Since two layers are printed successively, the ordering of the layers is investigated. The printing ordering of the cadmium and thiourea layers influences the morphology of the final film. Figure 6.3a to d shows the printing process for Cd as the first layer and TU as the second layer (Cd→TU). The printed cadmium layers shows a stripe pattern which was already mentioned in this work (appendix A.1.2). After the drying, the TU layer was printed and the morphology is relatively smooth. Once dried, the sample still exhibits a stripe pattern and after annealing, this pattern is still visible, however the film morphology is generally smooth except for the height fluctuation due to the stripe pattern.

Figure 6.3e to h shows the opposite layer ordering (TU → Cd). The printed TU layer also has a stripe pattern which does not bring any serious concern. However, its drying creates a needle shape pattern because of TU crystallization. This shape has never been discussed for TU to the best of our knowledge. However, urea which is the same molecule as TU except that the S atom is exchanged with an O atom, was shown to have a pronounced preferential crystal growth. Indeed, the {001} and {110} faces are known to respectively grow fast and slow [153]. It is hypothesized in this chapter that the same behaviour happens for TU molecules.

When the Cd is printed on this crystallized layer, it does not spread correctly and the annealed samples shows an inhomogeneous morphology. When comparing figure 6.3d and h, the best morphology for the buffer layer is clearly shown by the Cd→TU layer ordering.
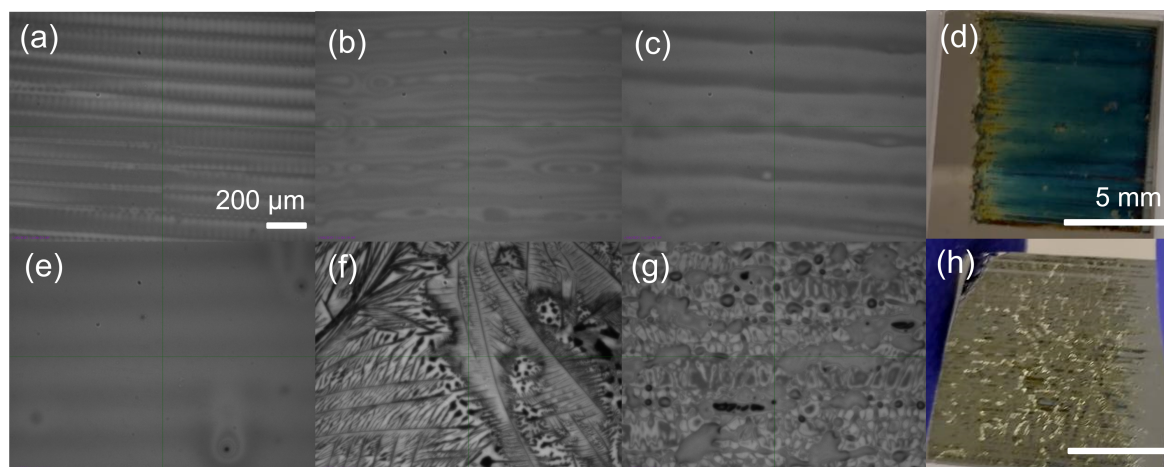
Figure 6.3: Optical images of inkjet printed Cadmium and thiourea layers. First row represents the deposition of Cd and then TU. (a) printed cadmium layer, (b) printed TU layer on Cd layer, (c) stack of 2 layers dried, (d) annealed at 200°C Cd→TU sample. The second row shows the deposition of TU and then Cd. (e) Printed TU layer, (f) dried TU layer, (g) printed Cd layer on TU layer and (h) annealed at 200°C TU→Cd. The scale of (a) to (c) and (e) to (g) is identical. The scale of (d) and (h) are identical.

The micro morphology of the annealed samples is shown on figure 6.4. The Cd→TU has smooth morphology with some slightly bulging features, while the TU→Cd has a porous structure similar to the [S]/[In]=3 of the indium sulfide buffer layer. It was hypothesized in the latter case that the porosity arises from the solid state dewetting and was not related to the evaporation of excess thiourea (subsection 5.6.1). This experiment shows another hint that the energy of the solid (dried) film is responsible for the porosity. Indeed, the amount of TU is similar in both films, however only the film with Cd in direct contact with the substrate has a dense morphology. It is hypothesized that when the TU layer is in contact with the substrate, there is solid state dewetting because of the non ideal free energy of thiourea that was already observed for In_2S_3 (subsection 5.6.1). Since the TU→Cd film does not show a smooth macro-morphology, the crystalline structure

and chemical composition will not be studied since both XRD and XPS are sensible to roughness.
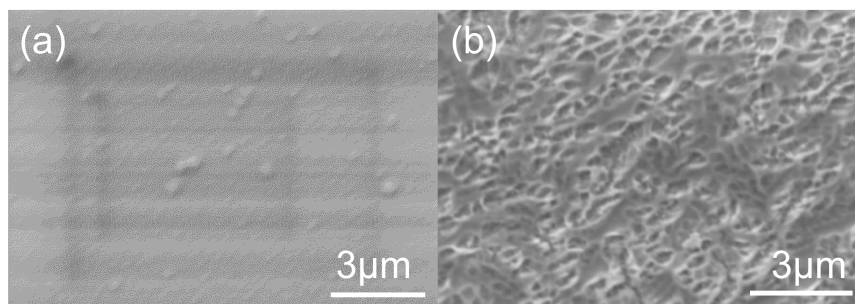

Figure 6.4: SEM images of annealed inkjet printed CdS with the layers ordering (a) Cd→TU and (b) TU→Cd.

The crystalline structure of the inkjet printed CdS was investigated to ensure that CdS was indeed formed. The XRD pattern and corresponding crystallites size and lattice constants are reported in figure 6.5 and table 6.1 for the inkjet printed CdS and a reference chemical bath deposited (CBD) CdS. The peaks positions are similar for both films. However, less peaks can be found for the inkjet printed CdS in the 20-30° range because of the large FWHM which produces an overlap of the different peaks and makes a single large peak.
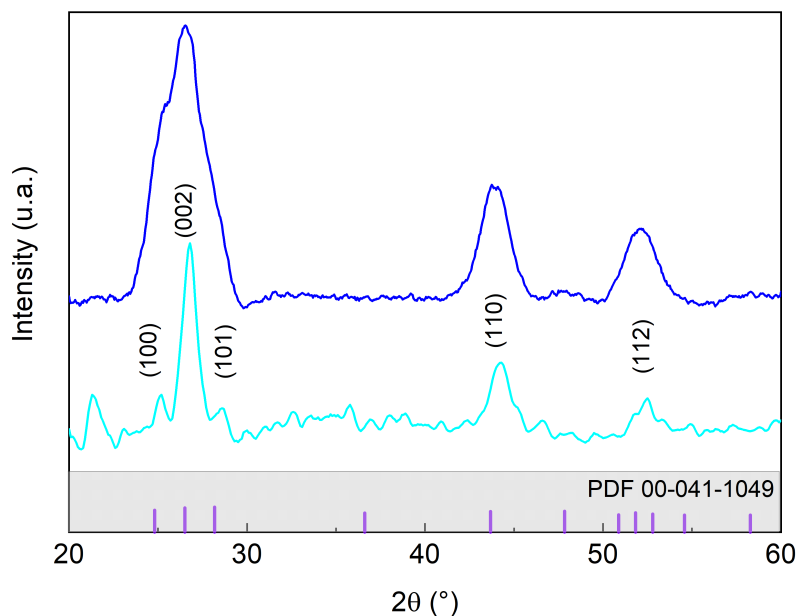
Figure 6.5: GIXRD of inkjet printed CdS (Cd →TU) (blue) and CBD CdS (cyan) deposited on glass substrate. The inkjet printed CdS was annealed at 200°C.

The CBD CdS has bigger crystal coherence length (6 nm) compared to the inkjet printed CdS (4 nm). Both inkjet printed and CBD CdS have a hexagonal structure. The CBD CdS shows a shift in the peaks position compared to the literature which

155

might indicate the incorporation of oxygen in the lattice. The unit cell parameters were calculated using the equation for hexagonal cell

$$sin^2\theta = \frac{\lambda^2}{3}\frac{(h^2 + hk + k^2)}{a^2} + \frac{\lambda^2}{4}\frac{l^2}{c^2} \tag{6.1}$$

The unit cell of CBD CdS has a smaller volume which is coherent with the introduction of oxygen (table 6.1). The presence of $Cd(OH,S)_x$ in the final film is possible since it is an intermediate product of the chemical reaction leading to CdS [23]. The inkjet printed CdS has a unit cell volume nearly identical to the reference, showing a higher purity than CBD.

	(110) peak position(°)	FWHM(°)	Coherence length (nm)	a (Å)	c (Å)	V (Å^3)
CBD	44.22 ± 0.02	1.22 ± 0.06	6.03 ± 0.05	4.09	6.65	96.34
Inkjet printed	43.92 ± 0.01	1.87 ± 0.03	3.94 ± 0.05	4.12	6.70	98.49
Literature	N.A.	N.A.	N.A.	4.14	6.72	99.79

Table 6.1: Crystallographic data from XRD data of inkjet printed and CBD CdS films. The literature reference is PDF4+ 00-041-1049.

The chemical composition of an inkjet printed CdS film (Cd→TU) deposited on Mo coated glass was determined using XPS. Figure 6.6a shows that the CdS layer is dense until 200 s of sputtering, after which Mo appears even though Cd and S can still be detected, which might arise because of two reasons. The first one is that some porosity might be present at the back of the thin film which enable the collection from both the film and the substrate. The second reason is that the signal collected comes from a 10 nm depth which means that when arriving at the back of the film, both the substrate and the film are detected. Since the sputtering rate was not calibrated, none of these explanation can be ruled out.

A significant amount of C (around 10%) is reported. Two arguments can be brought up to explain this amount. First, the ink used for this XPS measurement contains ppg, while the ink used for the solar devices is ppg free[1]. However, it was shown with Raman measured on dried films in the chapter 5 that ppg is not present after a 70°C drying step, which excludes a carbon residue from ppg. Secondly, the fitting of C in XPS is extremely sensitive: a slight change in the background removal changes significantly the C content. In summary, C is probably present but its amount might be much lower than what is reported here. The S was found in three phases: the metal sulfide, metal sulfate and in S−(C−H) corresponding to non-decomposed thiourea. The [S]/[Cd] ratio is slightly lower than stoichiometry, however, preferential sputtering of sulfur probably

---

[1]this change in the ink happens because of the short lifetime of the cartridge. Some parts of the study were performed later and required the production of new cartridges and thus an ink that was easily inkjet printable and for which the cartridge lifetime is longer was preferred.
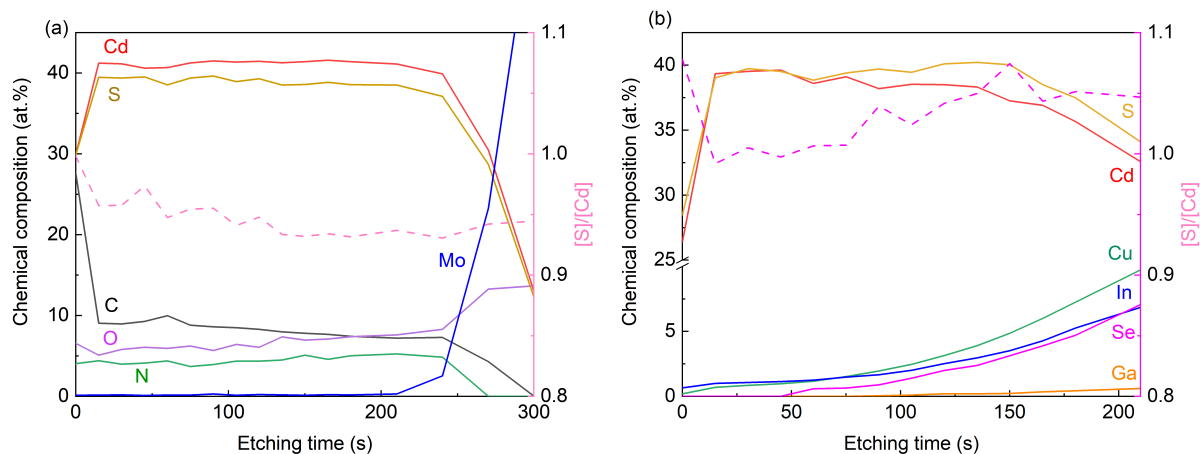
Figure 6.6: XPS spectrum of an inkjet printed CdS (Cd→TU) annealed at 200°C deposited on (a) Mo and (b) CIGSSe (O, and N were removed from the graph for clarity). The error bar are 0.5 at.%. The dashed line in represents the [S]/[Cd] ratio.

occurred [154]. The presence of O could indicate the formation of CdO_x, however a single peak fitting was enough to fit the Cd peak, meaning that O did not represent a significant phase in the material. Moreover, XRD just showed that the lattice constants were nearly identical to the literature, which can rule out the incorporation of oxygen in the lattice. The composition of a CdS film annealed in nitrogen (not shown) did not show any difference with an annealing in air. In summary, the CdS is in pure phase, the carbon content is probably over evaluated and the oxygen could be related to sulfate and also bonded to N.

Since the CdS layer appears dense, it might be possible to determine if some atoms from the CIGSSe diffused toward the buffer and inversely (assuming that the morphology is the same on Mo and CIGSSe). Figure 6.6b shows that Cu, In and Se diffused toward the buffer layer. Indeed, the same buffer layer thickness was deposited on both Mo and CIGSSe. Figure 6.6a showed that the buffer layer was dense until at least 200 s of sputtering. The film deposited on CIGSSe already shows the presence of Cu, In, Ga, Se atoms before 200 s of sputtering. The diffusion of Cd and S is possible. However, the composition could not be determined at deeper depths because several peaks of CIGSSe are nearly overlapping with peaks of the buffer (N with Ga, C with Se, S with Ga) and the chemical composition would be unreliable deeper in the film. The sulfur content is found to be higher when deposited on CIGSSe. CIGSSe contains sulfur and since several atoms were found to diffuse, S can be expected to diffuse as well, increasing the total signal of S. All this reasoning was done based on the assumption that CIGSSe is fully covered by CdS. However, chapter 5 showed that some parts of CIGSSe are not covered by the In_2S_3 buffer. If this is taken into account, the diffusion of Cu, In and Se can not be determined. In summary, XPS showed that the CdS layer deposited on Mo and annealed at 200°C looks dense and has a sub-stoichiometric [S]/[Cd] ratio which might is probably

related to preferential sputtering. When deposited on CIGSSe, the [S]/[Cd] ratio of CdS is above stoichiometry which might be due to diffusion of sulfur from CIGSSe to the buffer.

Since the inkjet printed material is confirmed to be CdS, it was deposited on CIGSSe to form a solar cell device. The performance of the devices with different layer ordering is shown on figure 6.7. The efficiency of the ordering Cd→TU is double the opposite ordering and is similar to the CBD reference. The voltage is much lower and spread for TU→Cd than Cd→TU meaning that the charge carriers are difficult to separate. The J_{sc} is low because of a lack of collection which is coherent with the low charge separation. Finally, the low FF also proves that the pn junction is defective. This low FF is related to a very high series resistance. The shunt resistance is widely spread and corresponds to an inhomogeneous sample. The Cd→TU on the other hand showed similar V_{oc}, J_{sc} and FF as the CBD reference.
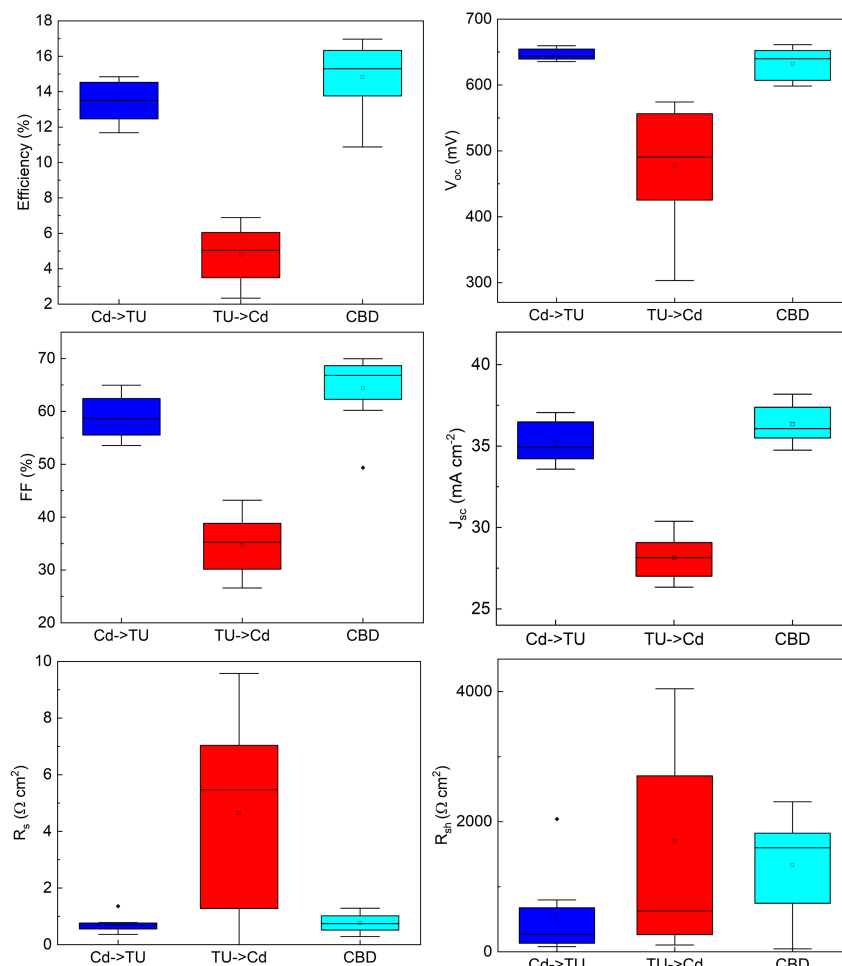
Figure 6.7: Optoelectronic properties of solar devices with an inkjet printed Cds buffer and a CBD CdS reference. The ordering of the cadmium and thiourea layers was varied, i.e. Cd then TU (blue) or TU then Cd (red).

EQE (fig 6.8) shows the blue defect for all the CdS, however it is slightly less pro-

nounced for the inkjet printed CdS. The derivative of the EQE gives an average band gap of 2.6 eV and 2.55 eV for the inkjet printed and CBD CdS respectively. The collection at all wavelengths is higher for the CBD CdS. The EQE of the TU→Cd sample shows a defective pn junction with a pronounced lack of collection at all wavelengths.
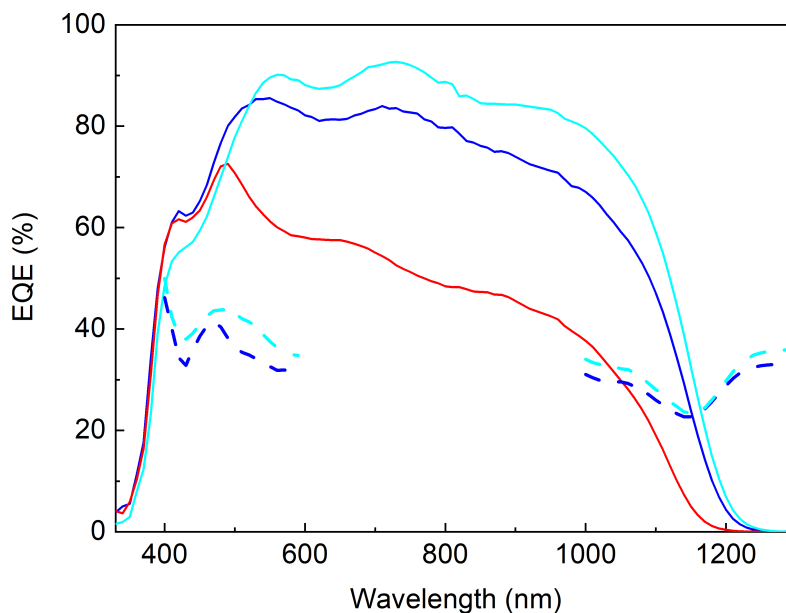
Figure 6.8: EQE of devices with an inkjet printed CdS buffer layer with the layer ordering Cd→TU (blue) and TU→Cd (red) and a CBD CdS (cyan). The dots curves represents the derivative of the curves.

This study showed that CdS can be deposited using successive inkjet printing of the Cd and S sources. The crystalline structure is coherent with literature and the chemical composition showed a nearly stoichiometric [S]/[Cd] ratio with a low organic residue content. This new layer performed well in a CIGSSe device with an efficiency similar to the CBD reference.[2] The investigation of the layer ordering showed that the system is unstable. Indeed, only the Cd→TU showed good performance in the cell, probably because the TU→Cd layer has a defective morphology.

---

[2]The solar cells results shown here were part of a first trial. To further confirm the trend and the performance of this buffer layer, another batch of solar cells would be required and is part of the outlook of this work.

Chapter 7

Quantum confinement in buffer layers

The band gap of the inkjet printed In_2S_3 and CdS buffer layers were found higher than the bulk materials band gap. An increase in the band gap can often be associated to the incorporation of oxygen into the lattice or Na in the case of In_2S_3. However, it was shown that oxygen and Na were not incorporated in significant amount in XPS and Raman measurements. Another explanation of the increased band gap could be the presence of very small crystallites. Indeed, quantum dots are known to have higher band gap than their bulk counterparts. It is thus hypothesized that the thin films are made of small crystallites that increase the band gap of the film. The Brus theory can give a rough trend regarding this blue shift in the band gap. This theory is introduced and is then applied to the inkjet printed buffer layer to verify if a relationship between the crystallite size and the band gap can be found. Moreover, the crystallite size of the materials is varied by changing the annealing conditions of the films.

7.1 Theory

When the size of the crystallites in a material decreases drastically, the bulk optical properties may be changed. Quantum dots, which are 0D materials, typically show an increased band gap compared to the bulk optical value. Brus [155] created a model to assess the energy of the lowest excited state. The model was extended to the calculation of the band gap of materials under confinement with the characteristic equation

$$E^* = E_g + \frac{\hbar^2 \pi^2}{2R^2} \left[\frac{1}{m_e^*} + \frac{1}{m_h^*} \right] - \frac{1.8e^2}{4\pi\epsilon_0\epsilon R} \tag{7.1}$$

where m_e^* and m_h^* are the effective masses of the electron and the hole, ϵ_0 and ϵ are the dielectric constant of vacuum and the semiconductor, e is the electron charge, $\hbar$ is

the reduced Planck constant, E_g and E^* are the band gap of the bulk material and the material with quantum confinement, and R is the radius of the particle. The second term represents the localization of the electron and hole and the third term is the Coulomb interaction. The effective masses are most of the time smaller than the electron mass and correspond to the curvature of the dispersion curve at the conduction band minima and valence band maxima. The Coulomb interaction is actually most of the time negligible because of the dielectric constant which generally ranges from 5 to 12 for most semiconductors. This model was created by analogy with the hydrogenic model where the Bohr radius is given by $a_0 = \frac{4\pi\epsilon_0\epsilon\hbar^2}{me^2}$ with m, the mass of the electron. This radius was obtained by resolving dE/dR=0. Similarly, the characteristic exciton radius, called exciton Bohr radius, is defined by $a_B = a_0 m/\mu$ which gives [156]

$$a_B = \frac{4\pi\epsilon_0\epsilon\hbar^2}{\mu e^2} \tag{7.2}$$

where μ is the reduced exciton mass and and $1/\mu = 1/m_e^* + 1/m_h^*$.

The analogy with the hydrogenic model is true under the condition that the Bohr exciton radius exceeds many times the crystal lattice constant (a_L), i.e. $a_B >> a_L$ (fig 7.1a). If this condition is not met, the description of interacting electron and hole through a medium of dielectric constant ϵ is wrong. This is the case for example for NaCl, in which the exciton is known as a Frenkel exciton and cannot be described through the hydrogenic model [157]. The Bohr radius represents the crystallite size threshold for quantum confinement. Different confinement regimes exist and are discussed extensively in [156] and briefly addressed here:

1. Weak confinement occurs when the radius of the crystallite $R \gg a_B \iff R \gg a_e$ and $R \gg a_h$, where $a_B = a_h + a_e$ (fig 5.25b). a_h and a_e are the hole and electron Bohr radius and given by [156]

$$a_h = \frac{4\pi\epsilon_0\epsilon\hbar^2}{m_h^* e^2} \tag{7.3}$$

$$a_e = \frac{4\pi\epsilon_0\epsilon\hbar^2}{m_e^* e^2} \tag{7.4}$$

The Coulomb interaction is dominant and there is quantization of the motion of the exciton. The ground-state exciton energy is shifted by $\triangle E \approx \frac{\hbar^2\pi^2}{2MR^2}$, where M is the mass of the exciton, i.e. the sum of the electron and hole effective masses $m_e^* + m_h^*$

2. Strong confinement corresponds to $R \ll a_e$ and $R \ll a_h$. The coulomb interaction is negligible and acts as a perturbation term. The electron and the hole are isolated

particles and the exciton is not formed. The shift in energy is now given by $\triangle E \approx \frac{\hbar^2 \pi^2}{2\mu R^2}$.

3. Intermediate confinement happens when $a_h < R < a_e$ meaning that the crystallite size is smaller than the electron Bohr radius but larger than the hole Bohr radius. This case occurs for many direct band gap semiconductors. The confinement is significant for the movement of the electron but not for the hole. However, the motion of the hole will be influenced by the Coulomb interaction between the hole and the electron. In short, the hole moves in a cloud of electrons under strong confinement which creates a mean Coulomb potential. Since the confinement essentially occurs on the electrons, the quantization of the energy is given by $\triangle E \approx \frac{\hbar^2 \pi^2}{m_e^* R^2}$.
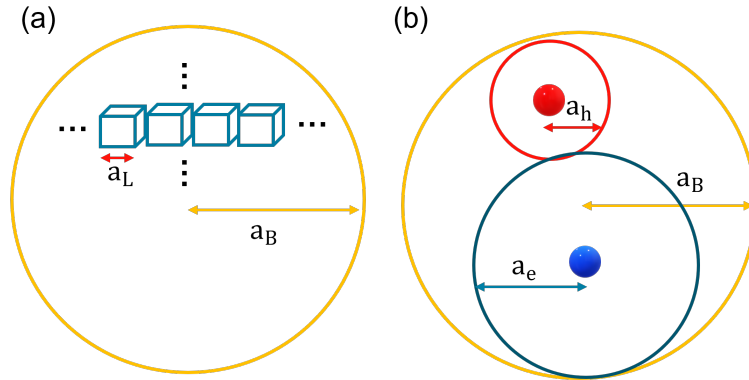
Figure 7.1: Sketch of (a) the exciton Bohr radius a_B and lattice constant a_L and (b) the electron and hole Bohr radius a_e and a_h.

This model is based on the effective mass approximation (EMA). However, it shows some limitations. For example, it can break down for $R < 10$ Å because of possible surface effects and change in the structure [156]. The EMA is unfortunately known to lead to an overestimation of the band gap because it hypothesizes that the bands are parabolic which is true only around the $\vec{k}$=0 point. Many models have been created to overcome the different problems inherent to the EMA but this discussion is out of the scope of the thesis and the following results obtained using the EMA approximation have to be carefully interpreted. The reader should remember that the values are overestimated but the Brus equation stays interesting to give trends.

The method used in this thesis to determine the band gap of the materials is the Tauc plot which was discussed in subsection 3.5. However, this technique is based on the density of states of 3D materials (fig 7.2a). It could be argued that the Tauc plot can not be used because the crystallites are considered as 0D materials with an associated density of states for 0D (fig 7.2b). However, Feng et al. [158] showed that the Tauc plot can be used in the case of materials made of nanocrystals. Indeed, the material is not strictly 0D because it contains hundreds of crystals. This material made of small crystallites are
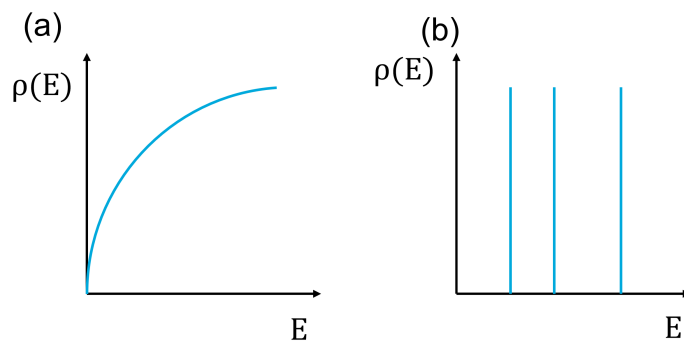
Figure 7.2: Density of states of (a) 3D and (b) 0D semiconductor.

called quantum dot solids. Similarly to the solids made of atoms, the quantum dots (QD) are building blocks of the QD solid [159]. When the QD have a large interdot distance, the energy levels are degenerate. When this distance decreases, the energy levels turn into bands. In general, inhomogeneities are present in the QD solid: varying interdot distance, QD size and shape,... Our materials probably present various shapes and size, however, they will be shown to be dense via TEM which rules out a varying interdot distance. These imperfections increase the smearing of the discrete energy levels participating to the formation of bands. The density of states resembles thus the one of 3D materials.

The basic Tauc plot with an exponent of 0.5 for direct band gap is however not the best representative exponent of the QD solid. It was shown that in order to be accurate, the exponent should be modified [158]. The model showed the same exponent for the 3D limit (0.5) but an exponent of 1 for the 0D limit. In order to check the sensitivity of the exponent on the extraction of the band gap for our data, the exponent value corresponding to a crystal size of 4.2 nm (inkjet printed CdS annealed at 100°C discussed in the next section) was extracted from [158]. The Tauc plot method was applied with the extracted exponent, i.e. 0.77, and compared with a Tauc plot with a standard 0.5 coefficient. It was found that the band gap is overestimated by 0.1 eV, i.e. it is 3.0 eV instead of 3.1 eV when using the standard 0.5 exponent. Since this difference is small, the standard Tauc plot with an exponent of 0.5 will be used.

7.2   Results

Brus equation established a relation between the size of the crystallite and the band gap of the material. When the crystallite is smaller than the exciton Bohr radius, the band gap is increased roughly following the trend given by equation 7.1. In the following sections, this theory is applied to the materials already discussed in chapters 5 and 6, namely In_2S_3 and CdS. Morevoer, inkjet printed Zn(O,S) will also be studied in this chapter. The crystallites size will be measured with XRD and TEM and the band gap

will be extracted from the Tauc plot for all the materials. Then, the Brus model will be applied to compare the expected band gap (based on the measured radius inserted in the Brus equation) with the measured band gap.

7.2.1 Crystallites size in In$_2$S$_3$, CdS and Zn(O,S)

In this section, the radius of the particle is measured using two techniques. The full width at half maximum of a peak gives the coherence length which can be approximated as the crystallite diameter as detailed in section 3.3.1. TEM wich shows direct image of the crystallites (section 3.3.2) is also used to cross check the crystallites size determined through XRD.

Figure 7.3 shows the TEM images and the respective selected area electron diffraction pattern (SAED) and Fast Fourier transform (FFT) of inkjet printed In$_2$S$_3$, CdS, Zn(O,S) and CBD CdS . All the inkjet printed thin films are made up of small crystallites. The CdS shows denser packing than the other materials. Contrarily to chapter 6, the CdS was annealed at 100°C (and not 200°C) to enhance the quantum confinement. A thin layer of CBD CdS was hard to grow on the TEM grid and a thick layer was obtained explaining the dark contrast. The Zn(O,S) was also barely present on the grid: the dark stains are Zn(O,S) crystals while the rest is the amorphous carbon layer. The In$_2$S$_3$ and inkjet printed CdS images contain enough crystals to create a SAED image, while it was not possible for CBD CdS and Zn(O,S) and a post treatment of the image with FFT was applied. The pattern is circular in SAED because of the various crystals orientations.
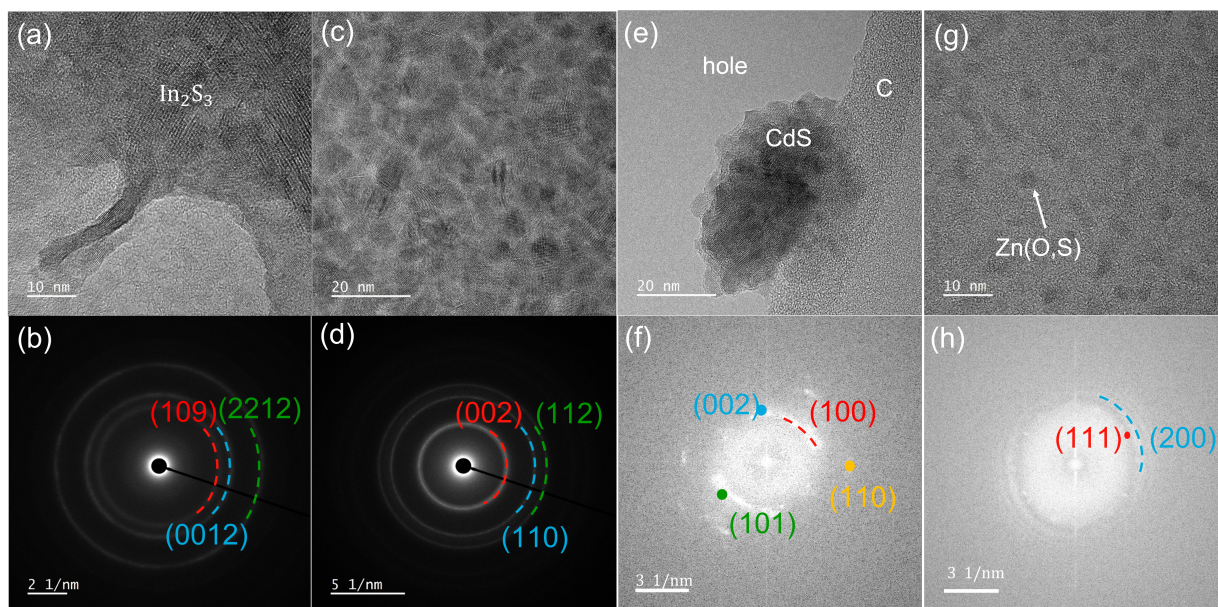
Figure 7.3: TEM images and the respective SAED/FFT of (a),(b) In$_2$S$_3$ annealed at 250°C, (c),(d) inkjet printed CdS annealed at 100°C, (e),(f) CBD CdS and (g),(h) Zn(O,S) annealed at 250°C.

The Zn(O,S) is a material that has not yet been discussed in this thesis. It was synthesized following Chu et al. [58]. The exact composition of the Zn(O,S) deposited on Si as measured with EDX is $ZnO_{0.04}S_{0.96}$. Its diffractrogram is shown on figure 7.4. The peaks can be assigned to cubic structure.
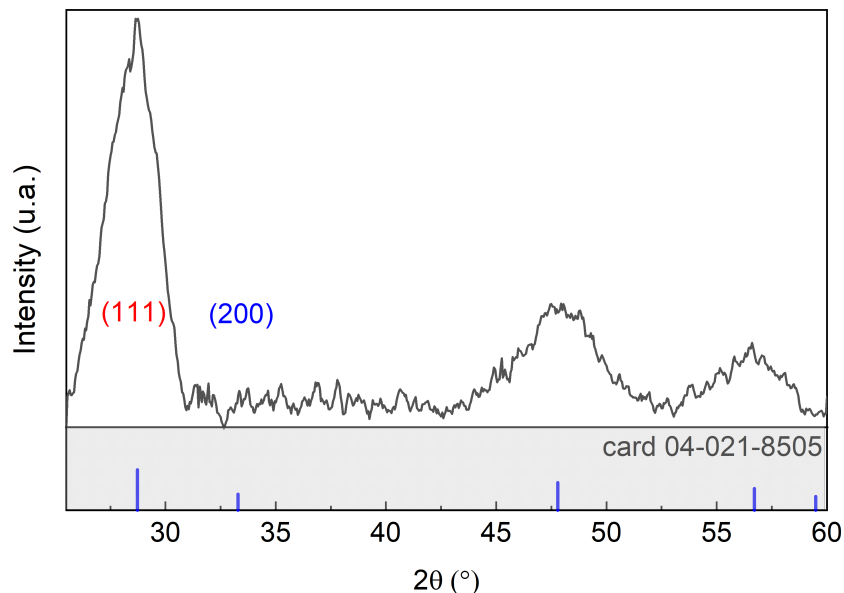
Figure 7.4: GIXRD of inkjet printed Zn(O,S) annealed at 250°C. The reference is PDF4+ 04-021-8505 for a $ZnO_{0.96}S_{0.04}$

Table 7.1 shows the crystallite size determined through XRD and TEM. The TEM radius were taken as the average crystallites radius measured with imageJ [160]. The radius could not be determined through XRD for the inkjet printed CdS because of the overlapping of several peaks. In chapter 6, the CdS was annealed at 200°C. However, the CdS discussed here was annealed at 100°C and its XRD is shown on figure (fig 7.8). The influence of temperature on the crystallographic and optical properties will be discussed in section 7.2.3. The XRD and TEM radii are similar, proving that the XRD radius is a good approximation of the actual radius of the particles. For example, the XRD radius of In_2S_3 determined through XRD is 3.1 nm while the approximate radius extracted through TEM is 3.2 nm. Among the inkjet printed materials, In_2S_3 has the biggest crystallites and Zn(O,S) has the smallest, which are half of the In_2S_3 crystallite size. The XRD radius will be used for the study on the relation between the crystallite size and band gap in the next section.

7.2.2   Band gap of In_2S_3, CdS and Zn(O,S)

The exciton Bohr radii and band gaps of the materials under confinement were calculated from equations 7.2 and 7.1 using the effective masses of electron and holes, the dielectric constant, the bulk band gap and the measured radii from section 7.2.1 (reported

in table 7.1) and are reported in the same table. Since the Zn(O,S) effective masses were not available in literature, the data of pure ZnS were used. The bulk band gap of Zn(O,S) was extracted from [53] using the specific chemical composition measured in our work. Figure 7.5 shows a quick comparison of the calculated Bohr exciton radii and the XRD crystallite radii of the materials. When the Bohr exciton radius (yellow) is bigger than the crystallite radius (blue), quantum confinement effects are expected to increase the band gap of the material compared to the bulk counterpart. Inkjet printed materials do show this configuration while the CBD CdS has bigger crystallites than the exciton Bohr radius meaning that it should not show an increased band gap.

	In_2S_3	Zn(O,S)	CdS	CBD CdS
$m_e^*(m_0)$	0.162	0.34	0.21	0.21
$m_h^*(m_0)$	0.470	0.23	0.8	0.8
ϵ	11	5.2	8.6	8.6
XRD radius (nm)	3.2 ± 0.1	1.4 ± 0.1	N.A.	6.0 ± 0.3
TEM radius (nm)	3.1 ± 0.3	1.3 ± 0.3	2.1 ± 0.5	6.5 ± 1.5
Exciton Bohr radius (nm)	4.8	2.0	2.8	2.8
Electron Bohr radius (nm)	3.6	0.8	2.2	2.2
Hole Bohr radius (nm)	1.2	1.2	0.6	0.6
Bulk E_g (eV)	2.5	3.1 [53]	2.4 [23]	2.4
Brus E_g (eV)	2.7	4.1	2.8	2.4
Tauc E_g (eV)	2.7	4.1	3.1	2.4

Table 7.1: Crystallographic and optical data of inkjet printed In_2S_3 annealed at 250°C, Zn(O,S) annealed at 250°C, CdS annealed at 100°C and CBD CdS films. m_e^*, m_h^* are the effective masses of the electron and hole, ϵ is the dielectric constant of the materials. Model parameters are sourced from [33] for In_2S_3, [161] for Zn(O,S) and [162] for CdS.
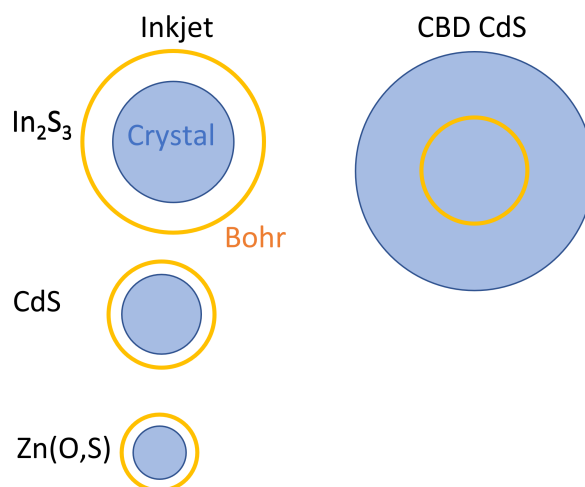
Figure 7.5: Comparison of the exciton Bohr radius (yellow) and crystallite size (blue) of inkjet printed In_2S_3, CdS and Zn(O,S) and CBD CdS.

In order to determine in which confinement regime the exciton is, the electron and hole Bohr radii were calculated and reported in table 7.1 using equations 7.3 and 7.4. In the case of In_2S_3, the XRD radius (R) is bigger than the hole Bohr radius but smaller than the electron's, which corresponds to the intermediate confinement as discussed in section 7.1. For inkjet printed CdS, $a_h < R < a_e$ which is also an intermediate confinement. The Zn(O,S) is different. Indeed, $R < a_B$ which corresponds to quantum confinement. However, $a_e < R < a_h$ which is the opposite case described in section 7.1. Nevertheless, this case can be described by an intermediate confinement too, in which the hole and the electron hole are reversed. It is thus expected to observe a moderate increase in the band gap.

The band gaps of the materials are extracted from the Tauc plot for direct band gap semiconductors (fig 7.6). The band gap of bulk CdS is 2.4 eV [23] which is identical to the band gap of the CBD CdS. A value of 2.55 eV for CBD CdS was found in chapter 6 by taking the derivative of the EQE of a complete device. These values do not match probably because the films were grown on different substrates which might influence the crystallite size. The band gap of the inkjet printed CdS annealed at 100°C is 3.1 eV which is more than 0.5 eV higher than the bulk value. Based on the radius measured with TEM, the band gap calculated from Brus equation is 2.8 eV, which is lower than the measured value. This can easily be justified by the fact that the crystallite radius had to be visually extracted from the TEM images by averaging the measured crystallites size. However, this measurement is hardly as reliable as the radius extracted from XRD. The direct band gap of In_2S_3 is 2.7 eV, which is 0.2 eV higher than the bulk value. The Brus equation confirms a band gap of 2.7 eV with the XRD radius. Finally, Zn(O,S) shows a band gap of 4.1 eV, which is 1 eV higher than the band gap of the bulk and is coherent with Brus model.

As already stated, the inkjet printed CdS that was analyzed here was annealed at 100°C. This choice was motivated by the colour of the sample. Indeed, the samples were annealed at different temperature, as will be discussed in section 7.2.3. The CdS annealed at 100°C was colourless, while the other two (annealed at higher temperature) were yellow, which is the typical colour of CdS. It was hypothesized that the band gap was higher and this sample was selected for the band gap VS crystallite size study through TEM.

In summary, the band gap of inkjet printed In_2S_3, CdS and Zn(O,S) were found to be higher than their bulk counterparts. This increase can be associated with an intermediate quantum confinement which is related to the small size of the crystallites as shown by TEM. In the next two sections, the influence of the annealing temperature on the crystallite size and associated band gap is shown for CdS and In_2S_3.
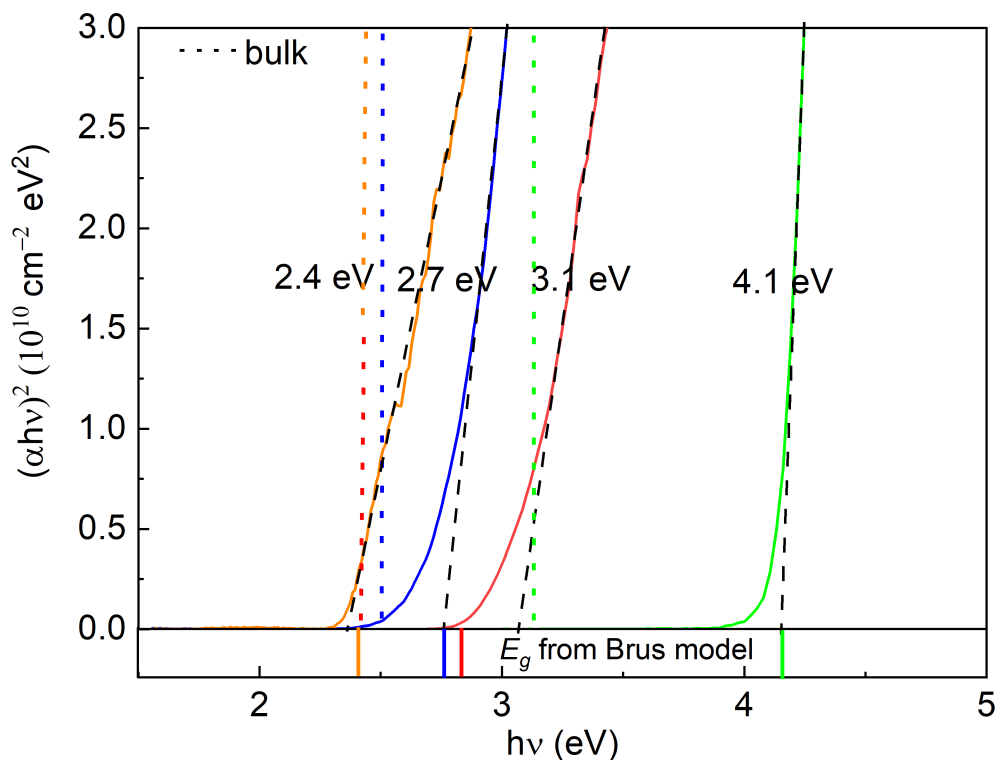
Figure 7.6: Tauc plot for direct band gap semiconductors of inkjet printed In$_2$S$_3$ (blue), CdS (red), Zn(O,S) (green) and CBD CdS (orange). The value written next to the curves are the extracted band gap. The dot lines represents the band gap of the bulk material. The bottom inset is the band gap of the material under confinement obtained from the Brus equation.

7.2.3 Influence of temperature for CdS

It was briefly mentioned in section 7.2 that the XRD spectra of CdS annealed at 100°C and 200°C are different and this will be further discussed in this section. The following study will show the influence of temperature on the properties of the material. Raman (fig 7.7) shows that the CdS films annealed at 100°C, 150°C and 200°C have the characteristic peaks of CdS. Three prominent peaks could be identified as 1LO (longitudinal optical vibration), 2LO and 3LO at 303, 604 and 904 cm^{-1} in accordance with literature [163]. The LO corresponds to the displacement of atoms from their positions of equilibrium in the same direction as the propagation of wave producing the vibration. Kumar et al. [163] showed that the 2LO peak becomes stronger and 1LO weaker with increasing particle size meaning that 2LO/1LO peak height ratio increases with particle size. The 2LO/1LO ratio was calculated for the different temperatures: 2LO/1LO= 0.43, 0.45 and 0.24 for 200°C, 150°C and 100°C respectively. The ratio is similar for 150°C and 200°C which indicates that the particle size is similar. The ratio for 100°C is much smaller than the other temperatures so the particle size is smaller.

XRD measurement shows that the CBD CdS and inkjet printed films annealed at

T(°C)	2LO/1LO
100	0.23
150	0.45
200	0.43
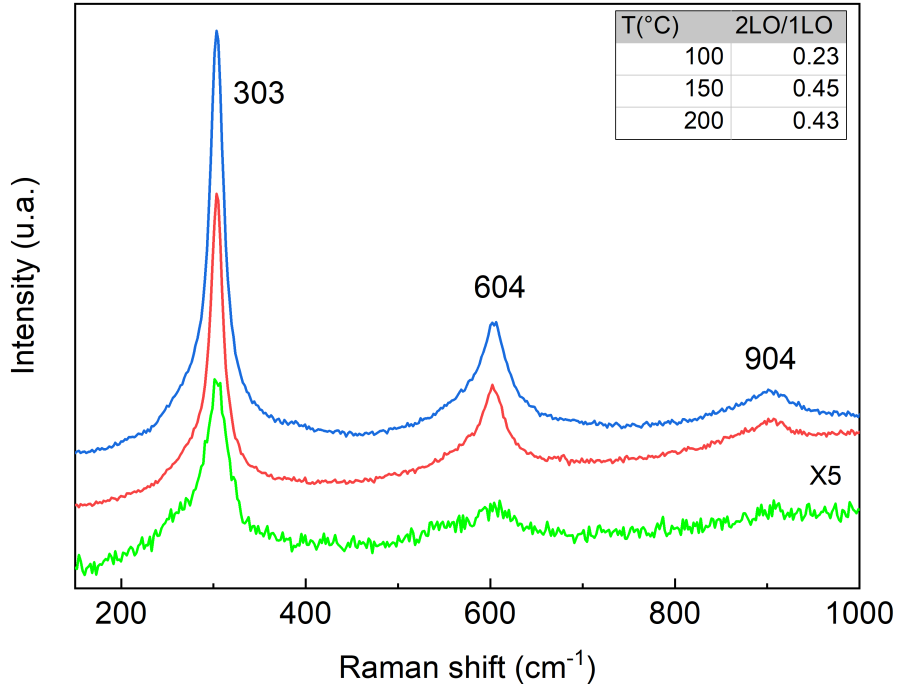
Figure 7.7: Raman spectra of inkjet printed CdS annealed at 100°C (green), 150°C (red) and 200°C (blue). The spectrum of 100°C was multiplied by 5 to increase the intensity. The fitting is not shown for clarity.

150°C have a crystalline structure with prominent peaks, while the CdS annealed at 100°C is nearly amorphous with a wide peak consisting in the overlapping of several peaks.[1] The width of the peaks is smaller for the CBD samples as shown by the (100), (101) and (002) which are distinct thanks to a small FWHM. The particle size is estimated to 6.3 nm. For the inkjet printed samples, these 3 peaks are partially overlapping. The coherence length, i.e. crystallite size, was extracted from the (110) peak from except for the 100°C because too many peaks were involved in the fitting. The crystallite size of the 150°C sample is 6.1 nm, which is slightly lower than the CBD sample. Nevertheless, both of these samples have a particle radius bigger than the exciton Bohr radius and should not exhibit quantum confinement effect, contrarily to the 100°C sample as shown in section 7.2.

The band gaps of the inkjet printed CdS annealed at different temperatures are shown on figure 7.9. The band gap of films annealed at 150°C and 200°C are very similar with the 150°C being slightly lower which is in agreement with the moderately higher peaks ratio found in Raman. The band gap of 150°C and 200°C is very similar to the CBD CdS which is known to be 2.4 eV. As already shown in section 7.2, the band gap of the 100°C is 3.1 eV which is much wider.

Since the films were shown to have an increased band gap with a lower annealing

---

[1]the spectrum of 200°C is not shown for simplicity since Raman showed that 150°C and 200°C are similar.

169
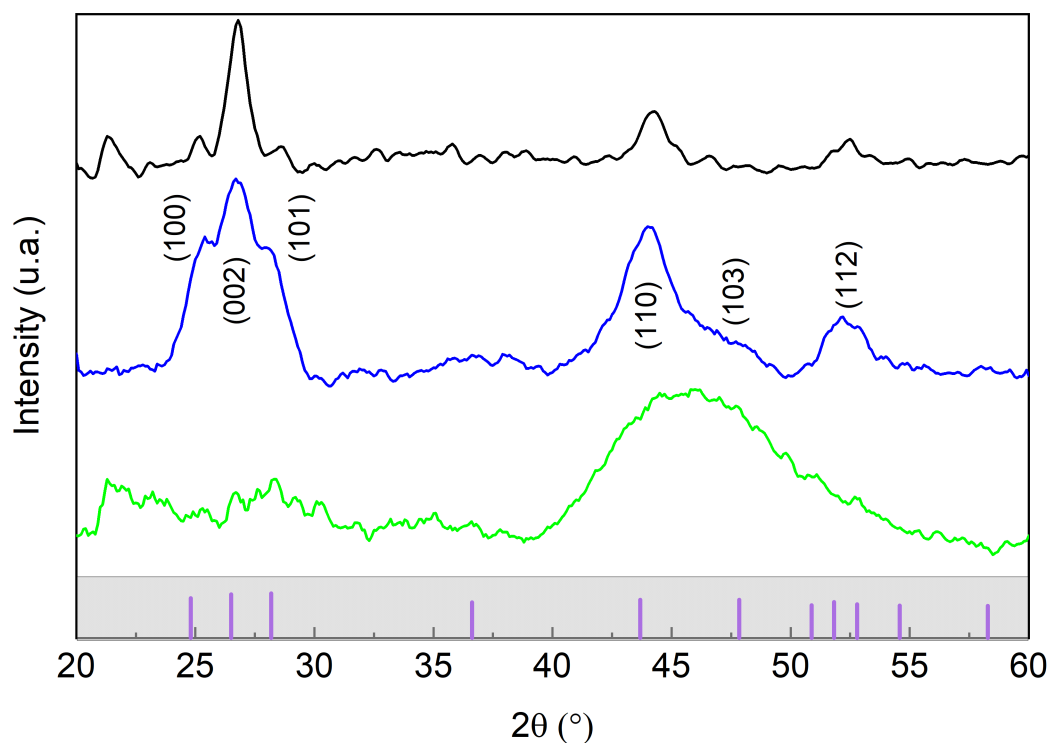
Figure 7.8: XRD spectra of inkjet printed CdS annealed at 100°C (green), and 150°C (blue) and a CBD CdS (black).
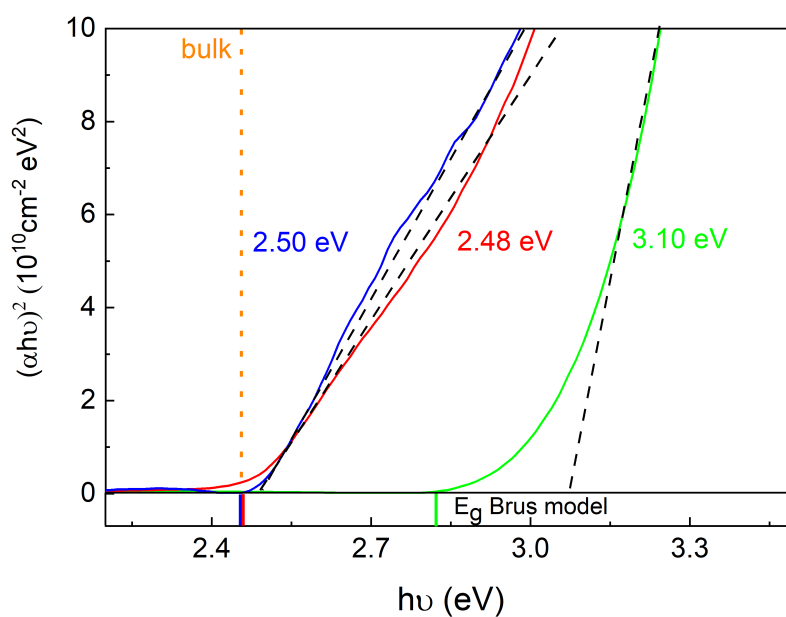
Figure 7.9: Tauc plot for direct band gap semiconductor of inkjet printed CdS film annealed at 100°C (green), 150°C (red) and 200°C (blue).

temperature, it might be interesting to use this phenomenon to remove the typical blue defect in solar cells with a CBD CdS. However, the annealing temperature is also used to evaporate the residues from the film. Figure 7.10a shows the chemical composition of inkjet printed CdS films annealed at 100°C, 150°C and 200°C. The Cd and S signal

decreases with temperature which can simply be explained by the higher content of foreign atoms. The [S]/[Cd] ratio is below stoichiometry for 200°C and stoichiometric for 150°C and 100°C which is unexpected since XRD did not show any oxygen incorporation in the lattice. However, taking into account the error, [S]/[Cd]=0.96 for the 200°C CdS which is nearly stoichiometric. Moreover, only the uncertainty of the machine is taken into account in the error calculation. However, the fitting by itself adds to the uncertainty and it can be hypothesize that all samples are stoichiometric.

The carbon and nitrogen content steadily increase with a decreasing annealing temperature. The carbon content is nearly as high as the Cd for the 100°C sample, meaning that a significant amount of non-radiative recombinations could occur when applied to a solar cell. The C content is similar for 150°C and 200°C with the latter being slightly lower. The N content is the lowest for 200°C and half of the 150°C. The N content is half of the Cd content for the 100°C indicating a high content of foreign atoms that might again contribute as recombination centers. The XPS Cd peak (not shown) can be fitted by a single peak, corresponding to CdS.
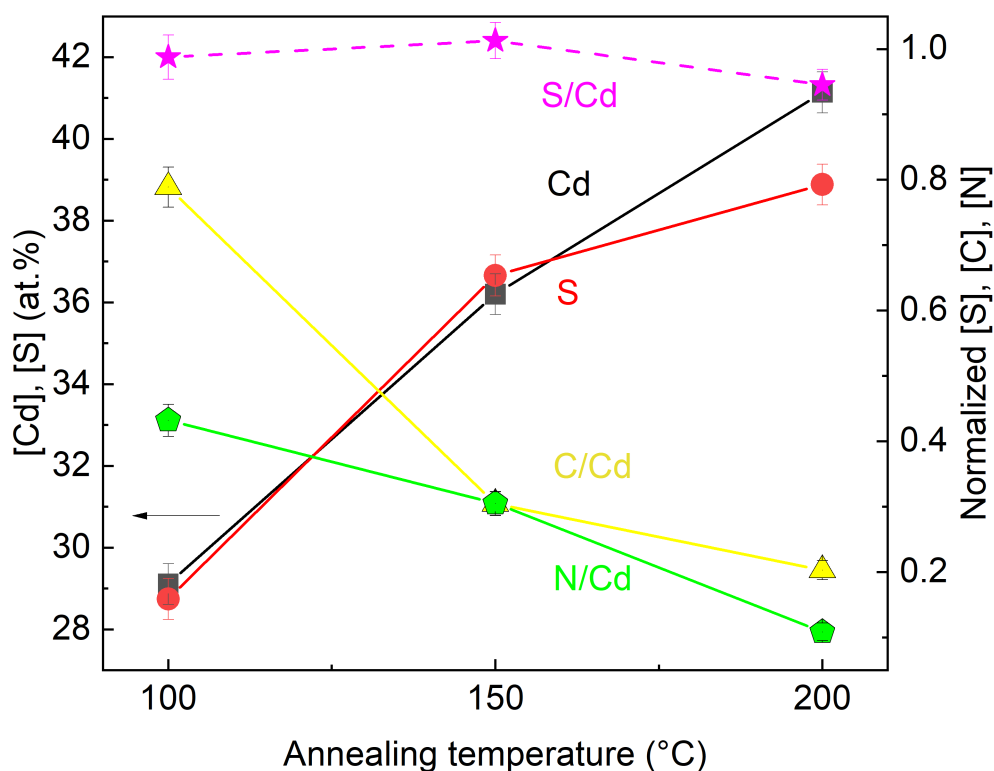
Figure 7.10: XPS measurement of inkjet printed CdS on Mo annealed at 100°C, 150°C and 200°C. Left y axis is for [Cd] and [S]. Right y axis is for all the others.

The fitting of the sulfur peak (not shown) showed an increasing S−C component when decreasing temperature corresponding to the bond in thiourea. It shows that even though CdS is formed, the break in the S−C does not occur. In summary, all the annealing temperatures (100°C, 150°C, 200°C) lead to the formation of CdS. The difference between

these samples lies in the residues content (N and C) that increases with a decreasing temperature. This could eventually lead to lower quality n-type semiconductor and thus less efficient solar cells due to recombination. A trade-off between the high band gap and the residues content should be found.

In short, the band gap of the inkjet printed films annealed at 100°C is 3.1 eV which is higher than the bulk band gap of 2.4 eV. The 150°C and 200°C have a similar band gap of 2.5 eV. It was shown with Raman and XRD that this increased band gap is related to the crystallite size. However, decreasing the annealing temperature leads to more residues content such as N and C which might act as recombination centers in a solar cell.

7.2.4 Influence of temperature for In_2S_3

As it was shown in 7.2.3, the band gap of CdS can be tuned by changing the annealing temperature. A similar tuning is shown in this section for In_2S_3. Figure 7.11 shows the band gap of inkjet printed In_2S_3 annealed at 250°C, 280°C and 310°C. A complete analysis of these films have been shown in section 5.7. The band gaps were extracted using a Tauc plot for direct band gap semiconductor and is not shown for the sake of brevity. The band gap of In_2S_3 decreases with an increasing annealing temperature which corresponds to an increase crystallite size. It is hypothesized that an increase in the heat provided to the sample promotes the crystal growth. The band gap of the sample annealed at 310°C is 2.6 eV which is 0.1 eV higher than the bulk value. This means that in order to have the bulk optical properties, the In_2S_3 has to be heated to a temperature higher than 310°C. In the case of solar cells, a high annealing temperature is undesirable since it might hurt the CIGSSe. Moreover, an annealing at 310°C led to the incorporation of oxygen in the lattice (section 5.7). Finally, an increase in the band gap is desirable to avoid the blue defect in the solar cells. An annealing temperature lower than 250°C could be tried to increase the band gap of the material by decreasing its crystallite size. Indeed, the TGA shown in section 5.1 points to a minimum annealing temperature of 240°C. However, this measurement was performed on bulk powder which means that the required annealing temperature for a thin film might be lower.

In summary, this chapter shows that the band gap [2] of the inkjet printed materials is higher than their bulk counterparts. This can be explained by the size of the small crystallites that form the material. When applying the Brus model, that links the band gap to the crystallite size, the expected band gap was similar to the measured band gap obtained with Tauc plot. The Brus model should however be interpreted with care since it has limitations and uses approximations. Furthermore, the band gap was tuned for CdS and In_2S_3 by changing the annealing temperature of the materials that modifies the

---

[2]The band gap was measured on films deposited on glass or quartz and should only be used as an indication since it might different on CIGSSe which is the actual interesting band gap.
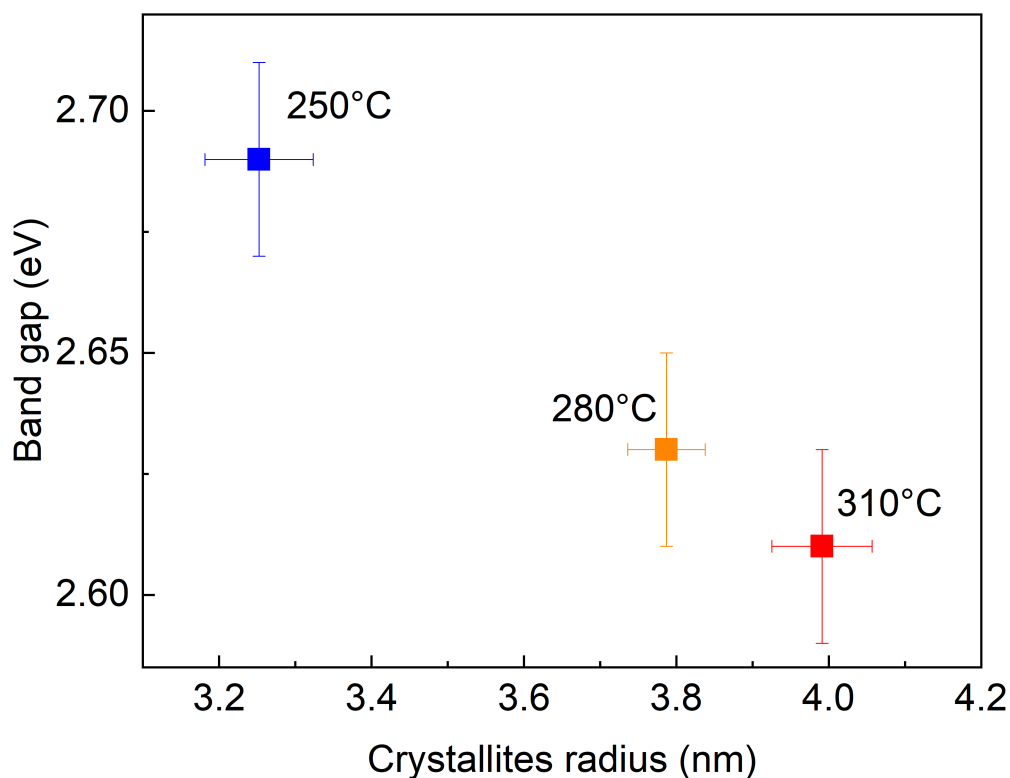
Figure 7.11: Band gap as a function of the crystallite size for inkjet printed In_2S_3 annealed at 250°C, 280°C and 310°C.

crystallite sizes. It has to be kept in mind that the annealing temperature is also used to evaporate the residues which means that a lower annealing temperature might lead to a higher residues content. Moreover, a higher annealing temperature can promote the incorporation of oxygen in the lattice. Figure 7.12 is a summary graph of the variation of the band gap with the crystallite size for In_2S_3 and CdS.
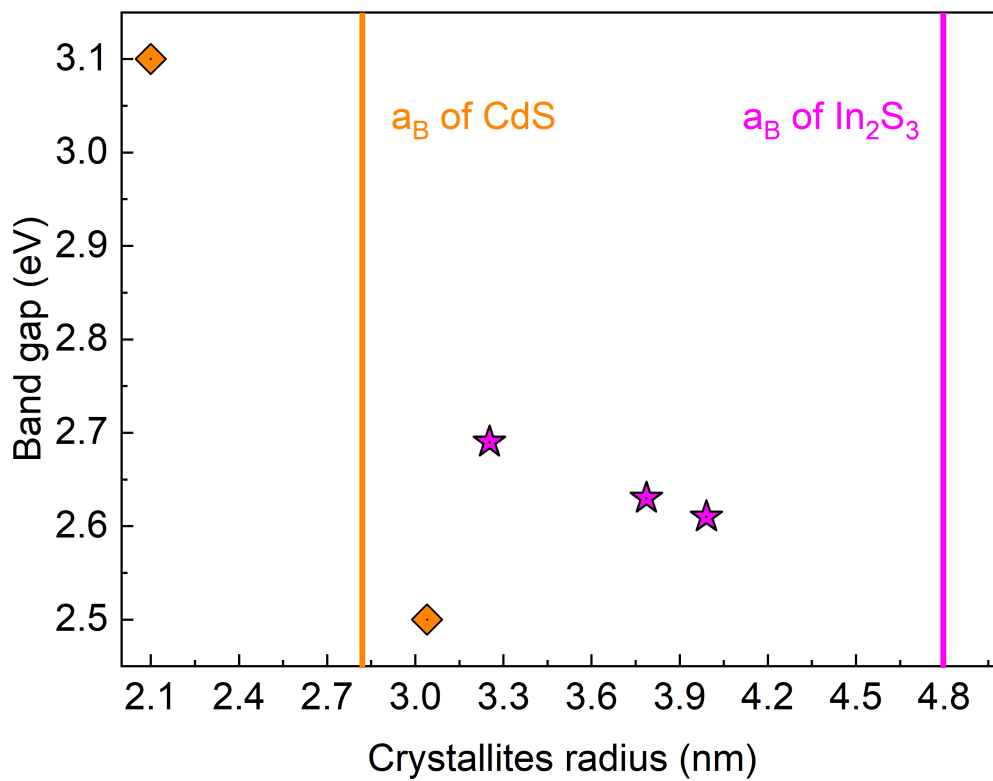
Figure 7.12: Band gap as a function of the crystallite size for inkjet printed In_2S_3 (pink) and CdS (orange). The vertical lines indicate the exciton Bohr radius. The x error is smaller than the symbols.

Chapter 8

Summary and outlook

In this work, In$_2$S$_3$ and CdS buffer layers were inkjet printed on CIGSSe and annealed. Additionally, the optical properties of Zn(O,S) were investigated. The inkjet printing followed by the annealing is a high temperature process contrarily to the chemical bath deposition.

Inkjet printing the buffer requires the synthesis of an ink containing the precursor of the materials. The printability of the various inks was assessed using the printing framework suggested by Derby. This required the measurement of the surface tension and viscosity. The solvent mixture was adapted to ensure a single drop ejection with a constant size and jetting rate. The wetting of these inks on different substrates was assessed and tuned by using UV ozone treatment. A wetting model was applied to predict the wettability of all potential salts free solvents on our substrates and the final solvent mixture has a volume ratio 1:1:2 water:propylene glycol:ethanol.

Inkjet printing being a versatile technique, the effect of a subtle variation of the buffer coverage on CIGSSe could be studied. This coverage was varied from a continuous film to a network of separated drops by applying a UV ozone treatment on CIGSSe prior to inkjet printing. The maximum efficiency was found for a fully covering buffer layer. The lower efficiency in the non/partially buffered devices was attributed to the sputtering damage occurring during the window deposition.

The role of ink composition on the morphology, composition and opto-electronic properties of the buffer layer was investigated. This study was done in the case of In$_2$S$_3$ buffer synthesized from an ink containing InCl$_3$ and thiourea (CH$_4$N$_2$S). The first parameter that was varied is the solvent mixture. It was stated above that the final solvent mixture contains propylene glycol (ppg). It was found that inks free of ppg or containing less ppg led to a higher film macro-roughness. The ink with the highest ppg content gave a smooth buffer layer macro-morphology and eased the printing process by decreasing the ink evaporation rate and increasing the viscosity. Even though the morphology of the buffer was smoother with a higher ppg content, the addition of this carbon source was a concern since carbon residues are known as recombination centers in solution processed

CIGSSe. Carbon and nitrogen (which originates from the thiourea molecule) residues were barely found in the buffer. Chlorine (from $InCl_3$) was present in around 3 at.%. in the film. Moreover, the annealing process to turn the precursor film into In_2S_3 was found to be responsible for the formation of an OVC, proving that Cu diffuses toward the buffer layer. The highest device efficiency was obtained with the smoothest buffer (i.e. highest ppg content). It was concluded that the improved efficiency was solely related to the macro-roughness of the film since no carbon residue was found.

The second parameter that was varied in the ink is the salts coordination. The pre-synthesis of an In-S bond as part of a complex prior to the dissolution in the ink as recommended in literature was shown unnecessary. A bond between $InCl_3$ and thiourea spontaneously formed in the solution as attested by Raman measurements. Different degrees of complex formation were found microscopically which were associated to different chemical environments. XRD showed that the In_2S_3 formed were free from oxygen and the unit cell is similar to the literature reference. The solar cells performed similarly for the pre-formed In-S bond and the simpler ink as well as an industrial reference cell with $Zn(O,S)$ buffer.

In the previous study, the sulfur to indium ($[S]/[In]$) ratio in the ink was 3. Since the pre-formed complex was shown to be unnecessary, the $[S]/[In]$ is free to be varied. The stoichiometric ratio of sulfur to indium for In_2S_3 buffer is 1.5. However, the stoichiometry of the salts in the ink, to maximize the efficiency of the solar cell, was found to be higher. Indeed, inks with a sulfur to indium ratio of 3, 2, 1.5 and 1 were synthesized. The resulting thin films showed higher purity in terms of composition and crystallography for the sulfur rich inks. This resulted in high performance for the solar cells with the ratio of 2 being the record solar cell (16.5%), exceeding the efficiency of a reference device with an industrial $Zn(O,S)$ (16.0%). This was possible thanks to an increase in the V_{oc} of 30 mV. The sulfur poor samples had a low performance, with the ratio of 1.5 being the worst. The morphology of these layers was getting denser microscopically with a decreasing sulfur to indium ratio. The sulfur rich samples had a porous morphology (pores on the order of 300 nm to 1 μm), while the sulfur poor were dense. This was associated to a solid state dewetting process related to the free energy of thiourea, which is the sulfur source in the ink. The porosity was confirmed by HIM-SIMS to expose the CIGSSe underneath. In terms of devices, no shunt issues (that could be spotted in a low shunt resistance) were found. It is hypothesized that the buffer essentially covers the (sparsed) pinholes which are often located in fully buffered regions. XRD showed that the stoichiometric and sulfur poor samples incorporated oxygen into the In_2S_3 material. The chlorine content was twice higher for these two films compared to the sulfur rich samples which is coherent with other processes involving $InCl_3$ as an indium source (such as spray pyrolisis). In a nutshell, the inkjet printed In_2S_3 produced less waste than other techniques such as spin coating, CBD, physical vapor deposition and sputtering while keeping good chemical

composition and crystal structure. The efficiency of the printed In_2S_3 buffered device was similar to the well performing sputtered Zn(O,S) buffered reference which is often preferred to other buffer layers.

CdS buffer layer has been used for decades and is commonly deposited through the wasteful CBD. However, its toxicity reduces its use even though it often performs well in CIGSSe devices. Inkjet printing is proposed as an alternative deposition technique for CdS to decrease the toxicity by lowering the waste. The first attempt was not successful due to the spontaneous reaction of the sulfur and cadmium sources in solution. The buffer was synthesized by printing successively the cadmium salt and the thiourea molecule on the sample. The layer ordering was shown to be crucial to achieve a favorable morphology. Indeed, when the thiourea layer was deposited first, the drying of the layer led to the formation of needle shapes related to a preferential growth of the crystal. This perturbed morphology influenced the spreading of the cadmium containing layer. Ultimately, the final morphology of the annealed buffer layer was highly inhomogeneous due to the detrimental first layer. The resulting pn junction was very low quality. On the other hand, printing the cadmium layer first led to a generally homogeneous morphology, solely perturbed by periodic thickness oscillation due to a machine-related defective printing process. The efficiency of the buffered device with the later layer ordering was similar to the efficiency with a CBD CdS. In summary, a CdS having similar properties to the CBD CdS and performing similarly in CIGSSe devices can be formed using inkjet printing and generate nearly zero waste. CdS can thus be used again in PV with much lower impact on the environment.

The band gap of the buffer layer is preferred to be wide in order to decrease/remove the parasitic blue defect. The band gap of In_2S_3 which can arguably be considered direct or indirect was extracted from reflectance and transmittance data. It was found to range from 2.7 eV to 3.5 eV for the direct band gap, which is high compared to the bulk value 2.5 eV. The Brus model linking the band gap to the crystallite size was used to explain this increased band gap. This model proposes that a smaller crystallite size corresponds to a wider band gap. The model and experimental data correlated well, however the model uses approximations that can lead to deviations. This result should thus be interpreted with care. The band gap of inkjet printed CdS and Zn(O,S) materials were also higher than their bulk counterparts and the Brus model proposed a similar blue shift in the band gap to the experimental data. Finally, it was found that the band gap could be manipulated by tuning the annealing temperature of the materials which controls the grain size. It is hypothesized that the heat provided during the annealing induces the growth of the crystal. However, the residues content is linked to the annealing temperature. A low temperature increases the band gap by reducing the grain size, however the residues content increases which could annihilates the benefit of a wide band gap.

Inkjet printing of buffer layers is a new work which offers lots of freedom to explore the field. To the best of our knowledge, only one paper on inkjet printed In_2S_3 buffer was published and none on inkjet printed CdS as a buffer. The results presented in this thesis raised many new questions and ideas. The first one treats the substrate treatment prior to the inkjet printing process. UV ozone treatment was used to adapt the wetting of the films. However, a low contact angle actually promotes the coffee ring effect that is undesirable. A high contact angle can be obtained by bypassing the UV ozone treatment. However, the numbers of defects in the film dramatically increases because of unremoved contamination. A treatment that cleans the surface and ensure a high contact angle could decrease the buffer porosity, increase the surface coverage and eventually increase the device efficiency.

The morphology of the sulfur rich based In_2S_3 films were porous and related to solid state dewetting. Since it is hypothesized that the dewetting is partially stopped because of the fast annealing that freezes the film with the observed morphology, a faster annealing could be used to completely stop the dewetting. In order to verify this hypothesis, a long annealing at the melting temperature of thiourea (182°C) should be performed. Once thiourea is melted, the solid state dewetting can occur and proceed to the next stages of dewetting, i.e. formation of separated islands instead of the current porous network. If dewetting is confirmed, flash lamp annealing (which is a technique that enables the heating of the film in a couple of seconds) can be used to bypass the dewetting. Another possibility is to exchange thiourea, i.e. the sulfur source, with another compound since thiourea is presumably responsible for this dewetting. Thioacetamide could be used as an alternative since it is soluble in water. Since dewetting depends on the interaction with the substrate, the morphology of the buffer can not be predicted and experimentation is essential.

A lack of collection at long wavelengths that might be related to a low doping of the buffer was observed in this thesis. The doping of the buffer layer was already shown to increase the efficiency of the cells in literature. Kim et al. [164] showed that an In_2S_3 buffer doped with 3% Sn^{4+} showed an increase efficiency of 40% relative to the undoped In_2S_3. Moreover, it was shown through HIM-SIMS that Na diffused toward the buffer layer. Na is often used as a dopant for both absorber and buffer layers. The impact of different dopants such as Sn, Na, Rb and K could easily be controlled by inkjet printing. Indeed, each dopant can be inkjet printed independently from a separate cartridge and their concentrations can be controlled through the drop spacing. The layer ordering, i.e. the dopant followed by the buffer material or the opposite, can also be studied.

The CdS buffer layer was synthesized with a [S]/[Cd] ratio of 1. However, a slight sulfur excess was shown to be profitable in the case of In_2S_3 and could be applied to CdS. A complete study of the crystallinity, morphology and chemical composition would be required. Moreover, the TU→Cd layer ordering was shown to lead to a detrimental

morphology due to the growth of needles during the drying of the TU layer. As discussed earlier, this phenomenon has been observed for urea and strategies have been studied to control this preferential growth mechanism. Inhibitors were added to the aqueous solution and these molecules would selectively bind to the fast growing face {001}. Acetone was found to decrease the growth rate of this face while the others stayed unaltered [165]. This strategy could be used to improve the morphology of the TU→Cd if this deposition ordering is required or preferred.

As shown with the case of CdS, the deposition of multiple layers leads to the formation of the final material. ZnMgO is a new material that attracts interest. Indeed, it was shown that ZnMgO can replace both the CdS and iZO in a CIGSSe device and give higher efficiency than a standard device with CdS/iZO [166]. Moreover, it was shown that the material stoichiometry, i.e. Zn_xMg_yO, can be tuned to increase the device efficiency. This tuning is easily done with inkjet printing using separate cartridges for Zn and Mg.

Thanks to the flexibility of inkjet printing, many more works than those cited above can be imagined and the future of inkjet printing in the field of photovoltaics is hopefully bright.

Appendix A

Appendix to chapter 4

A.1 Theory

A.1.1 Surface tension

As discussed in the main text, the surface tension of liquids is temperature dependent. Figure A.1a shows the surface tension of water and ethanol decreasing with temperature (up to 100°C). In order to control the surface tension a bit further, solvents mixtures can be considered. Figure A.1b shows that the surface tension of a water-ethanol mixture with an increase ethanol mole fraction. This decrease in surface tension is related to the interfacial mole fraction of ethanol as discussed in the main text.
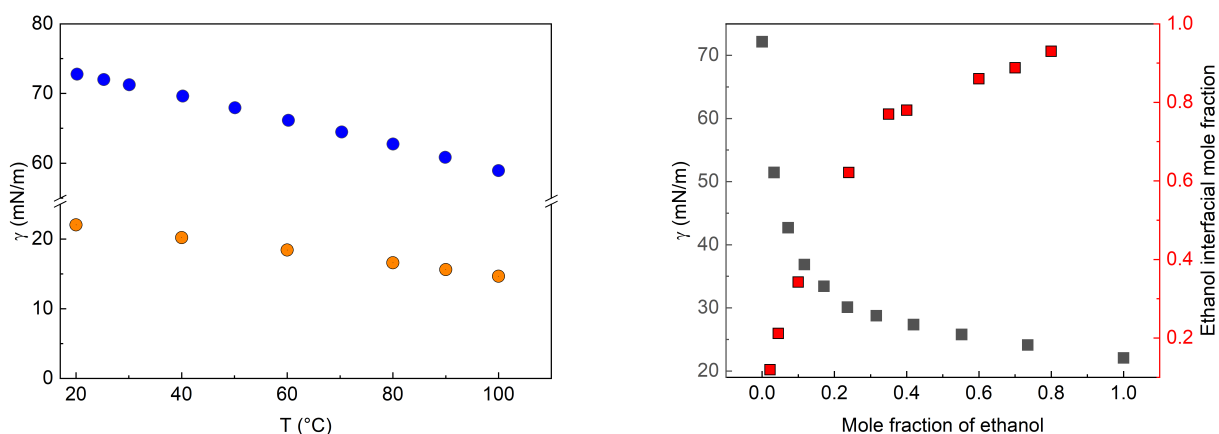
(a) Variation of the surface tension of pure water (blue circles) (re-plotted from [167] and pure ethanol (orange circles) (re-plotted from [168]) as a function of temperature.

(b) Surface tension (black squares) [83] and interfacial mole fraction (red squares) [86] of a water-ethanol mixture at 25°C.

Figure A.1

Ethanol was used to decrease the surface tension of the ink. However, the solubility of thiourea, which is a compound in nearly all the inks, is lower in water than in ethanol

[169]. This could lead to precipitation of thiourea and clogging of the nozzles. The concentration is thus limited but enough for the buffer layers. An alternative to solvents mixture to decrease the surface tension lies in the addition of surfactant. The advantage of these molecules, such as sodium dodecyl sulfate (SDS) or Triton X-100, is that the critical micelle concentration (CMC) is very low (0.008 M for SDS), implying that a small concentration of this molecule will be enough to decrease the surface tension of the ink. However, when a new surface is formed, such as during the formation of a droplet before jetting in inkjet printing, the surfactant needs time to move from the bulk to the interface [170]. Kommeren et al. compared the time needed for 1-pentanol and a surfactant (capstone) to decrease the surface tension of an aqueous solution [171]. Figure A.2 shows 1-pentanol decreased the surface tension of water from 72 to 35 mN/m in less than 10 ms, which is the limit of the measurement method used. The capstone however, took 1000 ms to reach the equilibrium surface tension, which is around 18 mN/m. The lowest frequency used with our printer is 1000 Hz, meaning that one drop is ejected every 60 ms. Since this time is much smaller than the time needed to diffuse the surfactant from the bulk to the interface, this molecule has no effect on the surface tension for the jetting. Solvents mixture is thus the ideal method to decrease the surface tension (without considering the temperature).
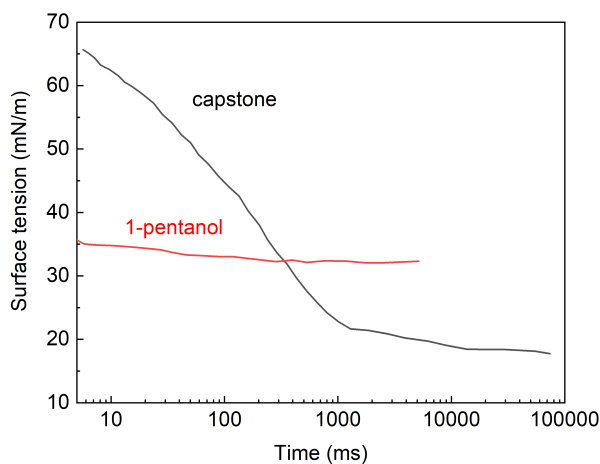
Figure A.2: Dynamic surface tension of an aqueous solution containing either 1-pentanol (2wt%) or capstone (0.1wt%). Data from [171].

A.1.2 Possible issues during inkjet printing

Once the rheology has been optimized, issues can still occur because of the sensibility of inkjet printing to small perturbations. Here are detailed some of the most important ones:

- Clogging: the liquid at the nozzle is in contact with air at room temperature. The

volume of solvents contained at the nozzle surface is small. Solvents such as water and ethanol are quick to evaporate and when doing so, the diluted salts precipitate at the nozzle. This forms a plug preventing new liquid from jetting. In general, the nozzle are unclogged by forcing the cartridge to purge some liquid. However, this process might not be sufficient in the case of serious clogging. In this case, a bath of the head in a good solvent for the salts is required in order to dissolve the salts from the outside of the cartridge. It happens that neither the purge, nor the bath are saving grace and that the head is considered dead. If the concentration of the salts in the ink allows (solubility decreases with temperature), keeping the cartridge at low temperature (in a fridge) extends the lifetime of the head.

- Deviated jetting: any impurity at the nozzle, such as salts residue or contamination, might act parasitically on the stability of the jetting. When the jet reaches that impurity, the trajectory is disturbed and the drop does not fly straight. The consequence is an uncontrollable pattern on the substrate. The solution is a purge to remove the salts, a bath of the head or a light cleaning with a lint free tissue soaked with a good solvent.

- No jetting or incoherent behaviour: because of the presence of high vapor pressures liquids such as ethanol and water, the composition of the ternary mixture changes with time. The viscosity can increase because of the evaporation of the low viscosity liquids as well as because of the increase in concentration of the salts. Since the first liquid to evaporate will be ethanol, the surface tension will also increase. An increased surface tension and viscosity can push the ink outside of the printable zone in the phase diagram. At this stage, even with the highest actuation voltage and temperature, the ink might not jet anymore. The only solution to this issue is to prepare a new cartridge.

- Difference in drop spacing in x and y direction: figure A.3a shows inkjet printed drops with three active nozzles and two printing cycles resulting in 6 rows of drops. The drop spacing in x direction is 207 µm which is similar in the y direction in the same printing cycle, i.e. y_1. The y spacing between two printing cycle, i.e. y_2 is however different (369 µm). It results in a spacing difference of 162 µm, which is the size of a drop. This means that this problem is similar to a missing drop because of a clogged nozzle. The repeatability of the printer is 25 µm, which is well below the difference in x and y drop spacing and can thus not be solely responsible for the gap. This issue can influence the morphology of an inkjet printed film. if the drop spacing is similar or smaller than this gap, the thickness of the film varies (fig A.3b). If the drop spacing is much smaller than the unintended gap, the film is smooth and nearly free of height variation (fig A.3c). This problem is actually a

bit more complex because the spreading of the drop has to be taken into account. For a constant drop spacing and unintended gap, a wider drop can diminish the issue, while a smaller drop increases the distance between the edges of the drops and enhances the issue.
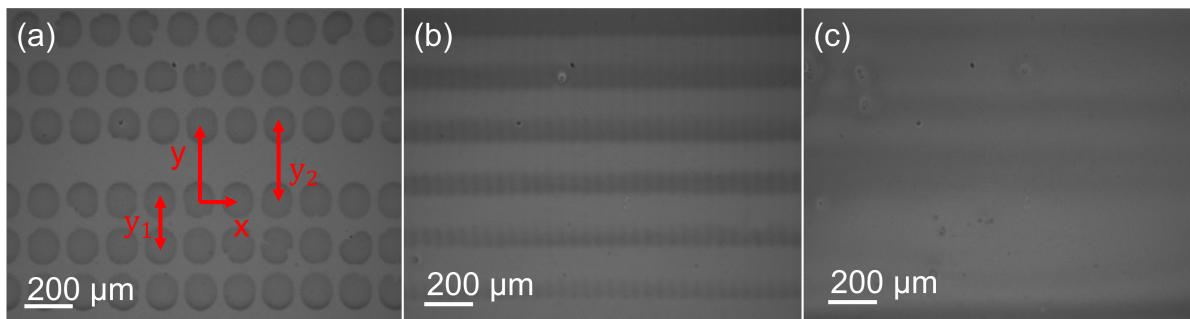
Figure A.3: (a) inkjet printed drops with three active nozzle and two printing cycles showing a difference in drop spacing between printing cycles. (b) inkjet printed film in which the drop spacing is similar to the gap size. (c) inkjet printed film in which the drop spacing is much smaller than the drop gap size.

A.1.3 UV ozone treatment

UV-ozone treatment uses radiations of two different wavelengths: 184.9 nm and 253.7 nm [172]. The first one is used to decompose O_2 into two oxygen radicals and form O_3. The second one enables the decomposition of ozone (O_3) into a molecular O_2 and a single activated O radical, which is a strong oxidizing agent. The energy per mol produced by a UV ray with a wavelength of 184.9 nm is

$$E = \frac{N_A hc}{\lambda} = \frac{6.022 \ 10^{23} \ \times 6.626 \ 10^{-34} \ \times 3 \ 10^8}{184.9 \ 10^{-9}} = 647 \ kJ/mol \qquad (A.1)$$

with N_A, h, c and λ, the Avogadro number, the Planck constant, the light speed and the wavelength of the UV light. Similarly, the energy per mol for a wavelength of 253.7 nm is 472 kJ/mol. This energy is also used to break the bounds in the organic molecules. Some examples of bonding energies are reported in the table A.1. In the case of the $C-C$ bond commonly found in organic impurities, both radiations will produce enough energy to break the bond. Reaction with the activated O will form oxides such as CO_2, H_2O and O_2 that will evaporate. It has to be noted that the surface under the contamination is also impacted by the treatment: the highly reactive oxygen oxidizes the surface.

John R. Vig showed that the presence of both radiations and ozone is not mandatory but dramatically increases the efficiency of the impurity removal [172]. Metal surfaces can be cleaned without any damage as long as the exposure is strictly the time needed to clean the surface. This time can be as low as 1 minute for surfaces which are well precleaned [172].

Bond	Bond energy (kJ/mol)
O−O	138
O=O	490
O−H	462
C−C	347
C−H	413
C=C	607

Table A.1: Bonding energy of typical organic impurities. Data from [173]

Appendix B

Appendix to chapter 5

B.1   Surface coverage

The surface coverage of the buffer layer is expected to have an effect on the series and shunt resistances of the devices. Figure B.1 shows that the series resistance is similar for all the devices. However, the shunt resistance is highly influenced by the coverage. Indeed, shunt paths are present in the absorber. If these pinholes are covered by a resistive layer (i.e. the buffer layer), they are closed and the shunt is avoided. The shunt resistance indeed increases with the surface coverage. The CdS reference device however also shows a low shunt resistance. It is hypothesized that when doing CBD, the buffer is not covering pinholes because of the small thickness of the film and that the buffer layer does not nucleate above the holes present in the CIGSSe absorber.
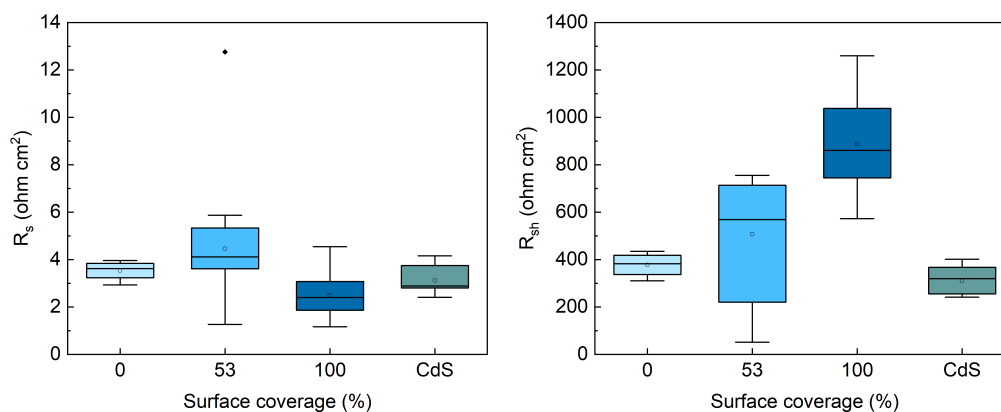
Figure B.1: series (R_s) and shunt (R_{sh}) resistances as a function of the surface coverage by the In_2S_3 buffer and reference cell with CdS buffer.

B.2   Complex/No Complex

After the annealing process, several residues can be expected in the buffer layer: carbon, essentially coming from the propylene glycol, nitrogen from the thiourea, chlorine from indium chloride and oxygen from the combustion reaction. XPS (fig B.2a) shows that the carbon content is very high at the front of the sample for both In_2S_3 covered CIGSSe and bare CIGSSe. Since it is also present on the bare absorber, this is attributed to the air contamination. The oxygen content is also higher in the bare CIGSSe than in the other samples and the same argument as for the carbon is applied here. The absence of oxygen after one sputtering cycle (within the detection limit which is around 1 at.%) confirms the absence of the bulk formation of oxide as shown previously with XRD measurement. The nitrogen residue is found to disappear after one etching round and was either pushed to the front surface during the annealing or is a contamination from air. The chlorine residue is found deeper in the layer and a difference of profile can be spotted between complex and No Complex. Different arguments can be proposed such as the porosity of the layer that spatially varies or the fact that the chlorine concentration is near the detection limit of the machine and make this quantification barely reliable. The sulfur to indium ratio (fig B.2b) is higher than the expected ratio for the very front surface and then decreases to ± 1.5 for around 1000 s and drops again to lower values. The copper to indium ratio (figure B.2c) is relatively constant in the film for the bare absorber except at the front surface. The trend in [Cu]/[In] ratio is the same for Complex and No Complex.

As discussed in section 5.5, the shunt and series resistances (fig B.3) trends are unrelated to the fill factor of the complex. Moreover, the series resistance of Zn(O,S) is higher than the indium sulfide and the shunt resistance is lower which would give a lower FF, opposite to the actual behaviour. The series resistance data spreading seems to be large, however the impact on the FF is around 1% which is lower than the measured variance on the FF.

An optimization of the thickness of the buffer is shown on figure B.4. Since the films are porous, the determination of a thickness is hardly reliable and the drop spacing (DS) is used as a thickness parameter. A smaller drop spacing corresponds to a thicker film. The extreme thicknesses, i.e. the thickest and thinnest films, have a lower efficiency. The qFLs of the bare absorbers are all similar (10 meV being considered as the error). After the buffer deposition, the qFLs is decreased by more than 10 meV. The V_{oc} has tight distribution for the thickest sample with a mean value at 620 mV, which is 40 mV lower than the qFLs. In the case of the intermediate thickness, the distribution is wider but the mean value is centered at 635 mV which is 15 mV lower than the qFLs. The mean V_{oc} is thus higher than the thicker film and the voltage loss is smaller. The thinnest buffer has the lowest mean value (below 610 mV) with the largest distribution. The voltage loss
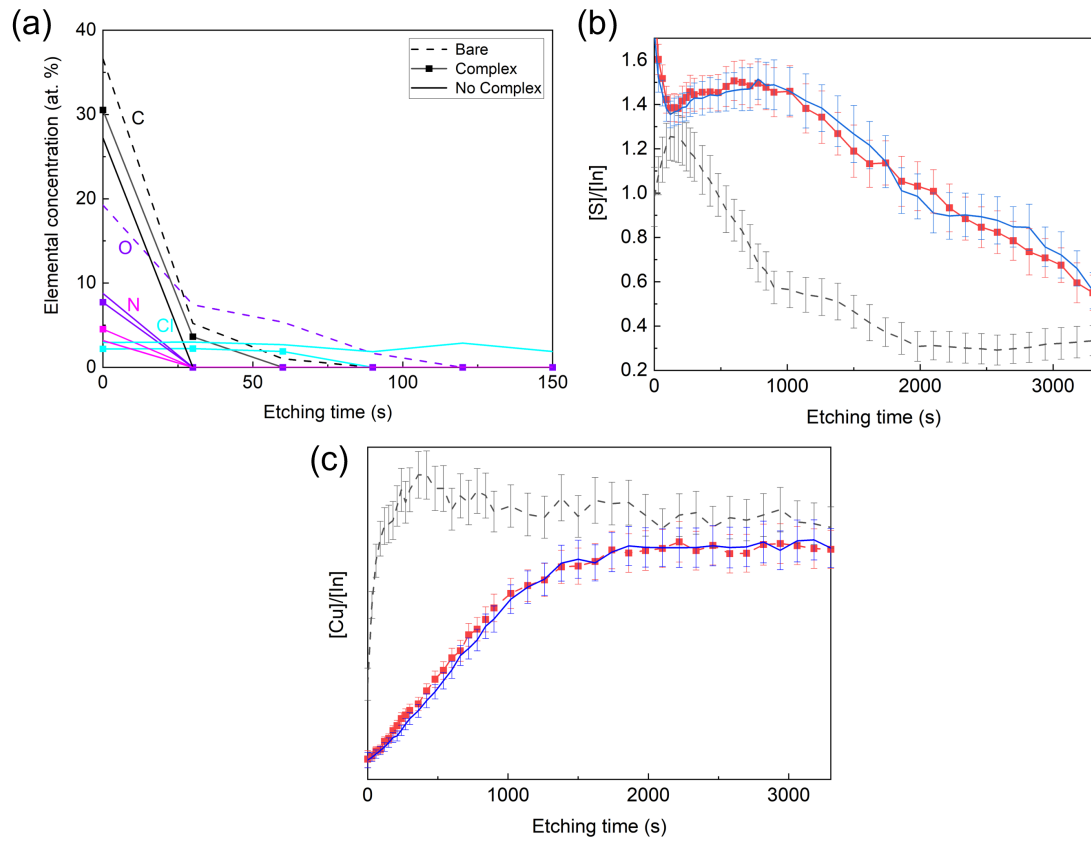
Figure B.2: XPS depth profiling of bare CIGSSe and In_2S_3/CIGSSe stacks where the buffer is based on complex and No Complex inks. (a) residues (C, O, N and Cl) at the front (small etching time), (b) [S]/[In] and (c) [Cu]/[In]. The error bars ($\pm$ 1 at.% were omitted in (a) for clarity of the data.
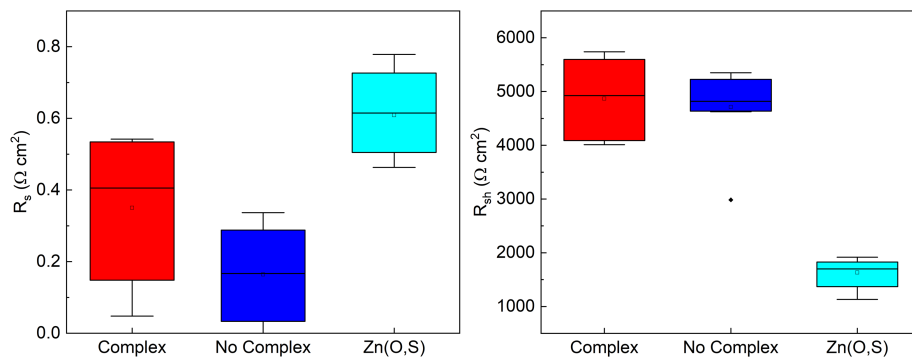
Figure B.3: series and shunt resistances for cells with an In_2S_3 buffer from complex and No Complex inks and the reference with Zn(O,S)

is as high as 50 mV. The intermediate thickness thus give the highest voltage and the lowest voltage loss. The fill factor is equal for the intermediate and thinnest sample but is lower for the thickest. This can not be explained by the series and shunt resistances that do not follow the same trend: the series resistance should be the highest for the

thicker film and similar for the other two. Moreover, the shunt resistance is so high that the variation between the devices has negligible effects. The J_{sc} is also higher for the intermediate thickness compared to the thickest and thinnest film. The ideal thickness was thus determined as the DS 40.
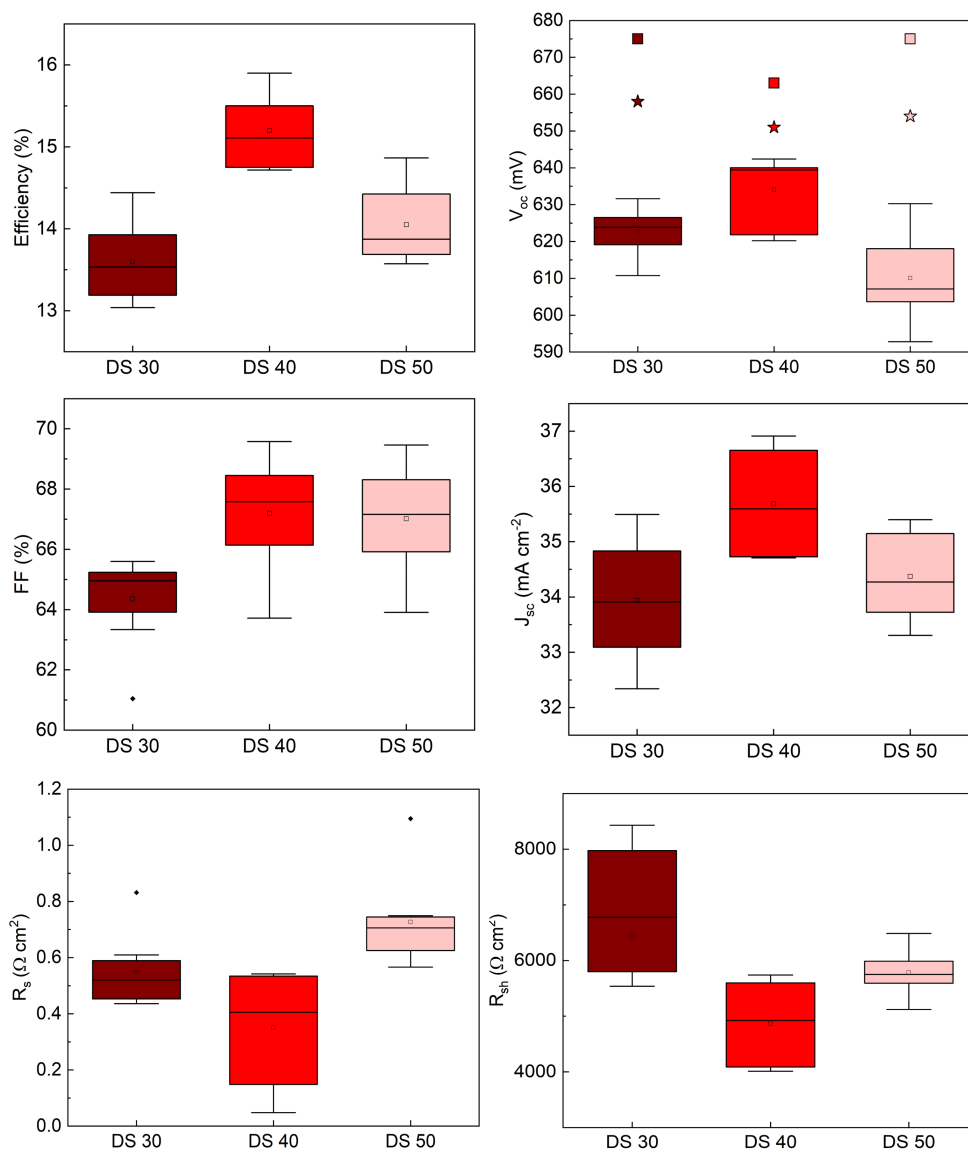
Figure B.4: Optoelectronic properties of solar cells with different thicknesses (DS) of an In_2S_3 buffer layer from the complex ink: efficiency, V_{oc}, FF, J_{sc}, R_s and R_{sh}. The squares and stars in V_{oc} represents the qFLs before and after the deposition of the buffers respectively.

B.3 Sulfur to indium ratio

In order to determine whether the porosity of the film found for [S]/[In]=3 is due to the concentration of the salts, the concentration of the ink was divided by four. The

interaction of the ink with the substrate changed as shown in figure B.5a,b. The size of a drop from the low concentration ink, called [S]/[In]=3 low c has a diameter of 150 μm, while the higher concentration, called [S]/[In]=3 is 90 μm. As mentioned in table 4.1, the surface tension of both inks is identical inside the error. Based on the Young equation, the contact angle can be influence by the free energy between the solid and the liquid, the solid and the vapor and/or the liquid and the vapor (surface tension). Since the latter is constant and that we can safely hypothesize that the interaction between the solid and the vapor is also constant, the free energy between the liquid and the solid is solely responsible for the change in the contact angle, i.e. the drop diameter. This means that the salt concentration modifies the interaction between the solid and the liquid, inducing a better wetting for the low concentration.

When drying and annealing both drops using the same process, the micro morphology looks very similar with porous structures (fig B.5 c,d). The micro morphology is taken from a film because the signal from a drop is blurrier. Indeed, as shown in figure B.6b taken on a drop, the porosity is barely visible compared to figure B.5d. This is simply due to charging effect because only Mo can be contacted with copper tape in the case of the drop, while this tape can be applied to the film and enable the removal of charges from the insulating indium sulfide.
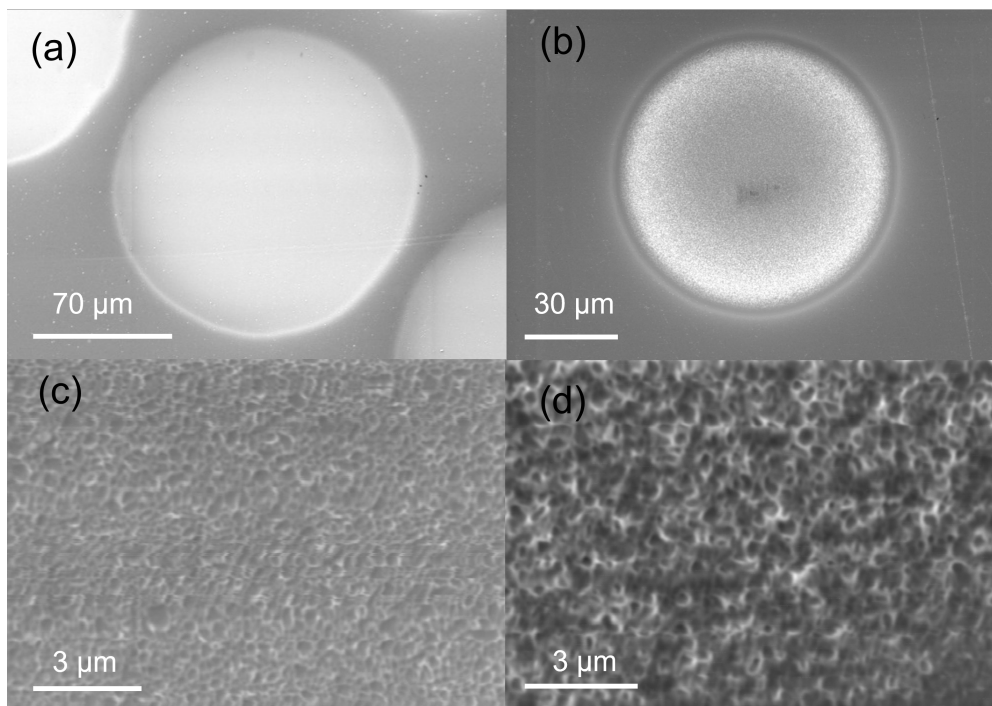
Figure B.5: SEM images of inkjet printed 2.4 pL drops of (a) [S]/[In]=3 low and (b) [S]/[In]=3 and (c) and (d) their associated micro morphology.

Nevertheless, figure B.6 shows that the apparent gradient of colours in the drop actually corresponds to different morphologies. In the middle, the morphology has small holes that become bigger when moving toward the edge. The dark edge was too hazy to be

resolved. An EDX mapping could not be obtained at this magnification for the annealed film because of the constant drifting due to the charging. Indeed, the acquisition time of an EDX map is much longer than for a simple SEM image. It can be concluded that the porosity is unrelated to the total concentration of the ink.
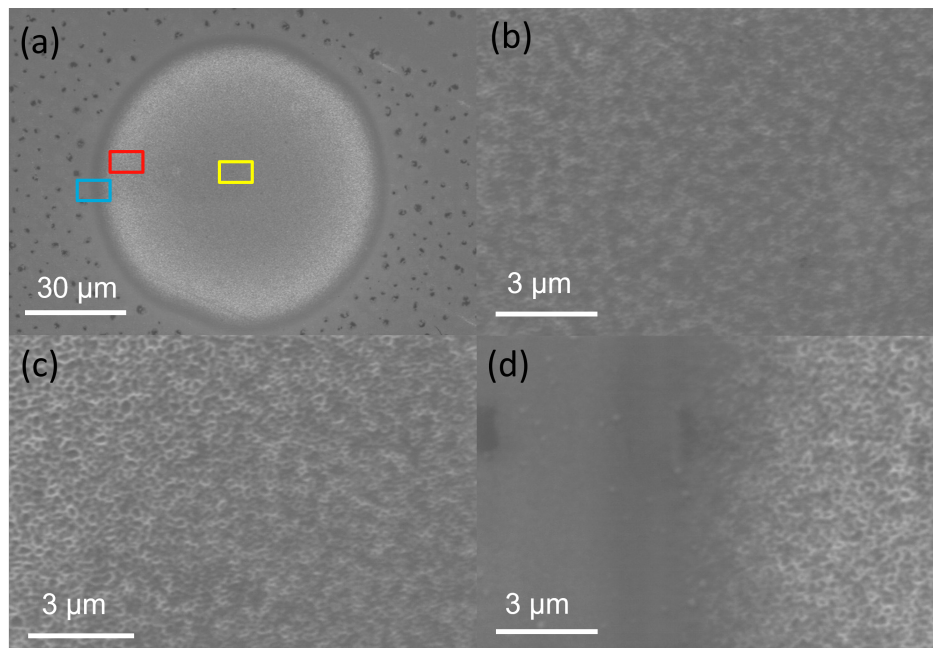
Figure B.6: SEM images of inkjet printed 2.4 pL drops of [S]/[In]=3. (a) Macro image. (b), (c) and (d) show the micro morphology of the drop in the regions highlighted in (a). Yellow, red and blue rectangle are image (b), (c) and (d) respectively.

The shunt resistance of the devices with different [S]/[In] ratios were found to be high for all devices even though the stoichiometric and sulfur poor showed low efficiency (fig B.7). This rules out the shunting of the cells. The series resistance are not shown because its extraction is done on the illuminated curve. However, the diode model could not be fitted correctly for the stoichiometric and sulfur poor samples. The series resistance is thus not commented in this work.

Similarly to the thickness optimization of the buffer in the Complex/No Complex section, different thicknesses were tried for the best performing device, i.e. [S]/[In]=2. The efficiency of the thickest buffer is similar to the intermediate thickness that was used in the previous experiment. However, the homogeneity seems to be higher since the distribution is tighter. The thinnest buffer is found to be detrimental for the cell. All V_{oc} and qFLs are similar for the different thicknesses. The efficiency trends is actually mostly influenced by the FF. Indeed, it decreases with the thickness of the buffer. Based on equation 3.16, the maximum FF is 73% which is the value of the best performing device. The FF trend could however not be explained by the resistances. Indeed, the series resistance is the highest for the thickest sample, contrary to the FF. Anyway, the values of the series resistance are very low and do not have a big influence on the FF.
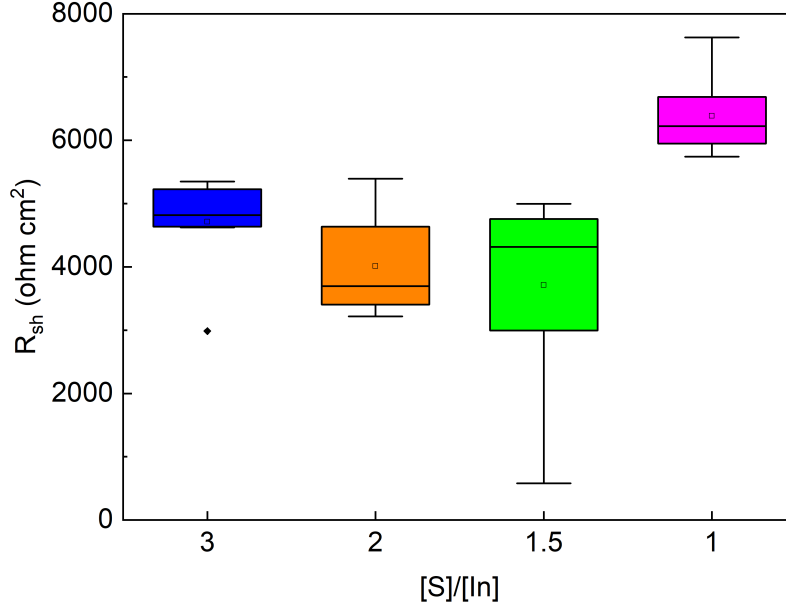
Figure B.7: Shunt resistance in the dark of cells with different [S]/[In] ratios.

The shunt resistances are high and relatively similar.

The J_{sc} is the highest for the intermediate thickness and similar for the thickest and thinnest films. This trend can be further investigated with EQE (fig B.9). Compared to the middle thickness (DS 40), both the thickest (DS 30) and thinnest (DS 50) films show a lack of collection at long wavelengths. These two samples were processed in a second batch and all the samples from this batch showed a lack of collection at long wavelengths, independently on the process (air, nitrogen, drop spacing, ...). This lack of collection is probably unrelated to the buffer itself but rather to an unknown issue during the processing. A second observation is that both DS 40 and 50 show oscillations in the EQE corresponding to interference of the light because of the layers stack. The difference in thickness of the buffer can be seen in the shift of the oscillations peaks toward longer wavelengths. The very short wavelengths (around 400 nm) show a pronounced loss for DS 30 and 50 that might actually be related to the windows (for example a different thickness). The thickest film shows damped oscillation that is probably related to the thickness of the layer preventing interference. The extracted J_{sc} from EQE are 34.6 mA/cm^2, 35.8 mA/cm^2 and 34.3 mA/cm^2 for DS 30, 40 and 50 respectively. The lack of collection at the back does not have too much influence on the J_{sc}. Since the J_{sc} obtained from IV is dependent on an area measurement, it is often considered to be less reliable than the J_{sc} from EQE. Table B.1 shows the parameters of the best devices. The efficiency was recalculated based on the J_{sc} from EQE. It is lower by around 0.5% absolute.

The annealing in nitrogen of [S]/[In]=1 showed a dramatic increase in efficiency. In order to improve the [S]/[In]=1.5 devices, the cell was annealed in nitrogen. Figure B.10
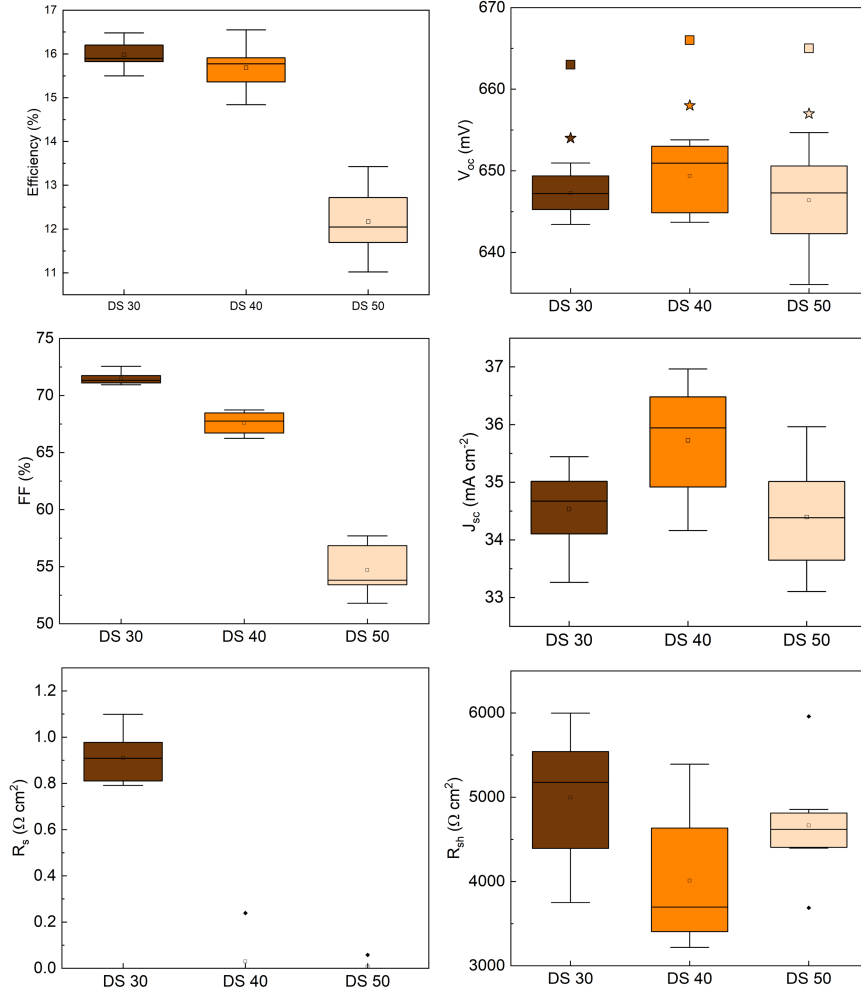
Figure B.8: Optoelectronic properties of 8 cells with varying In$_2$S$_3$ buffer thickness from inks containing a [S]/[In]=2. The star squares and stars on the V$_{oc}$ graph represent the qFLs before and after the buffer deposition.

	Eff$_{IV}$ (%)	V$_{oc}$ (mV)	FF (%)	IV J_{sc} (mA/cm^2)	EQE J_{sc} (mA/cm^2)	Eff$_{EQE}$ (%)
DS 30	16.5	650	73	35.4	34.6	16.1
DS 40	16.5	651	69	37.0	35.8	16.0
DS 50	13.4	647	58	36.0	34.3	12.8

Table B.1: Best devices parameters for [S]/[In]=2.

shows the performance of the cell with a buffer with [S]/[In]=1.5 annealed in air and in nitrogen. The average efficiency is slightly increased when the buffer is annealed in nitrogen, however the data spreading is bigger pointing to inhomogeneities. The open circuit voltage and fill factor are lower but the short circuit current density is higher. The series resistance can not be commented because of the S-Shape of the JV curve mentioned earlier preventing the correct extraction of R_s. The shunt resistances are similar and in
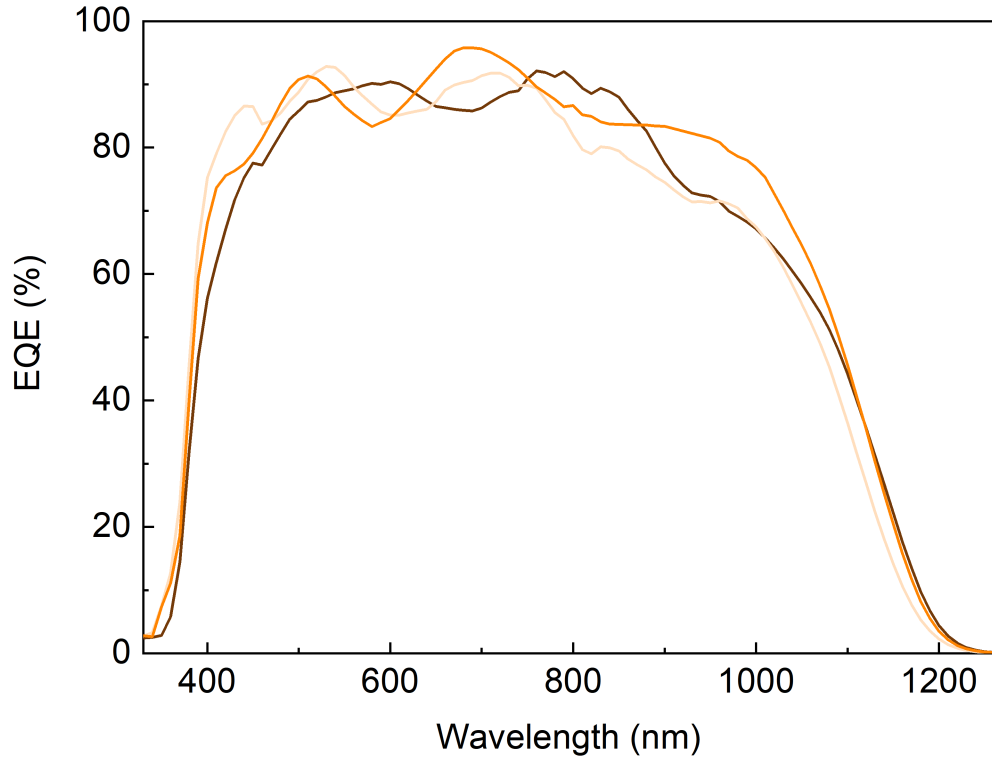
Figure B.9: EQE of best devices with an In_2S_3 buffer from inks with [S]/[In]=2 with different drop spacing: DS 30 (dark orange), DS 40 (orange) and DS 50 (light orange).

the range of 5000 Ωcm^2.
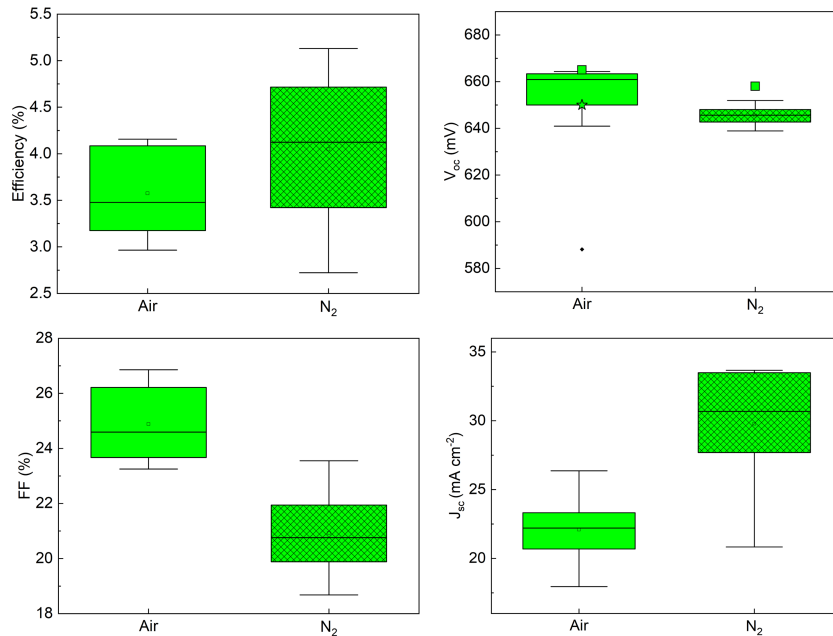
Figure B.10: Optoelectronic properties of 8 cells with $In(O,OH,S)_x$ buffer from the ink containing a [S]/[In]=1.5 annealed in air and in nitrogen. The star squares and stars on the V_{oc} graph represent the qFLs before and after the buffer deposition.

Figure B.11 shows that the interference peaks are shifted between the air and the nitrogen samples, indicating a variation in the thickness of the front layers or to a change in the refractive index of the buffer. The EQE is generally higher in the visible range for the nitrogen sample and both samples have a lack of collection at the back. The J_{sc} is 32.0 and 36.0 mA/cm^2 for nitrogen and air annealed samples respectively. Interestingly, the J_{sc} from EQE and IV match for the nitrogen sample while it is quite different for the air sample as already discussed. The quality of the pn junction probably improved by annealing in nitrogen but the FF decreased and dragged the efficiency down. No significant improvement is obtained by annealing in nitrogen.
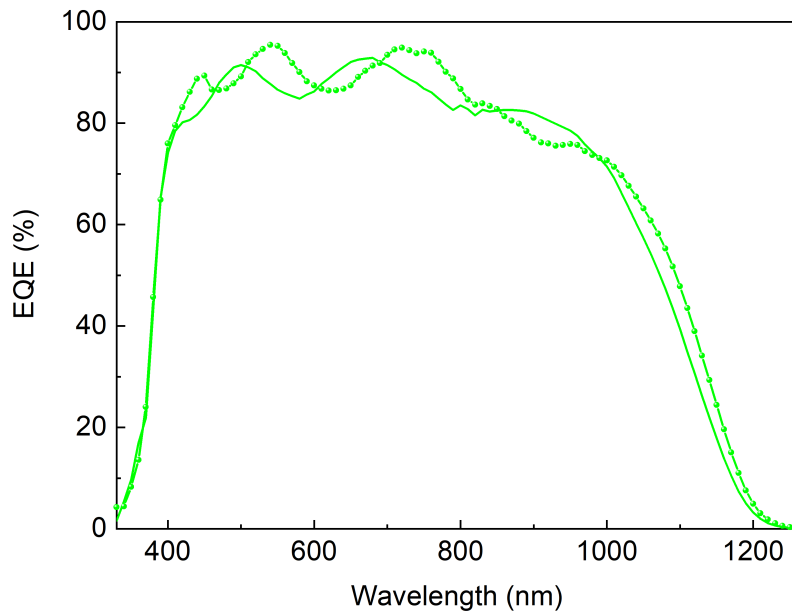
Figure B.11: EQE of best devices with an In(O,OH,S)$_x$ buffer from inks with [S]/[In]=1.5 annealed in different media: air (solid line) and nitrogen (line+symbols).

Acknowledgements

thanks goes to my Mom. She always gave her everything so that I could achieve all my dreams. She is the reason I never gave up even in the darkest moments when I only wanted to stop everything and go live in the mountains. I will forever be grateful for everything she gave me in life.

The last words go to my Cats. Robin, Alvin and Sethy are always waiting for me at home and meowing to cheer me up. Even though they sometimes drive me crazy, they are the little Suns in my life.

Bibliography

[1] *International energy agency, World Energy Outlook 2019.* URL: https://www.iea.org/.

[2] O. Hoegh-Guldberg et al. "Chapter 3: Impacts of 1.5°C global warming on natural and human systems". In: *Special Report, Intergovernmental Panel on Climate Change* ISBN 978-92-9169-151-7 (2018), pp. 175–311.

[3] Valérie Masson-Delmotte et al. *Global warming of 1.5°C - Summary for Policymakers.* 2018, p. 32. ISBN: 9789291691517. URL: https://report.ipcc.ch/sr15/pdf/sr15_spm_final.pdf%0A.

[4] J. Rogelj et al. "Chapter 2:Mitigation Pathways Compatible with 1.5°C in the Context of Sustainable Development". In: *IPCC special report Global Warming of 1.5 ⁰C* (2018), 82pp. URL: https://www.ipcc.ch/site/assets/uploads/sites/2/2019/02/SR15_Chapter2_Low_Res.pdf.

[5] Roland Scheer and Hans-Werner Schock. *Chalcogenide Photovoltaics.* 2011. ISBN: 9783527326471. DOI: 10.1002/9783527633708.

[6] William N. Shafarman, Susanne Sieventritt, and Lars Stolt. *Photovoltaic Science Handbook of Photovoltaic Science.* 2011. ISBN: 9780470721698.

[7] D. C. Northrop. *Book Review: Solar Cells: Operating Principles, Technology and System Applications.* 1983. DOI: 10.1177/002072098302000219.

[8] Meng Tao. *Physics of solar cells.* 2014. ISBN: 3527404287. DOI: 10.1007/978-1-4471-5643-7{_}3.

[9] Jenny Nelson. *The physics of solar cells.* 2003.

[10] Marika Bodegard, Angela Kylner, and Lars Stolt. "ZnO/CdS/Cu(In,Ga)Se2 thin film solar cells with improved performance". In: *IEEE* (1993).

[11] Marika Bodegard et al. "The behaviour of Na implanted into Mo thin films during annealing". In: *Solar energy materials & solar cells* 58 (1999), pp. 199–208.

[12] Nandang Mufti et al. "Review of CIGS-based solar cells manufacturing by structural engineering". In: *Solar Energy* 207.July (2020), pp. 1146–1157. ISSN: 0038-092X. DOI: 10.1016/j.solener.2020.07.065.

[13] Xunyan Lyu et al. "Influences of sulfurization on performances of Cu(In,Ga)(Se,S)2 cells fabricated based on the method of sputtering CIGSe quaternary target". In: *Journal of Alloys and Compounds* 791 (2019), pp. 1193–1199. ISSN: 09258388. DOI: 10.1016/j.jallcom.2019.03.355.

[14] M. Bär et al. "Determination of the band gap depth profile of the penternary Cu(In (1-x)Gax)(SySe(1-y))2 chalcopyrite from its composition gradient". In: *Journal of Applied Physics* 96.7 (2004), pp. 3857–3860. ISSN: 00218979. DOI: 10.1063/1.1786340.

[15] Zacharie Jehl Li Kao, Taizo Kobayashi, and Tokio Nakada. "Modeling of the surface sulfurization of CIGSe-based solar cells". In: *Solar Energy* 110 (2014), pp. 50–55. ISSN: 0038092X. DOI: 10.1016/j.solener.2014.08.004.

[16] Ramis Hertwig et al. "Investigation and Mitigation of Sputter Damage on Co-Evaporated Cu(In,Ga)Se2 Absorbers for Photovoltaic Applications". In: *Solar RRL* 6.9 (2022), pp. 1–9. ISSN: 2367198X. DOI: 10.1002/solr.202200268.

[17] B. Misic et al. "Shunt mitigation in ZnO:Al/i-ZnO/CdS/Cu(In,Ga)Se2 solar modules by the i-ZnO/CdS buffer combination". In: *Physica Status Solidi (A) Applications and Materials Science* 212.3 (2015), pp. 541–546. ISSN: 18626319. DOI: 10.1002/pssa.201431496.

[18] D. Hariskos, S. Spiering, and M. Powalla. "Buffer layers in Cu(In,Ga)Se2 solar cells and modules". In: *Thin Solid Films* 480-481 (2005), pp. 99–109. ISSN: 00406090. DOI: 10.1016/j.tsf.2004.11.118.

[19] Motoshi Nakamura et al. "Cd-Free Cu(In,Ga)(Se,S)2 thin-film solar cell with record efficiency of 23.35%". In: *IEEE Journal of Photovoltaics* 9.6 (2019), pp. 1863–1867. ISSN: 21563403. DOI: 10.1109/JPHOTOV.2019.2937218.

[20] Pedro M.P. Salome et al. "Cd and Cu Interdiffusion in Cu(In, Ga)Se2/CdS Hetero-Interfaces". In: *IEEE Journal of Photovoltaics* 7.3 (2017), pp. 858–863. ISSN: 21563381. DOI: 10.1109/JPHOTOV.2017.2666550.

[21] Sol Lee et al. "Effect of annealing treatment on CdS / CIGS thin film solar cells depending on different CdS deposition temperatures". In: *Solar Energy Materials and Solar Cells* 141 (2015), pp. 299–308. ISSN: 0927-0248. DOI: 10.1016/j.solmat.2015.05.052.

[22] Kannan Ramanathan et al. "Properties of 19.2 % Efficiency ZnO/CdS/CuInGaSe2 thin-film solar cells". In: *Progress in Photovoltaics: Research and Applications* 11 (2003), pp. 225–230. DOI: 10.1002/pip.494.

[23]   A. S. Najm et al. "An in-depth analysis of nucleation and growth mechanism of CdS thin film synthesized by chemical bath deposition (CBD) technique". In: *Scientific Reports* 12.1 (2022), pp. 1–20. ISSN: 20452322. DOI: 10.1038/s41598-022-19340-z.

[24]   Fouad Ouachtari et al. "Influence of Bath Temperature , Deposition Time and [S]/[Cd] Ratio on the Structure, Surface Morphology, Chemical Composition and Optical Properties of CdS Thin Films Elaborated by Chemical Bath Deposition". In: *Journal of Modern physics* 2 (2011), pp. 1073–1082. DOI: 10.4236/jmp.2011.29131.

[25]   Miguel A Contreras et al. "Optimization of CBD CdS process in high-efficiency Cu (In , Ga) Se 2 -based solar cells". In: *Thin Solid Films* 403-404 (2002), pp. 204–211.

[26]   A. Romeo et al. "Development of thin-film Cu(In,Ga)Se2 and CdTe solar cells". In: *Progress in Photovoltaics: Research and Applications* 12.23 (2004), pp. 93–111. ISSN: 1062-7995. DOI: 10.1002/pip.527.

[27]   D Abou-ras et al. "Structural and chemical investigations of CBD- and PVD-CdS buffer layers and interfaces in Cu(In,Ga)Se2 -based thin film solar cells". In: *Thin Solid Films* 481 (2005), pp. 118–123. DOI: 10.1016/j.tsf.2004.11.033.

[28]   Jayesh Patel et al. "Spin-coating deposition of PbS and CdS thin films for solar cell application". In: *Applied Physics A: Materials Science and Processing* 117.4 (2014), pp. 1791–1799. ISSN: 14320630. DOI: 10.1007/s00339-014-8659-x.

[29]   Jiang Cheng et al. "High-efficiency Sb2Se3 thin-film solar cells based on Cd (S , O) buffer layers prepared via spin-coating". In: *Materials Chemistry and Physics* 303.99 (2023). DOI: 10.1016/j.matchemphys.2023.127794.

[30]   J C Ramos et al. "Inkjet Printed Thin Film Transistors Using Cadmium Sulfide as Active Layer Prepared by In-Situ Micro-Reaction". In: *ECS solid state letters* 2.9 (2013), pp. 2013–2015. DOI: 10.1149/2.004309ssl.

[31]   N Barreau. "Indium sulfide and relatives in the world of photovoltaics". In: *Solar Energy* 83.3 (2009), pp. 363–371. ISSN: 0038-092X. DOI: 10.1016/j.solener.2008.08.008.

[32]   K Kambas, A Anagnostopoulos, and J Spyridelis. "Optical Absorption Edge Investigation of CdIn2S4 and beta-In2S3 Compounds". In: *Phys. Stat. Sol.* 201 (1985), pp. 201–208.

[33]   Zongyan Zhao et al. "Band-edge electronic structure of β-In2S3: The role of s or p orbitals of atoms at different lattice positions". In: *ChemPhysChem* 13.6 (2012), pp. 1551–1556. ISSN: 14397641. DOI: 10.1002/cphc.201100968.

[34] A. A. El Shazly et al. "Electrical properties of beta-In2S3 thin films". In: *J. Phys. Condens. Matter* 10 (1998), pp. 5943–5954.

[35] J George et al. "Reactively Evaporated Films of Indium Sulphide". In: *Phys. Stat. Sol.* 123.106 (1988), pp. 123–131.

[36] N Barreau, S Marsillac, and J C Berne. "Optical Properties of Wide Band Gap Indium Sulphide Thin Films Obtained by Physical Vapor Deposition". In: *Phys. Stat. Sol.* 186.1 (2001), pp. 179–186.

[37] N Naghavi et al. "Growth studies and characterisation of In 2 S 3 thin films deposited by atomic layer deposition (ALD)". In: *Applied Surface Science* 222 (2004), pp. 65–73. DOI: 10.1016/j.apsusc.2003.08.011.

[38] E. B. Yousfi et al. "Cadmium-free buffer layers deposited by atomic layer epitaxy for copper indium diselenide solar cells". In: *Thin Solid Films* 361 (2000), pp. 183–186. ISSN: 00406090. DOI: 10.1016/S0040-6090(99)00860-3.

[39] R. Bayon, C Maffiotte, and J Herrero. "Chemical bath deposition of indium hydroxy sulphide thin: process and XPS characterization". In: *Thin Solid Films* 353 (1999), pp. 100–107.

[40] R. Bayon and J. Herrero. "CBD-In(OH)xSy thin films: an approach to the growth mechanism". In: *Mat. Res. Soc. Symp. Proc. Vol* 668 (2001), pp. 1–6.

[41] Dimitri Hariskos et al. "A novel cadmium free buffer layer for Cu(In,Ga)Se2 based solar cells". In: *Solar Energy Materials and Solar Cells* 41-42 (1996), pp. 345–353. ISSN: 09270248. DOI: 10.1016/0927-0248(96)80009-2.

[42] C. D. Lokhande et al. "Chemical bath deposition of indium sulphide thin films: preparation and characterization". In: *Thin Solid Films* 340.1 (1999), pp. 18–23. ISSN: 00406090. DOI: 10.1016/S0040-6090(98)00980-8.

[43] Whatek Kim and Changdae Kim. "Optical energy gaps of beta-In2S3 thin films grown by spray pyrolysis". In: *Journal of Applied Physics* 2631.1986 (2013), pp. 2–5. DOI: 10.1063/1.337137.

[44] Thierno Sall et al. "Synthesis of In2S3 thin films by spray pyrolysis from precursors with different [S]/[In] ratios". In: *Journal of Semiconductors* 35.6 (2014). ISSN: 16744926. DOI: 10.1088/1674-4926/35/6/063002.

[45] S. Buecheler et al. "Interface formation between CuIn1-xGaxSe2 absorber and In2S3 buffer layer deposited by ultrasonic spray pyrolysis". In: *Thin Solid Films* 519.21 (2011), pp. 7560–7563. ISSN: 00406090. DOI: 10.1016/j.tsf.2011.01.370.

[46] Qing Gao et al. "Efficiency improvement of electrodeposition-processed Cu(In,Ga)Se2 solar cell with widen surface bandgap by spin-coating In2S3 thin film". In: *Applied Surface Science* 578.November 2021 (2022), p. 152063. ISSN: 0169-4332. DOI: 10.1016/j.apsusc.2021.152063.

[47] Lan Wang et al. "Solution-processed In 2 S 3 buffer layer for chalcopyrite thin film solar cells". In: *EPJ Photovoltaics* 7 (2016). ISSN: 21050716. DOI: 10.1051/epjpv/2016001.

[48] T. Yoshida et al. "Chemical bath deposition of band gap tailored indium sulfide thin films". In: *Electrochem. Soc. Proc.* 37 (1997), pp. 97–20.

[49] T. Asikainen, M. Ritala, and M. Leskelä. "Growth of In2S3 thin films by atomic layer epitaxy". In: *Applied Surface Science* 82-83.C (1994), pp. 122–125. ISSN: 01694332. DOI: [10.1016/0169-4332(94)90206-2](10.1016/0169-4332(94)90206-2).

[50] N. Boughuila et al. "Effet de la température de fabrication sur les propriétés structurales et morphologiques des couches épaisses de In2S3 "spray"". In: *J. Phys. III France* 7 (1997), pp. 1647–1660.

[51] Purvesh Soni et al. "Sputtering as a viable route for In2S3 buffer layer deposition in high efficiency Cu(In,Ga)Se2 solar cells". In: *Energy Science and Engineering* 7.2 (2019), pp. 478–487. ISSN: 20500505. DOI: [10.1002/ese3.295](10.1002/ese3.295).

[52] N. Naghavi et al. "High-efficiency copper indium gallium diselenide (CIGS) solar cells with indium sulfide buffer layers deposited by atomic layer chemical vapor deposition (ALCVD)". In: *Progress in Photovoltaics: Research and Applications* 443.March (2003), pp. 437–443. DOI: [10.1002/pip.508](10.1002/pip.508).

[53] Gustavo Baldissera et al. "Understanding the optical properties of ZnO 1 2 x S x and ZnO 1 2 x Se x alloys". In: 045704 (2016). DOI: [10.1063/1.4940700](10.1063/1.4940700).

[54] A. Grimm et al. "Zn(O, S) layers for chalcoyprite solar cells sputtered from a single target". In: *EPJ Photovoltaics* 3 (2012), pp. 3–6. ISSN: 21050716. DOI: 10.1051/epjpv/2012011.

[55] C. Platzer-Björkman et al. "Zn(O, S) buffer layers by atomic layer deposition in Cu(In, Ga)Se 2 based thin film solar cells: Band alignment and sulfur gradient". In: *Journal of Applied Physics* 100.4 (2006). ISSN: 00218979. DOI: [10.1063/1.2222067](10.1063/1.2222067).

[56] Raghu N. Bhattacharya, Miguel A. Contreras, and Glenn Teeter. "18.5% Copper indium gallium diselenide (CIGS) device using single-layer, chemical-bath-deposited ZnS(O,OH)". In: *Japanese Journal of Applied Physics, Part 2: Letters* 43.11 B (2004), pp. 1475–1477. ISSN: 00214922. DOI: 10.1143/JJAP.43.L1475.

[57] M. Buffière et al. "Fast chemical bath deposition of Zn(O,S) buffer layers for Cu(In,Ga)Se 2 solar cells". In: *Thin Solid Films* 519.21 (2011), pp. 7575–7578. ISSN: 00406090. DOI: 10.1016/j.tsf.2011.01.104.

[58] Van Ben Chu et al. "Waste- And Cd-Free Inkjet-Printed Zn(O,S) Buffer for Cu(In,Ga)(S,Se)2Thin-Film Solar Cells". In: *ACS Applied Materials and Interfaces* 13.11 (2021), pp. 13009–13021. ISSN: 19448252. DOI: 10.1021/acsami.0c16860.

[59] D. A. Johnston et al. "Chemical bath deposition of zinc sulfide based buffer layers using low toxicity materials". In: *Thin Solid Films* 403-404 (2002), pp. 102–106. ISSN: 00406090. DOI: 10.1016/S0040-6090(01)01536-X.

[60] J Drelich, Ch. Fang, and C.L. White. "Measurement of interfacial tension in fluid-fluid systems". In: *Encyclopedia of surface and colloid science* (2002), pp. 3152–3166.

[61] Joseph D Berry et al. "Measurement of surface and interfacial tension using pendant drop tensiometry". In: *journal of colloid and interface science* 454 (2015), pp. 226–237. ISSN: 0021-9797. DOI: 10.1016/j.jcis.2015.05.012.

[62] Tobias Winkler. "Determining the surface tension of liquids by measurements on pendant drops". In: *Technical Note* 49.40 (2010), pp. 1–5.

[63] Dealy J.M. and Wissbrun K.F. "Chapter 8 Flow in Capillaries , Slits and dies". In: *Melt Rheology and its role in plastics processing* (), pp. 298–344.

[64] *Rheosense VROC data sheet.* URL: https://www.rheosense.com/hs-fs/hub/296746/file-2438655427-pdf/Application_Notes/VROC_-_Principle.pdf?hsLang=en.

[65] L A Giannuzzi and F A Stevie. "A review of focused ion beam milling techniques for TEM specimen preparation". In: *Micron* 30 (1999), pp. 197–204.

[66] Meltem Sezen. "Focused Ion Beams (FIB) — Novel Methodologies and Recent Applications for Multidisciplinary Sciences". In: *Modern Electron Microscopy in Physical and Life Sciences* (2016). DOI: 10.5772/61634.

[67] Joseph I. Goldstein et al. "Focused Ion Beam Applications in the SEM Laboratory". In: *Scanning Electron Microscopy and X-Ray Microanalysis* (2018), pp. 517–528. DOI: 10.1007/978-1-4939-6676-9{_}30.

[68] Wilhelm Melitz et al. "Kelvin probe force microscopy and its application". In: *Surface Science Reports* 66.1 (2011), pp. 1–27. ISSN: 01675729. DOI: 10.1016/j.surfrep.2010.10.001.

[69] Akhilesh Pandey. "Structural characterization of polycrystalline thin films by X-ray diffraction techniques". In: *Journal of Materials Science: Materials in Electronics* 32.2 (2021), pp. 1341–1368. ISSN: 1573-482X. DOI: 10.1007/s10854-020-04998-w.

[70] P. Scherrer and P. Debye. "Determination of the Size and Internal Structure of Colloidal Particles using X-Rays". In: *Nachrichten von der Gesellschaft der Wissenschaften zu Göttingen, Mathematisch-Physikalische Klasse* 2 (1918), pp. 98–100.

[71] J.I.; Langford and A.J.C. Wilson. "Scherrer after sixty years: a survey and some new results in the determination of crystallite size". In: *J. Appl. Cryst.* 11 (1978), pp. 102–113. DOI: 10.1061/9780784479896.140.

[72] De Graef M. *Introduction to conventional transmission electron microscopy: Basic crystallography 1.1.* 2010. ISBN: 9780511615092.

[73] Gatan. *Periodic table.* URL: https://www.edax.com/resources/interactive-periodic-table#thumb.

[74] D. Nanda Gopala Krishna and John Philip. "Review on surface-characterization applications of X-ray photoelectron spectroscopy (XPS): Recent developments and challenges". In: *Applied Surface Science Advances* 12.November (2022), p. 100332. ISSN: 26665239. DOI: 10.1016/j.apsadv.2022.100332.

[75] Andrzej Kudelski. "Analytical applications of Raman spectroscopy". In: *Talanta* 76.1 (2008), pp. 1–8. ISSN: 00399140. DOI: 10.1016/j.talanta.2008.02.042.

[76] Jeffrey L. Taylor and Perkin Ellmer. "Integrating Sphere Functionality : The Scatter Transmission Measurement". In: *Technical note Perkin Elmer* (2013), pp. 1–6.

[77] Thomas Paul Weiss et al. "Thin-film (Sb,Bi)2Se3 Semiconducting layers with tunable band gaps below 1 ev for photovoltaic applications". In: *Physical Review Applied* 14.2 (2020), p. 1. ISSN: 23317019. DOI: 10.1103/PhysRevApplied.14.024014.

[78] Alex Redinger and Susanne Siebentritt. "Optical properties and electronic structure of amorphous germanium". In: *Phys. stat. sol.* 15 (1966), p. 627. DOI: 10.1002/9781118437865.ch16.

[79] C. Honsberg and S. Bowden. *PV education.* URL: https://www.pveducation.org/.

[80] Arno H M Smets et al. "Solar Cell Parameters and Equivalent Circuit". In: *Solar energy : the physics and engineering of photovoltaic conversion, technologies and systems* (2016), pp. 113–121. URL: https://ocw.tudelft.nl/wp-content/uploads/solar_energy_section_9_1_9_3.pdf.

[81] Tetsuya Ishida, Koichi Maekawa, and Toshiharu Kishi. "Enhanced modeling of moisture equilibrium and transport in cementitious materials under arbitrary temperature and relative humidity history". In: *Cement and Concrete Research* 37.4 (2007), pp. 565–578. ISSN: 00088846. DOI: 10.1016/j.cemconres.2006.11.015.

[82] F. A.M.M. Gonalves et al. "PVT, viscosity, and surface tension of ethanol: New measurements and literature data evaluation". In: *Journal of Chemical Thermodynamics* 42.8 (2010), pp. 1039–1049. ISSN: 00219614. DOI: 10.1016/j.jct.2010.03.022.

[83] Ibrahim Sadek Khattab et al. "Density, viscosity, and surface tension of water+ethanol mixtures from 293 to 323K". In: *Korean Journal of Chemical Engineering* 29.6 (2012), pp. 812–817. ISSN: 02561115. DOI: 10.1007/s11814-011-0239-6.

[84] Tejraj M. Aminabhavi and Bindu Gopalakrishna. "Density, Viscosity, Refractive Index, and Speed of Sound in Aqueous Mixtures of N,N-Dimethylformamide, Dimethyl Sulfoxide, N,N-Dimethylacetamide, Acetonitrile, Ethylene Glycol, Diethylene Glycol, 1,4-Dioxane, Tetrahydrofuran, 2-Methoxyethanol, and 2-Ethox". In: *Journal of Chemical and Engineering Data* 40.4 (1995), pp. 856–861. ISSN: 15205134. DOI: 10.1021/je00020a026.

[85] R. Belda, J. V. Herraez, and O. Diez. "A study of the refractive index and surface tension synergy of the binary water/ethanol: Influence of concentration". In: *Physics and Chemistry of Liquids* 43.1 (2005), pp. 91–101. ISSN: 00319104. DOI: 10.1080/00319100512331327342.

[86] G. Raina, G. U. Kulkarni, and C. N.R. Rao. "Mass spectrometric determination of the surface compositions of ethanol-water mixtures". In: *International Journal of Mass Spectrometry* 212.1-3 (2001), pp. 267–271. ISSN: 13873806. DOI: 10.1016/S1387-3806(01)00461-4.

[87] P.K. Weissenborn and R.J. Pugh. "Surface Tension of Aqueous Solutions of Electrolytes: Relationship with Ion Hydration, Oxygen Solubility, and Bubble Coalescence". In: *journal of colloid and interface science* 184 (1996), pp. 550–563.

[88] S. Song and C. Peng. "Viscosities of Binary and Ternary Mixtures of Water , Alcohol , Acetone , and Hexane Viscosities of Binary and Ternary Mixtures of Water , Alcohol , Acetone , and Hexane". In: *Journal of dispersion science and technology* October 2013 (), pp. 37–41. DOI: 10.1080/01932690802313006.

[89] Jacob N. Israelachvili. *Intermolecular and surface forces*. 2011. ISBN: 9780123751829. DOI: 10.1021/ie50534a061.

[90] Arun Nikumbh and Ganesh Kulkarni. "Density and Viscosity Study of Binary Mixtures of Ethanol -Water at Different Temperatures". In: *science journal of pure and applied chemistry* 1 (2013), pp. 1–13. DOI: 10.7237/sjpac/196.

[91] F J Millero et al. "Viscosity of Water at Various Temperatures". In: *The Journal of Physical Chemistry* 90.23 (1968), pp. 34–39.

[92] *Anton Paar*. URL: https://wiki.anton-paar.com/en/ethanol/.

[93] Ibrahim S. Khattab et al. "Density, viscosity, surface tension, and molar volume of propylene glycol + water mixtures from 293 to 323 K and correlations by the Jouyban–Acree model". In: *Arabian Journal of Chemistry* 10 (2017), S71–S75. ISSN: 18785352. DOI: 10.1016/j.arabjc.2012.07.012. URL: http://dx.doi.org/10.1016/j.arabjc.2012.07.012.

[94] Tongfan Sun, Amyn S Teja, and Biomolecular Engineering. "Density , Viscosity and Thermal Conductivity of Aqueous Solutions of Propylene Glycol , Dipropylene Glycol , and Tripropylene Glycol between 290 K and 460 K". In: *J. Chem. Eng. Data* 49 (2004), pp. 1311–1317.

[95] Grinnell Jones and Malcolm Dole. "The viscosity of aqueous solutions of strong electrolytes with special reference to barium chloride". In: *Journal of the American Chemical Society* 51.10 (1929), pp. 2950–2964. ISSN: 15205126. DOI: 10.1021/ja01385a012.

[96] Muhammad Afzal, Muhammad J. Iqbal, and Habib Ahmad. "Temperature Dependence of Viscosity B-Coefficients of Aqueous Solutions of Chlorides of Na+, K+, Mg2+, Ca2+, Ba2+, Sr2+, Co2+, Ni2+, Cu2+ and Cr3+". In: *Collection of Czechoslovak Chemical Communications* 59.6 (1994), pp. 1296–1300. ISSN: 0010-0765. DOI: 10.1135/cccc19941296.

[97] Y. Marcus. "Viscosity B-coefficients, structural entropies and heat capacities, and the effects of ions on the structure of water". In: *Journal of Solution Chemistry* 23.7 (1994), pp. 831–848. ISSN: 00959782. DOI: 10.1007/BF00972677.

[98] William H.R. Shaw and David G. Walker. "The Decomposition of Thiourea in Water Solutions". In: *Journal of the American Chemical Society* 78.22 (1956), pp. 5769–5772. ISSN: 15205126. DOI: 10.1021/ja01603a014.

[99] Rehana Saeed et al. "Viscosities of ammonium salts in water and ethanol + water systems at different temperatures". In: *Journal of Molecular Liquids* 146.3 (2009), pp. 112–115. ISSN: 01677322. DOI: 10.1016/j.molliq.2009.02.009.

[100] Sonika et al. "Molecular Interactions of Transition Metal Chlorides in Water and Water–Ethanol Mixtures at 298–318 K on Viscometric Data". In: *Russian Journal of Physical Chemistry A* 92.13 (2018), pp. 2701–2709. ISSN: 00360244. DOI: 10. 1134/S0036024418130307.

[101] Brian Derby. "Inkjet Printing of Functional and Structural Materials: Fluid Property Requirements, Feature Stability, and Resolution". In: *Annual Review of Materials Research* 40.1 (2010), pp. 395–414. ISSN: 1531-7331. DOI: 10.1146/annurev-matsci-070909-104502.

[102] Graham D Martin, Stephen D Hoath, and Ian M Hutchings. "Inkjet printing - the physics of manipulating liquid jets and drops". In: *journal of physics: Conference series* 105 (2008). DOI: 10.1088/1742-6596/105/1/012001.

[103] Stephen D Hoath. *Fundamentals of inkjet printing*. 2016. ISBN: 9783527337859.

[104] N Reis and B Derby. "Experiments of Droplet Formation". In: *Materials Research* 625 (2000), pp. 117–122.

[105] P.C. Duineveld et al. "Ink-jet printing of polymer light-emitting devices". In: *Proc. SPIE* 4464 (2001), pp. 59–67.

[106] C D Stow and M G Hadfield. "An experimental investigation of fluid flow resulting from the impact of a water drop with an unyielding dry surface". In: *Proceedings of the Royal Society of London. A. Mathematical and Physical Sciences* 373.1755 (1981), pp. 419–441. ISSN: 0080-4630. DOI: 10.1098/rspa.1981.0002.

[107] Brian Derby. "Experimental study of the parameters for stable drop-on-demand inkjet performance". In: *physics of fluids* 31 (2019). DOI: 10.1063/1.5085868.

[108] Eunjeong Kim and Jehyun Baek. "Numerical study on the effects of non-dimensional parameters on drop-on-demand droplet formation dynamics and printability range in the up-scaled model". In: *Physics of Fluids* 24.8 (2012). ISSN: 10706631. DOI: 10.1063/1.4742913.

[109] P. Krüger, R. Knes, and J. Friedrich. "Surface cleaning by plasma-enhanced desorption of contaminants (PEDC)". In: *Surface and Coatings Technology* 112.1-3 (1999), pp. 240–244. ISSN: 02578972. DOI: 10.1016/S0257-8972(98)00777-4.

[110] Zhihu Zhou et al. "The Fundamental Mechanisms of Laser Cleaning Technology and Its Typical Applications in Industry". In: *Processes* 11.5 (2023). ISSN: 22279717. DOI: 10.3390/pr11051445.

[111] Rajiv Kohli. *UV-Ozone Cleaning for Removal of Surface Contaminants*. Vol. 8. Elsevier Inc., 2015, pp. 71–104. ISBN: 9780323299619. DOI: 10.1016/b978-0-323-29961-9.00002-8.

[112] D. K. Owens and R. C. Wendt. "Estimation of the surface free energy of polymers". In: *Journal of Applied Polymer Science* 13.8 (1969), pp. 1741–1747. ISSN: 10974628. DOI: 10.1002/app.1969.070130815.

[113] Robert J. Good and Carel J. van Oss. "The Modern Theory of Contact Angles and the Hydrogen Bond Components of Surface Energies". In: *Modern Approaches to Wettability* (1992), pp. 1–27. DOI: 10.1007/978-1-4899-1176-6{_}1.

[114] Frederick M Fowkes. "Attractive Forces at Interfaces". In: *the interface symposium 5* 56.12 (1964).

[115] J.H. Hildebrand, J.M Prausnitz, and R.L. Scott. *The solubility of gases, liquids and solids:Regular and related solutions.* 1970.

[116] Kenneth A Connors and James L Wright. "Dependence of Surface Tension on Composition of Binary Aqueous-Organic Solutions". In: *Analytical Chemistry* 61 (1989), pp. 194–198.

[117] Ziyang Zhang et al. "Binary Liquid Mixture Contact-Angle Measurements for Precise Estimation of Surface Free Energy". In: *Langmuir* (2019). DOI: 10.1021/acs.langmuir.9b01252.

[118] Karin Jacobs, Ralf Seemann, and Stephan Herminghaus. "Stability and Dewetting of Thin Liquid Films". In: *arXiv* (2008), pp. 243–265. DOI: 10.1142/9789812818829{_}0010.

[119] Robert D Deegan, Olgica Bakajin, and Todd F Dupont. "Capillary flow as the cause of ring stains from dried liquid drops". In: *Nature* 389 (1997), pp. 827–829.

[120] Mainak Majumder et al. "Overcoming the " Coffee-Stain " Effect by Compositional Marangoni-flow assisted drop drying". In: *The Journal of Physical Chemistry B* 116 (2012), pp. 6536–6542.

[121] *Accu Dyne Test.* URL: https://www.accudynetest.com/surface_tension_table.html.

[122] Yanan Li et al. "Rate-dependent interface capture beyond the coffee-ring effect". In: *Nature Publishing Group* April (2016), pp. 1–8. DOI: 10.1038/srep24628. URL: http://dx.doi.org/10.1038/srep24628.

[123] Dong Hyeop Shin et al. "Study of Band Structure at the Zn(S,O,OH)/Cu(In,Ga)Se2 Interface via Rapid Thermal Annealing and Their Effect on the Photovoltaic Properties". In: *ACS Applied Materials and Interfaces* 5 (2013), pp. 12921–12927.

[124] Jae-hyung Wi et al. "Photovoltaic Performance and Interface Behaviors of Cu(In,Ga)Se2 Solar Cells with a Sputtered-Zn(O,S) Buffer Layer by High-Temperature Annealing". In: *ACS Applied Materials and Interfaces* (2015). DOI: 10.1021/acsami.5b04815.

[125] Kairi Otto et al. "Structure and evolved gas analyses (TG/DTA-MS and TG-FTIR) of mer-trichlorotris(thiourea)-indium(III), a precursor for indium sulfide thin films". In: *Journal of Thermal Analysis and Calorimetry* 105.1 (2011), pp. 83–91. ISSN: 13886150. DOI: 10.1007/s10973-011-1524-7.

[126] R. Souissi et al. "Substrate temperature effect on microstructure, oxygen adsorption and ethanol sensing response of sprayed In2S3 films". In: *Journal of Materials Science: Materials in Electronics* 30.22 (2019), pp. 20069–20078. ISSN: 1573482X. DOI: 10.1007/s10854-019-02378-7.

[127] B Hemanth Kumar and S Shaji M C Santhosh. "Fabrication of visible light photodetector using co - evaporated Indium Sulfide thin films". In: *Journal of Materials Science: Materials in Electronics* 0123456789 (2019). ISSN: 1573-482X. DOI: 10.1007/s10854-019-02152-9.

[128] Victor R Van Maris et al. "Impact of UV-Induced Ozone and Low-Energy Ar + -Ion Cleaning on the Chemical Structure of Cu (In ,Ga)(S,Se)2 Absorber Surfaces". In: *Journal of Applied Physics* 128.15 (2020), pp. 1–8. DOI: 10.1063/5.0020253.

[129] K Sharma et al. "Expanding Thermal Plasma Chemical Vapour Deposition of ZnO : Al Layers for CIGS Solar Cells". In: 2014 (2014).

[130] Alice Debot et al. "Inkjet-printed indium sulfide buffer layer for Cu(In,Ga)(S,Se)2 thin film solar cells". In: *Thin Solid Films* 745.December 2021 (2022). ISSN: 00406090. DOI: 10.1016/j.tsf.2022.139096.

[131] Robert Baier et al. "Electronic properties of grain boundaries in Cu(In,Ga)Se 2 thin films with various Ga-contents". In: *Solar Energy Materials and Solar Cells* 103 (2012), pp. 86–92. ISSN: 09270248. DOI: 10.1016/j.solmat.2012.04.002.

[132] David Regesch et al. "Degradation and passivation of CuInSe 2 Degradation and passivation of CuInSe2". In: *Applied Physics Letters* 101 (2012). DOI: 10.1063/1.4752165.

[133] W K Metzger et al. "Recombination kinetics and stability in polycrystalline Cu (In , Ga) Se 2 solar cells". In: *Thin Solid Films* 517 (2009), pp. 2360–2364. DOI: 10.1016/j.tsf.2008.11.050.

[134] Qijie Guo et al. "Sulfide Nanocrystal Inks for Dense Cu(In1- x Ga x)(S1 - y Se y)2 Absorber Films and Their Photovoltaic Performance". In: *Nano letters* 9 (2009), pp. 3060–3065.

[135] Wei Liu et al. "12% Efficiency CuIn(Se,S)2 photovoltaic device prepared using a hydrazine solution process". In: *Chemistry of Materials* 22.3 (2010), pp. 1010–1014. ISSN: 08974756. DOI: 10.1021/cm901950q.

[136] Xianzhong Lin et al. "11.3% efficiency Cu(In,Ga)(S,Se)2 thin film solar cells: Via drop-on-demand inkjet printing". In: *Energy and Environmental Science* 9.6 (2016), pp. 2037–2043. ISSN: 17545706. DOI: 10.1039/c6ee00587j.

[137] Steven M Mcleod et al. "Synthesis and characterization of 15 % efficient CIGSSe solar cells from nanoparticle inks". In: *Progress in Photovoltaics: Research and Applications* (2015). DOI: 10.1002/pip.

[138] C Laurencic, L Arzel, and N Barreau. "Investigation of Cu(In,Ga)Se2 / In2S3 diffuse interface by Raman scattering". In: *Thin Solid Films* 519.21 (2011), pp. 7553–7555. ISSN: 0040-6090. DOI: 10.1016/j.tsf.2010.12.089.

[139] Jes K. Larsen et al. "Sulfurization of Co-Evaporated Cu(In,Ga)Se2 as a Postdeposition Treatment". In: *IEEE Journal of Photovoltaics* 8.2 (2018), pp. 604–610. ISSN: 21563381. DOI: 10.1109/JPHOTOV.2018.2793759.

[140] Wolfram Witte et al. "Influence of the GA content on the MO/CU(IN,GA)SE2 interface formation". In: *Conference Record of the 2006 IEEE 4th World Conference on Photovoltaic Energy Conversion, WCPEC-4* 1 (2006), pp. 553–556. DOI: 10.1109/WCPEC.2006.279515.

[141] Sanping Wu et al. "Over 12 % efficient low-bandgap CuIn (S , Se) 2 solar cells with the absorber processed from aqueous metal complexes solution in air". In: *Nano Energy* 62.June (2019), pp. 818–822. ISSN: 2211-2855. DOI: 10.1016/j.nanoen.2019.06.010.

[142] R. Geetha Kumari et al. "Raman spectral investigation of thiourea complexes". In: *Spectrochimica Acta - Part A: Molecular and Biomolecular Spectroscopy* 73.2 (2009), pp. 263–267. ISSN: 13861425. DOI: 10.1016/j.saa.2009.02.009.

[143] M. S. Mathur, J. H.K. Ho, and G. C. Tabisz. "Raman Study Of Incl3". In: *Spectroscopy Letters* 14.6 (1981), pp. 395–404. ISSN: 15322289. DOI: 10.1080/00387018108062599.

[144] N. Barreau et al. "Recent studies on In2S3 containing oxygen thin films". In: *Solid State Communications* 122.7-8 (2002), pp. 445–450. ISSN: 00381098. DOI: 10.1016/S0038-1098(02)00099-6.

[145] Carl V Thompson. "Solid-State Dewetting of Thin Films". In: *Annual Review of materials research* April (2012), pp. 1–36. DOI: 10.1146/annurev-matsci-070511-155048.

[146] T.T. John et al. "Characterization of spray pyrolysed indium sulfide thin films". In: *Semicond. Sci. Technol.* 491.18 (2003), pp. 491–500.

[147] S. Buecheler et al. "Ultrasonically sprayed indium sulfide buffer layers for Cu(In,Ga) (S,Se)2 thin-film solar cells". In: *Thin Solid Films* 517.7 (2009), pp. 2312–2315. ISSN: 00406090. DOI: 10.1016/j.tsf.2008.10.135.

[148] D. Bhattacharyya, S. Chaudhuri, and A.K. Pal. "Bandgap and optical transitions reflectance measurements". In: *vacuum* 43 (1992), pp. 313–316.

[149] Pankove J.I. *Optical processes in semiconductors.* 1971. ISBN: 9780486138701.

[150] N. Barreau et al. "Optical Properties of Wide Band Gap Indium Sulphide Thin Films Obtained by Physical Vapor Deposition". In: *Physica status solidi (A) applied research* 184 (2001), pp. 179–186. DOI: 10.1002/1521-396X(200103)184.

[151] A R Zanatta. "Revisiting the optical bandgap of semiconductors and the proposal of a unified methodology to its determination". In: *Scientific Reports* October 2018 (2019), pp. 1–12. ISSN: 2045-2322. DOI: 10.1038/s41598-019-47670-y. URL: http://dx.doi.org/10.1038/s41598-019-47670-y.

[152] Michael J. Hertaeg et al. "Predicting coffee ring formation upon drying in droplets of particle suspensions". In: *Journal of Colloid and Interface Science* 591 (2021), pp. 52–57. ISSN: 10957103. DOI: 10.1016/j.jcis.2021.01.092. URL: https://doi.org/10.1016/j.jcis.2021.01.092.

[153] Matteo Salvalaglio et al. "Uncovering molecular details of urea crystal growth in the presence of additives". In: *J. Am. Chem. Soc.* 134 (2012), pp. 17221–17233.

[154] M. A. Baker et al. "XPS investigation of preferential sputtering of S from MoS2 and determination of MoSx stoichiometry from Mo and S peak positions". In: *Applied Surface Science* 150.1 (1999), pp. 255–262. ISSN: 01694332. DOI: 10.1016/S0169-4332(99)00253-6.

[155] L E Brus. "Electron – electron and electronhole interactions in small semiconductor crystallites : The size dependence of the lowest excited electronic state". In: *The Journal of Chemical Physics* 4403.80 (1984). DOI: 10.1063/1.447218.

[156] A D Yoffe. "Low-dimensional systems : quantum size effects and electronic properties of semiconductor microcrystallites (zero-dimensional systems) and some quasi-two-dimensional systems". In: *Advances in Physics* July 2012 (2006), pp. 37–41.

[157] Sergey V Gaponenko and Hilmi Volkan Demir. *Applied Nanophotonics.* 2019. ISBN: 9781107145504.

[158] Y Feng et al. "Can Tauc plot extrapolation be used for direct-band-gap semiconductor nanocrystals ? Can Tauc plot extrapolation be used for direct-band-gap semiconductor nanocrystals ?" In: 125701 (2015). DOI: 10.1063/1.4916090.

[159] Cherie R Kagan and Christopher B Murray. "dot solids". In: *Nature Publishing Group* November (2015), pp. 1–14. ISSN: 1748-3387. DOI: 10.1038/nnano.2015.247. URL: http://dx.doi.org/10.1038/nnano.2015.247.

[160] Wayne Rasband. *ImageJ*. URL: https://imagej.net/ij/index.html.

[161] J. P. Borah, J. Barman, and K.C. Sarma. "Structual and optical properties of ZnS nanoparticles". In: *Chalcogenide Letters* 5.9 (2008), pp. 201–208.

[162] Yashaswi Nandan and Mohan Singh Mehata. "Wavefunction Engineering of Type-I/Type-II Excitons of CdSe/CdS Core-Shell Quantum Dots". In: *Scientific Reports* 9.1 (2019), pp. 1–11. ISSN: 20452322. DOI: 10.1038/s41598-018-37676-3.

[163] Pragati Kumar et al. "Nanotwinning and structural phase transition in CdS quantum dots". In: *Nanoscale Research Letters* 7.1 (2012), p. 1. ISSN: Nanoscale Research Letters. DOI: 10.1186/1556-276X-7-584. URL: Nanoscale%20Research%20Letters.

[164] Seong Yeon Kim et al. "Application of a Sn4+ doped In2S3 thin film in a CIGS solar cell as a buffer layer". In: *Sustainable Energy and Fuels* 4.1 (2019), pp. 362–368. ISSN: 23984902. DOI: 10.1039/c9se00778d.

[165] M. K. Singh. "Controlling the aqueous growth of urea crystals with different growth inhibitors: a molecular-scale study". In: *RSC Advances* 11.21 (2021), pp. 12938–12950. ISSN: 20462069. DOI: 10.1039/d0ra10401a.

[166] Hao Tong et al. "Influences of Mg concentration in ZnMgO film on energy band alignment at CIGSSe / Zn1-x Mgx O interface and performances of CIGSSe solar cells". In: *Solar Energy* 246.June (2022), pp. 216–223. ISSN: 0038-092X. DOI: 10.1016/j.solener.2022.09.039. URL: https://doi.org/10.1016/j.solener.2022.09.039.

[167] Maruzen. *Science Handbook*. 2002.

[168] William Ramsay and John Shields. "The Variation of Molecular Surface-Energy with Temperature." In: *Royal Society Philosophical transaction* 184 (1893), pp. 647–673. DOI: 10.1098/rsta.1893.0013.

[169] Louis Shnidman. "The solubility of thiourea in water, methanol and ethanol". In: *J. Phys. Chem.* 3 (1933), pp. 693–700.

[170] J. Eastoe and J. S. Dalton. "Dynamic surface tension and adsorption mechanisms of surfactants at the air-water interface". In: *Advances in Colloid and Interface Science* 85.2 (2000), pp. 103–144. ISSN: 00018686. DOI: 10.1016/S0001-8686(99)00017-2.

[171] Sander Kommeren et al. "Combining solvents and surfactants for inkjet printing PEDOT:PSS on P3HT/PCBM in organic solar cells". In: *Organic Electronics* 61.February (2018), pp. 282–288. ISSN: 15661199. DOI: 10.1016/j.orgel.2018. 06.004. URL: https://doi.org/10.1016/j.orgel.2018.06.004.

[172] John R. Vig. "UV/ozone cleaning of surfaces". In: *Proceedings - The Electrochemical Society* 90.9 (1990), pp. 105–113. ISSN: 01616374. DOI: 10.1116/1.573115.

[173] Hachioji-shi. "Ultraviolet-Ozone Surface Treatment, Three Bond Tech. News". In: *Three Bond Technical News* (1987), pp. 1–10.

Acronyms and symbols

Acronym	Description
AFM	Atomic Force Microscopy
CB	Conduction band
CBM	Conduction band minimum
CBD	Chemical bath deposition
CIGSe	$Cu(In,Ga)Se_2$
CIGSSe	$Cu(In,Ga)(S,Se)_2$
DOD	Drop on demand
DS	Drop spacing
EDX	Energy dispersive X-Ray
EQE	External quantum efficiency
FFT	Fast Fourier Transform
FIB SEM	Focused Ion Beam Secondary Ion Microscopy
FWHM	Full width at half maximum
GI-XRD	Grazing incidence X-Ray diffraction
HIM-SIMS	Helium Ion Microscopy with Secondary Ion Mass Spectrometry
J-V	Current density - Voltage characteristics
Oh	Ohnesorge number
PL	Photoluminescence
Ppg	Propylene glycol
PV	Photovoltaics
qFLs	Quasi Fermi level splitting
Re	Reynold number
SAED	Selected Area Electron Diffraction
SE	Secondary electron
SEM	Scanning electron microscopy
SIM	Secondary Ion Microscopy
TEM	Transmission Electron Microscopy
TU	Thiourea
VB	Valence band
VBM	Valence band maximum
We	Weber number
XPS	X-Ray Phototoelectron Spectroscopy
Z	Inverse of Ohnesorge number

Symbol	Description
α	Absorption coefficient
γ	Surface tension
η	Viscosity
γ^p	Polar component of the free energy
γ^d	Dispersive component of the free energy
FF	Fill factor
V_{oc}	Open circuit voltage
J_{sc}	Short circuit current density
R_s	Serie resistance
R_{sh}	Shunt resistance
eff	Efficiency
E_g	Band gap
E_F	Fermi level
k_B	Boltzmann constant
λ	Wavelength
N_A	Avogadro number